University of Southampton

Faculty of Engineering and Physical Sciences

Chemistry

A Spectroscopic Investigation of the Structure and Interactions of Hierarchical Zeotype Catalysts for the Beckmann Rearrangement

by

Stephanie Chapman

Thesis for the degree of Doctor of Philosophy

March 2019

University of Southampton

Abstract

Faculty of Engineering and Physical Sciences

Chemistry

Thesis for the degree of Doctor of Philosophy

A Spectroscopic Investigation of the Structure and Interactions of Hierarchical Zeotype Catalysts for the Beckmann Rearrangement

by

Stephanie Chapman

The acid-catalysed Beckmann rearrangement (BR) of cyclohexanone oxime is a key step in the production of ε-caprolactam, a high-value bulk chemical and the precursor to nylon-6. Conventionally, the BR is effected by a mineral acid catalyst, but the hazards and inefficiencies of the homogeneous process have motivated research into heterogeneous alternatives. Whilst zeotype materials have proven effective as solid-acid catalysts for the BR, their performance is subject to the steric constraints of the micropores. In this regard, the development of hierarchically-porous (HP) zeotypes has provided a means to combine the catalytic properties of a microporous (MP) framework with the mass transport properties of a secondary, mesoporous network.

Recently, organosilane-templated HP silicoaluminophosphates (SAPOs) were investigated as catalysts for the vapour-phase BR, with the result of enhanced activity and lifetime relative to their MP analogues. In this case, the improved performance of the HP SAPOs was not solely attributed to mass transport effects, since the organosilane mesoporogen also created weakly acidic silanol sites in the mesopores. The silanol sites were implicated in the catalytic activity of the HP SAPOs, yet the mode and degree to which they might have facilitated the BR was unknown. To this end, an integrated empirical and theoretical study has been undertaken to determine whether the siliceous mesopores play a catalytic role in the BR, or simply facilitate mass transport to the Brønsted acid sites in the micropores. In this undertaking, neutron spectroscopies have provided a unique insight into the substrate-framework interactions in HP SAPOs, allowing reactive species to be studied near independent of the catalyst matrix. Inelastic neutron spectroscopy (with complementary FTIR, NMR, and computational studies) has evidenced substrate-activating interactions in the mesopores, which facilitate the protonation of cyclohexanone oxime in a physical mixture at ambient temperature. Moreover, quasi-elastic neutron spectroscopy has revealed that these substrate-silanol interactions lead to an interesting interplay with the molecular dynamics in HP SAPO. Significantly, these studies suggest that the HP structure allows the siliceous mesopores to act in concert with the Brønsted sites in the micropores to catalyse the BR.

These investigations also provided a rationale for the application of the organosilane mesoporogen in the synthesis of a new HP SAPO-37 material. By this synthetic route, HP SAPO-37 was prepared the crystalline FAU-type structure, notwithstanding the mesoporosity

detected by low-angle XRD, gas adsorption, positron annihilation lifetime spectroscopy, and TEM imaging. Probe-based characterisation (including TPD, FTIR, and NMR) revealed that the acidity of SAPO-37 was moderated by soft-templating, yet this proved effective for the vapour-phase BR (300 °C), in which HP SAPO-37 maintained > 99 % conversion of cyclohexanone oxime (whilst the activity of MP SAPO-37 declined to < 35 %) over 8 hours on-stream. The sustained performance of HP SAPO-37 also elaborated the role of the siliceous mesopores, which were identified to increase resistance to deactivation through coking.

These investigations demonstrate how a multifaceted spectroscopic and computational analysis can support the design of targeted, solid acid-catalysts.

Table of Contents

Table of Tables

Table of Figures

Research Thesis: Declaration of Authorship

Print name:	Stephanie Chapman

Title of thesis:	A Spectroscopic Investigation of the Structure and Interactions of Hierarchical Zeotype Catalysts for the Beckmann Rearrangement

I declare that this thesis and the work presented in it are my own and has been generated by me as the result of my own original research.

I confirm that:

1. This work was done wholly or mainly while in candidature for a research degree at this University;
2. Where any part of this thesis has previously been submitted for a degree or any other qualification at this University or any other institution, this has been clearly stated;
3. Where I have consulted the published work of others, this is always clearly attributed;
4. Where I have quoted from the work of others, the source is always given. With the exception of such quotations, this thesis is entirely my own work;
5. I have acknowledged all main sources of help;
6. Where the thesis is based on work done by myself jointly with others, I have made clear exactly what was done by others and what I have contributed myself;
7. Parts of this work have been published as:

Chapman, S.; O'Malley, A.; Miletto, I.; Carravetta, M.; Cox, P.; Gianotti, E.; Marchese, L.; Parker, S.; Raja, R., Integrated theoretical and empirical studies for probing substrate-framework interactions in hierarchical catalysts. *Chem. Eur. J.* **2019**, Accepted.

Chapman, S.; O'Malley, A.; Parker, S. F.; Raja, R., Comprehensive Vibrational Spectroscopic Characterization of Nylon-6 Precursors for Precise Tracking of the Beckmann Rearrangement. *ChemPhysChem* **2018**, *19* (23), 3196-3203

Chapman, S.; Potter, M.; Raja, R., The Molecular Design of Active Sites in Nanoporous Materials for Sustainable Catalysis. *Molecules* **2017**, *22* (12), 2127.

Chapman, S.; Raja, R., Expanding Beyond the Micropore: Catalysis with Hierarchical Architectures. *Adv. Sci. Lett.* **2017**, *23* (6), 5995-5997.

Poster presentation at the EuropaCat Conference 2017, Florence, Italy.

Oral presentation at the International Zeolite Conference 2016, Rio de Janeiro, Brazil.

Poster presentation at the ISIS Neutron Training Course 2016, Oxfordshire, U.K.

Poster presentation at the SpectroCat Workshop 2016, Caen, France.

Signature:		Date:	

Acknowledgements

As the start of my undergraduate degree, I would never have imagined that I might pursue a PhD in Chemistry. Nonetheless, as I have progressed through my academic career at the University of Southampton, the curiosity that was first sparked by my school science teachers has been fostered by my lecturers and peers. It was their enthusiasm that inspired me to pursue my studies in this fascinating and meaningful subject.

First and foremost, I wish to express my sincere and heartfelt thanks to my supervisor, Professor Robert Raja; I could not have asked for a more supportive mentor. His continued encouragement has enabled me to progress my research skills, gain confidence, and flourish. My time in his research group has given me the opportunity to travel abroad for both learning and collaborative research, which has been both intellectually stimulating and personally enriching.

I have also had the support of many scientific collaborators, who have kindly shared their time and expertise to allow me expand my scientific competences. I wish to thank AdvanSix Inc. for providing funding towards my PhD research project, and in particular Dr Scott Keenan and his team for their enlightening scientific discussions and constructive advice. Many thanks to Dr Marina Carravetta at the University of Southampton for her continued assistance in conducting solid-state NMR experiments, to Dr Cara Doherty of the CSIRO in Australia for providing access to the PALS technique, and to Dr Paul Cox for facilitating computational studies. To Professor Enrica Gianotti, Dr Ivana Miletto, and all the lovely people who made me feel so welcome when I visited the Università degli Studi del Piemonte Orientale in Alessandria - thank you for taking the time to assist me with FTIR experiments, introducing me to some amazing food and, of course, for all the espresso!

During my PhD studies, I have been fortunate to have had the rare and exciting opportunity to undertake neutron experiments at the ISIS Pulsed Neutron and Muon Source at the Rutherford Appleton Laboratories in Oxfordshire. I express my immense gratitude to the STFC for granting access to these facilities. I must also convey particular thanks to Dr Stewart Parker, Dr Alex O'Malley, Dr Ian Silverwood, and Dr Tristan Youngs for their time and assistance with beam times. I also kindly acknowledge Dr James Taylor and Hannah Dixon at the ISIS Hydrogen and Catalysis laboratory for their assistance with NH_3-TPD analyses.

Having worked in the Raja group since my summer placement as a second year undergraduate, I have been fortunate to work alongside many wonderful individuals. Whilst there have been many iterations of the Raja group, I have always known it to be a friendly and supportive environment (which is probably why I have never stayed away for long!). To this I

must credit my colleagues, who have made my time in the Raja group so enjoyable and entertaining, and for whose guidance and support I am most grateful. There are several people to whom I would like to give my special thanks. Firstly, Dr Matthew Potter who has been a source of knowledge and inspiration throughout my time in the Raja group, and to whom I am indebted for his time, support, advice, and friendship. Dr Stephanie Newland, the founding member of 'Team AlPO', who taught me the ropes in the lab, and Dr Christopher Hinde, arguably the person responsible for recruiting me to the Raja group when I was a fledgling undergraduate student in teaching labs. Thank you also to Sivan Van Aswegan and Will Webb for helping me to get re-established in the lab at the start of my PhD. And of course, to all the members of the Raja group who have helped to make my time here so enjoyable: Arran, Thomas, Agnieszka, Elpi, Jack, Dan, Panashe, Jaime, Marcos, Hamza, Sarah, Ingrid, Alice, and Josh – thank you. I would also like to thank my project students Ioli, Ryan, Shannon, and Lauren for their hard work and enthusiasm, I wish you all the best for the future.

I would like to give a special thanks to my wonderful friends and fellow PhD students, Cameron, India and Luke who have made this experience so much fun. Thanks for the hilarious stories, the tea, cake and ice cream breaks - and all the gym sessions that have gone some way to balance that out! I would also like to thank Will Richardson, whose kindness, patience, and support knows no bounds. You are so thoughtful and considerate, and always keep me smiling.

Lastly, I wish to express my heartfelt gratitude to my parents Rosemary and Colin, my sister Marysa, and to all my family. To you I dedicate my achievements, in the knowledge that I could never have accomplished so much without your love, support, and continued encouragement throughout my studies.

Abbreviations

ACI	Accessibility index
AF	Accessibility factor
AlPO	Aluminophosphate
ATR-IR	Attenuated Total Reflectance Infrared Spectroscopy
BET	Brunauer-Emmett-Teller
BJH	Barrett-Joyner-Halenda
B3LYP	Becke three-parameter Lee-Yang-Parr
BR	Beckmann rearrangement
CDO	Cyclohexanone-d_{10} oxime
CHA	Chabazite
CHN	Carbon, hydrogen, nitrogen
CHNS	Carbon, hydrogen, nitrogen, sulphur
CHO	Cyclohexanone oxime
CTAB	Hexadecyltrimethylammonium bromide
DFT	Density functional theory
DMOD	Dimethyloctadecyl[(3-(trimethoxysilyl)propyl]ammonium chloride
DNP	Double numerical plus polarization
DNP NMR	Dynamic nuclear polarisation nuclear magnetic resonance
2,6-dTBP	2,6-di-*tert*-butylpyridine
EISF	Elastic incoherent structure factor
elwin	Elastic window scan
EM	Electron microscopy
EPB	Extracted proton beamline
FAU	Faujasite
FCC	Fluid catalytic cracking
FID	Flame ionisation detector
FTIR	Fourier-transform infrared
FWHM	Full-width at half-maximum

GC	Gas chromatography
GGA	Generalised gradient approximation
HF	Hartree-Fock
HP	Hierarchically-porous
HWHM	Half-width at half-maximum
ICP-OES	Inductively coupled plasma optical emission spectroscopy
INS	Inelastic neutron scattering
IP	In-plane
IR	Infrared
ISC	Incoherent scattering cross-section
IUPAC	International Union of Pure and Applied Chemistry
IZA	International Zeolite Association
LDA	Local density approximation
MAS NMR	Magic-angle spinning nuclear magnetic resonance
MeAlPO	Metal-doped aluminophosphate
MM	Molecular mechanics
MOR	Mordenite
MP	Microporous
MTH	Methanol-to-hydrocarbon
MTO	Methanol-to-olefin
OEA	Organic elemental analysis
OES	Optical emission spectroscopy
OMS	Ordered mesoporous silicas
OOP	Out-of-plane
PALS	Positron annihilation lifetime spectroscopy
PBU	Primary building unit
PES	Potential energy surface
PFG NMR	Pulsed-field gradient nuclear magnetic resonance
Ps	Positronium

o-Ps	*ortho*-Positronium
p-Ps	*para*-Positronium
PSD	Pore-size distribution
QENS	Quasi-elastic neutron scattering
QM	Quantum mechanical
RF	Response factor
RRF	Relative retention factor
SAPO	Silicoaluminophosphate
SBU	Secondary building unit
SDA	Structure-directing agent
SE	Secondary electron
SEM	Scanning electron microscopy
TCD	Thermal conductivity detector
TEA	Triethylamine
TEAOH	Tetraethylammonium hydroxide
TEM	Transmission electron microscopy
TGA	Thermogravimetric analysis
TMAOH	Tetramethylammonium hydroxide
TOF	Time-of-flight
TPAOH	Tetra-*n*-propylammonium hydroxide
TPD	Temperature-programmed desorption
TS	Tkatcheko and Scheffer
USY	Ultra-stable Zeolite-Y
WHSV	Weight hourly space velocity
XRD	X-ray diffraction

Chapter 1 Introduction

1.1 Heterogeneous catalysis

A catalyst is a species that increases the rate of a thermodynamically-feasible process by providing a reaction pathway with transition states at a lower energy than the un-catalysed route (**Figure 1.1.1**).[1] Since catalysis is a kinetic phenomenon it does not modify the position of thermodynamic equilibrium, only the rate at which the equilibrium state is achieved.[2]

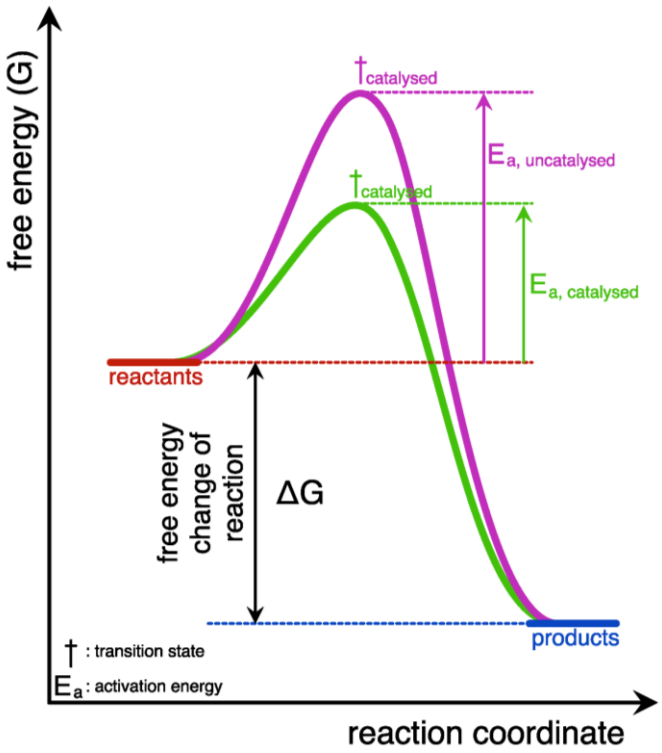

Figure 1.1.1: A comparison of the reaction profiles for a single-step transformation of reactant to product, with and without a catalyst. The catalysed pathway has a reduced activation energy (E_a) but the free energy change of the reaction (ΔG) remains unaltered.

There are many advantages in employing catalytic reagents, besides reducing the energetic requirements of a chemical process.[3] For example, an active catalyst can significantly increase the rate of substrate conversion,[2, 4] whilst a selective catalyst can improve atom economy by minimising by-product formation.[3, 5] The presence of a catalyst may also allow aggressive reagents to be substituted for more benign alternatives, or may be used to generate hazardous compounds *in situ*.[6] And since catalysts are not consumed in a reaction, they can facilitate numerous catalytic cycles,[4] which makes them an economical alternative to stoichiometric reagents.[5] Overall, catalysis has proven a viable means to improve the sustainability of a range of chemical reactions; hence their application in over 90 % of industrial processes.[5]

Many large-scale chemical processes in the fine-, bulk-, and petro-chemical industries employ heterogeneous catalysis,[2, 7, 8] where a solid-phase catalyst is interfaced with fluid-phase reagents. In industrial applications, a particular advantage of the heterogeneous catalyst is the relative ease with which it can be extracted (and subsequently recycled) from a liquid- or vapour-phase process.[4] Moreover, heterogeneous systems typically exhibit a high physicochemical stability, which makes them resilient to a wide range of operating conditions.[2]

As a surface reaction, the mechanism of heterogeneous catalysis can be broken down into a sequence of elementary steps.[2, 4, 9, 10] As conveyed in **Figure 1.1.2**, heterogeneous catalysis is the product of both chemical and physical processes, and so the overall reaction rate may not be determined by the surface chemistry alone.[9] For example, if a (liquid-phase) reaction suffers slow diffusion to/from the active site, catalysis may become mass transfer-limited, in which case the surface reaction is no longer the rate-determining step.[4] As such, an understanding of sorption and diffusion phenomena, as well as catalyst reactivity, is important in rationalising the outcome of a heterogeneously-catalysed process.[11]

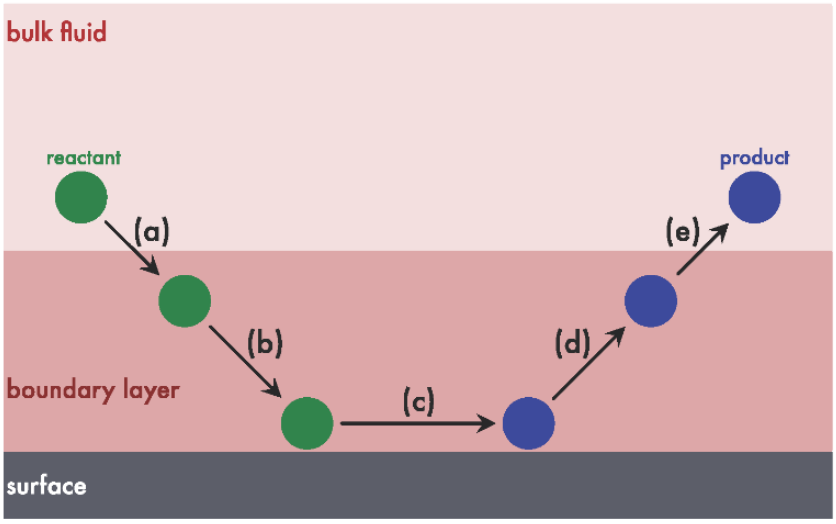

Figure 1.1.2: The process of heterogeneous catalysis occurs in a number of steps. The reactant diffuses from the bulk fluid, through the boundary layer **(a)** to adsorb on the solid surface **(b)**. Surface reaction transforms the reactant molecule to product **(c)**, which then diffuses across the boundary layer **(d)** to enter the bulk **(e)**.

1.2 Porous materials in catalysis

A porous material is a (typically solid) matrix that contains random or ordered voids (i.e. pores). [12] Typically, the nanoporous materials used in catalysis are classified under the IUPAC convention, which characterises the pore dimensions of micro- (< 2 nm), meso- (2 - 50 nm)

and macro- (> 50 nm) porous materials by their gas adsorption properties.[13, 14] Pores may also be characterised by their accessibility to the surroundings, such that an open pore is accessible from the external surface, whereas a closed pore is isolated within the material.[15] Unlike open porosity, closed pores do not influence the adsorption characteristics of a material; however, both types of pore can affect the mechanical properties of the system. In general, porous matrices have lower densities and larger surface areas than non-porous materials,[12] which is, in part, why they feature so prevalently in heterogeneous catalysis.[16] Since heterogeneous catalysis is restricted to the fluid-solid interface, a larger surface area of solid usually corresponds to an increased catalytic turnover.[7, 17] Where porous materials have surfaces available throughout their bulk,[18] a large number of active sites can be made available, per unit mass of solid.[19]

In many cases, the practical application of a porous material is dependent on the size, shape, and interconnectivity of its voids. For example, in catalysis, materials that contain channels and cavities of molecular dimensions are often used for shape-selective catalysis, which is achieved by regulation of the molecules that enter, leave, or form within the pores.[20, 21] For this, and other uses of the molecular sieving phenomenon, size exclusion is most effective when the pores are uniform, and have a narrow size-distribution. Indeed, many applications of nanoporous materials benefit from the more homogeneous physicochemical properties of ordered, porous materials, such as zeolites.[16, 18, 22]

1.3 Zeolites

Zeolites are a group of highly-crystalline, inorganic-oxide frameworks with general composition $A^{n+}_{x/n}[Si_{1-x}Al_xO_2].mH_2O$, where A^{n+} is an extra-framework cation.[23] The backbone of a zeolite comprises corner-sharing $[SiO_4]$ and $[AlO_4]$ tetrahedra, which are known as the T-atoms, or primary building units (PBUs) of the aluminosilicate network.[24] A secondary building unit (SBU) is a topological construct that is used to describe the extended, three-dimensional structure of a zeolite in terms of simpler components, such as chains, rings and polyhedra.[25] Each unique framework type also has an identifying three letter code, which is designated by the International Zeolite Association (IZA).[24]

Besides the framework architecture, the properties (and hence applications) of a zeolite will also depend on the elemental composition of the material.[26] Whereas a silicate network (which comprises only $[SiO_4]$ units) is electronically neutral, zeolites acquire a net negative charge for every tetravalent Al(III) species that is incorporated into the framework (**Figure 1.3.1**). Due to unfavourable electrostatic interactions, Al-O-Al linkages tend to be avoided (Lowenstein's rule) and, as such, the composition of the aluminosilicate backbone is

typically Si/Al ≥ 1.[27] In order to achieve net charge-neutrality, a zeolite will often accommodate charge-balancing guest cations (such as metal ions or small molecules), in addition to water.[28] The size, charge and location of these guest species in the framework can have a significant impact on the electrostatic, catalytic, and adsorptive properties of a zeolite.[26] For example, Brønsted acidity can be developed if the negative framework charge is compensated by a framework-bound proton, and subsequent dehydroxylation can be used to create Lewis acidic, trivalent aluminium sites.[29, 30]

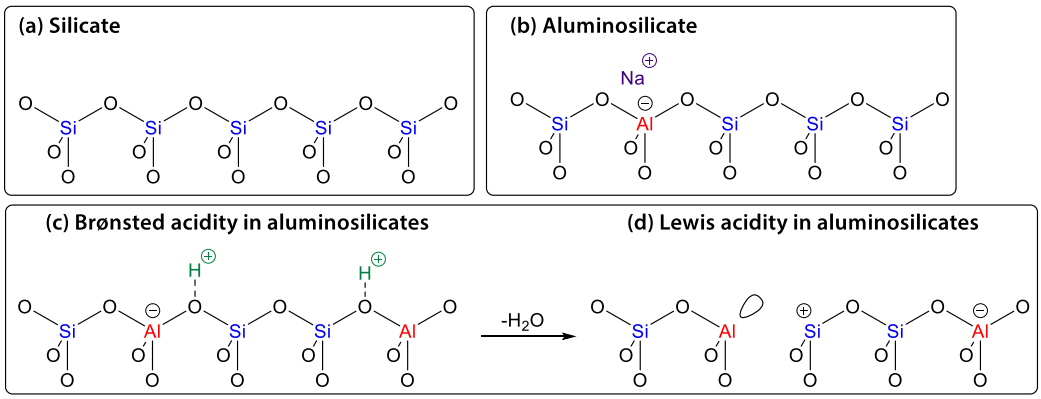

Figure 1.3.1: (a) The silicate network, which comprises [SiO_4] T-atoms, is charge-neutral. **(b)** In an aluminosilicate, the negative charge associated with each [AlO_4] T-atom is compensated by an extra-framework cation (e.g. Na^+). **(c)** If the counter-cation is a proton, the zeolite will contain Brønsted acid sites which can be **(d)** dehydroxylated to form Lewis acid centres.

The ability to manipulate both the framework composition and the identity of guest species has provided considerable scope to modulate the properties of zeolite materials. For example, by controlling the Si/Al ratio of the aluminosilicate backbone, it is possible to fine tune zeolite hydrophobicity,[31] thermochemical stability,[32] and (strength, density, and type of) acidity.[30, 33] By combination with properties such as large surface areas, high-stabilities, and molecular sieving capabilities, zeolites have found extensive application as solid-acid catalysts.[26, 28] In industry, zeolites are used on an immense scale in acid-catalysed processes such as hydrocarbon cracking, alkylation, and isomerisation.[30, 34, 35]

Another approach to modify the physicochemical characteristics of a zeolite is the isomorphous substitution of heteroatoms (e.g. Ti, Ga, P) into the aluminosilicate backbone.[26] The resulting 'zeotype' systems share many properties with zeolites but offer further scope to modify the structure and chemistry of the molecular sieves. One example is the selective oxidation catalyst, TS-1, which was created by doping small amounts of titanium into Silicalite-1 (MFI).[36] TS-1 is widely used in commercial redox transformations, including the epoxidation of olefins, the ammoximation of ketones, the oxidation of alkanes, and the hydroxylation of aromatics.[37]

1.4 Aluminophosphate molecular sieves

In 1982, Wilson *et al.* reported the synthesis of the aluminophosphates (AlPOs): the first, crystalline, inorganic molecular-sieves to be prepared without silicon.[38] The backbone of an AlPO is formed from an ordered assembly of [AlO_4] and [PO_4] T-atoms in strict alternation. Consequently, AlPOs are intrinsically neutral frameworks and their ring structures contain an even number of PBUs.[23] Nevertheless, AlPOs have been prepared in a range of structures, both novel and isostructural with zeolites.[39]

Whilst classified as a zeotype material, there are some important differences in the structure and chemistry of an AlPO *versus* a zeolite.[23] Whereas the aluminosilicate backbone of a zeolite is predominantly covalent in character, computational modelling indicates that AlPOs are best considered as molecular-ionic systems, composed of discrete Al^{3+} and $(PO_4)^{3-}$ entities.[40] These studies also found evidence that the AlPO exhibits greater flexibility in the T-O-T angle than the aluminosilicate counterpart. Collectively, these factors are thought to be responsible for the particular receptivity of AlPOs towards the isomorphous substitution of heteroatoms. More than 25 main group and *d*-block elements have been incorporated into AlPOs,[41, 42] giving rise to diverse chemistry in otherwise electrovalently neutral systems.

Based on a consideration of bonding patterns and potential heteroatom siting in AlPOs,[43] three mechanisms of isomorphous substitution have been defined.[44] In Type I substitution, framework Al(III) is replaced by a heteroatom, typically in the +2 or +3 oxidation state. In Type II substitution, P(V) is replaced by a dopant atom, usually with a formal charge of +4 or +5.[45] Importantly, if the formal oxidation state of the dopant is less than that of the framework atom it replaces, the charge imbalance must be compensated with an extra-framework cation (**Figure 1.4.1**).[46]

Particularly with transition metal dopants, strong interaction with water favours a proton counter-cation, which remains weakly bound to a bridging oxygen atom.[47] As a result, a substituted AlPO may develop Brønsted acidity in proximity to a Lewis-acidic metal centre.[45] Correspondingly, metal-doped AlPOs (MeAlPOs) have found various applications in acid-catalysed reactions, such as the Beckmann rearrangement,[48] methanol dehydration,[49] and the isopropylation of benzene.[50] Moreover, the variety of heteroatom dopants,[45] and their various multi-metallic combinations, has provided scope to tailor the acid characteristics of MeAlPOs for various transformations.[50-55] MeAlPOs may also exhibit redox capabilities, if the metal dopant is a transition element with multiple, stable oxidation states. Redox activity in MeAlPOs has been exploited in the oxidation of hydrocarbons (Me = Co, Fe, Mn)[56, 57] and olefins (Me = Ru, Sn, Cr),[52, 58] and in the ammoximation of ketones (Me = Co, Mn, Fe).[48, 59]

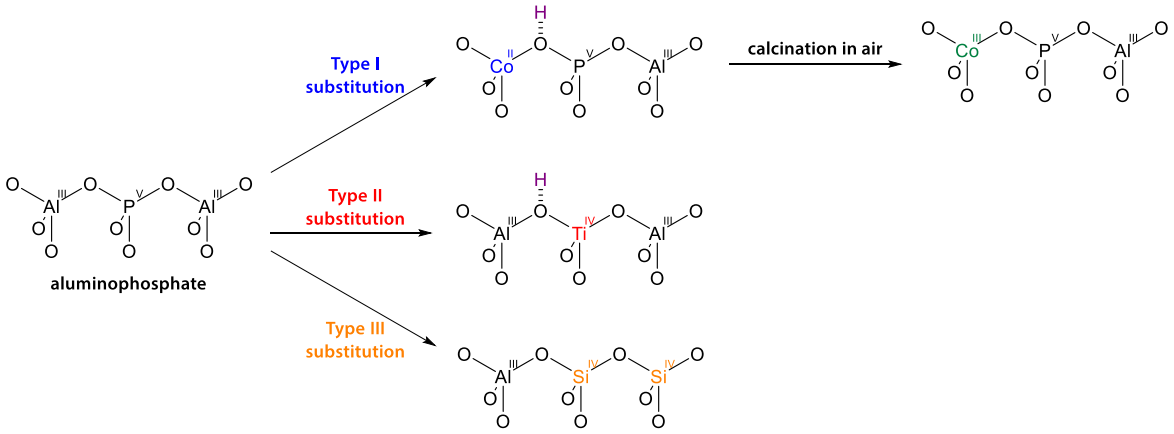

Figure 1.4.1: A schematic of the isomorphous substitution of heteroatoms into the AlPO framework. In Type I substitution, Al(III) is replaced by a heteroatom (e.g. Co(II)). In Type II substitution, P(V) is replaced by a heteroatom (e.g. Ti(IV)). In Type III substitution, Al(III) and P(V) are both substituted for Si(IV). The flexibility of the framework allows for redox cycling at a metal centre having multiple, stable oxidation states.

The third mechanism of isomorphous substitution, which is observed when the heteroatom is Si(IV), provides yet further scope to modulate the acidity of AlPO materials. Firstly, Si can be incorporated into an AlPO *via* Type II substitution of P, in which case an isolated Brønsted acid site is developed. (The unfavourable energetics of Si-O-P bonding precludes Type I substitution of Al).[60] However, it is also possible that two Si(IV) atoms will replace both Al(III) and P(V) simultaneously, forming a charge-neutral, siliceous zone, detectable by ^{29}Si MAS NMR spectroscopy.[61] In Type III substitution, the avoidance of Si–O–P bonding prohibits the 'homogenous' substitution of adjacent Al and P centres (**Figure 1.4.2 a**). However, silicon islands, with Si–O–Si and Si–O–Al bonding, can be formed through a 'heterogeneous' Type III mechanism (i.e. Type III substitution accompanied by Type II (**Figure 1.4.2 b**)).[44] Any aluminosilicate regions within, or at the perimeter of the siliceous zones will have net negative charge, and with charge-compensation, Brønsted acidity is developed.[62]

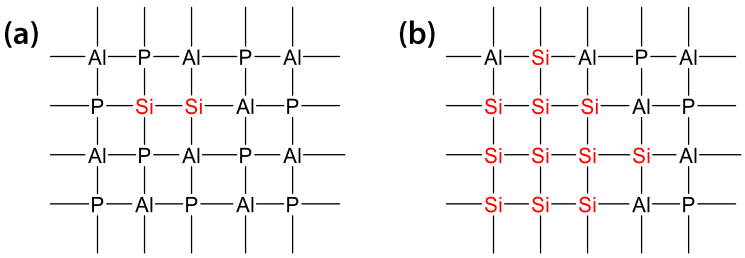

Figure 1.4.2: Bonding schemes for Type III substitution of Si(IV) into an AlPO framework, where the lines represent the bridging oxygen atoms. **(a)** Homogeneous substitution of an Al and a P by two Si atoms is not observed due to the instability of Si-O-P bonding. **(b)** Silicon islands may be formed *via* a heterogeneous Type III substitution mechanism, where both Type II and Type III substitution of Si occur simultaneously.

1.5 Silicoaluminophosphates as solid-acid catalysts

Despite the structural similarity of their Brønsted sites (i.e. SiO(H)Al), the acidity of the silicoaluminophosphates (SAPOs)[63, 64] can differ quite markedly from their aluminosilicate relatives.[65] In zeotype systems, the strength of an acid-site is dependent on its atomic environment, namely the bond lengths and angles, and the electrostatic influence of atoms in the local coordination sphere. For a zeolite, the first coordination sphere of T-atoms around Al invariably comprises [SiO_4], whereas in a SAPO, tetrahedral Al may be bonded, *via* oxygen, to either P or Si. Using a topological approach, supported by ^{29}Si MAS NMR studies, Barathomeuf deduced that acid-site strength in a SAPO increases as the first coordination sphere of Al contains more Si, and the second sphere contains more P.[62] As such, for a particular framework structure, Type III substitution will create stronger Brønsted acid sites than Type II. The Type III mechanism also produces fewer acid sites per Si atom, although the exact number of will depend on the coordination environment of each Si atom in the island (i.e. a purely siliceous island creates fewer acid sites than a Si-Al domain with the same number of T-atoms).[62]

The mole fraction of silicon in a SAPO typically varies between 0.04 - 0.20, depending on the synthesis conditions and the framework type.[41] In general, low Si loadings favour site-isolation, as this creates little perturbation in the framework structure.[66] However, there is a limit on the amount of Si that can be incorporated by the Type II mechanism, and so higher loadings are often accommodated as silicon islands (**Figure 1.5.1**).[62]

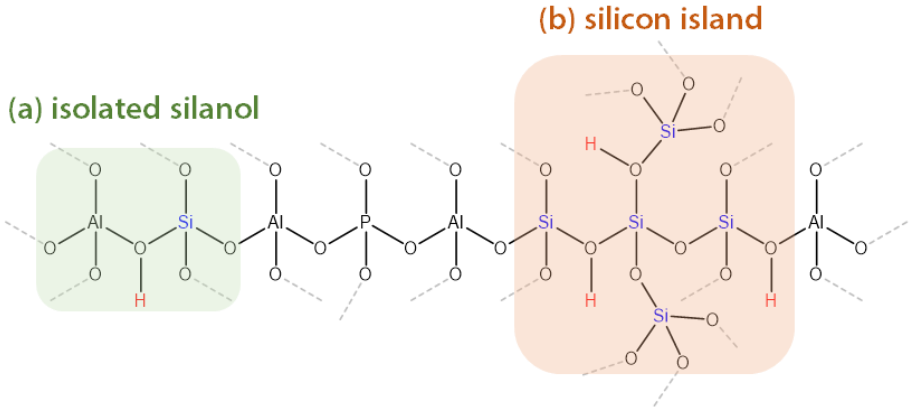

Figure 1.5.1: A diagram showing a section of a SAPO framework that contains Brønsted acid sites in the form of **(a)** isolated silanols, from Type II isomorphous substitution of Si into the framework and **(b)** silicon islands, from Type II + Type III isomorphous substitution of Si into the framework.

Since the flexibility of the framework affects the stability of siliceous zones, the threshold concentration for Type III substitution varies considerably with the SAPO topology.[60] To examine the relationship between framework topology and Si distribution, Sastre *et al.*

studied the energetics of Si incorporation in SAPO-5 (AFI) and SAPO-34 (CHA).[66] The calculations revealed that the formation energy of an isolated Brønsted site is almost identical in the two SAPOs, and so the difference in their acidities[41] must be due to the presence of silicon islands. SAPO-5 is known to accommodate larger silicon islands than SAPO-34, and does so at a lower Si concentration.[67] On the basis of the earlier discussion, a tendency towards Si islanding might be expected to create stronger acidity in SAPO-5 than SAPO-34. In fact, SAPO-5 is more weakly acidic than SAPO-34, when both have a similar Si loading.[68, 69] This is because the strength of an acid site is more specifically related to the geometry of the framework (namely the Al-O(H)-Si angle). For this reason, the acidity of different SAPO frameworks cannot be predicted on the basis of the Si substitution mechanism alone; rather, it is assessed experimentally, typically by means of a chemical probe (as in TPD, FTIR, or catalysis).[70-72]

It is possible to exert some synthetic control over the incorporation of Si into SAPOs through the choice of micropore-templating, structure-directing agent (SDA).[65] The SDAs that are typically employed for AlPO-templating are amine molecules, which are protonated under the acidic conditions of the synthesis gel.[63] As such, the SDA not only plays a space-filling role but also provides charge-balance to facilitate the Type II substitution of Si(IV) into the AlPO framework.[66] For Si to be incorporated solely as isolated sites, the net negative charge on the framework must be compensated in a 1:1 ratio with the positive charge on a template molecule. However, the size of the SDA restricts the number of molecules that can be accommodated within the framework, simultaneously placing a limit on the number Si(IV) atoms that can be incorporated by the Type II mechanism. Since the number of positive charges required to neutralise a silicon island is less than the number of Si atoms incorporated, a higher Si content can be supported with fewer template molecules. The impact of the SDA on the substitution mechanism in SAPO-34 was investigated by Vomscheid *et al.*,[73] who characterised the Si distribution in SAPO-34 catalysts templated by morpholine and by tetraethylammonium hydroxide (TEAOH). As the chabazite cages can accommodate two molecules of morpholine but only a single molecule of TEAOH, the number of isolated Si sites was increased when morpholine was used as the SDA.

SAPOs have found a variety of applications as solid-acid catalysts due to their structural diversity and tuneable acidity.[70, 72] In industry, SAPO-34 (CHA) is used in the methanol-to-olefin (MTO) process,[74] where the predominance of milder, isolated acid-sites, and the narrow pore aperture (3.8 Å) confer a high selectivity for ethylene and propylene products.[75, 76] In contrast, silicon-rich SAPO-5, which exhibits high levels of Si-islanding, is used in processes that benefit from strong acidity, such as the hydrocracking of *n*-alkanes[77] and the isomerisation of *o*-xylene.[78]

1.6 Addressing mass transport restrictions in microporous frameworks

In heterogeneous catalysis, diffusion processes mean that the observed reaction rate will always be slower than the rate predicted on the basis of the surface chemistry alone.[2] However, mass transport effects tend to be exacerbated in (micro)porous catalysts, as travel to and from the active site is not only subject to external concentration gradients, but also internal effects, such as long diffusion paths and the resistance of the pore walls.[11] In some catalytic transformations, (for example, the isomerisation of *meta*-xylene with ZSM-5)[79] close conformity between the dimensions of the reactive species and the pore can enhance reaction selectivity. Otherwise, restricted mass transport can significantly impair catalytic performance by limiting access to the active sites, or by promoting side-reactions and coking.[80, 81]

Synthetic efforts to address the mass transport limitations of microporous, zeolitic materials have largely focussed on one of two approaches.[82] One option is to reduce zeolite particle size, as this increases surface area : volume ratio, exposing more pore-windows per unit mass of catalyst.[83] Also, since nano-sized zeolites have shorter diffusion path-lengths, the molecular residence time, and hence the risk of by-product formation, is reduced. However, the difficulty of controlling particle growth, and the challenges of recycling nano-sized zeolites has limited their practical application.[82] Another strategy to improve molecular diffusion is to increase pore diameters. Whilst large-pore zeolites initially proved elusive, zeotype analogues comprising P with Al or Ga were successfully prepared. However, the commercial viability of large-pore, phosphate-based materials has proven limited, as the stability of these materials is often undermined by mixed metal-ion coordination, terminal hydroxyls, and non-tetrahedral framework species.[18] Moreover, the structure of the early, large-pore zeotypes provided little enhancement in mass transport *versus* microporous systems.[16] For example, the unusual pore shape and protruding hydroxyls of the large-pore gallophosphate, Cloverite[85] (**Figure 1.6.1 a**), were found to impede molecular diffusion, whilst stacking disorder and deformation of the 18-member rings of aluminophosphate VPI-5 (**Figure 1.6.1 b**),[86] diminished the effective pore diameter.[73] Even the first extra-large pore zeolite, UTD-1 (**Figure 1.6.1 c**),[87] has found few applications due to its low thermal stability and complications arising from the use of an organometallic template.

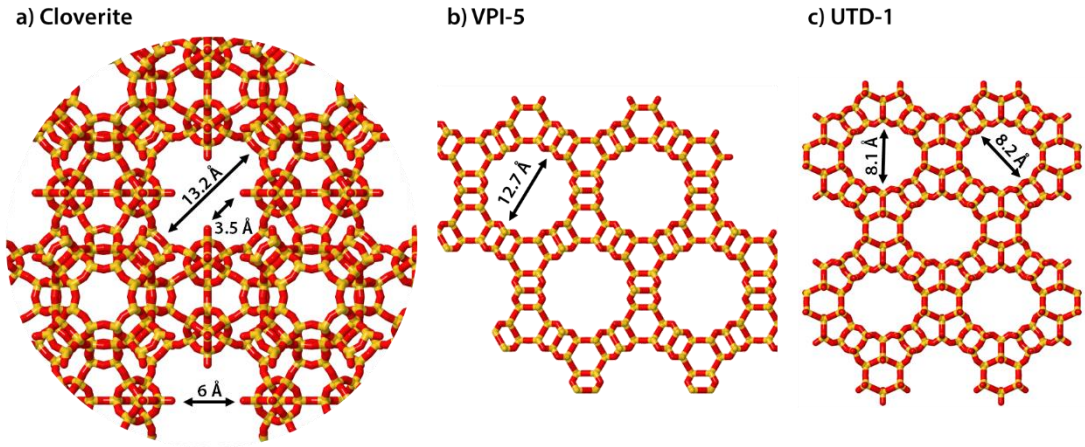

Figure 1.6.1: The framework structures of **(a)** Cloverite, **(b)** VPI-5, and **(c)** UTD-1, with pore dimensions labelled.[88]

In 1992, researchers at Mobil Oil Corporation reported the synthesis of MCM-41, the first mesoporous material with ordered porosity and a narrow pore-size distribution.[89] The group of ordered mesoporous silicas (OMS) quickly proliferated, giving rise to the M41S family of mesoporous molecular sieves (**Figure 1.6.2**).[90]

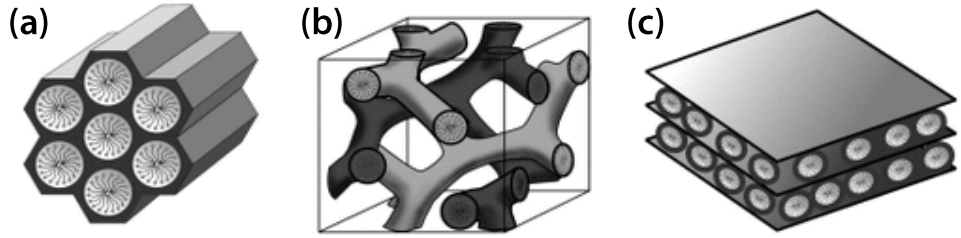

Figure 1.6.2: The M41S family of mesoporous silicas include: **(a)** 2D-hexagonal MCM-41, **(b)** cubic MCM-48, and **(c)** lamellar MCM-50. Image reproduced with permission from John Wiley & Sons Inc..[91]

The high surface areas and regular porosity of OMS materials were appealing for applications requiring molecular sieves with enhanced diffusion capabilities and a large adsorption capacity. For instance, Al-doped OMS were anticipated to be well-suited to the catalytic cracking of heavy petroleum residues.[92] However, unlike the crystalline aluminosilicates, Al-MCM-41 materials suffer low hydrothermal stability, and are only weakly acidic - irrespective of aluminium loading.[93] Nonetheless, for mild hydrocracking reactions, MCM-41 catalysts were found to be operative.[94, 95] For example, in catalytic cracking of long-chain hydrocarbons to liquid fuels, the activity of Al-MCM-41 approaches that of the industrial, microporous catalyst, ultra-stable Zeolite-Y (USY) - albeit with less selectivity for lighter gasoline products. However, with shorter-chain feedstocks, mass transport restrictions are less problematic, and as such, the activity of MCM-41 is far inferior to USY zeolite, as the latter benefits from an abundance of strong acid sites.

In general, commercial application of OMS has been restricted by their low thermochemical stability, which is a consequence of their amorphous pore walls.[16] In catalytic applications, mesoporous materials also tend to lack the high selectivity of microporous sieves due to their larger pores and variable crystallinity.[18] Since, both micro- and meso-porous architectures present advantages and limitations, there has been considerable interest in the development of hierarchical materials that combine desirable attributes of both pore systems.[82]

1.7 Templating hierarchically-porous zeotypes

A hierarchically-porous (HP) material integrates multiple levels of porosity (micro-, meso-, macro-pores) within a single system. In zeotypes, a second level of porosity may be introduced to alleviate the diffusion limitations of the micropore system.[96] Hierarchical porosity can be especially beneficial in catalysis,[80, 97] as a HP zeotype can retain the well-defined active sites and physicochemical stability of the microporous framework, whilst benefiting from the reduced steric constraints, enhanced reaction rates, and increased lifetime of a larger-pore network.[98] However, to take advantage of structural hierarchy, careful engineering is required to ensure the accessibility and interconnectivity of the various pore systems.[80] There are a number of synthetic protocols for the preparation of zeotypes with intracrystalline, hierarchical porosity. Broadly, these methodologies are classified as either top-down or bottom-up approaches.[99] A top-down approach involves post-synthetic modification of the microporous framework, which can be achieved through chemical treatment (e.g. demetallation under acidic or basic conditions),[100] or by etching with heavy ions (**Figure 1.7.1**).[101]

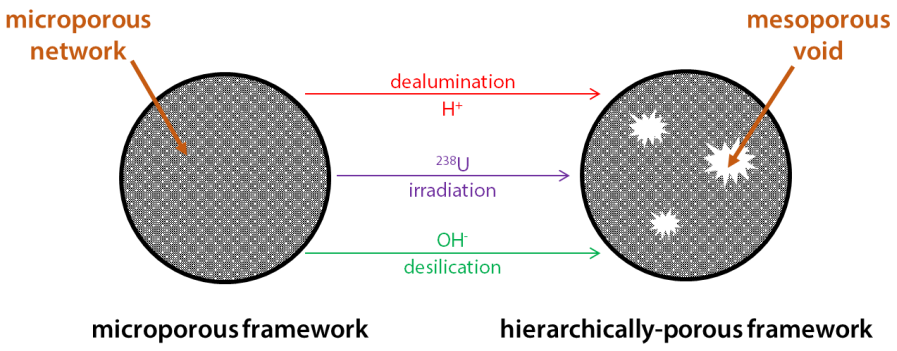

Figure 1.7.1: Top-down routes for the synthesis of hierarchically-porous frameworks involve the removal of atoms from a pre-formed microporous network.

In any case, extraction of framework atoms leads to localised collapse of the microporous network and the formation of mesoporous voids. Although the crystallinity of the microporous zeolite network is largely maintained, post-synthetic treatments can generate

defect sites, irrevocably modifying the textural and acidic properties of the microporous framework.[81, 102] Nonetheless, top-down syntheses have been widely reported for the production of hierarchical aluminosilicates.[103-105] Post-synthetic modification of AlPOs and SAPOs has also been achieved,[106, 107] although controlled formation of the meso-phase has proven challenging, and often leads to significant changes in the physicochemical properties of the microporous framework. Hence, constructive, bottom-up approaches are more often used for the production of hierarchical AlPOs.[108]

In a bottom-up approach, both a micropore-templating SDA and a mesoporogen are added to the synthesis gel that contains the framework precursors.[98] During crystallisation both micropores and mesopores are formed and so, with template removal, a hierarchically-porous framework is obtained. Dual-templating is a relatively straightforward method to generate hierarchical zeotypes, as it is compatible with the traditional 'one-pot' synthesis of these materials.

Two types of mesoporogen may be employed for the preparation of hierarchical zeotypes: hard-templates or soft-templates (**Figure 1.7.2**).[100] Hard-templates are porous matrices or nanoparticles (e.g. carbon nano-particles and -tubes, polystyrene beads, and inorganic nanoparticles) about which the framework precursors assemble.[80] After confined crystallisation, the resulting meso-phase is an inverse construct of the hard template, which affords a high level of uniformity in the mesoporous constructs.[81] Whilst the choice of hard template offers the potential for minute control over the structure of the mesopores,[100] the removal of the hard template can require harsh conditions that destroy the zeolite structure or modify the acidity of the framework.[98] Alternatively, dual-templating may be performed with soft-templates: supramolecular micelles that are formed by the spontaneous self-assembly of amphiphilic surfactant molecules.[109] To obtain the hierarchical material, both surfactant and SDA can be eliminated simultaneously by aerobic calcination. When using soft-templates, mesostructural control can be achieved through the structure of the surfactant molecule,[110] or by the use of additives, such as swelling agents.[111, 112]

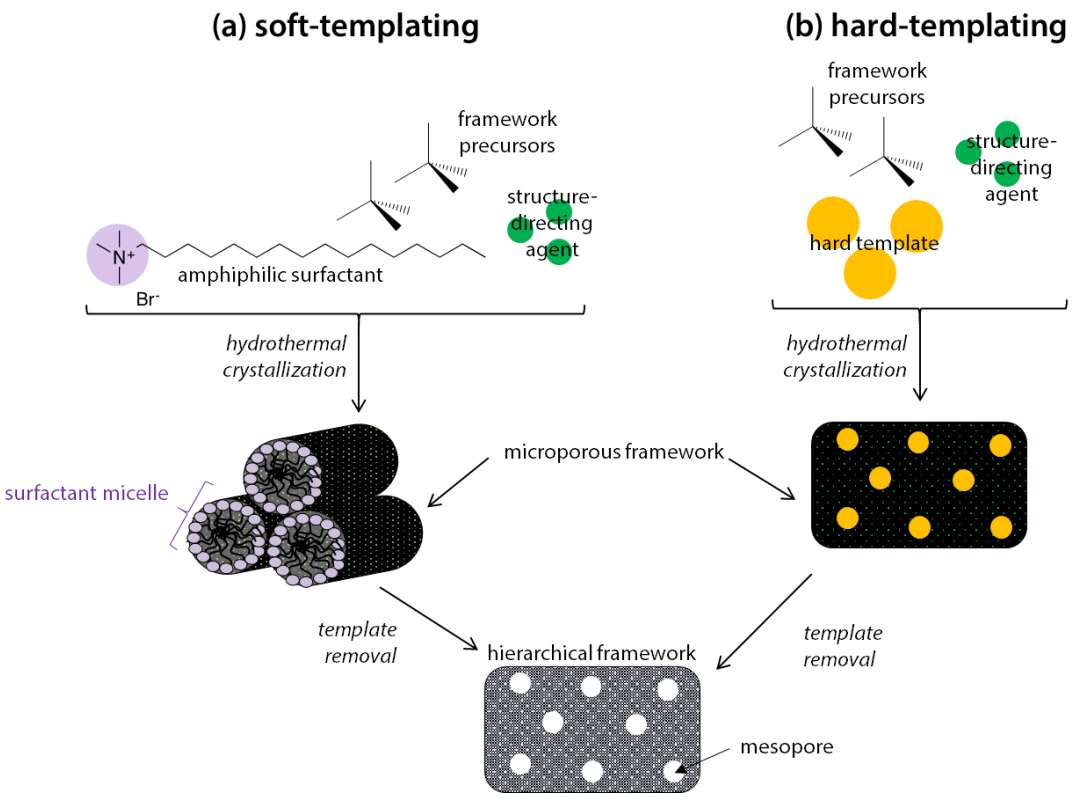

Figure 1.7.2: Two bottom-up methodologies can be used to prepare hierarchically-porous materials. **(a)** In soft-templating, the mesoporogen is a micelle, formed by the spontaneous self-assembly of amphiphilic surfactant molecules in aqueous solution. **(b)** Hard-templating forms mesopores that are the inverse construct of a solid template. In both cases, the framework precursors crystallise about the mesoporogen and SDA, and elimination of the templates yields a hierarchically-porous material.

Both top-down and bottom-up methodologies have been applied in the synthesis of hierarchical AlPOs, with varying results. Danilina *et al.* investigated a number of procedures to prepare HP SAPO-5, including hard-templating with carbon black, and soft templating with amphiphilic surfactant (dodecyltrimethylammonium bromide), organosilane surfactant ([3-(trimethoxysilyl)propyl]hexadecyldimethylammonium chloride), a phosphorus-containing molecule (mono-*n*-dodecylphosphate) and an aluminium-containing molecule (aluminium-dihydroxo-mono-heptadecylester).[113] All but the organosilane mesoporogen yielded frameworks that were either amorphous, impure, non-porous, or far less acidic than the microporous SAPO-5. In fact, of the various soft-templates investigated for the synthesis of HP AlPOs,[108, 114] the organosilanes have had particular success in generating a homogeneous, bimodal, pore-architecture, whilst retaining the characteristics of the microporous phase.[115]

1.7.1 Hierarchical zeotypes by dual-templating with organosilane surfactant

A particular challenge associated with the dual-templating approach is phase-segregation, which occurs when the mesoporogen is expelled from the crystallising microporous phase.[98] Based on the rationale that organosilanes exhibit a high affinity for zeolitic precursors, Choi *et al.* designed an amphiphilic, surfactant mesoporogen containing a structure-directing head-group (i.e. a quaternary ammonium moiety), a hydrophobic alkyl chain, and, strategically, a hydrolysable trimethoxysilyl group (**Figure 1.7.3**).[110] It was anticipated that the methoxysiliyl moiety of the surfactant would engage in strong, covalent interactions with the growing zeolite domains, and that this would encourage the growth of a single, hierarchical phase. Indeed, XRD and electron microscopy independently confirmed that micro- and meso-pores were crystallised simultaneously in the organosilane-directed synthesis of hierarchical MFI zeolite.[110] Furthermore, high-resolution scanning electron micrographs of hierarchical LTA zeolite revealed that the mesoporosity was intracrystalline, and penetrated the microporous zeolite crystal.[116] The same authors[110] were also able to characterise the cylindrical, wormhole-like structure of the organosilane-templated mesopores by correlating the low-angle XRD pattern and TEM images of the HP MFI with mesoporous silicas that were previously studied using Pt-wire intergrowth.[117, 118]

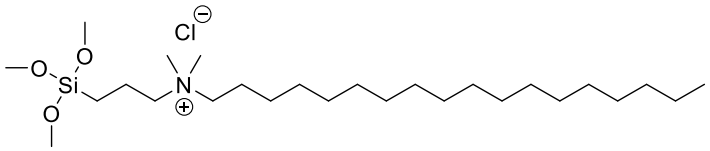

Figure 1.7.3: The structure of dimethyloctadecyl[3-(trimethoxysilyl)propyl]ammonium chloride; an example of the organosilane surfactant designed by Choi *et al.* for soft-templating hierarchical zeotypes.[110]

Dual-templating with organosilane surfactant has proven an effective strategy to prepare a variety of hierarchical zeolite (MFI,[110, 119, 120] LTA,[121] BEA,[122] FAU[123] and SOD[121]) and zeotype materials (AlPOs[115]) with increased surface area and significant mesopore volume. These hierarchical frameworks exhibit a narrow pore-size distribution, which can be tailored in the range of 2–20 nm *via* the length of the surfactant chain and/or the conditions of hydrothermal synthesis.[81] Aluminophosphates including AlPO-5, AlPO-11,[115] SAPO-34, and SAPO-5[124] have also been prepared as their hierarchical analogues by crystallisation with organosilane template. When organosilane-templated HP AlPOs have been investigated catalytically, the presence of mesopores has been found to offer improved activity and lifetime *versus* their purely microporous counterparts. For example, Danilina *et al.* investigated organosilane-templated HP SAPO-5 as a solid-acid catalyst for the alkylation of benzene with benzyl alcohol (353 K, autogenous pressure).[113] Although the acid characteristics of HP and microporous SAPO-5 were comparable, in the space-demanding

alkylation, HP SAPO-5 achieved 98 % conversion of benzyl alcohol within 3.5 hours, whilst SAPO-5 achieved only 66 % conversion in the same period (**Figure 1.7.4 a**). In another example, Sun *et al.* explored the use of organosilane-templated SAPO catalyst for the MTO process.[125] The authors reported that the hierarchical porosity, weaker acidity, and smaller crystallite size of HP SAPO-34 extended catalyst lifetime fourfold, and gave > 10% higher selectivity towards light olefins (ethene, propene) than microporous SAPO-34 (**Figure 1.7.4 b**). Separately, Tao *et al.* reported a Pt/HP SAPO-11 catalyst where the enhanced mass transport properties of the mesoporous network improved isomerisation selectivity in the hydroisomerisation of *n*-dodecane (**Figure 1.7.4 c**).[126]

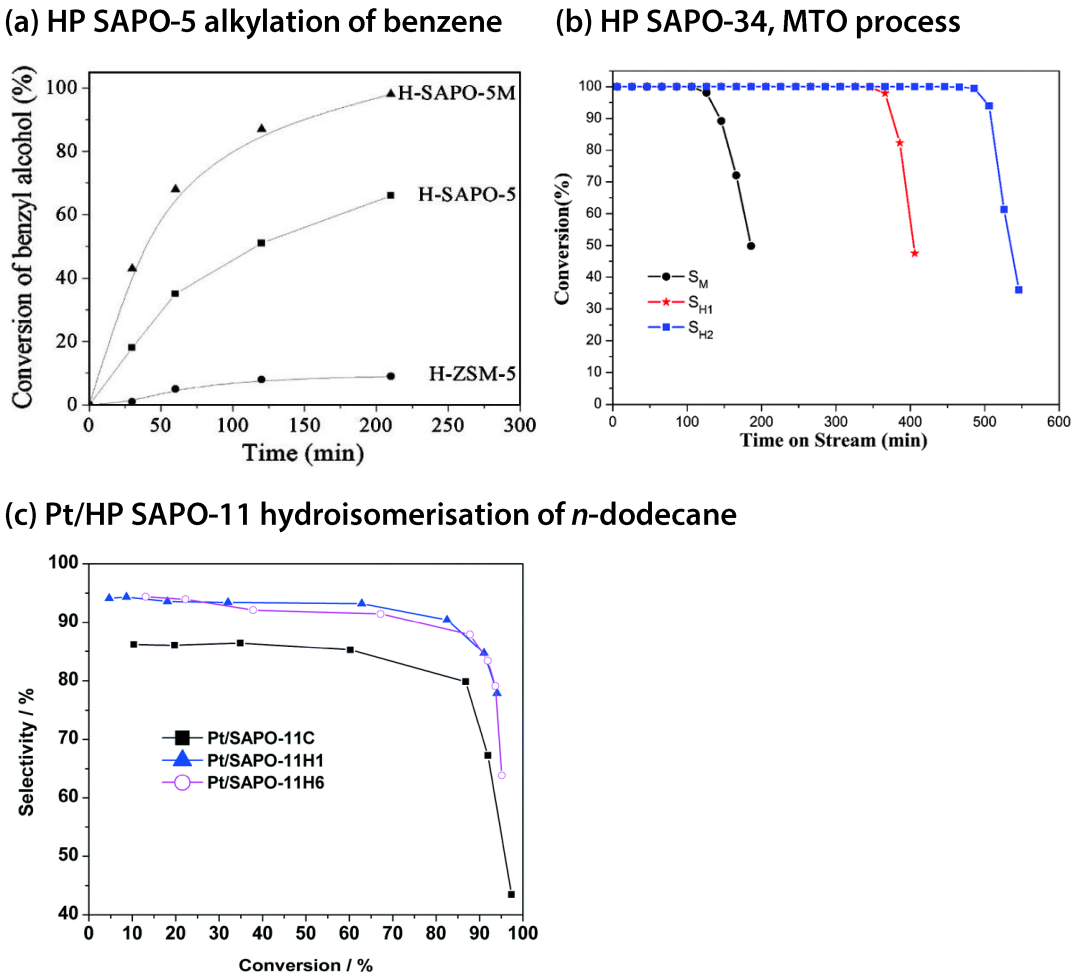

Figure 1.7.4: (a) The conversion of benzyl alcohol in the alkylation of benzene, catalysed by hierarchical SAPO-5 (H-SAPO-5M), microporous SAPO-5 (H-SAPO-5), and H-ZSM-5 (25 - 27 bar and 433 K).[113] Figure reproduced with permission from Elsevier. **(b)** Methanol conversion with time-on-stream over microporous (S_M) and hierarchical SAPO-34 (S_{H1} and S_{H2}) catalysts (WHSV = 2 h^{-1} , 673 K).[125] Figure reproduced with permission from the Royal Society of Chemistry. **(c)** Selectivity towards *n*-dodecane isomers (as opposed to hydrocracking) against *n*-dodecane conversion with hierarchical (Pt/SAPO-11H1, Pt/SAPO-11H6) and microporous (SAPO-11-C) Pt/SAPO-11 catalysts. (WHSV = 2 h^{-1}, H_2 : *n*-dodecane = 15, 8.0 MPa).[126] Figure reproduced with permission from the Royal Society of Chemistry.

A notable (and potentially useful) corollary of the organosilane template is that siliceous species are incorporated into the walls of the mesopores. On calcination the mesoporogen is removed, leaving the internal surfaces of the mesopores terminated with a high concentration of silanol groups (Si-OH).[122, 124, 127] However, the presence of pendant silanols has several implications for the catalytic properties of soft-templated AlPOs. In reactions requiring acid catalysis, the presence of silanols has been found to modulate the acid characteristics of the framework. For instance, in the vapour-phase Beckmann rearrangement of cyclohexanone oxime, the presence of weakly acidic silanols in HP SAPO-5 and HP SAPO-34 was found to enhance selectivity towards the desired caprolactam product, and increase resistance to coking. These effects, in combination with the improved diffusion characteristics of the HP network, were found to improve the performance and lifetime of the HP SAPOs, relative to their microporous counterparts.[124] In another example, the weaker acidity and reduced crystallite-size of organosilane-templated SAPO-34 was found to significantly prolong catalyst lifetime in the methanol-to-olefin (MTO) reaction, and also increased selectivity towards ethylene and propylene products.[125]

The organosilane, soft-templating protocol also increases the functionalisation potential of HP AlPO frameworks (**Figure 1.7.5**). The abundance of Si-OH groups provide anchor points for covalent tethering of catalytic species.[127, 128] Thus, the prospective catalytic applications of organosilane-templated hierarchical AlPOs is vast; not only due to their improved mass transport properties, but also their immense scope for functionalisation by both isomorphous substitution and covalent anchoring routes.

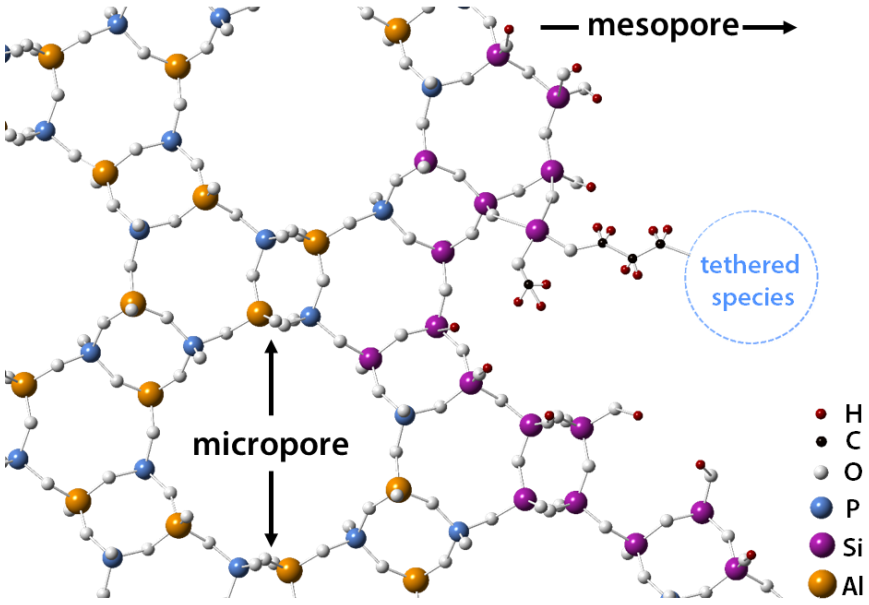

Figure 1.7.5: Pendant silanols in the mesopores of organosilane-templated HP AlPOs provide opportunities for functionalisation *via* covalent tethering.

1.8 The Beckmann rearrangement

1.8.1 The industrial Beckmann rearrangement

Although the earliest synthetic polymers to be manufactured commercially, the polyamides (or nylons) have remained amongst the most widely used synthetic materials in large scale production.[129] Of the aliphatic polyamides, nylon-6 and nylon-6,6 are notable for their extensive use as textile fibres and engineering resins; applications that exploit their characteristic strength, ductility, and physicochemical stability.[130] Due to a high demand for lightweight, durable plastics, the global market for nylon-6 and nylon-6,6 has been valued at $ 41.13 billion for 2026.[131]

There are currently two major industrial routes for the manufacture of nylon polymers.[129] The earliest of these was commercialised by DuPont in 1938,[132] and it yields AABB-type nylons (e.g. nylon-6,6) by the irreversible condensation reaction between a diamine and a dicarboxylic acid (**Figure 1.8.1 a**).[129] In the alternative process, a cyclic lactam is partially hydrolysed into an amino acid, which is then polymerised to form an AB-type nylon (e.g. nylon-6, **Figure 1.8.1 b**).[129] An advantage of the lactam route is that AB-nylons can be depolymerized to the monomer and then recycled.[133] For this reason, nylon-6 is considered a 'green' alternative to nylon-6,6, as the latter can only be down-cycled for low-performance applications, and ultimately terminates in landfill.[134] In 2017, nylon-6 accounted for approximately 60% of the global demand for nylon resin.[131]

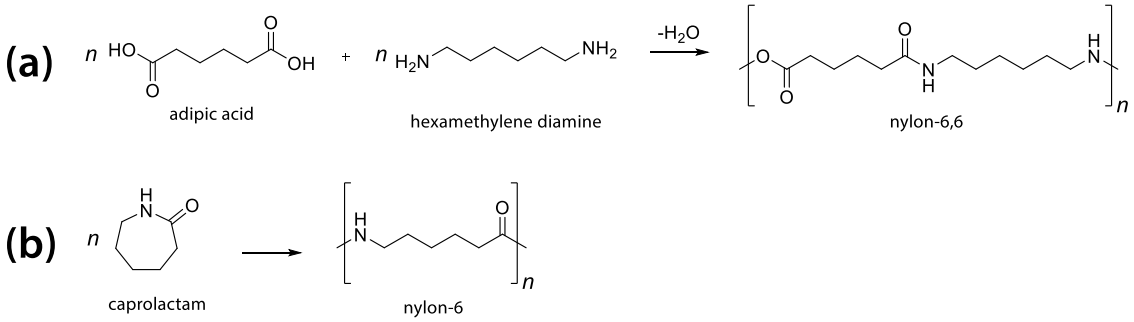

Figure 1.8.1: Schemes for the synthesis of **(a)** the nylon-6,6 polymer *via* the irreversible condensation reaction between adipic acid and hexamethylene diamine, and **(b)** the nylon-6 polymer by ring-opening polymerisation of ε-caprolactam.

The nylon-6 monomer, ε-caprolactam, is a high-value bulk chemical (with a global market value projected at $ 5.74 billion by 2022),[135] of which approximately 90 % is produced *via* the acid-catalysed Beckmann rearrangement (BR) of cyclohexanone oxime.[136] In industry, the BR is typically effected by a concentrated sulphuric acid catalyst, in a multi-step process that generates a disproportionate quantity of ammonium sulphate by-product (**Figure 1.8.2**). As this is both dangerous and inefficient, there has been considerable interest in the

development of heterogeneous catalysts that eliminate the need for a harsh mineral acid, and simultaneously mitigate the huge quantities of low-value ammonium sulphate by-product.[137] Of the various heterogeneous catalysts that have been explored for the BR,[138] the zeotype materials are predominant. The diversity in the structure and composition of zeolitic materials offers considerable scope to optimise the physicochemical characteristics of the catalyst for the Beckmann rearrangement. Moreover, the mechanochemical stability of the inorganic porous oxides makes them well-suited to industrial application.[139]

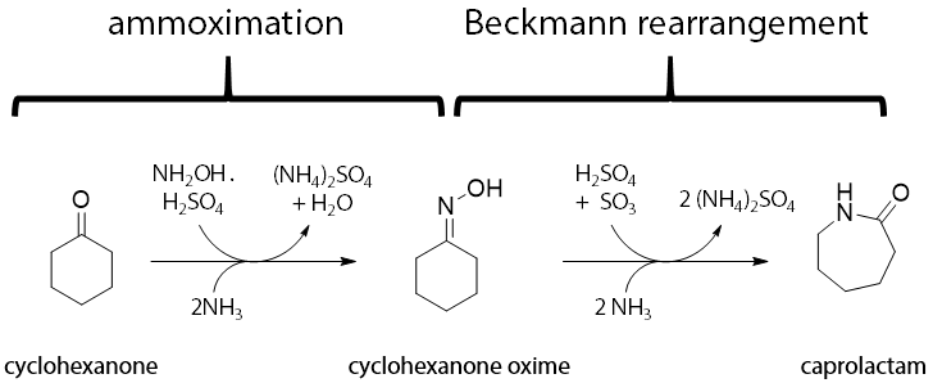

Figure 1.8.2: The conventional industrial synthesis of ε-caprolactam is a multi-step process that produces a large quantity of ammonium sulphate by-product. In the first step, the ammoxim cyclohexanone yields cyclohexanone oxime. In the second step, a strong homogeneous acid catalyst is used to effect the Beckmann rearrangement of cyclohexanone oxime to ε-caprolactam.[48, 140]

In the pursuit of a commercial, heterogeneous catalyst for the vapour-phase Beckmann rearrangement, the Sumitomo Chemical Co. Ltd. discovered an MFI-zeolite (ZSM-5) with high selectivity for ε-caprolactam.[141] With this discovery, the researchers developed a new industrial process in which vaporised oxime was exposed to the zeolite catalyst *via* a fluidised-bed reactor (at 350 – 400 °C and ambient pressures), allowing continuous operation and *in situ* catalyst regeneration.[142] Significantly, the new BR process proved viable on a scale to rival the conventional technologies, and Sumitomo established the first oleum-free caprolactam plant in the world.[140] The factory in Ehime (Japan) has been operational since 2003, and produces ~60,000 tons of ε-caprolactam *p.a.*.

The success of the Sumitomo process has motivated considerable research to correlate the properties of the heterogeneous catalyst with the outcome of the vapour-phase BR. One aspect that has been studied in detail is the influence of the acid-site strength on the yield of caprolactam.[138, 140] In zeolites, framework acidity can be controlled through the Si/Al ratio. For ZSM-5, the framework acidity has been found to decrease linearly with increasing Si/Al:[143] as the amount of framework Al is reduced, the number of stronger Brønsted sites is diminished as more weakly-acidic silanol sites are developed.[144] A variety of silanol sites have

been characterised in zeolites; these are denoted terminal, geminal, vicinal, or nest, depending on the number of Si-O-Si bonds and their proximity to other silanol species (**Figure 1.8.3**).

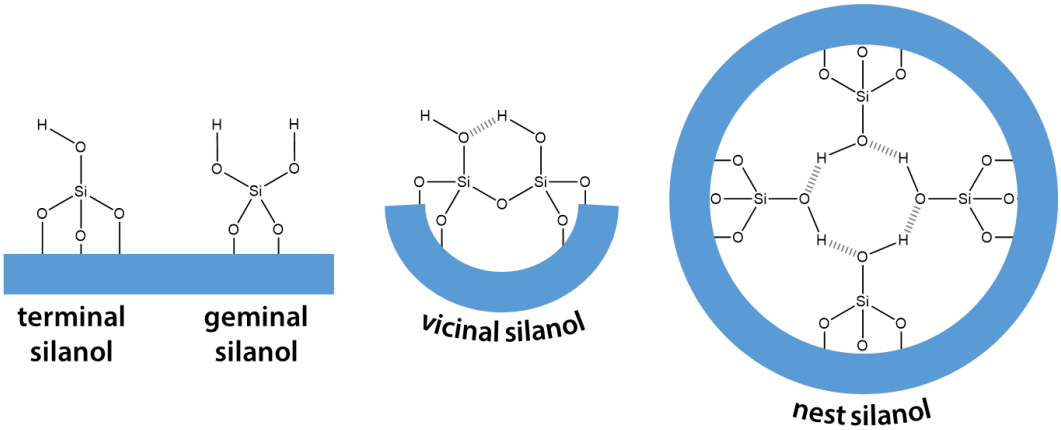

Figure 1.8.3: A depiction of the different types of silanol sites identified in siliceous zeotype frameworks (represented in blue).[145]

When Sato *et al.* at the Sumitomo Chemical Co. Ltd. studied ZSM-5 framework compositions in the range Si/Al = 8 to 11,000, they found that by increasing silicon content, both oxime conversion and caprolactam selectivity were improved (**Figure 1.8.4**).[146, 147] The same authors also investigated a very siliceous MFI zeolite (Silicalite-1, Si/Al = 147,000) that was anticipated to have almost no acidity, yet still achieved 100% conversion and 80 % lactam selectivity.[148, 149] Thus, the authors concluded that, under vapour-phase conditions, it is the very weakly acidic silanol groups that favour a high yield of caprolactam.

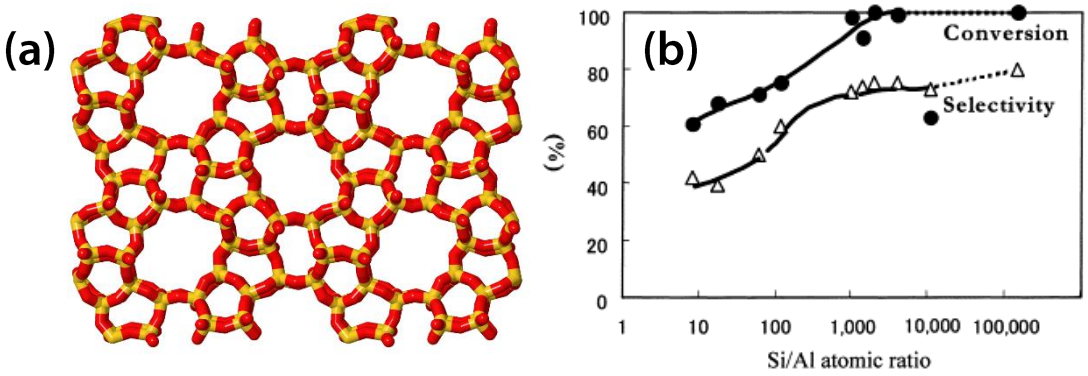

Figure 1.8.4: (a) The structure of the MFI-framework-type of ZSM-5 and Silicalite-1.[88] **(b)** The influence of the Si/Al atomic ratio of ZSM-5 on the conversion of cyclohexanone oxime (•) and the selectivity to caprolactam (▵) in the vapour-phase Beckmann rearrangement (8 wt. % cyclohexanone oxime in benzene, WHSV = 3 h^{-1}, 623 K).[147] Graph reproduced with permission from Elsevier.

To better understand the nature of the sites that are most favourable for the vapour-phase Beckmann rearrangement, Hölderich *et al*. undertook a study to correlate the nature of the silanol sites with their selectivity for caprolactam.[150] Using FTIR spectroscopy, the hydroxyl-

stretching modes of terminal silanols (~3740 cm^{-1}), vicinal silanols (~3690 cm^{-1}) and silanol nests (~3500 cm^{-1}) in MFI-type catalysts were characterised.[151, 152] Of these siliceous species, the vicinal, hydrogen-bonded silanols were found to be considerably more selective for caprolactam than the isolated terminal sites. However, the silanol nests were deemed to be the most effective sites for the vapour-phase BR, since their presence was corresponded with a marked increase in both oxime conversion and lactam selectivity.[153]

Later, the efficacy of very weak acid sites in the Beckmann rearrangement was rationalised by Marthala *et al.*,[154] who used MAS NMR to study the reaction of ^{15}N-labelled oxime in various ZSM-5 catalysts. The NMR experiments revealed that although stronger acid sites are catalytically active, they tend to protonate the caprolactam product, which is then strongly adsorbed to the framework. Not only does the bound lactam reduce catalyst activity by blocking the active sites, it also reduces catalyst selectivity and lifetime by increasing the risk of consecutive reaction and coking. It was thus, by capping the terminal silanol sites of siliceous ZSM-5 (Si/Al ⩾ 1000) with chlorotrimethylsilane vapour (**Figure 1.8.5**), that Sato *et al*. were able to enhance lactam selectivity from 87 % to 92 %.[155, 156] Analogously, in the Sumitomo process the substrate is co-fed with methanol, which, at high temperature, reacts with the terminal silanols of the ZSM-5 catalyst, passivating them as methylsilylether.[147, 157] In addition, methanol (and ethanol) has proven effective at displacing caprolactam from the active sites, which further reduces the risk of product retention and multiple readsorption.[158]

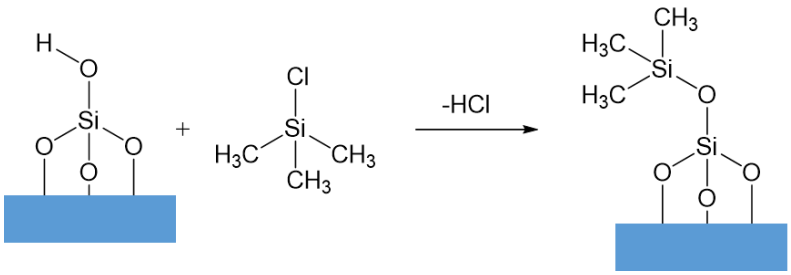

Figure 1.8.5: The more acidic terminal silanol sites in ZSM-5 can be passivated by reaction with chlorotrimethylsilane.[155, 156] The extended ZSM-5 framework is represented in blue.

Besides a consideration of the acid strength of the MFI framework, there has been much debate as to location of the catalytic Beckmann rearrangement. Fundamentally, the small pore aperture (~5.6 Å),[24] of the MFI framework hinders the ability of cyclohexanone oxime and caprolactam (with effective diameters 5.8 Å and 6.3 Å, respectively)[146] to migrate within the framework. When Yashima *et al.* investigated a number of frameworks (H-ZSM-5, H-ferrierite, H-mordenite, Ca-zeolite A, H-borosilicate (MFI), and H-SAPO-5) for the vapour-phase BR, they found that the catalysts with a pore window smaller than the molecular size of cyclohexanone oxime showed high selectivity towards caprolactam. In the case of the small-pore systems, catalysis was restricted to the active sites on the surface where there was almost no diffusional resistance, and so the likelihood of side-reactions was minimised.[155]

However, in the catalysts where caprolactam could be formed within the pores, slow egress of the product led to the accumulation of nitrogenous residues in the pores,[159] resulting in gradual catalyst deactivation and low lactam selectivity. It was also observed that as the surface area of the MFI catalyst is increased, the rate of conversion and selectivity were improved.[146] Therefore, on the basis of these studies, it was concluded that the selective formation of caprolactam occurs at active sites on the external surface of the MFI zeolite.

Kath *et al.* later refuted the theory that the vapour-phase Beckmann rearrangement occurred only at external active sites of the MFI framework, as their adsorption studies indicated that both cyclohexanone oxime and caprolactam could be internalised by Silicalite-1.[160] A separate computational modelling experiment also confirmed that cyclohexanone oxime could enter the pores of the MFI framework, but there was little evidence to suggest that caprolactam could escape the pores.[161] Therefore, based on the high selectivity of siliceous ZSM-5 observed experimentally, the current consensus is that the vapour-phase Beckmann rearrangement occurs at nest silanols located on the surface or just inside the pore mouths of the MFI framework.[138]

1.8.2 Some current targets for the heterogeneously-catalysed Beckmann rearrangement

Whilst solid-acid catalysts are achieving high caprolactam yields (> 95 mol. %)[156, 162] in the Beckmann rearrangement, there are some disadvantages associated with the use of vapour-phase conditions. Primarily, the high temperature required to maintain the substrate and product in the gas-phase accelerates coke deposition, which impairs both catalyst activity and lifetime.[163] Therefore, to avoid pore congestion and improve mass transport, a variety of hierarchically-structured zeotypes have been evaluated for the vapour-phase BR (**Table 1.8.1**). In general, hierarchical catalysts have shown a marked and sustained improvement in catalyst activity due to the enhanced accessibility of the active sites and their resistance to pore blockage. Additionally, hierarchical materials are providing scope to effect the Beckmann rearrangement of more sterically-demanding substrates, such as cyclooctanone oxime[124] and cyclododecanone oxime.[164]

Table 1.8.1: A comparison of the catalytic performance of some hierarchical and microporous zeotypes in the vapour-phase Beckmann rearrangement of cyclohexanone oxime. Table continued overleaf.

Catalyst	Structure[a]	Mesopore template	Acid sites	Catalyst performance		Reaction conditions[e]	Conclusions
				Conv. / %	Sel. / %		
Silicalite -1	MP	-	Vicinal silanols.[b]	37 [d]	48 [d]	**TOS**: 4 hr **Temp.**: 300 °C **WHSV**: 5 hr^{-1} **Solvent**: toluene	Higher activity with improved access to silanol nests.[165]
	HP	polyvinyl alcohol	Also silanol nests.[b]	68 [d]	95 [d]		
Silicalite -1	MP	-	Small amount of terminal silanols.[b]	48	5	**TOS**: 2 hr **Temp.**: 350 °C **WHSV**: 3 hr^{-1} **Solvent**: ethanol	Performance of nanosheet attributed to accessibility of silanol groups on the external surfaces.[166]
	HP (nanosheet)	surfactant	Terminal silanols.[b]	77	92		
	HP	NH_3/NH_4^+ treatment	Also vicinal and nest silanols.[b]	49	4.7		
SAPO-5	MP	-	Brønsted sites: isolated SAPO-type and silicon islands.[c]	26 [d]	72 [d]	**TOS**: 7 hr **Temp.**: 325 °C **WHSV**: 0.79 hr^{-1} **Solvent**: ethanol	Weak acid sites and improved mass transport results in high catalyst activity and lifetime.[124]
	HP	organosilane	Also terminal silanols.[b]	> 98	77		
SAPO-34	MP	-	Brønsted sites: isolated SAPO-type and silicon islands.[c]	84 [d]	86 [d]		
	HP	organosilane	Also terminal silanols.[b]	96 [d]	76 [d]		
SAPO-34	MP	-	Brønsted sites: isolated SAPO-type and silicon islands.[c]	56	92	**TOS**: 6 hr **Temp.**: 325 °C **WHSV**: 0.79 hr^{-1} **Solvent**: ethanol	Acidity of parent is retained but mass transport is improved in HP SAPO-34.[167]
	HP	MCM-41 and surfactant	Also terminal and nest silanols.[b]	> 99	96		

[a] MP = microporous; HP = hierarchically-porous. HP materials are micro-/meso-porous, unless otherwise specified in parentheses.

[b] See **Figure 1.5.1**.

[c] See **Figure 1.8.3**.

[d] Information extracted from graphical data.

[e] TOS = time-on-stream; Temp. = temperature; WHSV = weight hourly space velocity (mass of substrate fed to the reactor per hour / mass of the catalyst)

Table 1.8.1 continued: A comparison of the catalytic performance of some hierarchical and microporous zeotypes in the vapour-phase Beckmann rearrangement of cyclohexanone oxime.

Catalyst	Structure[a]	Mesopore template	Acid sites	Catalyst productivity / 10^{-2} mmol (lactam) g^{-1} (catalyst) hr^{-1}	Reaction conditions[e]	Conclusions
H-ETS-10	MP	-	Terminal Si–OH and Ti–OH groups. Brønsted sites [Ti-(OH)-Si].	0.05	**TOS**: 1 hr **Temp.**: 280 °C **WHSV**: 1.95 hr^{-1} **Solvent**: toluene	The larger external surface area of HP catalyst increases the accessibility of Ti-(OH)-Si sites.[168]
	HP	H_2O_2, microwave irradiation	Increased concentration of terminal silanols.[c]	0.16		
TS-1	MP		Terminal Si–OH and Ti–OH groups. Brønsted sites [Ti-(OH)-Si].[d]	0.01 [d]	**TOS**: 4 hr **Temp.**: 280 °C **WHSV**: 1.95 hr^{-1} **Solvent**: toluene	Additional mesopore surfaces increase catalyst activity and lifetime.[169]
	HP (crosslinked)	1,7-dichloro-octamethyl-tetrasiloxane linker	Increased concentration of hydroxyl groups.	1.16 [d]		

[a] MP = microporous; HP = hierarchically-porous. HP materials are micro-/meso-porous, unless otherwise specified in parentheses.

[b] See **Figure 1.5.1**.

[c] See **Figure 1.8.3**.

[d] Information extracted from graphical data.

[e] TOS = time-on-stream; Temp. = temperature; WHSV = weight hourly space velocity (mass of substrate fed to the reactor per hour / mass of the catalyst)

Besides rapid catalyst deactivation, the high temperatures of the vapour-phase reaction are problematic for the sustainability of the industrial BR. As such, there has been a growing interest in developing catalysts to facilitate the BR under liquid-phase conditions. Camblor *et al.* synthesised a series of zeolite-β materials with varying concentrations of internal and external silanols framework Al, in order to establish nature of the active sites for the liquid-phase reaction.[170] Under liquid-phase conditions (130 °C, chlorobenzene solvent), the purely siliceous (Si/Al > 10000) catalysts with very weakly acidic, external silanols achieved negligible conversion of cyclohexanone oxime (< 0.2 % due to hydrolysis of the oxime to cyclohexanone). However, by introducing internal silanol defects with stronger acidity, the catalytic conversion was increased to 38 %. Yet, the most effective catalysts were those containing framework Al, as this led to the development of strong Brønsted acid sites: H-zeolite-β (Si/Al = 31) containing both Brønsted sites and internal silanol achieved 68 % conversion of oxime, with > 98 % selectivity towards caprolactam. Thus, the authors concluded that bridging-hydroxyl groups (Si-O(H)-Al) are most active in the liquid-phase Beckmann rearrangement, but internal silanols may also play a role - either catalytically, or by increasing the polarity of the pores to enhance oxime uptake.

Similarly, an investigation of mesoporous MCM-41 identified that surface silanols alone were insufficient acidic to catalyse the liquid-phase BR with significant caprolactam yield.[171] However, both catalyst activity and selectivity were improved as the Al loading of the framework was increased, correlating with the formation of more, stronger Brønsted acid sites (**Figure 1.8.6**).

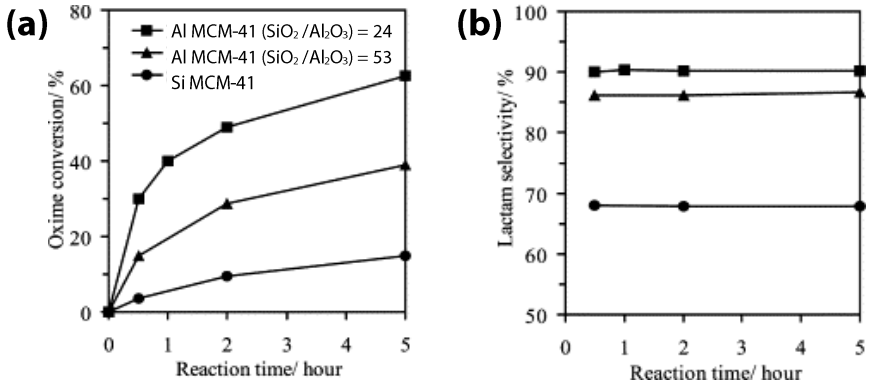

Figure 1.8.6: The influence of the Si/Al ratio of MCM-41 catalysts on **(a)** oxime conversion and **(b)** caprolactam selectivity in the liquid-phase Beckmann rearrangement (130 °C, benzonitrile solvent).[171] Graph reproduced with permission from Elsevier.

However, acid strength is not the only influential parameter in the BR; the nature of the acidity is also important. For example, acid treatment of USY zeolite proved detrimental to caprolactam selectivity due to the formation of Lewis acidic, extra-framework aluminium sites, which catalysed the hydrolysis of cyclohexanone oxime to cyclohexanone.[172]

1.8.3 Silicoaluminophosphate catalysts for the Beckmann rearrangement

As the preceding discussions have highlighted, the location, nature, and strength of acid sites are decisive properties in a heterogeneous catalyst for the Beckmann rearrangement. Moreover, the acid site characteristics must be suitably tailored to the process conditions in order to achieve a high yield of caprolactam. Collectively, the silicoaluminophosphates offer considerable scope to meet the requirements of both the liquid- and vapour-phase Beckmann rearrangements due to their tuneable acidity and structural diversity.

A variety of SAPO frameworks have been tested in the Beckmann rearrangement (**Table 1.8.2**). One of the most promising candidates in both the liquid- and vapour-phase BR is SAPO-37, which has the faujasite (FAU) structure. In the vapour-phase BR catalysed by SAPOs, there is a trend that isolated Brønsted acid sites (from Type II substitution) of moderate acidity are more selective for caprolactam than the stronger acid sites associated with siliceous domains (from Type III substitution).[68, 124, 173] Advantageously, due to a preference for Type II isomorphous substitution, it is possible to synthesise SAPO-37 with almost exclusively isolated Brønsted sites.[174] In the vapour-phase BR (300 °C), the relatively high proportion of Brønsted sites, combined with the accessibility of the three-dimensional FAU pores (7.4 Å), results in high conversion (92.6 %) and lactam selectivity (95.1 %) using SAPO-37 catalyst.

The tendency towards site-isolation in SAPO-37 has also been exploited in the liquid-phase BR. Potter *et al.* contrasted the activity of SAPO-37 with ZSM-5 (MFI) and Zeolite-Y (FAU) at 130 °C.[175] With the ZSM-5 catalyst, the small pore aperture (~ 5.4 Å) was found to preclude the uptake of cyclohexanone oxime, and so catalysis was restricted to active sites on the external surface and pore mouths. In the liquid-phase BR, the inaccessibility of the internal active sites correlated with a low catalytic activity for ZSM-5. In contrast, the acid sites inside the larger (7.4 Å) micropores of the FAU-type frameworks permitted access to cyclohexanone oxime and, correspondingly, SAPO-37 and Zeolite-Y achieved 100 % substrate conversion within 6 hours. Significantly, the SAPO-37 catalyst was considerably more selective towards caprolactam than Zeolite-Y. The authors attributed the low selectivity of Zeolite-Y to its strong acidity, which catalysed side-reactions. In contrast, the weaker, isolated Brønsted acid sites in SAPO-37 proved strong enough to catalyse the rearrangement, and yet still weak enough to desorb the lactam product, which was formed in near-quantitative yield.

Table 1.8.2: A summary of the yield of caprolactam obtained for different silicon-doped AlPO catalysts in the vapour- and liquid-phase Beckmann rearrangement.

Catalyst	Reaction Conditions [a]	Caprolactam Yield /%	Ref.
Vapour-phase Beckmann rearrangement			
SAPO-5	300 °C WHSV = 0.4 hr^{-1} 10 wt. % cyclohexanone oxime in ethanol 1 hr on stream.	65.7	68
SAPO-34		27.4	
SAPO-37		88.1	
SAPO-41		79.3	
SAPO-11	390 °C WHSV = 9 hr^{-1} 5 wt. % cyclohexanone oxime in acetonitrile 1.5 hr on stream.	85.6	173
SAPO-5	325 °C WHSV = 0.79 hr^{-1} 10 wt. % cyclohexanone oxime in ethanol 7 hr on stream.	19 [b]	124
HP SAPO-5		76 [b]	
SAPO-34		72 [b]	
HP SAPO-34		73 [b]	
SAPO-5	400 °C WHSV = 3.3 hr^{-1} 300 g L^{-1} cyclohexanone oxime in methanol	52 [b]	55, 176
MgSiAlPO-5		58 [b]	
ZnSiAlPO-5		48 [b]	50, 55
Liquid-phase Beckmann rearrangement			
SAPO-5	130 °C benzonitrile solvent 7 hr reaction.	6.8	68
SAPO-34		16.2	
SAPO-37		92.5	
SAPO-41		29.1	
SAPO-37	130 °C, anhydrous benzonitrile solvent, 7 hr reaction.	97.6	177
SAPO-34	130 °C, anhydrous benzonitrile solvent, 6 hr reaction.	37.9	178
HP SAPO-34		14.7	

[a] WHSV = weight hourly space velocity (mass of substrate fed to the reactor per hour / mass of the catalyst)

[b] Value extracted from graphical data.

Nonetheless, the small pore apertures of microporous SAPOs can pose a problem for their catalytic lifetime, particularly in the vapour-phase BR. For example, Singh *et al.* reported a SAPO-11 catalyst that achieved > 99 % conversion of cyclohexanone (with 85.7 % lactam selectivity) at 1.5 hours on-stream in the vapour-phase BR (390 °C). However, due to the restrictive, one-dimensional pore structure of the AEL framework, SAPO-11 was rapidly deactivated, so that with ~3.5 hours on-stream, oxime conversion had declined to < 55 %.[173]

However, the issue of catalyst deactivation in the BR is being addressed by the development of HP SAPO. For example, HP SAPO-34 templated with MCM-41 scaffold,[167] and HP SAPO-5 templated with organosilane surfactant,[124] have both been able to sustain > 99 % catalytic conversion of cyclohexanone oxime for 6 hours on-stream in the vapour-phase BR (325 °C). In contrast, the respective microporous SAPOs are gradually coked, leading to a decline in catalytic activity with time-on-stream in the vapour-phase BR (**Figure 1.8.7**).[124, 167]

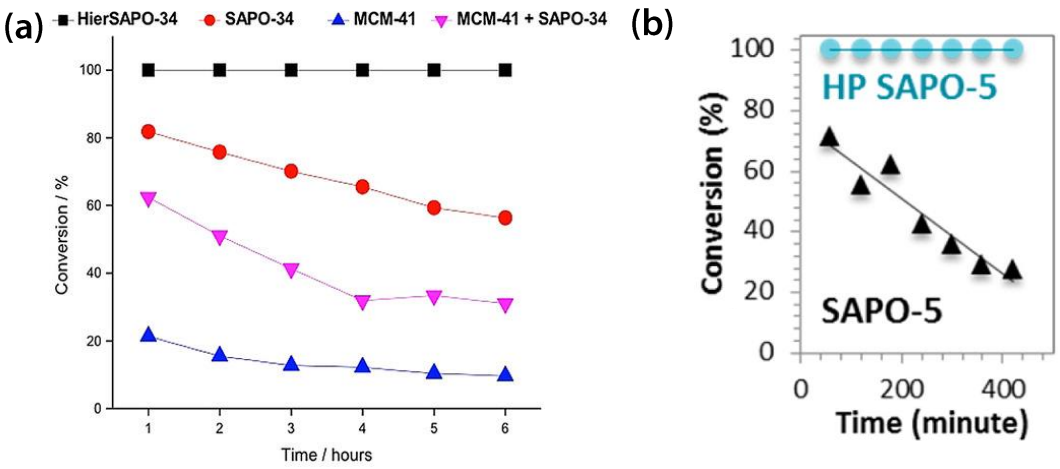

Figure 1.8.7: (a) In the vapour-phase Beckmann rearrangement (325 °C, WHSV = 0.79 hr^{-1}), MCM-41-templated HP SAPO-34 achieves a higher yield than either MCM-41 or microporous SAPO-34, highlighting the importance of both the acidity and the mass transport characteristics of the catalyst framework.[167] Figure reproduced with the permission of John Wiley & Sons Inc.. **(b)** Organosilane-templated HP SAPO-5 sustains > 99 % conversion of cyclohexanone oxime over 7 hours on-stream in the vapour-phase Beckmann rearrangement (325 °C, WHSV = 0.79 hr^{-1}), whereas microporous SAPO-5 is gradually deactivated under the same conditions.[124] Adapted with permission from the American Chemical Society.

Hierarchical SAPOs have also shown promise in the liquid-phase BR. Recently, Miletto *et al.* used a range of mono- and di-saccharides to template HP SAPO-34 (**Figure 1.8.8 a**).[178] Although the acid-site distributions of the HP SAPO-34 materials were almost identical on templating with glucose, sucrose, or fructose (**Figure 1.8.8 b**), the accessibility of the acid sites, and the textural characteristics of the framework (assessed using bulky, basic 2,4,6-trimethylpyridine probe and N_2 gas adsorption) were altered. The sucrose-templated HP SAPO-34 was associated with the largest mesopore volume and surface area and

correspondingly (**Figure 1.8.8 c**), it achieved the biggest enhancement in caprolactam yield - more than 2.5 times that of microporous SAPO-34 after 6 hours under liquid-phase conditions (**Figure 1.8.8 d**).

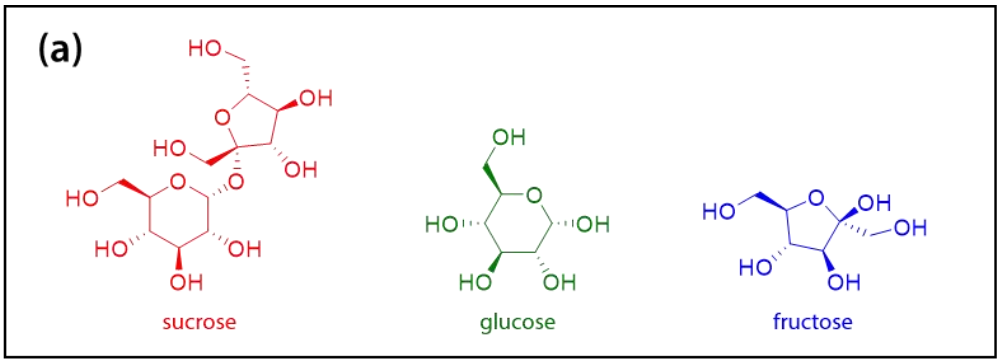

(b)

^{1}H chemical shift / ppm	Assignment	^{1}H species in sugar-templated HP SAPO-34 / %		
		Glucose-templated	Fructose-templated	Sucrose-templated
1.8	Si-OH	9	7	5
2.6	P-OH	19	18	20
3.6	Brønsted acid site	21	30	29
4.0		20	14	16
5.5	Hydrogen-bonded hydroxyls	29	30	30

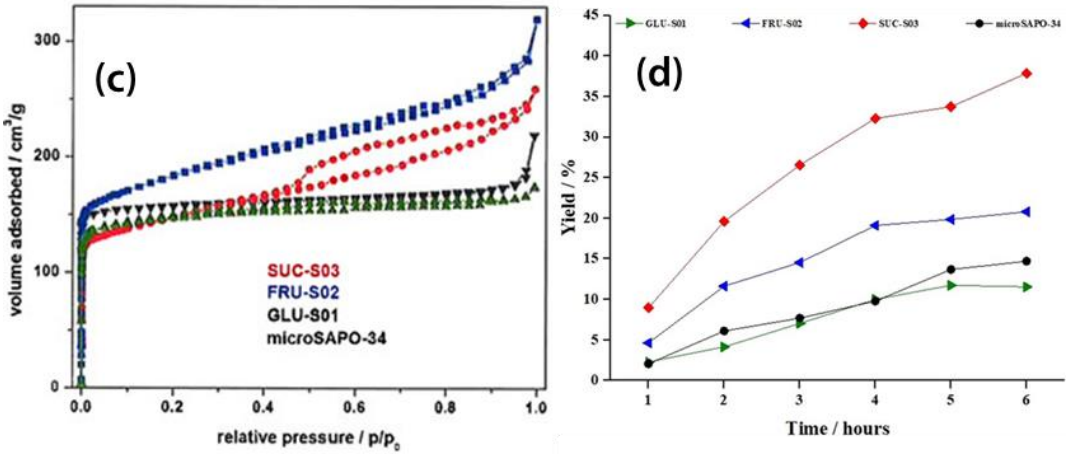

Figure 1.8.8: (a) The structure of the simple saccharides used to template HP SAPO-34: sucrose = SUC-S03, glucose = GLU-S01, fructose = FRU-S02. **(b)** The distribution of acid sites in the sugar-templated catalysts as quantified by ^{1}H MAS NMR studies. **(c)** The SUC-S03 sample was the only catalyst that exhibited a substantial hysteresis in its N_2 adsorption-desorption isotherm, indicating that a significant amount of mesoporosity was templated by sucrose. **(d)** Correspondingly, the sucrose-templated HP SAPO-34 (SUC-S03) achieved the highest yield of caprolactam in the liquid-phase Beckmann rearrangement (130 °C, benzonitrile solvent).[178]

In conclusion, a range of SAPO materials have been explored for both the liquid- and vapour-phase Beckmann rearrangement (**Table 1.8.2**). Although microporous SAPOs show good activity under vapour-phase conditions, they tend to suffer rapid deactivation due to the high-temperature conditions.[124, 167, 173] Equally, under the milder conditions of the liquid-phase BR, slow diffusion of substrate to/from the active sites has been found to severely impair the activity microporous catalysts.[175] Therefore, by addressing the mass transport limitations of the microporous network, HP SAPOs are improving catalyst activity and lifetime in both the liquid-[178] and vapour-phase[124] BR. Whilst the structure and acidity of SAPOs have been characterised in great detail (e.g. *via* XRD, BET probe-FTIR, MAS NMR, and NH_3-TPD),[115, 124, 167, 178] mechanistic aspects of the BR in HP SAPOs are less well known. Therefore, an investigation of the effect of mesopore-templating on the mass transport properties and substrate-interactions of HP SAPOs might offer new insights for the optimisation of solid-acid catalysts for the Beckmann rearrangement.

1.9 Aims and Objectives

Hierarchical silicoaluminophosphates (HP SAPOs) prepared by soft-templating with organosilane surfactant have been shown to improve catalyst activity and lifetime in both the liquid- and vapour-phase Beckmann rearrangement. However, the nature of the organosilane mesoporogen is such that siliceous species are incorporated into the walls of the mesopores, and thus the soft-templating protocol has implications for both the structure and acidity of the resulting HP SAPOs.

The investigations reported in this thesis seek to improve understanding of the effect of the organosilane, soft-templating strategy on the structure and acidity of HP SAPOs, with a view to evaluating the structure-activity relationships that underpin their catalytic activity in the Beckmann rearrangement. The detailed physicochemical characterisation of organosilane-templated HP SAPO aim to provide a means to align catalyst properties with the reaction conditions, in order to improve catalytic outcomes in the Beckmann rearrangement.

Principal objectives:

- To perform a detailed physicochemical characterisation of HP SAPO using spectroscopic and probe-based techniques in order to assess:
    - the structure and interconnectivity of the micro- and meso-pores,
    - the nature of the acid sites within the micro- and meso-pores.

- To investigate how the soft-templating synthesis modifies the interaction between HP SAPO and cyclohexanone oxime, with a view to ascertaining the impact of the siliceous mesopores on the mechanism of the Beckmann rearrangement.

- To probe the mass transport properties of the HP SAPO in the context of the Beckmann rearrangement by quantifying the mobility of cyclohexanone oxime at a microscopic level.

- To apply the soft-templating protocol in the development of a new, HP catalyst based on the active SAPO-37 framework in order to:
    - address the progressive deactivation of microporous SAPO-37 with time-on-stream in the vapour-phase Beckmann rearrangement,
    - overcome the reduced mass transport associated with the lower temperature conditions of the liquid-phase Beckmann rearrangement.

1.10 References

1. I. Chorkendorff and J. W. Niemantsverdriet, *Concepts of Modern Catalysis and Kinetics*, John Wiley & Sons, Inc., Weinheim, 3 edn., 2017.

2. J. H. Clark and C. N. Rhodes, *Clean Synthesis Using Porous Inorganic Solid Catalysts and Supported Reagents*, Royal Society of Chemistry, Cambridge, 2000.

3. P. T. Anastas and M. M. Kirchhoff, *Acc. Chem. Res.*, 2002, **35**, 686-694.

4. J. Hagen, *Industrial Catalysis: A Practical Approach*, John Wiley & Sons, Inc., Berlin, 2015.

5. M. Lancaster, *Green Chemistry: An Introductory Text*, Royal Society of Chemistry, Cambridge, 2002.

6. J. M. Thomas, R. Raja, G. Sankar, R. G. Bell and D. W. Lewis, *Pure Appl. Chem.*, 2001, **73**, 1087-1101.

7. J. M. Thomas and W. J. Thomas, *Principles and Practice of Heterogeneous Catalysis*, John Wiley & Sons, Inc., Weinheim, 2014.

8. R. A. Sheldon and H. van Bekkum, *Fine Chemicals through Heterogeneous Catalysis*, John Wiley & Sons, Inc., Weinheim, 2001.

9. H. Liu, *Ammonia Synthesis Catalysts: Innovation and Practice*, World Scientific Publishing Company Ltd., Singapore, 2013.

10. *Heterogeneous Catalysis at Nanoscale for Energy Applications*, John Wiley & Sons, Inc., New Jersey, 2014.

11. F. G. Helfferich in *Kinetics of Multistep Reactions*, ed. F. G. Helfferich, Elsevier, Amsterdam, 2 edn., 2004, vol. 40, ch. 9, pp 273-308.

12. N. Pal and A. Bhaumik, *Adv. Colloid Interfac.*, 2013, **189-190**, 21-41.

13. T. J. Barton, L. M. Bull, W. G. Klemperer, D. A. Loy, B. McEnaney, M. Misono, P. A. Monson, G. Pez, G. W. Scherer, J. C. Vartuli and O. M. Yaghi, *Chem. Mater.*, 1999, **11**, 2633-2656.

14. M. Thommes, K. Kaneko, V. Neimark Alexander, P. Olivier James, F. Rodriguez-Reinoso, J. Rouquerol and S. W. Sing Kenneth, *Pure Appl. Chem.*, 2015, **87**, 1051-1069.

15. B. D. Zdravkov, J. J. Čermák, M. Šefara and J. Janků, *Cent. Eur. J. Chem.*, 2007, **5**, 385-395.

16. A. Corma, *Chem. Rev.*, 1997, **97**, 2373-2420.

17. K. K. Kolasinski, *Surface Science: Foundations of Catalysis and Nanoscience*, John Wiley & Sons, Inc., Chichester, 3 edn., 2012.

18. M. E. Davis, *Nature*, 2002, **417**, 813.

19. J. M. Thomas, *Design and Applications of Single-Site Heterogeneous Catalysts: Contributions to Green Chemistry, Clean Technology and Sustainability*, Imperial College Press, London, 2012.

20. S. M. Csicsery, *Zeolites*, 1984, **4**, 202-213.

21. P. B. Weisz and V. J. Frilette, *J. Phys. Chem.*, 1960, **64**, 382-382.

22. *Introduction to Zeolite Science and Practice*, ed. H. van Bekkum, E. M. Flanigen, P. A. Jacobs, J. C. Jansen, Elsevier, Amsterdam, 2001.

23. A. K. Cheetham, G. Férey and T. Loiseau, *Angew. Chem., Int. Ed.*, 1999, **38**, 3268-3292.

24. C. Baerlocher, L. B. McCusker, W. M. Meier and D. H. Olson, *Atlas of Zeolite Framework Types*, Elsevier, Amsterdam, 6 edn., 2007.

25. R. Xu, W. Pang, J. Yu, Q. Huo and J. Chen, *Chemistry of Zeolites and Related Porous Materials: Synthesis and Structure*, John Wiley & Sons, Inc., Singapore, 2007.

26. S. M. Auerbach, K. A. Carrado and P. K. Dutta, *Handbook of Zeolite Science and Technology*, Marcel Dekker Inc., New York, 2003.

27. W. Loewenstein, *Am. Mineral.*, 1954, **39**, 92-96.

28. M. E. Davis and R. F. Lobo, *Chem. Mater.*, 1992, **4**, 756-768.

29. L. E. Smart and E. A. Moore, *Solid State Chemistry: An Introduction*, CRC Press, Boca Raton, 4 edn., 2012.

30. J. Weitkamp, *Solid State Ionics*, 2000, **131**, 175-188.

31. N. Y. Chen, *J. Phys. Chem.*, 1976, **80**, 60-64.

32. I. Petrovic, A. Navrotsky, M. E. Davis and S. I. Zones, *Chem. Mater.*, 1993, **5**, 1805-1813.

33. D. Barthomeuf, *Mater. Chem. Phys.*, 1987, **17**, 49-71.

34. C. S. Cundy and P. A. Cox, *Chem. Rev.*, 2003, **103**, 663-702.

35. K. Tanabe and W. F. Hölderich, *Appl. Catal., A*, 1999, **181**, 399-434.

36. US Pat., 4410501 A, 1983.

37. C. Perego, A. Carati, P. Ingallina, M. A. Mantegazza and G. Bellussi, *Appl. Catal., A*, 2001, **221**, 63-72.

38. S. T. Wilson, B. M. Lok, C. A. Messina, T. R. Cannan and E. M. Flanigen, *J. Am. Chem. Soc.,* 1982, **104**, 1146-1147.

39. J. Yu and R. Xu, *Acc. Chem. Res.*, 2003, **36**, 481-490.

40. F. Corà, M. Alfredsson, C. M. Barker, R. G. Bell, M. D. Foster, I. Saadoune, A. Simperler and C. R. A. Catlow, *J. Solid State Chem.*, 2003, **176**, 496-529.

41. E. M. Flanigen, B. M. Lok, R. L. Patton and S. T. Wilson, *Pure Appl. Chem.*, 1986, **58**, 1351-1358.

42. M. Hartmann and L. Kevan, *Chem. Rev.*, 1999, **99**, 635-664.

43. E. Flanigen, R. L. Patton and S. Wilson, *Stud. Surf. Sci. Catal.*, 1988, **37**, 13.

44. J. A. Martens and P. A. Jacobs, *Stud. Surf. Sci. Catal.*, 1994, **85**, 653-685.

45. M. Hartmann and L. Kevan, *Res. Chem. Intermed.*, 2002, **28**, 625-695.

46. B. M. Weckhuysen, R. R. Rao, J. A. Martens and R. A. Schoonheydt, *Eur. J. Inorg. Chem.*, 1999, **1999**, 565-577.

47. P. Feng, X. Bu and G. D. Stucky, *Nature*, 1997, **388**, 735.

48. J. M. Thomas and R. Raja, *Proc. Natl. Acad. Sci. U. S. A*, 2005, **102**, 13732-13736.

49. J. Chen and J. M. Thomas, *J. Chem. Soc., Chem. Commun.*, 1994, **5**, 603-604.

50. M. E. Potter, D. Sun, E. Gianotti, M. Manzoli and R. Raja, *Phys. Chem. Chem. Phys.*, 2013, **15**, 13288-13295.

51. R. M. Leithall, V. N. Shetti, S. Maurelli, M. Chiesa, E. Gianotti and R. Raja, *J. Am. Chem. Soc.*, 2013, **135**, 2915-2918.

52. M. E. Potter, A. J. Paterson and R. Raja, *ACS Catal.*, 2012, **2**, 2446-2451.

53. J. Paterson, M. Potter, E. Gianotti and R. Raja, *Chem. Commun.*, 2011, **47**, 517-519.

54. K. M. H. Mohammed, A. Chutia, J. Callison, P. P. Wells, E. K. Gibson, A. M. Beale, C. R. A. Catlow and R. Raja, *J. Mater. Chem. A*, 2016, **4**, 5706-5712.

55. M. E. Potter, D. Sun and R. Raja, *Catal. Sci. Technol.*, 2016, **6**, 2616-2622.

56. R. Raja, G. Sankar and J. M. Thomas, *J. Am. Chem. Soc.*, 1999, **121**, 11926-11927.

57. J. M. Thomas, R. Raja, G. Sankar and R. G. Bell, *Nature*, 1999, **398**, 227.

58. C. Subrahmanyam, B. Louis, F. Rainone, B. Viswanathan, A. Renken and T. K. Varadarajan, *Catal. Commun.*, 2002, **3**, 45-50.

59. R. Raja, G. Sankar and J. M. Thomas, *J. Am. Chem. Soc.*, 2001, **123**, 8153-8154.

60. G. Sastre, D. W. Lewis and C. R. A. Catlow, *J. Mol. Catal. A: Chem.*, 1997, **119**, 349-356.

61. C. S. Blackwell and R. L. Patton, *J. Phys. Chem.*, 1988, **92**, 3965-3970.

62. D. Barthomeuf, *Zeolites*, 1994, **14**, 394-401.

63. B. M. Lok, C. A. Messina, R. L. Patton, R. T. Gajek, T. R. Cannan and E. M. Flanigen, *J. Am. Chem. Soc.*, 1984, **106**, 6092-6093.

64. US Pat., 4440871 A, 1984.

65. H. O. Pastore, S. Coluccia and L. Marchese, *Annu. Rev.. Mater. Res.*, 2005, **35**, 351-395.

66. G. Sastre, D. W. Lewis and C. R. A. Catlow, *J. Phys. Chem. B*, 1997, **101**, 5249-5262.

67. J. A. Martens, M. Mertens, P. J. Grobet and P. A. Jacobs, *Stud. Surf. Sci. Catal.*, 1988, **37**, 97-105.

68. M. E. Potter, J. Kezina, R. Bounds, M. Carravetta, T. M. Mezza and R. Raja, *Catal. Sci. Technol.*, 2018, **8**, 5155-5164.

69. M. E. Potter, M. E. Cholerton, J. Kezina, R. Bounds, M. Carravetta, M. Manzoli, E. Gianotti, M. Lefenfeld and R. Raja, *ACS Catal.*, 2014, **4**, 4161-4169.

70. R. B. Borade and A. Clearfield, *J. Mol. Catal.*, 1994, **88**, 249-265.

71. S. G. Hedge, P. Ratnasamy, L. M. Kustov and V. B. Kazansky, *Zeolites*, 1988, **8**, 137-141.

72. J. A. Martens, P. J. Grobet and P. A. Jacobs, *J. Catal.*, 1990, **126**, 299-305.

73. R. Vomscheid, M. Briend, M. J. Peltre, P. P. Man and D. Barthomeuf, *J. Phys. Chem.*, 1994, **98**, 9614-9618.

74. US Pat. 4499327 A, 1985.

75. W. Dai, X. Wang, G. Wu, N. Guan, M. Hunger and L. Li, *ACS Catal.*, 2011, **1**, 292-299.

76. B. P. C. Hereijgers, F. Bleken, M. H. Nilsen, S. Svelle, K.-P. Lillerud, M. Bjørgen, B. M. Weckhuysen and U. Olsbye, *J. Catal.*, 2009, **264**, 77-87.

77. L. Wang, C. Guo, S. Yan, X. Huang and Q. Li, *Micropor. Mesopor. Mater.*, 2003, **64**, 63-68.

78. T. Masukawa, T. Komatsu and T. Yashima, *Zeolites*, 1997, **18**, 10-17.

79. R. Kumar, G. N. Rao and P. Ratnasamy, in *Stud. Surf. Sci. Catal.*, 1989, **49**, 1141-1150.

80. J. Pérez-Ramírez, C. H. Christensen, K. Egeblad, C. H. Christensen and J. C. Groen, *Chem. Soc. Rev.*, 2008, **37**, 2530-2542.

81. K. Na, M. Choi and R. Ryoo, *Micropor. Mesopor. Mater.*, 2013, **166**, 3-19.

82. M. Hartmann, *Angew. Chem., Int. Ed.*, 2004, **43**, 5880-5882.

83. S. van Donk, A. H. Janssen, J. H. Bitter and K. P. de Jong, *Catal. Rev.*, 2003, **45**, 297-319.

84. M. E. Davis, *Chem. – A Eur. J.*, 1997, **3**, 1745-1750.

85. M. Estermann, L. B. McCusker, C. Baerlocher, A. Merrouche and H. Kessler, *Nature*, 1991, **352**, 320.

86. M. E. Davis, C. Saldarriaga, C. Montes, J. Garces and C. Crowder, *Zeolites*, 1988, **8**, 362-366.

87. C. C. Freyhardt, M. Tsapatsis, R. F. Lobo, K. J. Balkus Jr and M. E. Davis, *Nature*, 1996, **381**, 295.

88. Database of Zeolite Structures, http://www.iza-structure.org/databases, (accessed January 2019).

89. C. T. Kresge, M. E. Leonowicz, W. J. Roth, J. C. Vartuli and J. S. Beck, *Nature*, 1992, **359**, 710.

90. J. S. Beck, J. C. Vartuli, W. J. Roth, M. E. Leonowicz, C. T. Kresge, K. D. Schmitt, C. T. W. Chu, D. H. Olson, E. W. Sheppard, S. B. McCullen, J. B. Higgins and J. L. Schlenker, *J. Am. Chem. Soc.*, 1992, **114**, 10834-10843.

91. F. Hoffmann, M. Cornelius, J. Morell and M. Fröba, *Angew. Chem., Int. Ed.*, 2006, **45**, 3216-3251.

92. A. Taguchi and F. Schüth, *Micropor. Mesopor. Mater.*, 2005, **77**, 1-45.

93. U. Ciesla and F. Schüth, *Micropor. Mesopor. Mater.*, 1999, **27**, 131-149.

94. US Pat., 5258114 A, 1993.

95. A. Corma, M. S. Grande, V. Gonzalez-Alfaro and A. V. Orchilles, *J. Catal.*, 1996, **159**, 375-382.

96. S. Lopez-Orozco, A. Inayat, A. Schwab, T. Selvam and W. Schwieger, *Adv. Mater.*, 2011, **23**, 2602-2615.

97. K. Na and G. A. Somorjai, *Catal. Lett.*, 2015, **145**, 193-213.

98. D. P. Serrano, J. M. Escola and P. Pizarro, *Chem. Soc. Rev.*, 2013, **42**, 4004-4035.

99. Y. Wei, T. E. Parmentier, K. P. de Jong and J. Zečević, *Chem. Soc. Rev.*, 2015, **44**, 7234-7261.

100. R. Chal, C. Gérardin, M. Bulut and S. van Donk, *ChemCatChem*, 2011, **3**, 67-81.

101. V. Valtchev, E. Balanzat, V. Mavrodinova, I. Diaz, J. El Fallah and J.-M. Goupil, *J. Am. Chem. Soc.*, 2011, **133**, 18950-18956.

102. D. Verboekend, G. Vilé and J. Pérez-Ramírez, *Adv. Funct. Mater.*, 2012, **22**, 916-928.

103. D. Verboekend and J. Pérez-Ramírez, *Catal. Sci. Technol.*, 2011, **1**, 879-890.

104. M. Milina, S. Mitchell, P. Crivelli, D. Cooke and J. Pérez-Ramírez, *Nature Commun.*, 2014, **5**, 3922.

105. S. Abelló, A. Bonilla and J. Pérez-Ramírez, *Appl. Catal. A: Gen.*, 2009, **364**, 191-198.

106. D. Verboekend, M. Milina and J. Pérez-Ramírez, *Chem. Mater.*, 2014, **26**, 4552-4562.

107. X. Chen, D. Xi, Q. Sun, N. Wang, Z. Dai, D. Fan, V. Valtchev and J. Yu, *Micropor. Mesopor. Mater.*, 2016, **234**, 401-408.

108. T. Kimura, *Micropor. Mesopor. Mater.*, 2005, **77**, 97-107.

109. A. Sorrenti, O. Illa and R. M. Ortuño, *Chem. Soc. Rev.*, 2013, **42**, 8200-8219.

110. M. Choi, H. S. Cho, R. Srivastava, C. Venkatesan, D.-H. Choi and R. Ryoo, *Nature Mater.*, 2006, **5**, 718.

111. M. Kruk, *Acc. Chem. Res.*, 2012, **45**, 1678-1687.

112. C. Jo, J. Jung and R. Ryoo, *Micropor. Mesopor. Mater.*, 2014, **194**, 83-89.

113. N. Danilina, F. Krumeich and J. A. van Bokhoven, *J. Catal.*, 2010, **272**, 37-43.

114. M. Tiemann and M. Fröba, *Chem. Mater.*, 2001, **13**, 3211-3217.

115. M. Choi, R. Srivastava and R. Ryoo, *Chem. Commun.*, 2006, **42**, 4380-4382.

116. K. Cho, R. Ryoo, S. Asahina, C. Xiao, M. Klingstedt, A. Umemura, M. W. Anderson and O. Terasaki, *Solid State Sci.*, 2011, **13**, 750-756.

117. R. Ryoo, J. M. Kim, C. H. Ko and C. H. Shin, *J. Phys. Chem.*, 1996, **100**, 17718-17721.

118. A. Galarneau, H. Cambon, F. Di Renzo, R. Ryoo, M. Choi and F. Fajula, *New J. Chem.*, 2003, **27**, 73-79.

119. A. J. J. Koekkoek, C. H. L. Tempelman, V. Degirmenci, M. Guo, Z. Feng, C. Li and E. J. M. Hensen, *Catal. Today*, 2011, **168**, 96-111.

120. V. N. Shetti, J. Kim, R. Srivastava, M. Choi and R. Ryoo, *J. Catal.*, 2008, **254**, 296-303.

121. M. Choi, D.-H. Lee, K. Na, B.-W. Yu and R. Ryoo, *Angew. Chem., Int. Ed.*, 2009, **48**, 3673-3676.

122. D.-H. Lee, M. Choi, B.-W. Yu and R. Ryoo, *Chem. Commun.*, 2009, 74-76.

123. A. Inayat, I. Knoke, E. Spiecker and W. Schwieger, *Angew. Chem., Int. Ed.*, 2012, **51**, 1962-1965.

124. S. H. Newland, W. Sinkler, T. Mezza, S. R. Bare, M. Carravetta, I. M. Haies, A. Levy, S. Keenan and R. Raja, *ACS Catal.*, 2015, **5**, 6587-6593.

125. Q. Sun, N. Wang, D. Xi, M. Yang and J. Yu, *Chem. Commun.*, 2014, **50**, 6502-6505.

126. S. Tao, X. Li, G. Lv, C. Wang, R. Xu, H. Ma and Z. Tian, *Catal. Sci. Technol.*, 2017, **7**, 5775-5784.

127. M.-J. Jin, A. Taher, H.-J. Kang, M. Choi and R. Ryoo, *Green Chem.*, 2009, **11**, 309-313.

128. S. H. Newland, D. J. Xuereb, E. Gianotti, L. Marchese, R. Rios and R. Raja, *Catal. Sci. Technol.*, 2015, **5**, 660-665.

129. *Synthetic Fibres: Nylon, Polyester, Acrylic, Polyolefin*, ed. J. E. McIntyre, Woodhead Publishing Ltd., Cambridge, 2005.

130. *Biocomposites: Design and Mechanical Performance*, ed. M. Misra, J. K. Pandey, A. K. Mohanty, Woodhead Publishing Ltd., Cambridge, 2015.

131. Nylon 6 & 66 Market Size Worth $41.13 Billion By 2025 | CAGR: 6.1%, https://www.grandviewresearch.com/press-release/global-nylon-6-66-market, (accessed January 2019).

132. G. B. Kauffman, *J. Chem. Educ.*, 1988, **65**, 803.

133. *Recycling of Polymers: Methods, Characterization and Applications*, John Wiley-VCH, Weinheim, 2016.

134. R. Raja, *Top. Catal.*, 2009, **52**, 322-332.

135. Caprolactam Market Size Worth $15.74 Billion By 2022 | CAGR 5.2%, https://www.grandviewresearch.com/press-release/global-caprolactam-market, (accessed January 2019).

136. R. J., H. Fuchs, H. Kieczka and W. C. Moran, in *Ullmann's Encyclopedia of Industrial Chemistry*, Wiley-VCH, Weinheim, 2011, DOI: doi:10.1002/14356007.a05_031.pub2.

137. R. A. Sheldon and R. S. Downing, *Appl. Catal. A: Gen.*, 1999, **189**, 163-183.

138. G. Dahlhoff, J. P. M. Niederer and W. F. Hoelderich, *Catal. Rev.*, 2001, **43**, 381-441.

139. *Zeolites in Industrial Separation and Catalysis*, Wiley-VCH, Germany, 2010.

140. Y. Izumi, H. Ichihashi, Y. Shimazu, M. Kitamura and H. Sato, *Bull. Chem. Soc. Jpn.*, 2007, **80**, 1280-1287.

141. US Pat. 4709024 A, 1987.

142. US Pat. 4717769 A, 1988.

143. D. H. Olson, W. O. Haag and R. M. Lago, *J. Catal.*, 1980, **61**, 390-396.

144. G. L. Woolery, L. B. Alemany, R. M. Dessau and A. W. Chester, *Zeolites*, 1986, **6**, 14-16.

145. R. Raja, M. E. Potter and S. H. Newland, *Chem. Commun.*, 2014, **50**, 5940-5957.

146. H. Sato, *Catal. Rev.*, 1997, **39**, 395-424.

147. H. Ichihashi and M. Kitamura, *Catal. Today*, 2002, **73**, 23-28.

148. A. Aucejo, M. C. Burguet, A. Corma and V. Fornes, *Appl. Catal.*, 1986, **22**, 187-200.

149. S. Hiroshi and H. Ken-ichi, *Chem. Lett.*, 1993, **22**, 1765-1766.

150. G. P. Heitmann, G. Dahlhoff and W. F. Hölderich, *J. Catal.*, 1999, **186**, 12-19.

151. W. F. Hölderich, J. Röseler, G. Heitmann and A. T. Liebens, *Catal. Today*, 1997, **37**, 353-366.

152. G. P. Heitmann, G. Dahlhoff, J. P. M. Niederer and W. F. Hölderich, *J. Catal.*, 2000, **194**, 122-129.

153. W. F. Hölderich and G. Heitmann, *Catal. Today*, 1997, **38**, 227-233.

154. V. R. R. Marthala, Y. Jiang, J. Huang, W. Wang, R. Gläser and M. Hunger, *J. Am. Chem. Soc.*, 2006, **128**, 14812-14813.

155. H. Sato, K. Hirose, M. Kitamura and Y. Nakamura, *Stud. Surf. Sci. Catal.,* 1989, **49**, 1213-1222.

156. H. Ichihashi and H. Sato, *Appl. Catal. A: Gen.*, 2001, **221**, 359-366.

157. M. Kitamura and H. Ichihashi, *Stud. Surf. Sci. Catal.*, 1994, **90**, 67-70.

158. T. Komatsu, T. Maeda and T. Yashima, *Micropor. Mesopor. Mater.*, 2000, **35-36**, 173-180.

159. P. Albers, K. Seibold, T. Haas, G. Prescher and W. F. Hölderich, *J. Catal.*, 1998, **176**, 561-568.

160. H. Kath, R. Gläser and J. Weitkamp, *Chem. Eng. Technol.*, 2001, **24**, 150-153.

161. H. Ichihashi, M. Ishida, A. Shiga, M. Kitamura, T. Suzuki, K. Suenobu and K. Sugita, *Catal. Surv. Asia*, 2003, **7**, 261-270.

162. S. Chapman, M. Potter and R. Raja, *Molecules*, 2017, **22**, 2127.

163. A. Cesana, S. Palmery, R. Buzzoni, G. Spanò, F. Rivetti and L. Carnelli, *Catal. Today*, 2010, **154**, 264-270.

164. P. Botella, A. Corma, S. Iborra, R. Montón, I. Rodríguez and V. Costa, *J. Catal.*, 2007, **250**, 161-170.

165. C. Yin, R. Ni, X. Bao and Y. Chen, *Micropor. Mesopor. Mater.*, 2015, **202**, 133-137.

166. J. Kim, W. Park and R. Ryoo, *ACS Catal.*, 2011, **1**, 337-341.

167. I. Miletto, G. Paul, S. Chapman, G. Gatti, L. Marchese, R. Raja and E. Gianotti, *Chem. – A Eur. J.*, 2017, **23**, 9952-9961.

168. C. C. Pavel, R. Palkovits, F. Schüth and W. Schmidt, *J. Catal.*, 2008, **254**, 84-90.

169. R. Palkovits, W. Schmidt, Y. Ilhan, A. Erdem-Şenatalar and F. Schüth, *Micropor. Mesopor. Mater.*, 2009, **117**, 228-232.

170. M. A. Camblor, A. Corma, H. García, V. Semmer-Herlédan and S. Valencia, *J. Catal.*, 1998, **177**, 267-272.

171. C. Ngamcharussrivichai, P. Wu and T. Tatsumi, *J. Catal.*, 2004, **227**, 448-458.

172. C. Ngamcharussrivichai, P. Wu and T. Tatsumi, *J. Catal.*, 2005, **235**, 139-149.

173. P. S. Singh, R. Bandyopadhyay, S. G. Hegde and B. S. Rao, *Appl. Catal. A: Gen.*, 1996, **136**, 249-263.

174. M. J. Peltre, P. P. Man, M. Briend, M. Derewinski and D. Barthomeuf, *Catal. Lett*, 1992, **16**, 123-128.

175. M. E. Potter, A. J. O'Malley, S. Chapman, J. Kezina, S. H. Newland, I. P. Silverwood, S. Mukhopadhyay, M. Carravetta, T. M. Mezza, S. F. Parker, C. R. A. Catlow and R. Raja, *ACS Catal.*, 2017, **7**, 2926-2934.

176. E. Gianotti, M. Manzoli, M. E. Potter, V. N. Shetti, D. Sun, J. Paterson, T. M. Mezza, A. Levy and R. Raja, *Chem. Sc.*, 2014, **5**, 1810-1819.

177. M. E. Potter, S. Chapman, A. J. O'Malley, A. Levy, M. Carravetta, T. M. Mezza, S. F. Parker and R. Raja, *ChemCatChem*, 2017, **9**, 1897-1900.

178. I. Miletto, C. Ivaldi, G. Paul, S. Chapman, L. Marchese, R. Raja and E. Gianotti, *ChemistryOpen*, 2018, **7**, 297-301.

Chapter 2 Experimental techniques

2.1 Quantifying catalysis: reaction analytics

2.1.1 Gas chromatography

Gas chromatography (GC) is an analytical technique that is used to isolate, characterise and quantify the chemical compounds in a mixture.[1, 2] In catalytic studies, GC may be used to assay a reaction mixture in order to quantify catalyst performance.

In general, chromatography describes a physical technique to separate the components of a mixture based on their partitioning between stationary and mobile phase.[2] Depending on its adsorption and solubility properties, a solute with a higher affinity for the stationary phase will travel more slowly through the column than a compound that preferentially partitions into the mobile phase.[3] As each component elutes from the column it is passed to a detector, which generates an output signal proportional to the amount of solute (**Figure 2.1.1**).

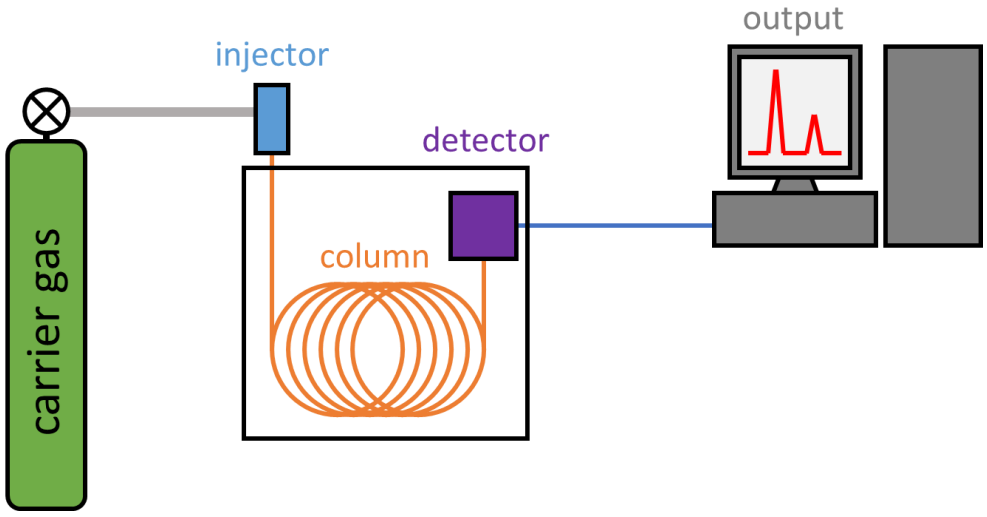

Figure 2.1.1: A schematic of a typical GC experiment. A sample entering *via* a heated injector port is vaporised before being transferred to the chromatographic column. Under a controlled flow of carrier gas (e.g. He), the sample mixture is transported along the column (usually coated with a high-boiling polymer) and the analytes are separated based on their relative affinity for each phase. The effluent stream is monitored in real-time by a detector, which produces a signal with intensity proportional to the quantity of analyte detected.[1, 2]

Detector outputs are transformed into a chromatogram, which is a plot of signal intensity *versus* retention time (**Figure 2.1.2**). If components cannot be characterised by their particular retention times, then GC may be coupled with another analysis (such as mass spectrometry) that can provide further structural information.[1]

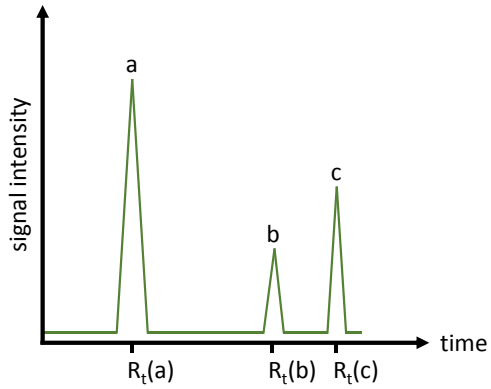

Figure 2.1.2: A gas chromatogram of a mixture that has been separated into the components, *a*, *b* and *c*, which are eluted at a retention time of $R_t(a)$, $R_t(b)$and $R_t(c)$, respectively.

With sufficient peak resolution, a GC signal can be related to the concentration of a particular analyte. However, as the detector response varies with the structure of the compound being analysed, each component is associated with a response factor (*RF*), which relates the peak area (A_x) to the moles of the analyte (n_x) detected (**Equation 2.1.1**).[4]

Equation 2.1.1: $$RF(x) = \frac{A_x}{n_x}$$

Since *RF*(*x*) is unknown, to determine the absolute concentration of *x*, it is necessary to define a relative retention factor (*RRF*(*x*)), using an inert reference standard (**Equation 2.1.2**).[4] The *RRF*(*x*) can be obtained from the retention factor of the reference standard (*RF*(*S*)) by performing a calibration.

Equation 2.1.2: $$RRF(x) = \frac{RF(x)}{RF(S)} = \frac{A_x}{n_x} \times \frac{n_S}{A_S}$$

Practically, calibration requires the preparation of a series of solutions, each containing a different known amount of analyte but a constant amount of the reference standard. A fixed volume of each solution is injected into the GC apparatus and a chromatogram obtained. Provided the quantity of analyte and standard are known accurately, it is possible to generate a calibration curve, which is the ratio of the peak area of the analyte to the internal standard (A_x/A_S), against the ratio of their molar quantities (n_S/n_x). From **Equation 2.1.2**, the calibration plot is a straight line that passes through the origin, with a gradient equal to *RRF*(*x*). Thereafter, when a test solution containing an unknown concentration of analyte, but

a known concentration of the internal standard, is analysed by GC, the *RRF* can be used to relate their relative peak intensities to the quantity of analyte present in the sample using **Equation 2.1.3**.

Equation 2.1.3: $$n_x = \frac{A_x}{A_S} \times \frac{n_S}{RRF(x)}$$

2.1.2 Parameters for assessing catalyst activity

If the components of a reaction mixture are analysed by gas chromatography, this information can be used to quantify catalyst performance:[5]

- Conversion, as defined in **Equation 2.1.4**, is the ratio of the amount of reagent, *x*, that has reacted ($n(x)_t$), to the initial amount of *x* that was added ($n(x)_0$).

Equation 2.1.4: $$Conversion\ (\%) = \frac{n(x)_0 - n(x)_t}{n(x)_0} \times 100\ \%$$

- Selectivity is the amount of starting material transformed into a particular product (*x*), as a fraction of the total moles of products ($n(products)$) formed (**Equation 2.1.5**).

Equation 2.1.5: $$Selectivity\ (\%) = \frac{n(x)}{n(products)} \times 100\%$$

- The yield of a desired product, *x*, can be calculated using **Equation 2.1.6**.

Equation 2.1.6: $$Yield\ (\%) = \frac{(\%\ conversion) \times (\%\ selectivity\ for\ x)}{100\ \%}$$

2.2 Materials characterisation

When designing and optimising functional, catalytic materials, it is important to understand how the structural and chemical properties of the catalyst affect the reaction pathway. Hence, materials characterisation is fundamental aspect of catalytic science, as it provides a means to probe the structure-property relationships that underpin catalyst activity, and to rationalise and predict catalytic outcomes.

In heterogeneous catalysis, characterisation is used to probe material structure, composition, and reactivity - particularly in proximity to the active site. Yet no single technique is capable of probing all aspects simultaneously, and so a variety of physical and chemical characterisation tools are required to comprehensively evaluate the catalyst properties (**Table 2.2.1**). In this way, it is possible access to information from the atomic-level to the macro-scale, and to target both surface and bulk properties. In addition, *in situ* and *in operando* experiments offer a means to study catalyst-substrate interactions in a more representative chemical environment, providing insight into the nature of adsorbed species, reactive intermediates, and catalyst mechanism.

Table 2.2.1: An overview of the experimental methods described in this discourse, and the information that has been extracted from each technique.

Experiment	Use
Powder X-ray diffraction	Phase identification, phase purity, and the quantification of unit cell parameters of crystalline samples.
Nitrogen gas adsorption-desorption	Surface area, pore volume, pore size distribution, pore structure, and pore interconnectivity of catalyst samples.
Positron annihilation lifetime spectroscopy	Pore size distributions in the catalysts.
Elemental analyses	Quantification of the elemental composition of the catalyst and encapsulated species.
Electron microscopy	Visualisation of the size and shape of catalyst particles, and the visualisation of mesoporous structures.
Thermogravimetric analysis	Identifying temperature-dependent physical (e.g. desorption) and chemical (e.g. thermal decomposition) processes, including framework degradation, decomposition of organic templating agents and the oxidation of coke deposits.
Temperature-programmed desorption of ammonia	Quantitative and qualitative analysis of the types and strength of acid sites in the catalysts.

Table 2.2.1 continued: An overview of the experimental methods described in this discourse and the information that has been extracted from each technique.

Experiment	Use
Fourier transform infrared spectroscopy	Vibrational characterisation of the framework acid sites.
with basic probe molecules	Quantitative and qualitative analysis of the strength and accessibility of acidic active sites.
with cyclohexanone oxime substrate	*In situ* studies of substrate-framework interactions.
Solid-state nuclear magnetic resonance spectroscopy	Characterisation of the local environment of spin-active nuclei in the catalyst (^{1}H, ^{27}Al, ^{29}Si, ^{31}P).
with basic probe molecules	Qualitative analysis of the strength, accessibility, and types of acidic active sites *via* ^{1}H and ^{15}N nuclei.
with cyclohexanone oxime substrate	*In situ* studies of substrate-framework interactions *via* the ^{1}H nucleus.
Neutron diffraction	Monitoring structural changes in the catalyst and substrate, including the uptake of substrate into the pores.
Inelastic neutron scattering	Vibrational analysis of substrate-framework interactions.
Quasi-elastic neutron scattering	Assessing the mobility of substrate within the porous catalyst framework.

2.2.1 Powder X-ray diffraction

Powder X-ray diffraction (XRD) is a non-destructive characterisation tool used to study the ordered atomic arrays in a polycrystalline sample. XRD is a relatively straightforward and accessible technique that is used routinely in materials science for phase identification, structure determination, and quantitative phase analysis. Whilst XRD is a bulk technique, it can be used to study aspects of microstructure, such as atomic substitutions and defects.[6]

2.2.1.1 Generating X-rays

X-rays are a form electromagnetic radiation that are produced by irradiating matter with high-energy photons or charged particles.[7] In a laboratory X-ray source (**Figure 2.2.1**) the charged particles are electrons produced by thermionic emission from a tungsten filament. By applying a large potential difference (20 – 60 kV), the ejected electrons are accelerated, *in vacuo*, towards a metal target (the anode).[8, 9] The impact of high-energy electrons on the target excites a cascade of electronic transitions in the atoms of the anode, and with subsequent relaxation to the ground state, X-rays are emitted. Therefore, the properties of the X-rays are determined by the composition of the anode. Suitable targets are typically high-melting metals with excellent electrical and thermal conductivity (e.g. Cu, Mo).

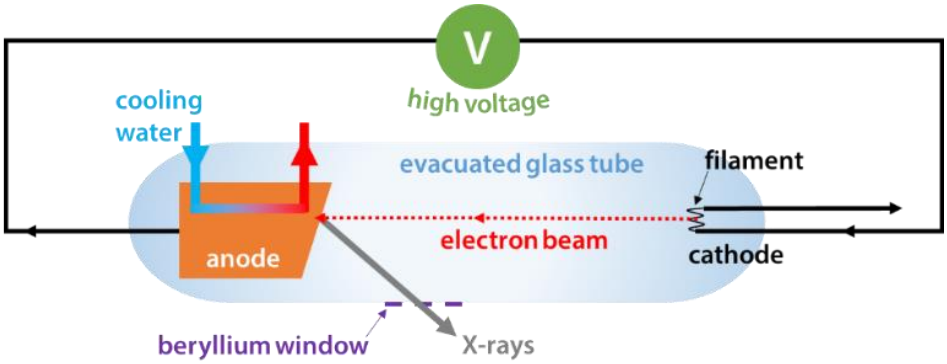

Figure 2.2.1: A schematic of a laboratory X-ray source. Electrons, generated by thermionic emission at the cathode, are accelerated towards a metal anode by a high potential difference. X-rays are emitted when electron impact excites electronic transitions in the anode atoms.[8]

The process of bombarding a metal anode with electrons produces an X-ray spectrum with two distinct components (**Figure 2.2.2**).[10] A background of 'white' X-rays (bremsstrahlung radiation) is produced when the impinging electrons transition between unquantised hyperbolic trajectories as they decelerate on impacting the anode.[11] Superimposed on the continuum of background X-rays are a series of sharp, characteristic lines.

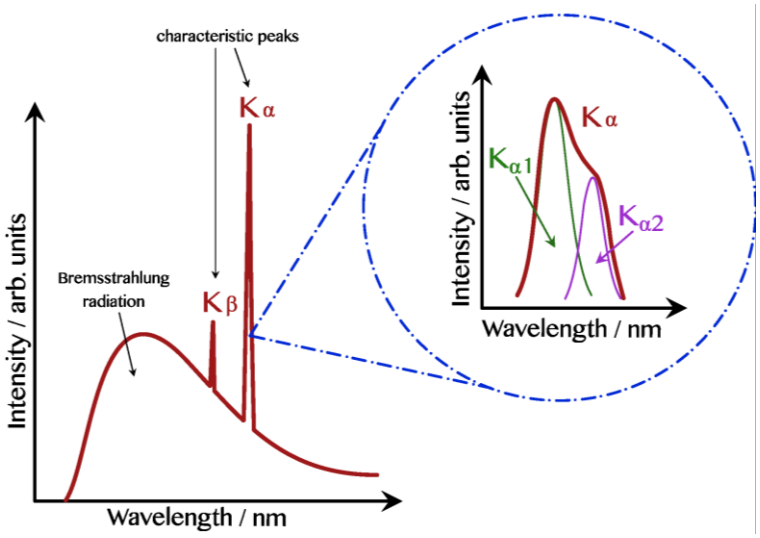

Figure 2.2.2: (a) The X-ray spectrum of a laboratory source typically comprises sharp characteristic lines (K_{α}, K_{β}), superimposed on a broad background of bremsstrahlung radiation. **(b)** The K_{α} peak comprises two lines, which may be resolved.[8]

Characteristic X-ray peaks will be observed if the energy of the incoming electrons exceeds a threshold value determined by the composition of the anode. If this condition is met, the collision with the anode can cause an electron to be ejected from the core shell of a target atom. As a valence electron relaxes to fill the vacancy, an X-ray photon is released with an energy equal to the transition energy between the two shells (**Figure 2.2.3**).[10] From the X-ray spectrum, the quantised characteristic X-rays (in particular the $K_{\alpha1}$ and $K_{\alpha2}$ lines) are used for X-ray diffraction studies. To achieve good resolution, monochromatisation is often used to suppress the background radiation and select the intense K_{α} line.[6]

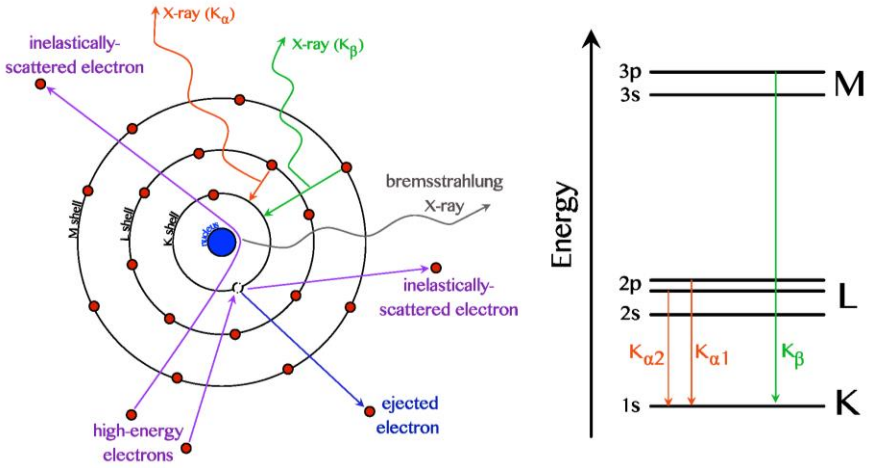

Figure 2.2.3: (a) On bombarding the metal anode, impinging electrons may be deflected with the emission of an X-ray that contributes to the bremsstrahlung radiation. Alternatively, electron impact may ionise a core electron and when a valence electron relaxes into the vacancy, a characteristic X-ray is emitted. Characteristic X-rays are labelled according to the orbitals between which the electron transition has occurred. **(b)** The energy level diagram depicts the electronic transitions that give rise to $K_{\alpha1}$, $K_{\alpha2}$ and K_{β} lines in an X-ray spectrum.[8]

2.2.1.2 X-ray diffraction theory

XRD involves measuring the intensity of X-rays that have been elastically scattered by interaction with the electron density at an atomic centre.[12] In an ordered material, a periodic array of lattice points, separated on the order of the X-ray wavelength (~ 1 Å), act as a diffraction grating towards X-rays. Depending on the position of the scattering centre, a diffracted X-ray from a monochromatic source will undergo a relative phase-shift.[8] If scattered wavefronts are in-phase, they interfere constructively and an intensity maximum is detected. Thus, the distribution of scattered X-rays reflects the distribution of electron density in the lattice.[12]

In a crystalline sample, intensity maxima are attributed to the 'reflection' of X-rays that have been scattered by lattice points occupying a particular lattice plane (a set of equidistant crystallographic surfaces). Since X-rays are highly penetrating, they can interact with lattice planes deep into the bulk of the material. The radiation diffracted by a series of parallel lattice planes is scattered in-phase and thus interfere constructively to give a peak of diffraction intensity. The condition for constructive interference by a lattice plane (denoted by the Miller Index *hkl*) is expressed by Bragg's Law (**Figure 2.2.4**).

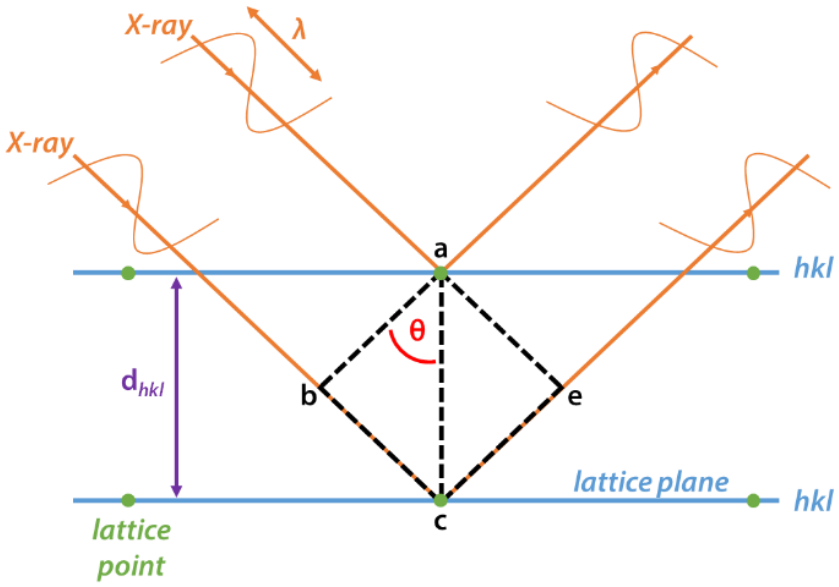

Figure 2.2.4: A visual description of Bragg's Law. Monochromatic X-rays of wavelength λ, impinge on a crystalline sample at an angle, θ, and are 'reflected' by interaction with lattice points. For an intensity maximum of diffracted X-rays to be detected, the X-rays must be scattered in phase by the lattice points occupying a set of parallel lattice planes (denoted *hkl*, and separated by a distance d_{hkl}). The Bragg condition is satisfied when the path difference (i.e. $bc + ce = 2\, d_{hkl} \sin\theta$) is equal to an integer number of wavelengths (i.e. $n\lambda$).[9]

2.2.1.3 Diffraction from a powder

A sample irradiated with a monochromatic beam will scatter X-rays in all directions, but only lattice planes oriented to satisfy the Bragg condition give rise to constructive interference. In a powder sample comprising many, randomly-oriented crystallites, the collective scattering from the sample is measured simultaneously, and by rotating the sample about an axis normal to the sample plate, the number of lattice planes brought into the diffracting condition is maximised.[9] The result is a series of coaxial Debye-Scherrer diffraction-cones of semiapex 2θ, each of which corresponds to a particular lattice plane (**Figure 2.2.5**). As a detector moves around the sample it takes one-dimensional cuts through the diffraction rings, generating a powder diffraction pattern of the scattered X-ray intensity *versus* 2θ.

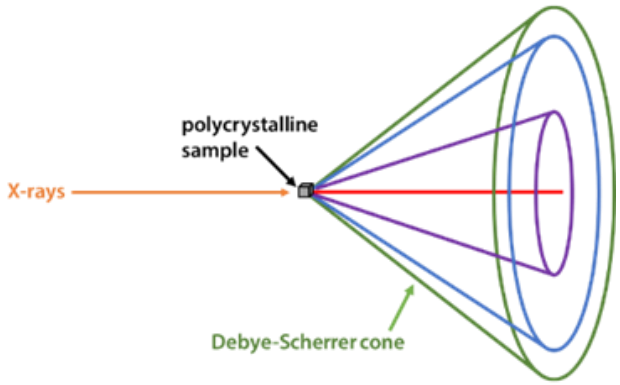

Figure 2.2.5: In a polycrystalline sample, there will be a large number of crystallites oriented so that a particular set of lattice planes meet the diffraction condition. X-rays reflected by a particular lattice plane lie on the surface of a Debye-Scherrer cone.[13]

2.2.1.4 Information from powder X-ray diffraction

Typically, three main aspects of an experimental XRD pattern are used to extract structural information about a polycrystalline sample.[13] Firstly, the position (and number) of peaks is informative of unit cell parameters and lattice type. By accurately determining peak positions, structure refinement can be used to calculate lattice parameters. Secondly, peak intensities are indicative of the spatial distribution and type of atoms occupying a lattice plane. Peak intensities can also reveal a preferred orientation of the crystallites (i.e. sample texture). Thirdly, peak shape can provide insight into material crystallinity and crystallite size, as well as structural stress and strain.

2.2.1.5 Structure refinement: the Rietveld method

If the XRD peaks are well resolved, the Rietveld method can be used to analyse the crystal structure.[9] In a Rietveld analysis, an overall line profile is calculated for the diffraction pattern, typically starting from a trial structure. By varying parameters such as atomic positions and lattice parameters, the information content of the XRD spectrum (peaks and background) is refined by a least-squares approach.[6] The variables are modified iteratively to achieve a best fit of the calculated pattern to the experimental data.

2.2.2 Physisorptive characterisation

When molecules in the gas phase approach a solid surface, their concentration at the fluid-solid interface increases.[14] Gas-enrichment at the interfacial layer, or adsorption, is driven by the reduced surface tension of the solid on interacting with a gas molecule. If a probe gas is physically adsorbed to a surface through van der Waals-type interactions, the chemical properties of both the adsorbate and the adsorbent are unchanged. Yet, these interactions can be exploited to study the texture of porous materials.[15] As well as informing on pore morphologies, gas adsorption-desorption experiments can be used to obtain quantitative surface area estimates, pore volumes, and pore size distributions (PSDs).

Due to the availability of liquid nitrogen, N_2 at 77 K is the typical adsorptive for porosity measurements.[16-18] Whilst limitations of the traditional N_2 system are widely acknowledged,[19] due to the availability of commercial apparatus and the abundance of comparable data, nitrogen adsorption remains routine in porosimetry.

2.2.2.1 Sorption mechanisms

Porous solids are typically categorised their by pore structure, with pore size being a fundamental descriptor. A sample may be classified as microporous (< 2 nm pore diameter), mesoporous (2 – 50 nm pore diameter), or macroporous (> 50 nm pore diameter),[19] based on their characteristic sorption phenomena (**Figure 2.2.6** and **Figure 2.2.7**) .[14]

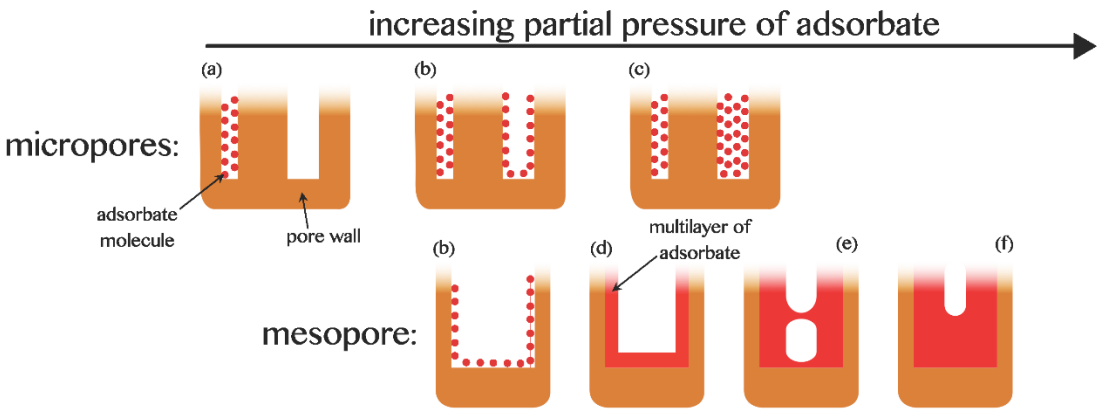

Figure 2.2.6: A schematic of gas adsorption mechanisms in micro- and meso-pores. **(a)** Gas molecules adsorb in the smallest micropores first, which may fill in a single step.[20] **(b)** Monolayer coverage is followed by **(c)** formation of a liquid-like multilayer at the surface, which fills the larger micropores. **(d)** As the partial pressure of adsorbate is increased, a multilayer accumulates in the mesopores. **(e)** Capillary condensation may occur if a meniscus bridges the liquid layers on opposing pore walls. **(f)** The mesopores are filled as the concentration of adsorbate is increased, and a fluid multilayer will continue to grow inside the largest macropores and on any unconfined surfaces.[14]

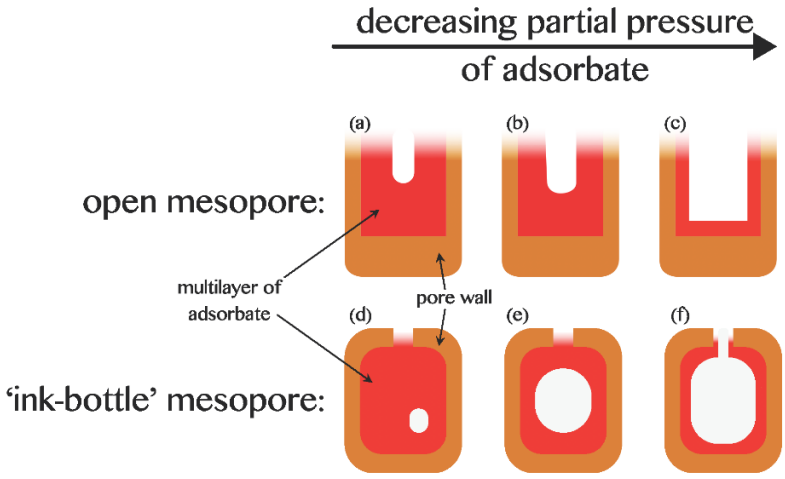

Figure 2.2.7: A schematic of gas desorption in a mesopore. **(a-c)** In an open mesopore, the multilayer of adsorbate is gradually thinned as the partial pressure of adsorbate gas is decreased. **(d)** If the pore opening is smaller than the pore body (e.g. an inkbottle mesopore), spontaneous cavitation creates a bubble inside the pore. **(e)** As the partial pressure of adsorbate is decreased, the body of the inkbottle mesopore is emptied, whilst the pore opening remains filled. **(f)** With further decrease in the partial pressure of adsorbate, the pore mouth is emptied, and the multilayer of adsorbate is thinned.[14]

2.2.2.2 Gas adsorption manometry

Gas adsorption manometry measures the pressure changes that occur when a sample, occupying a fixed-volume chamber, is exposed to a probe gas. In a typical gas adsorption experiment, a pressure-volume isotherm is obtained in four key steps:[14, 15, 19]

1. **Activation** of the sample by outgassing under conditions that remove physisorbed contaminants without disrupting its structural integrity.

At this stage, the sample mass is recorded and the sample cell transferred to the adsorption manifold (**Figure 2.2.8**). The mass is used to normalise adsorption data per gram of sample.[19]

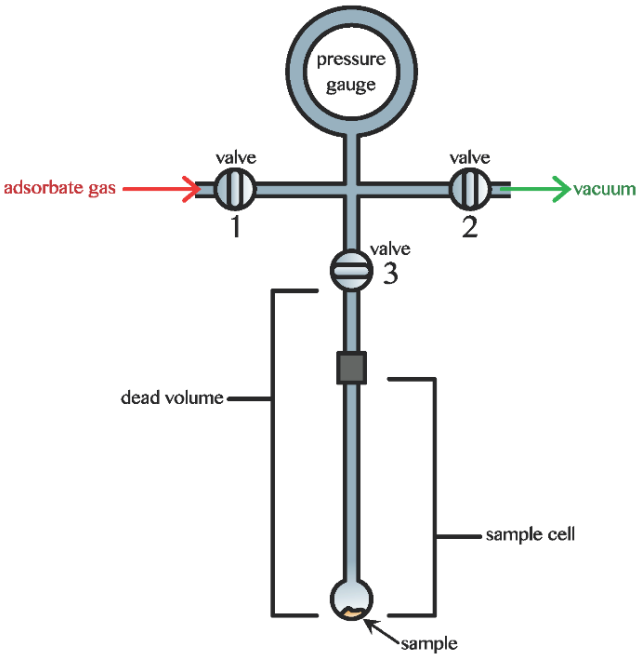

Figure 2.2.8: Gas adsorption manometry. By closing valve 2 and opening valves 1 and 3, the sample is dosed with adsorbate gas. When valve 1 is closed and valves 2 and 3 are open, the sample is exposed to a vacuum pressure and the adsorbed gas is removed.[14]

2. **Calibration of dead-space volume** around the adsorbent (i.e. the sample cell and part of the manifold) using a non-adsorbing gas (e.g. He).

3. **Adsorption** occurs when a known quantity of gas is admitted to the cell. As the gas physisorbs to the sample, the pressure decreases until a dynamic equilibrium is achieved. At equilibrium, the pressure is measured and the volume of gas in the dead space is calculated. The amount of adsorbed gas is the difference in the quantity of gas admitted and that in the dead space at equilibrium. Gas is dosed into the container at a constant temperature to generate a pressure-volume adsorption isotherm.

4. **Desorption** occurs as portions of gas are removed (at constant temperature) and a pressure-volume desorption isotherm is constructed.

2.2.2.3 Classification of gas adsorption-desorption isotherms

The shape of the isotherm obtained by gas sorption can provide qualitative information about the porosity of a sample.[15] Most isotherms can be classified under one of six systems defined by the International Union of Pure and Applied Chemistry (IUPAC) (**Figure 2.2.9**).[19]

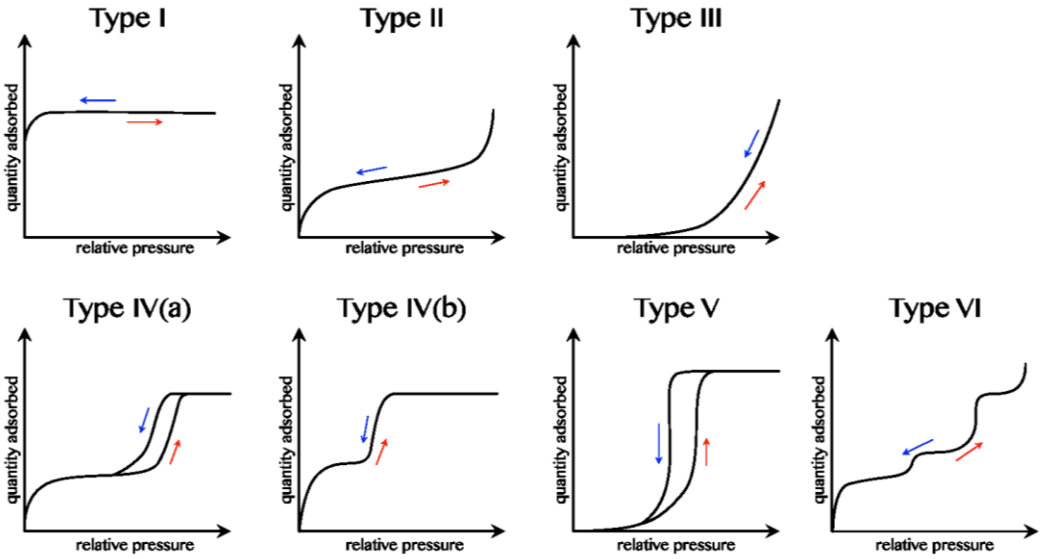

Figure 2.2.9: The structure of the gas physisorption isotherms classified by IUPAC.[19]

- A **Type I isotherm** is produced by reversible physisorption of gas on a microporous solid of small external surface area.
- A **Type II isotherm** is observed with reversible physisorption on a non-porous or macroporous material, where monolayer-multilayer adsorption is unrestricted to high relative pressures.
- The concave **Type III isotherm** occurs with physisorption on a non-porous or macroporous material when adsorbent-adsorbate interactions are weak. Adsorbed molecules amass at the most energetically favourable sites, without the formation of a monolayer.
- The **Type IV isotherm** is characteristic of a mesoporous adsorbent. Initial monolayer-multilayer adsorption follows a Type II isotherm but plateaus at high relative pressures due to capillary condensation. With different adsorption and desorption pathways, Type IV(a) isotherms exhibit a hysteresis loop. A reversible Type IV(b) isotherm may be observed with narrow mesopores, or conical mesopores that are closed at the tapered end.
- A **Type V isotherm** is observed for microporous and mesoporous materials with weak adsorbate-adsorbent interactions. Initially following a convex Type III isotherm, the Type V isotherm plateaus at high relative pressures, as molecular aggregation leads to pore filling. Due to different adsorption and desorption pathways, Type V isotherms exhibit hysteresis.

- The **Type VI isotherm** is a step isotherm produced by layer-by-layer adsorption on a regular, non-porous surface. The height of each step corresponds to the adsorption capacity of that layer.

2.2.2.4 Hysteresis in gas adsorption-desorption isotherms

Permanent hystereses loops are an artefact of capillary condensation, and indicate that gas adsorption and desorption proceed by different routes. In the case of an open pore, hysteresis arises when condensation is delayed by the metastability of the adsorbed multilayer. In contrast, desorption occurs with evaporation of the liquid-like condensate *via* a reversible liquid-to-vapour transition.[19] In systems with complex pore architectures, network effects and pore blockage are reflected in the shape of the hysteresis. Six types of hysteresis loop have been defined by IUPAC (**Figure 2.2.10**),[19] and each is attributed to a particular pore feature and sorption mechanism.

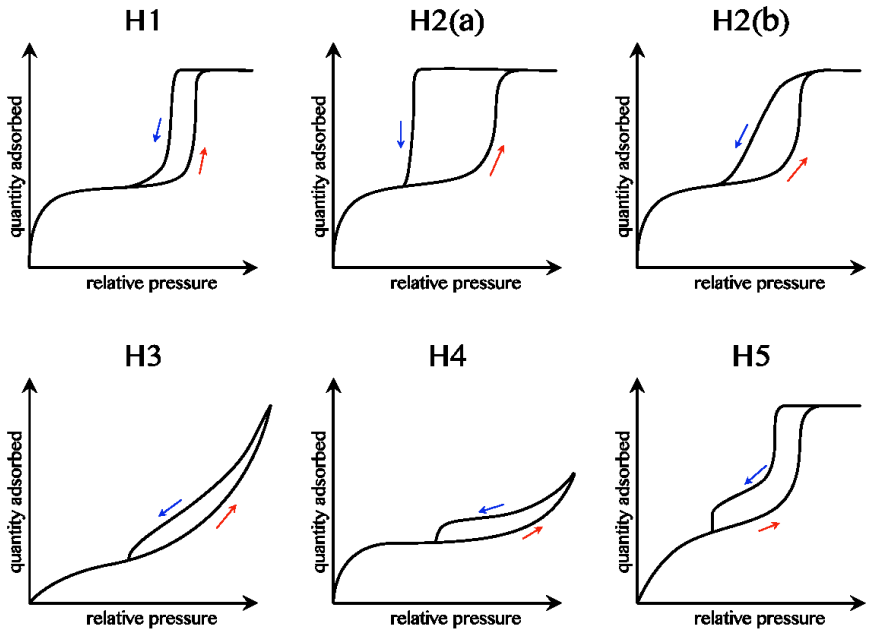

Figure 2.2.10: The structure of the hysteresis loops found in physisorption isotherms, as classified by IUPAC.[19]

- **Type H1** is observed for uniform mesopores with a narrow pore size distribution.
- **Type H2** is found in materials where network effects are significant. H2(a) has a steep desorption branch due to pore blockage, percolation by inkbottle pores, or cavitation-induced evaporation. H2(b) is indicative of a wide distribution of pore-neck diameters.
- **Type H3** is characterised by an adsorption branch that follows a Type II isotherm, and a desorption branch with a lower limit at the relative pressure of cavitation-induced evaporation. H3 is attributed to slit-shaped pores formed by aggregates of plate-like particles.

- **Type H4** hysteresis has an adsorption branch that is a combination of Type I and Type II isotherms, with a sharp uptake at low relative pressures due to micropore filling. This type of hysteresis is often observed for zeolite aggregates, mesoporous zeolites, and hierarchical materials, and is associated with slit-shaped pores with a narrow PSD.
- **Type H5** occurs if a material contains both open and partially blocked mesopores.

2.2.2.5 Interpreting physisorption data: empirical methods

2.2.2.5.1 Quantitative surface area estimates: BET theory

One of the main motives for undertaking a gas adsorption experiment is to determine the surface area of a porous sample. The Brunauer-Emmet-Teller (BET)[21] method is often used to evaluate the area of systems where multilayer adsorption applies.[14] BET is an extension of the Langmuir theory of monolayer adsorption[22] but unlike the Langmuir isotherm (which considers only the surface-adsorbate interactions) BET theory accounts for adsorbate-adsorbate interactions.[23] In BET theory, a homogeneous surface comprises discrete, single adsorption sites. Following gas adsorption, two phases can be defined: a primary phase comprising the first monolayer interacting with the surface, and a second, condensed phase that encompasses the subsequent adsorption layers.[23] There are no lateral interactions between adsorbate, but each molecule provides a single adsorption site for a molecule in the layer above. BET theory relies on a number of assumptions:

- the Langmuir isotherm applies to each layer;
- only exposed surfaces participate in sorption processes;
- at equilibrium, the distribution of adsorbate and the surface area it covers is constant;
- layers build up indefinitely. At the saturation pressure, the number of adsorbate layers tends to infinity;
- desorption is kinetically-limited and requires an input of energy equal to the adsorption energy, which is constant for a given layer;
- E_1 is the heat of adsorption for the first monolayer interacting with the surface;
- subsequent layers are represented as a condensed phase, with adsorption enthalpy, E_v, equal to the heat of liquefaction.

The BET equation is given by **Equation 2.2.1**, where p is the equilibrium pressure, p^θ is the saturation pressure at the adsorption temperature, n^σ is the total quantity of adsorbed gas, n^σ_m is the monolayer capacity, and C is the BET constant.

Equation 2.2.1: $$\frac{n^{\sigma}}{n_m^{\sigma}} = \frac{C\,p}{(p^{\Theta}-p)\left[1+(C-1)\left(\frac{p}{p^{\Theta}}\right)\right]}$$

The BET constant, which reflects adsorbate-adsorbent affinity, is defined by **Equation 2.2.2**, where E_1 is the adsorption energy for the first monolayer layer, and E_v is the heat of liquefaction (i.e. the adsorption energy of molecules comprising the condensed layers).

Equation 2.2.2: $$C = e^{\left(\frac{E_1-E_v}{RT}\right)}$$

The BET equation can be rearranged to give **Equation 2.2.3**, such that plotting $\frac{p}{n^{\sigma}(p^{\Theta}-p)}$ against relative pressure $\left(\frac{p}{p^{\Theta}}\right)$ gives a straight line from which C and n_m^{σ} can be extracted. However, the linear relationship expressed in **Equation 2.2.3** only strictly applies between $0.05 < \left(\frac{p}{p^{\Theta}}\right) < 0.3$, as it diverges from linearity at higher relative pressures.[15]

Equation 2.2.3: $$\frac{p}{n^{\sigma}(p^{o}-p)} = \frac{1}{C\,n_m^{\sigma}} + \frac{C-1}{C\,n_m^{\sigma}}\left(\frac{p}{p^{\Theta}}\right)$$

The total surface area (S) is calculated from the monolayer capacity using **Equation 2.2.4**, where N_A is Avogadro's number, A_x is the cross-sectional area of the adsorbate (N_2 at 77 K = 0.162 nm^2, Ar at 87 K = 0.142 nm^2),[19] and M is the adsorbate molecular weight.

Equation 2.2.4: $$S = \frac{n_m^{\sigma} N_A A_x}{M}$$

In reality, the BET equation is unsuited to the analysis of microporous systems and can be a poor description of multilayer adsorption (due to the large number of assumptions on which the method is based). Nonetheless, BET is widely used for the textural characterisation of micro-, meso- and macro-porous materials, allowing surface areas to be compared across a wide range of materials.

2.2.2.5.2 Mesopore-size analysis: BJH theory

Most procedures for assessing mesopore size, including the Barrett, Joyner and Halenda (BJH) method,[133] rely on the application of the modified Kelvin equation (**Equation 2.2.5**). The Kelvin equation relates the relative pressure ($\frac{P}{P_o}$) to the Kelvin radius (r_k), which is the critical radius of a cylindrical pore into which capillary condensation will occur with formation of a meniscus. In **Equation 2.2.5**, γ is the surface tension of the bulk fluid, V_m the molar liquid volume, R is the molar gas constant, and T is the temperature in Kelvin.

Equation 2.2.5: $$\ln\left(\frac{P}{P_o}\right) = \frac{-2\gamma V_m}{RT\, r_k}$$

The Kelvin equation, and hence the BJH method, assumes that the radius of a cylindrical pore (r_p) is described by the sum of the Kelvin radius (r_k) and the thickness of the adsorbed multilayer formed prior to condensation (t_c), such that **Equation 2.2.6** applies.

Equation 2.2.6: $$r_p = r_k + t_c$$

XRD and high-resolution transmission electron microscopy of highly ordered mesoporous materials have revealed that the BJH method significantly underestimates pore diameters. The method is particularly poor for the assessment of narrow mesopores, as enhanced pore curvature and surface forces impact the validity of the Kelvin equation.[131] Nonetheless, the BJH method is still widely used in quantitative pore size analyses, as it is relatively straightforward and accessible, and is applicable to almost all types of porous materials.

2.2.3 Thermal analyses

Thermal analysis refers to analytical methods that monitor and quantify heat-activated processes during a controlled temperature programme.[24] For solid samples, thermal analyses are used to study transformations such as decomposition, evaporation, and phase changes.[9]

2.2.3.1 Thermogravimetric analysis

Thermogravimetric analysis (TGA) is used to monitor the loss (or gain) of sample mass with temperature (**Figure 2.2.11**). TGA can be used to monitor the temperature-dependence of physical and chemical processes, such as decomposition, oxidation and desorption. Although TGA does not reveal the nature of thermal processes, it can be coupled to other characterisation (such as gas chromatography or mass spectrometry) in order to rationalise thermal events.[14]

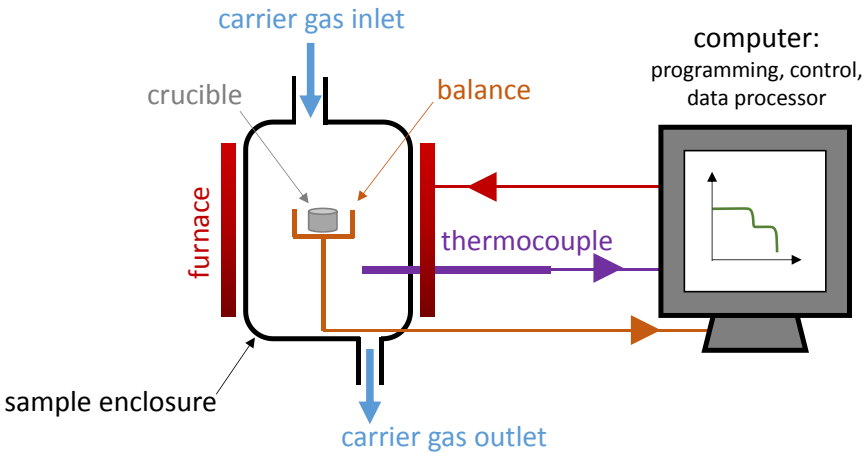

Figure 2.2.11: A schematic of the apparatus used for thermogravimetric analysis. A high-precision balance is used to monitor the change in mass of a sample (contained within a crucible), as it is heated in a furnace, under a flow of gas. The temperature of the sample is controlled *via* a feedback loop, in which the thermocouple reports the temperature of the sample to the computer, which uses this information to modify the temperature of the furnace. The computer records the change in sample mass as a function of temperature.[24]

2.2.3.2 Temperature-programmed desorption

Temperature-programmed desorption (TPD) is often used to characterise the surface properties of an adsorbent, by monitoring the desorption of a probe gas under a controlled temperature ramp.[25] In catalyst characterisation, thermal desorption of a basic molecule, such as ammonia, can be used to quantify the type and strength of accessible acid sites.

In a typical TPD experiment (**Figure 2.2.12**),[26] the sample is pre-treated to remove any adsorbed species. Then the sample is exposed to the adsorbate, followed by evacuation remove all but the chemisorbed species. The sample is then gradually heated in the flow of an inert carrier gas (e.g. helium), to remove the chemisorbed species. As temperature rises, the rate of desorption increases, passes through a maximum, and then declines as the adsorbate is depleted. By monitoring effluent stream of carrier gas, it is possible to construct a TPD spectrum, i.e. a plot of the concentration of desorbed gas *versus* temperature.

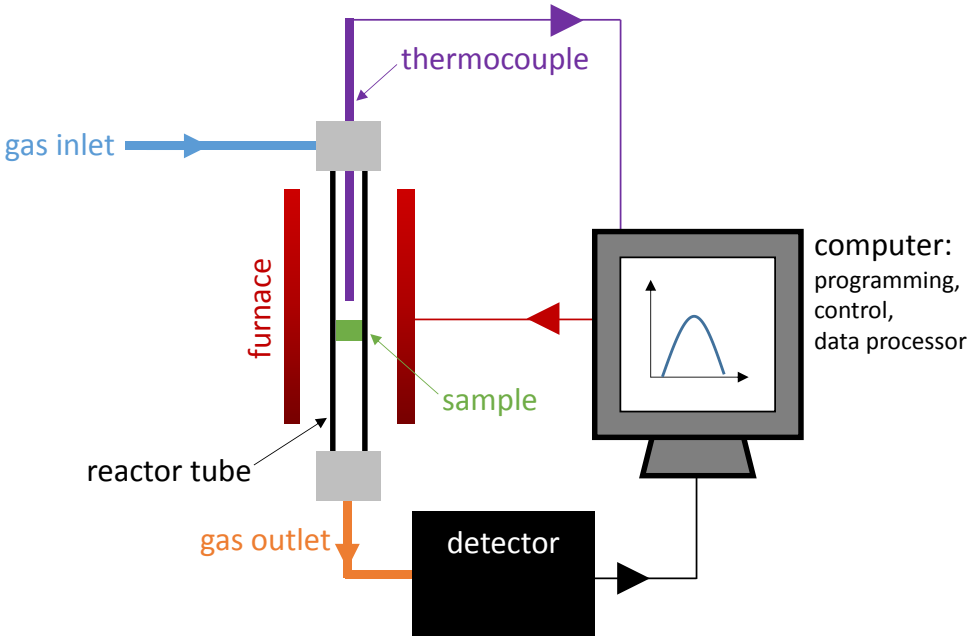

Figure 2.2.12: A schematic of the TPD setup. A sample in a reactor tube is exposed to a flow of probe gas in an inert carrier gas. The sample is heated and the outlet stream monitored by a detector, which is typically a mass spectrometer or TCD. The temperature of the sample is controlled *via* a feedback loop, in which the thermocouple reports the temperature of the sample to the computer, which uses this information to modify the temperature of the furnace. The computer records the detector output as a function of temperature.[26]

The TPD spectrum often appears as a series of peaks, each of which corresponds to a particular desorption process.[27] Generally, peak temperature can be used to assess the strength of surface-adsorbate bonding, with a higher desorption temperature corresponding to a higher activation energy for desorption.[25] If several peaks are observed, different desorption mechanisms, or multiple surface sites can be inferred. In the case of a basic probe (e.g. ammonia) the desorption temperature can be used to assess the acid-strength distribution of a sample surface.[26] Moreover, the area under the TPD curve is proportional to the volume of desorbed species, and hence peak integration yields the relative number of species desorbed in a particular process. For a basic probe, the total area under the TPD curve can be used to quantify the total number of accessible acid sites of a particular strength.[26]

2.2.4 Elemental analysis

Elemental analysis provides fundamental information about the elemental composition of a sample, including trace analyses and isotopic abundances. The procedure will depend on the nature of the sample and required information but, in general, involves sample decomposition, followed by an analysis of its constituents.

2.2.4.1 Organic elemental analysis

Organic elemental analysis (OEA) typically refers to the analysis of the elements carbon, hydrogen and nitrogen (CHN), and sometimes sulphur (CHNS).[28] The typical OEA experiment is described in **Figure 2.2.13**.[29]

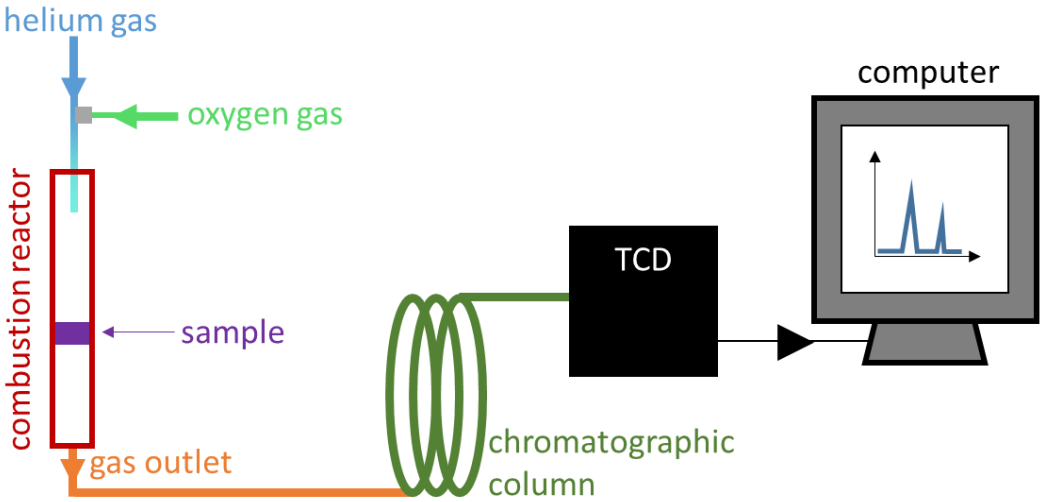

Figure 2.2.13: A schematic of organic elemental analysis. A sample is transferred to a high-temperature combustion reactor and the flow of He carrier gas temporarily enriched with oxygen. Any organic material in the sample is instantaneously and quantitatively oxidised by flash combustion, and the products are transported to the chromatographic column to be separated. As each product is transferred to the thermal conductivity detector (TCD) a signal is generated with an intensity proportional to the concentration of the combustion product.[29]

2.2.4.2 Inductively-coupled plasma optical emission spectroscopy

Inductively coupled plasma optical emission spectroscopy (ICP-OES) is often used for elemental analysis of inorganic samples (**Figure 2.2.14**). In ICP-OES, atomisation is effected by a plasma, as this provides a higher temperature and more inert chemical environment than a combustion flame.[30, 31]

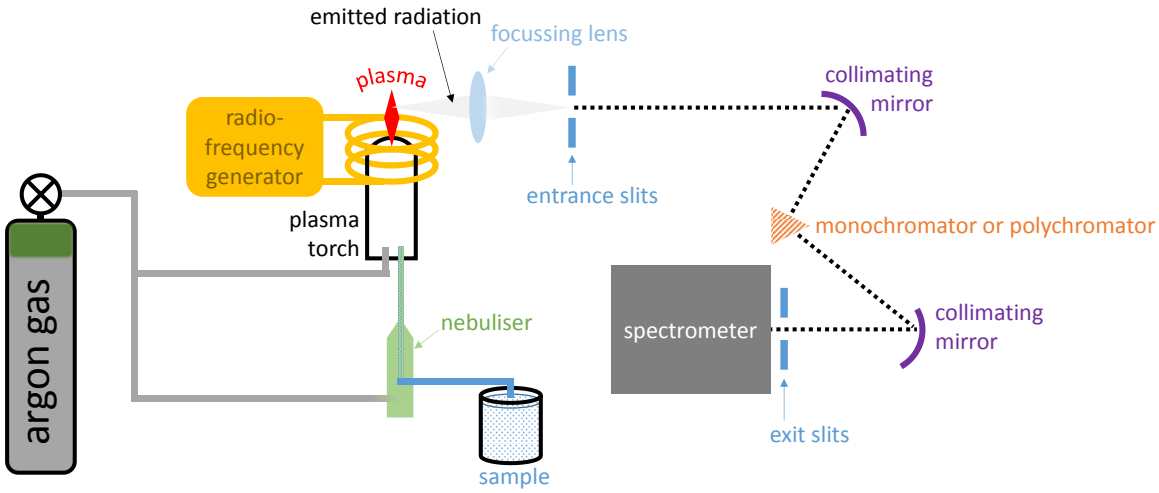

Figure 2.2.14: A sample nebulised into an argon plasma is atomised and ionised. Excitation of these atoms and ions leads to characteristic photon emission. After passing through a wavelength selector (i.e. a monochromator or polychromator) the characteristic radiation is collected and processed by a spectrometer.[32, 33]

2.2.5 Electron microscopy

Electron microscopy (EM) exploits electron-matter interactions to generate an image of a sample at a resolution on the order of nanometers.[34, 35] As well as visualising structure, morphology, and particle size, EM can be used to study element distributions.[9]

In EM, a sample is impacted by high-velocity electrons that have been accelerated though a potential difference (V). If the electrons are considered wave-like entities, they can be described by a de Broglie wavelength (λ), as in **Equation 2.2.7** (where p is momentum and h is the Planck constant). The electron wavelength is related to the accelerating voltage by **Equation 2.2.8**, where m, v, and e are the mass, velocity, and charge of the electron, respectively.

Equation 2.2.7: $$\lambda = \frac{h}{p}$$

Equation 2.2.8: $$\lambda = \frac{h}{\sqrt{2meV}}$$

2.2.5.1 Generating an electron beam

There are several methods to generate an electron beam for use in EM.[9, 34, 35] In a thermionic emission gun, electrons are produced by passing a current through a filament cathode, heating sufficiently that thermal energy overcomes the work function of the material. Tungsten filaments were once widely used as the cathode material, but modern microscopes achieve higher resolutions with lanthanum hexaboride (LaB_6), which has a lower work function. For very high resolution EM, a field emission gun is the preferred source of electrons.[34] In this case, a metal tip is exposed to a very high electric field to increase the probability of an electron leaving the surface by quantum mechanical tunnelling. As well producing electrons at over a thousand times the brightness of a thermionic emission gun,[35] the electrons from a field emission gun have a narrower energy distribution (<0.5 eV) than a those from a thermionic source (1 – 2 eV).

On ejection from the cathode, the electrons are accelerated towards an anode by applying a large potential difference (V). Since the resolution of the microscope is determined by the electron wavelength (λ), the negative potential applied at the cathode can be varied to alter the resolution of the microscope. The electrons are focussed through a series of electromagnetic lenses to a fine spot on the sample stage. To minimises scattering by extraneous particles, the electron microscope is maintained under high vacuum.[9]

2.2.5.2 Electron-matter interactions

A range of information can be obtained by studying the phenomena that occur when a beam of high-energy electrons interact with a sample. The incident, or primary electrons, will enter the sample, and the same, or new electrons may be ejected:[34]

- Elastic scattering describes an interaction where there is an essentially undetectable change in the energy of the primary electron. The electron may change direction, most likely at a small scattering angle. The mean free path for elastic scattering is reduced as the atomic number of the scattering atom increases.
- Inelastic scattering refers to any process where there is a detectable change in the energy of the primary electron. Most of the kinetic energy of the impinging electrons is transformed into the thermal energy of the sample, but some may be converted into photons or secondary electrons, which can be used for imaging and analysis.

2.2.5.3 Scanning electron microscopy

Scanning electron microscopy (SEM) is used to visualise the (near-) surface structure of a bulk specimen (e.g. the particle size and morphology). SEM generates images at a resolution of 0.5 to 20 nm, and may be equipped to analyse the elemental composition of the sample surface.[9]

In SEM, a primary beam of energetic electrons (1 – 30 keV)[34] is rastered across the surface of a sample. As electrons are strongly scattered by matter, the incident beam will only penetrate a small volume at the surface of a sample.[34] Within the interaction volume, the energy of the primary electrons is dissipated into various secondary radiations (**Figure 2.2.15**).

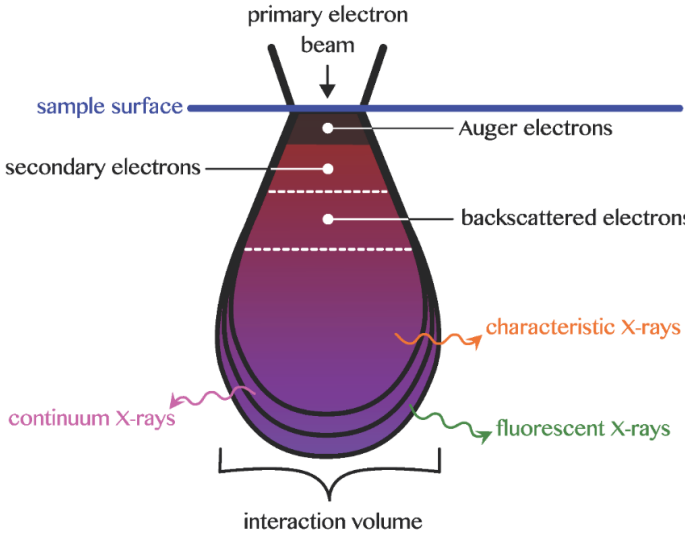

Figure 2.2.15: When a primary beam of high-energy electrons impacts a sample, the electrons are scattered and a mixture of secondary radiation (including electrons and X-rays) is produced. In SEM, the emissions that escape to a detector will originate from a small interaction volume near the surface of the sample.[35]

Topographic images are predominantly constructed from the secondary electrons (SEs), which are produced when an electron of the primary beam ionises a core-electron in the sample.[35] SEs that escape to the surface are accelerated towards a detector, and displayed as an image of brightness proportional to the number of detected electrons. Although SEs are produced throughout the interaction volume, only those emitted near the surface (at a depth of 5 -50 nm)[35] have sufficient energy to escape and be detected.

In stimulating SE emissions, the impact of a primary beam also generates characteristic X-rays (see, for example, **Figure 2.2.3**), which can be used to develop an elemental map of a sample.[34, 35] Compositional information can also be obtained from the backscattered electrons.[36] As backscattering is most efficient from heavier elements, regions near the sample surface that comprise atoms of high atomic number appear brighter in the SEM image.[36]

2.2.5.4 Transmission electron microscopy

Transmission electron microscopy (TEM) is used to visualise the micro-structure of a sample in ultrafine detail.[37] The high-resolution (< 1 Å)[9] images from TEM are produced using high accelerating voltages (40 - 200 kV)[34] that reduce the de Broglie wavelength of the primary electron beam to < 6 pm.[35] The high-energy electron beam is condensed and focussed on to a sample, causing the electrons to be scattered. Provided the TEM specimen is sufficiently thin (< 200 nm),[35] a significant proportion of the primary electrons can be transmitted to a detector beneath the sample stage.[38]

In TEM, the transmitted electrons are used to develop a two-dimensional projection of a sample. The specimen is visualised as variations in the brightness (i.e. detected electron intensity) of adjacent image points, which arise when elastic and inelastic scattering events deflect the transmitted electrons away from the primary beam. There are two contrast mechanisms by which electron scattering can give rise to a TEM image:[9, 34, 35]

- **Mass-density contrast** exploits the enhanced scattering of electrons in thick or dense regions of a sample. When a sample is placed in the primary electron beam, scattering events cause the electrons to be deflected over a range of different angles and energies. Regions of higher mass-density that scatter electrons more effectively, appear as dark features on the light background produced by the undeflected beam.
- **Diffraction contrast** may be observed when TEM is used to image a crystalline sample. Diffraction contrast arises when an atomic lattice plane diffracts the primary electron beam, increasing scattering intensity for a particular sample orientation. By tilting the specimen, different Bragg reflections can be brought into diffraction.

Since the detected electrons have penetrated through a specimen, TEM provides information on the bulk properties of a sample, including morphology, topography, and crystalline structure.[9] In addition, TEM may be coupled with energy-dispersive X-ray spectroscopy, which analyses characteristic X-ray emissions from the sample to develop an elemental map.

2.2.6 Infrared spectroscopy

Infrared (IR) spectroscopy is the study of changes in the vibrational state of a molecule on interaction with electromagnetic radiation of wavelength 10^{-3} - 10^{-7} m.[35, 39] By monitoring the absorption of IR radiation, it is possible to determine bond lengths and force constants, to identify characteristic absorptions, and thus elucidate aspects of molecular structure.[40]

2.2.6.1 Theoretical aspects of molecular vibration and IR spectroscopy

At temperatures above absolute zero, two atoms bonded through the overlap of their atomic orbitals will oscillate at an equilibrium separation (r_e) determined by their mutual interaction. Using classical mechanics, the diatomic bonding arrangement is modelled as two masses (m_1 and m_2) connected by a massless spring of strength, k (which describes the force constant of the bond). In this case, the diatomic is a harmonic oscillator that obeys Hooke's Law (**Equation 2.2.9**), and an elastic deformation will generate a restoring force, F, proportional to the linear displacement of the nuclei from their equilibrium position (r - r_e). For a harmonic oscillator, the frequency of molecular vibration, ω, is described by **Equation 2.2.10**, where μ is the reduced mass of the two atoms.

Equation 2.2.9: $$F = -k\,(r - r_e)$$

Equation 2.2.10: $$\omega = \frac{1}{2\pi}\sqrt{\frac{k}{\mu}} \qquad \text{where} \qquad \mu = \frac{m_1 m_2}{m_1 + m_2}$$

When a diatomic molecule is modelled as a classical harmonic oscillator, the potential energy (E) of the vibration is a symmetric parabolic potential well (**Figure 2.2.16**). As indicated by **Equation 2.2.11**, the potential energy of the harmonic oscillator system is minimised when the nuclei are at their equilibrium internuclear separation ($r = r_e$).[39]

Equation 2.2.11: $$E = \frac{1}{2}\,k\,(r - r_e)$$

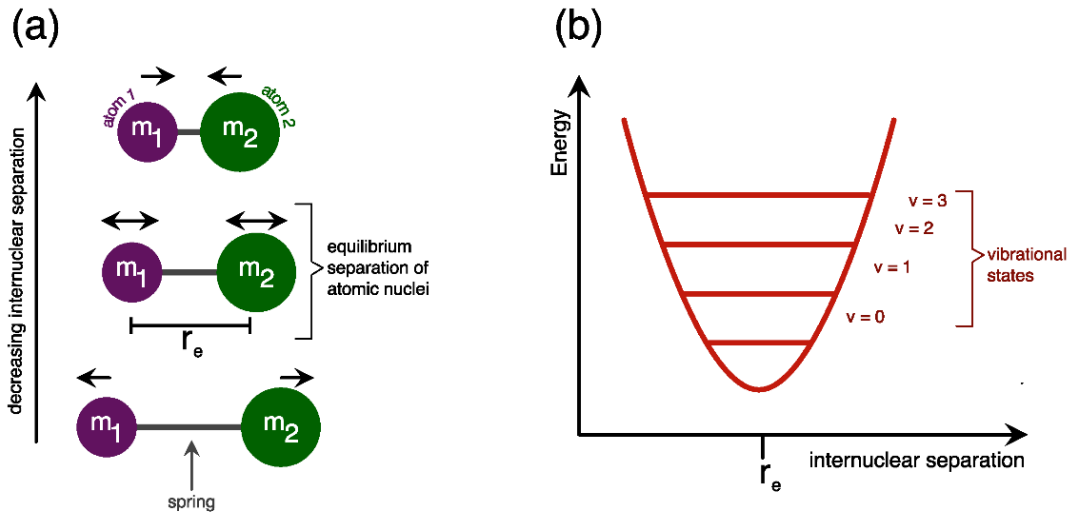

Figure 2.2.16: (a) A vibrating diatomic molecule modelled as a harmonic oscillator comprises two masses (m_1 and m_2) connected by a spring. **(b)** The potential energy of a harmonic oscillation is a parabolic well, which is divided into non-degenerate vibrational energy levels (ν) by quantum theory.

The classical harmonic oscillator model of a diatomic can be developed with a quantum mechanical approach, which gives a more realistic description of molecular vibration. Firstly, quantum mechanics accounts for the quantisation of energy levels (i.e. the molecular 'spring' can only be stretched in discrete steps).[40] For a harmonic oscillator, the non-degenerate vibrational states (ν) are equidistant, and their energy (E_ν) is described by **Equation 2.2.12**, where ω is the fundamental frequency. Since only $\Delta\nu = \pm 1$ transitions are allowed, the transition energy between adjacent vibrational states is $h\omega$. **Equation 2.2.12** also predicts that even in the lowest vibrational state ($\nu = 0$) the oscillator possesses an irremovable, zero-point energy, in accordance with the uncertainty principle.[39]

Equation 2.2.12: $$E_\nu = h\omega\,(\nu + \tfrac{1}{2}) \qquad \nu = 0, 1, 2, 3, \ldots$$

As illustrated by **Figure 2.2.17**, at small atomic displacements the harmonic model is a reasonable approximation of molecular vibration. However, a more realistic model of an oscillating diatomic is obtained by introducing anharmonicity, so that the restoring force is no longer proportional to the atomic displacement. By modelling the diatomic as an anharmonic oscillator, it is possible to account for the observation that a bond cannot be infinitely compressed (due to atom-atom repulsion) or stretched (due to bond dissociation). Thus, the relationship between potential energy and internuclear separation is better represented by a Morse potential well.[40] For an anharmonic oscillator, the energy separation between vibrational states decreases at higher ν, until the molecule dissociates.[39] Another

consequence of an anharmonic model is that, in addition to the fundamental bands ($\Delta v = \pm 1$), overtones ($\Delta v > \pm 2$) and combination bands may occur.

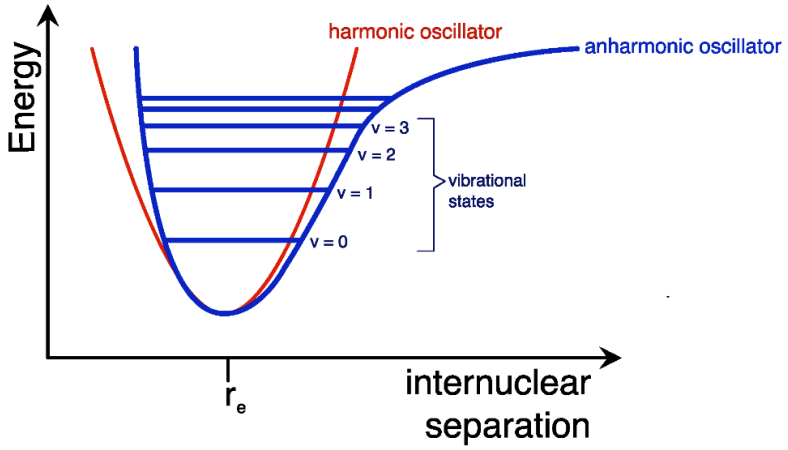

Figure 2.2.17: Near the equilibrium internuclear separation, a harmonic oscillator is a reasonable approximation of a vibrating diatomic. However, due to interatomic repulsions at small internuclear separation, and bond dissociation at large internuclear separation, an anharmonic oscillator is a more realistic description of molecular vibration. For the anharmonic oscillator, the energy separation of the vibrational states decreases with increasing vibrational quantum number (v).[39]

In the case of a polyatomic system, the complex vibrational motion of a molecule can be deconvoluted into a number of uncoupled oscillations, known as normal modes.[41] A normal vibration is characterised by the collective motion of nuclei about their equilibrium position, where they move in-phase and at the same frequency, without rigid-body movement or rotation.[35] These conditions can be satisfied by a stretching or bending vibration, depending on whether there is a change in the bond length or bond angle, respectively (**Figure 2.2.18**).

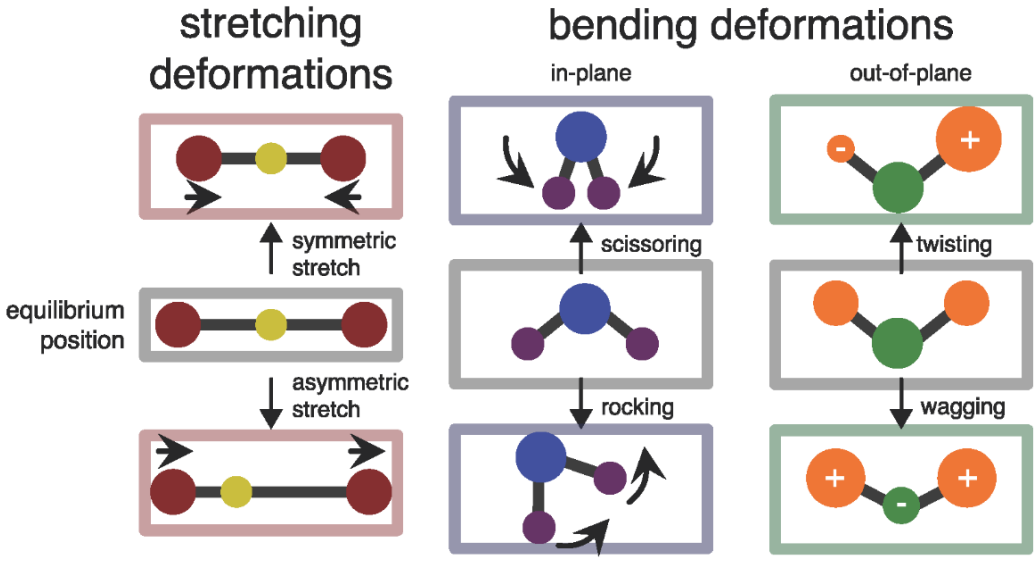

Figure 2.2.18: An illustration of the normal modes of some triatomic molecules, which include stretching and bending deformations.

If a molecule is exposed to IR radiation at the same frequency as a normal mode, the resonance condition is met but the mode may not be detected spectroscopically. For an IR photon to be absorbed, the normal vibration must also be associated with a change in the dipole moment of the molecule (the gross selection rule for IR spectroscopy).[39] If these conditions are satisfied, the vibrational mode is infrared active and photon absorption excites the molecule to a higher vibrational state. Vibrational transitions will typically obey the specific selection rule for IR spectroscopy ($\Delta v = \pm 1$) and spectra are often dominated by fundamental transitions from $v = 0$ to $v = 1$.[35]

2.2.6.2 The infrared experiment

In a typical IR experiment, the vibrational spectrum of a sample is obtained by monitoring the absorption, transmission, or reflectance of IR radiation as a function of the incident frequency. Formerly, IR spectroscopy was performed using dispersive instruments, which collect signal as a scanning monochromator sequentially irradiates a sample with a narrow frequency of IR radiation. These systems have since been superseded by Fourier transform infrared (FTIR) spectrometers that can measure a range of IR wavelengths simultaneously for rapid data collection with improved resolution (**Figure 2.2.19**).[35, 39]

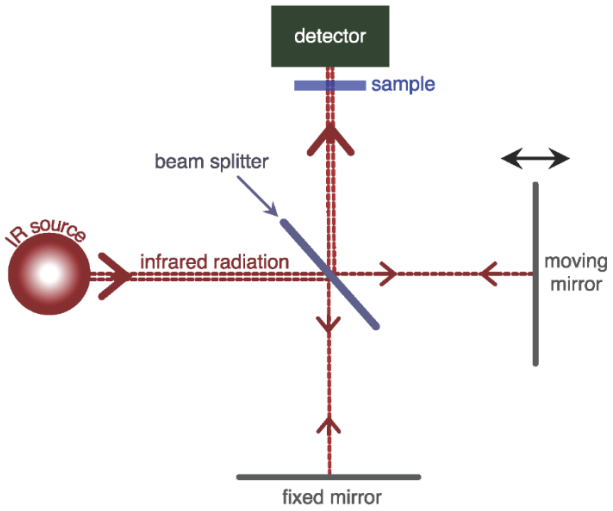

Figure 2.2.19: At the core of the FTIR spectrometer is the Michelson interferometer.[42] A beam of IR radiation is incident on a beam splitter that transmits part of the beam towards a movable mirror, and reflects the remainder towards a fixed mirror. The two beams are reflected back towards the beam splitter where they recombine and interfere.[35] The recombined beam is transmitted (or reflected) by a sample and then detected. The sinusoidal interferogram produced by moving the mobile mirror at a constant velocity can be converted into a single peak, at a characteristic frequency, by Fourier transform (FT). If a polychromatic IR source is used, the interferogram is a summation of the sinusoidal functions of all wavelengths, and the FT yields the IR spectrum for the entire range of incident wavelengths.[39]

2.2.6.3 Interpretation of IR spectra

One of the simplest methods to obtain structural information from an IR spectrum is by matching an IR spectrum (i.e. peak position and intensity) with a reference material.[35] For fingerprint analyses, the region below 1000 cm^{-1} is particularly useful, as low-frequency vibrations are sensitive to subtle chemical variations. Qualitative structural analysis are also achieved using characteristic group frequencies in the 4000 – 1000 cm^{-1} range, by correlating a spectral band that of a molecular fragment known to vibrate in that region.[43]

It is also possible to perform a quantitative analysis of an IR spectrum from the intensity of vibrational bands.[35] Using the Beer-Lambert Law (**Equation 2.2.13**) the absorbance (A) of a species can be related to its concentration (c), if the path length (l) and its absorptivity (a) at that wavenumber are known. To determine a, a calibration may be performed by measuring the absorbance of several samples of known concentration, at a fixed path length.

Equation 2.2.13: $$A = a\,c\,l$$

2.2.6.4 Using infrared to characterise crystalline solids: zeolites and zeotypes

For the analysis of zeolite structure and composition, mid-to-far IR (1400 – 300 cm^{-1}) radiation can be used to excite the vibrations of the T-O bonds of the primary building units.[44] The zeolite framework vibrations are usually divided into the *internal* modes of the TO_4 tetrahedra (which are largely insensitive to the structure of the zeolite) and the *external* linkage modes that are sensitive to the framework topology (**Table 2.2.2**).[45]

In addition, IR spectroscopy is often used to analyse the stretching (ν(OH) = 3800-3500 cm^{-1}) and bending (δ(OH)in-plane = 2000-1200 cm^{-1}, γ(OH)out-of-plane < 1500 cm^{-1}) vibrations of the O-H groups that terminate the surfaces of zeolites.[46, 47] Hydroxyl vibrations not only provide information about zeolite structure and defects, but also the acidity of the framework.[46] Using IR spectroscopy, a variety of acidic hydroxyl sites can be identified in zeolites (**Table 2.2.2**) and their relative acidities are gauged from the relationship between bond strength and stretching frequency.[48] However, ν(OH) does not provide an absolute measure of acidity.[44] Therefore, IR characterisation may be coupled with the adsorption of a basic molecule that interacts discriminately with OH sites based on their acid strength.[46] Acid-base interactions at a hydroxyl group can be detected spectroscopically as broadening of O-H bands, and a red-shift of ν(OH) as the O-H bond is weakened by hydrogen bonding interactions.[49]

Table 2.2.2: Assignment of the regions of the infrared spectrum corresponding to internal and external T-O vibrations,[45] and O-H vibrations[44, 46, 48] of a zeolite framework.

Internal T-O modes	Wavenumbers / cm^{-1}	External T-O modes	Wavenumbers / cm^{-1}	ν(O-H)	Wavenumbers / cm^{-1}
asymmetric stretching	1250 - 950	asymmetric stretching	1150 - 1050	Isolated silanol	3745 - 3740
symmetric stretching	720 - 650	symmetric stretching	820 - 750	Hydroxyl nest	~ 3720
bending	500 - 420	double-ring vibrations	650 - 500	Brønsted (Al(OH)Si)	3650 -3600
		pore-opening vibrations	300 - 420		

2.2.6.5 FTIR with adsorbed probe molecules

In materials characterisation, FTIR may be coupled with the adsorption of a probe molecule in order to study the textural and chemical properties of a surface.[44, 47, 49] On interacting with a surface site, a detectable change in the vibrational spectrum of an adsorbed molecule can provide indirect information about the local environment. A range of probe molecules have been used in conjunction with FTIR spectroscopy, exploiting differences in structure and interactions in order to discriminate adsorption sites based on their location and/or chemistry. To be suitable for analysis by IR spectroscopy, a probe molecule (or its adsorption complex) should have at least one distinctive vibrational band that undergoes a spectroscopically detectable change in intensity, position, or structure, depending on the environment of the adsorption site.[47, 50-52] In addition, the probe will often cause measurable perturbation of vibrational bands associated with the adsorption site.

Probe-based IR spectroscopy is widely used for the characterisation of solid-acid catalysts, providing information about the identity, quantity, and strength of surface acid sites. In this case, the probe is a basic species that will interact with an acid site to form a characteristic adduct (at a Lewis acid centre) or protonated species (at a Brønsted acid site), detectable by IR spectroscopy.[53] Depending on the properties of the probe molecule (e.g. basicity, kinetic diameter), a targeted study of acid sites is possible (**Table 2.2.3**). It is common practice to perform probe-FTIR studies with a range of molecules, for a more comprehensive evaluation of acid characteristics.[51, 54] Moreover, by monitoring the IR spectrum of a probe-adsorbent system over a range of temperatures, the sorptive properties of the probe can be used to analyse surface chemistry. If the probe species is a substrate molecule, *in situ* and *operando* spectroscopy may provide insight into the nature of substrate-active site interactions and catalytic reaction mechanism.[49]

Table 2.2.3: Some chemical and vibrational characteristics of basic probe molecules used for FTIR analysis of acidic surfaces.

Probe molecule	σ [a] / Å	Proton affinity (298 K) / kJ mol^{-1}	Nature of basicity	Diagnostic vibration(s) of probe					
				Identity	Approximate wavenumber / cm^{-1}				Ref
					Free species	Protonated at Brønsted site	Hydrogen bonded to Brønsted site	Adduct at Lewis site	
carbon monoxide	3.76 [55]	426 [56]	Very weak. Soft.[48, 57]	ν(CO)	2138	2155-2180	2150	2190-2240	[46, 50, 58-60]
aceto-nitrile-d_3	4.9 [61]	779 [56]	Weak. Soft.[62]	ν(CN)	2263	2285-2320	2275-2300	2320-2330	[46, 62-64]
ammonia	2.65 [65]	854 [56]	Strong. Hard.[57, 48]	ν_{asym}(NH) ν_{sym}(NH) δ_{asym}(NH) δ_{sym}(NH)	3444 3336 1628 950	3145 - - 1400	3408 3309 1625 1036	3320-3400 3070-3315 1565-1600 1000-1440	[46, 48, 66-69]
pyridine	5.8 [65]	930 [56, 70]	Strong. Moderate hardness.[57]	ν_{8a}(CC) ν_{19b}(CN)	1584 1440	1630-1640 1500-1545	1580-1600 1440-1445	1600-1630 1445-1460	[46, 50, 58, 66, 71, 72]
2,6-dimethyl-pyridine	6.7 [73]	963 [56]		ν_{8a}(CC) ν_{19b}(CN)	1584 1410	1640-1655 1415	1600 1410	1595-1620 1410	[46, 74, 75]
2,4,6-trimethyl-pyridine	7.4 [73]	981 [70]		ν_{8a}(CC)	1611	1637	1619	1633	[58, 60, 76-78]
2,6-di-*tert*-butyl-pyridine	10.5 [79]	983 [56]		ν(NH) ν_{8a}(CC)	- 1580	3370 1615	- 1600-1610	- 1590-1600	[80-82]

[a] Kinetic diameter.

2.2.7 Solid-state nuclear magnetic resonance

Nuclear magnetic resonance (NMR) spectroscopy is a powerful technique for atomic-level characterisation of chemical systems. Since most elements have at least one spin-active nuclide,[83] NMR can be used to study a variety of materials, irrespective of long- or short-range order.[84] NMR also benefits from a sensitivity to subtle changes in the structure and composition of the local environment, including dynamic processes. Formerly, poor spectral resolution and complex analyses were prohibitive of solid-state NMR but with technological advancement, NMR is now well-equipped to study a diverse range of solid materials.[84]

2.2.7.1 The basis of the NMR technique

Atomic nuclei possess an intrinsic spin angular momentum, described by a nuclear spin quantum number, I. Under an external magnetic field (B_0), Zeeman splitting (**Figure 2.2.20**) causes the nuclear magnetic moment of an $I > 0$ nucleus to become quantised in $2I + 1$ orientations along the axis defined by B_0 (typically the z-axis).[83] Each orientation is a non-degenerate spin state, with a magnetic quantum number (m_I) from $-I$ to $+I$, in unit steps.

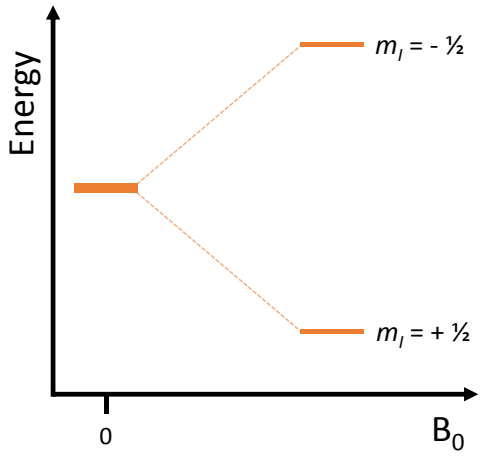

Figure 2.2.20: An energy diagram showing the Zeeman splitting of nuclear spin states when an I = ½ nucleus is exposed to an external magnetic field, B_0. Under the applied magnetic field, the degeneracy of the m_I = -1/2 and m_I = +1/2 states is removed, and their energy separation increases with the strength of the applied field.

The energy of a nuclear spin state (E_{m_I}) in a magnetic field, B_0, is described by **Equation 2.2.14**, where γ is the characteristic gyromagnetic ratio (i.e. the magnetic strength) of the nucleus.

Equation 2.2.14: $$E_{m_I} = -\gamma\, m_I\, \hbar\, B_0$$

Under an applied magnetic field, spin-active nuclei exist in thermal equilibrium, with a Boltzmann distribution of $I > 0$ nuclei across the non-degenerate spin states. At an equilibrium temperature, T, the relative population of a higher and lower energy spin-state (i.e. N_{upper}/N_{lower}) separated by energy, ΔE, is described by the Boltzmann equation (**Equation 2.2.15**), where k is the Boltzmann constant (1.38×10^{-23} J K^{-1}).

Equation 2.2.15: $$\frac{N_{upper}}{N_{lower}} = e^{\frac{-\Delta E}{kT}}$$

For a macroscopic sample at room temperature, thermal equilibrium corresponds to a near-equal distribution of spin-active nuclei across the available energy levels, with only a small net magnetisation in the direction of B_0.[84] At thermal equilibrium, spin-active nuclei will spontaneously, but infrequently, transition between non-degenerate spin states. However, it is possible to increase the transition frequency by supplying nuclei with energy equal to the separation of their spin states. When this condition is met, the nuclei are at resonance. In an NMR experiment, a sample in a magnetic field is irradiated with a radiofrequency pulse to excite transitions between the nuclear spins states. However, to be observed by NMR a nuclear transition must satisfy the $\Delta m_I = \pm 1$ selection rule; hence, the energy requirement for nuclear resonance is described by **Equation 2.2.16** (where h is the Planck constant).

Equation 2.2.16: $$\Delta E = -\frac{\gamma h B_0}{2\pi} = h\nu_0$$

At the Larmor frequency, ν_0, spin-active nuclei will absorb energy and their magnetic moment is displaced through an angle along the B_0-axis, determined by the duration of the radiofrequency pulse.[83] Due to the initial population imbalance, the 'spin flip' induced by a resonant-frequency pulse places the system in a net excited state, with more spins in a higher-energy level. When the radiofrequency pulse is terminated, the nuclear spins gradually relax back to thermal equilibrium by precessing about the B_0 axis (**Figure 2.2.21**).[83] As the net magnetisation of a system precesses, it induces a voltage in a surrounding coil of wire that can be amplified and recorded as a complex, time-dependent signal (a free induction decay). In order to obtain the NMR signal, the free induction decay is converted from the time domain to the frequency domain by performing a Fourier transform.[83, 84]

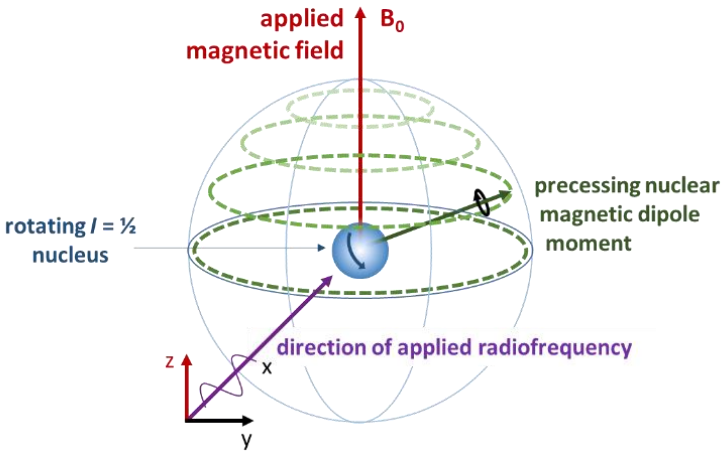

Figure 2.2.21: In an applied field (B_0), the nuclear magnetic moment of an I = ½ nucleus will precess at the Larmor frequency, parallel to the z-axis. If a radiofrequency pulse is applied at 90 ° to B_0 (i.e. along the x-axis), the precessional angle of the nuclear magnetic moment will gradually increase towards the xy-plane. When the radiofrequency pulse is terminated, the nucleus will gradually relax by precession into alignment with the z-axis and the dephasing of magnetisation in the xy-plane.[83]

2.2.7.2 Interactions in NMR spectroscopy

Besides the Zeeman interaction, a number of local interactions can modify the energy of a nuclear spin state (**Table 2.2.4**).[84]

Table 2.2.4: A summary of the interactions of a nuclear spin and their effect on an NMR spectrum.[83, 84]

Interaction	Description	Observation
Zeeman	The interaction of the nuclear magnetic moment with an external magnetic field.	Spectral peaks.
Shielding	Modifications of the magnetic field at a nucleus due to the magnetic field of a local electron current.	Peak shift.
Dipolar (J-) coupling	A through-space interaction between two nuclear magnetic moments, mediated by bonding electrons.	Peak splitting.
Quadrupolar	Coupling of the nuclear electric quadrupole moment of an I > ½ nucleus with the electric field gradient of the surrounding electrons.	Peak broadening.
Paramagnetic	Coupling of a nuclear magnetic moment with the magnetic moment of an unpaired electron.	Significant peak broadening.

Shielding interactions are often analysed by NMR in order to characterise the chemical environment of a spin-active nucleus. Since the degree of shielding is dependent on the vicinal electron density, local magnetic fields will differ between chemically inequivalent sites. Although variations in the local magnetic field are relatively small, shielding interactions can create a detectable change in the resonant frequency of a nucleus, which can be used to infer the structure and chemistry of the local environment.[83, 85] In order to quantify the shielding effects, the resonant frequency of a nucleus (ν_0) is reported as a chemical shift, relative to the same nuclide in a reference compound (ν_r). On the δ-scale, chemical shift (δ) is independent of the applied magnetic field, B_0 (**Equation 2.2.17**).[84]

Equation 2.2.17: $$\delta\ (in\ ppm) = \frac{\nu_0 - \nu_r}{\nu_r} \times 10^6$$

2.2.7.3 Considerations when performing NMR on solid-state samples

In traditional, liquid-phase NMR, orientation-dependent interactions within a sample are averaged by the continuous and rapid tumbling of molecules, leading to relatively well-resolved and uncomplicated spectra.[84] However, the particles in a solid are largely immobile and thus anisotropic internal interactions (e.g. chemical shielding, dipolar and quadrupolar coupling) depend strongly on the orientation of the solid in the applied magnetic field. As a result, solid-state NMR spectra are often complex and suffer significant peak broadening.[83]

Magic-angle spinning (MAS) NMR was developed to address the issue of spectral resolution for solid-state samples. MAS NMR exploits the orientation-dependence of the internal interactions, which are related to the angle of the applied magnetic field by a $(3\cos^2(\theta) - 1)$ term.[83] By packing a cylindrical, solid sample and inclining it at 54 °74‘ to the applied field, rotation about the cylindrical axis will partly time-average any anisotropic interactions. Provided magic-angle spinning is rapid, sharp NMR spectra can be acquired for solid samples.[84]

As well as MAS, a number of other technologies may be used to enhance the resolution of solid-state NMR. Since the intensity of an NMR signal is the product of the bulk magnetisation, the small population imbalance at thermal equilibrium limits sensitivity. To some extent, the equilibrium distribution of nuclei between the available spin states is determined by the intrinsic gyromagnetic ratio of the nuclide. However, it is possible to increase the net magnetisation of a sample by applying a greater magnetic field strength. With larger B_0, the energy separation of the nuclear spin states (and hence the population imbalance at equilibrium (**Equation 2.2.15**)) is increased, and the NMR sensitivity is improved.[85]

The long spin-lattice relaxation time associated with solid samples can also make the NMR experiment time consuming, especially if a large number of scans are required for good signal-to-noise ratio. In this case, cross-polarisation (a specially-designed, radiofrequency pulse-sequence) may be used to transfer polarisation from an abundant, high-γ nucleus to a more dilute, low-γ spin, in order to enhance the signal intensity of the latter.[84]

2.2.7.4 Using MAS NMR to characterise zeotype materials

MAS NMR has emerged as a valuable technique to probe the local structure and interactions of inorganic materials.[84] This includes zeotype materials, which are amenable to characterisation by MAS NMR *via* the naturally occurring isotopes of the framework T-atoms (**Table 2.2.5**).[44] Depending on the inherent properties of the nucleus (e.g. natural abundance, gyromagnetic ratio, quadrupole moment), MAS NMR may be used to resolve and characterise the various nuclear environments of the framework, and to extract information about their coordination geometry and nearest-neighbour atoms.[84] MAS NMR is also widely used to study the protonic sites in zeotype materials, these being associated with the acid characteristics (and hence catalytic activity) of the framework. The receptivity of the ^{1}H nucleus means that ^{1}H MAS NMR studies can be used to ascertain the type, quantity, strength, and interactions of the hydroxyl sites with good resolution.

Table 2.2.5: The properties of selected NMR-active nuclei found in zeolites and AlPOs, with some characteristic resonances of the nuclei in zeotype materials.

Nucleus	*I*	Natural abundance / %	γ / 10^7 rad s^{-1} T^{-1}	Characteristic resonances		
				δ / ppm	Assignment	Ref
^{27}Al	5/2	100	7.0	-10	Six-coordinate Al	86-90
				6 to 13	Five-coordinate Al	
				31 to 44	Tetrahedral Al(4P), AlPO	
				60	Tetrahedral Al(4Si), zeolitic	
^{29}Si	1/2	4.7	-5.3	-85 to - 88	Si(4Al), aluminosilicate region	86, 88-93
				-89 to -92	Si(4Al9P), SAPO-type	
				-92 to -94	Si(3AlSi), aluminosilicate region	
				-98	Si(2Al2Si), aluminosilicate region	
				-101 to - 106	Si(1Al3Si), aluminosilicate region	
				-106 to - 112	Si(4Si), siliceous region	
^{31}P	1/2	100	10.8	-26 to -28	P(4Al)	86-90
				-16 to-14	P-OH defect sites	
^{1}H	1/2	> 99	26.7	4.6 to 5.2	Si-O(H)-Al, Brønsted sites in small cavities or channels	89, 94-97
				3.6 to 4.8	Si-O(H)-Al, Brønsted sites in large cavities or channels	
				2.8 to 3.6	Al-OH (extra-framework)	
				1.6 to 2.4	Si-OH, P-OH (defects)	

2.2.8 Neutron techniques

The neutron is an uncharged, subatomic particle with spin-½ magnetic moment and a mass (m_n) of 1.009 amu.[98] As a neutral particle, the neutron interacts with the atomic nucleus *via* the nuclear force, which has range of only ~ 10^{-15} m.[99] Due to the short range of the nuclear force, a nucleus acts as a point scatterer towards neutrons, which are scattered isotropically.[99] However, as the nucleus is only ~1/1000 the atomic diameter,[100] the probability of neutron scattering is low and as such, neutrons are inherently penetrating of matter. Whilst a high penetrating power is advantageous for bulk analysis, the weak neutron-matter interactions, combined with a relatively low flux from neutron sources, can limit signal in neutron experiments.[99] Nonetheless, by designing specialised instruments to probe different aspects of neutron scattering, neutron spectroscopies can achieve structural and dynamical insights often inaccessible by other techniques.

2.2.8.1 Neutron scattering theory

To rationalise scattering phenomena, neutrons are treated as quantum-mechanical entities that exhibit wave-particle duality.[100, 101] When discussing the production and detection of neutrons, a particle description is most intuitive.[101] In this case, the neutron energy (E) is equated to the kinetic energy (**Equation 2.2.18**, where v is the neutron speed), leading to a useful relationship between temperature (T) and neutron energy (*via* k_B, the Boltzmann constant).[102]

Equation 2.2.18: $$E = \tfrac{1}{2} m_n v^2 = k_B T$$

In a discussion of diffraction and collective excitations, a wave description of the neutron is often more appropriate.[101] The wave description is developed from the de Broglie relation (**Equation 2.2.19**, where h is the Planck constant) that relates the momentum (p) of the neutron particle to a quantum mechanical wavelength (λ). Then, using the neutron kinetic energy, a relationship between wavelength and energy can be established (**Equation 2.2.20**).

Equation 2.2.19: $$\lambda = \frac{h}{p} \qquad where\ p = m_n v$$

Equation 2.2.20: $$E = \frac{h^2}{2m_n\lambda^2}$$

When a neutron interacts with a nucleus, the scattering event is characterised by the change in energy and/or momentum of the incident neutron.[102] To describe a scattering process it is typical to use the neutron wavevector, $\boldsymbol{k}$: a vector of magnitude $\frac{2\pi}{\lambda}$, directed along the neutron trajectory. As conveyed by **Equation 2.2.21** and **Equation 2.2.22**, $\boldsymbol{k}$ contains information about the neutron energy (E) and momentum ($\boldsymbol{p}$).[103] Thus, any scattering event accompanied by a change in the energy or momentum of the neutron, is associated with a change in the magnitude or direction of the neutron wavevector, respectively.

Equation 2.2.21: $$E = \frac{\hbar^2|\boldsymbol{k}|^2}{2m_n}$$

where $$\hbar = \frac{h}{2\pi}$$

Equation 2.2.22: $$\boldsymbol{p} = \hbar\,\boldsymbol{k}$$

If a neutron of incident wavevector $\boldsymbol{k_i}$ is scattered with a wavevector $\boldsymbol{k_f}$, the momentum change ($\boldsymbol{p}$) is given by **Equation 2.2.23**, where $\boldsymbol{Q}$ (the wavevector transfer) characterises the scattering geometry (**Figure 2.2.22**).[98, 102]

Equation 2.2.23: $$\boldsymbol{p} = \hbar(\boldsymbol{k_i} - \boldsymbol{k_f}) = \hbar Q$$

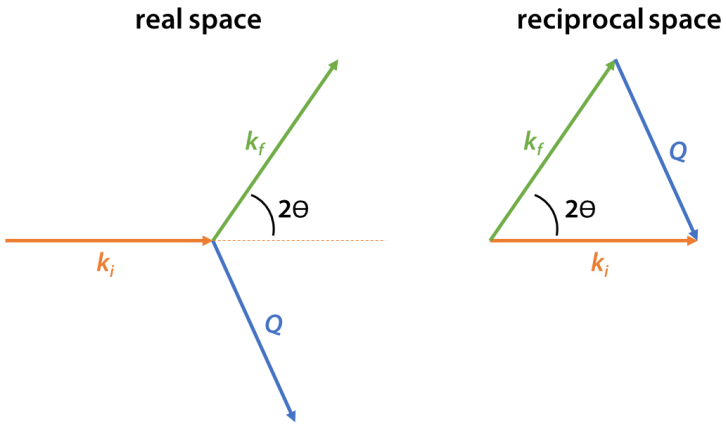

Figure 2.2.22: A graphical representation of the scattering vector, Q. The magnitude (i.e. energy) of incident and scattered wave vectors ($\boldsymbol{k_i}$ and $\boldsymbol{k_f}$, respectively) is represented by their length. The change in direction of a neutron during a scattering event is given by 2θ.

When evaluating the energy transferred during a neutron scattering event (E), it is typical to report the neutron energy as an angular frequency, ω.[84] If an incident neutron of angular frequency ω_i is scattered with an angular frequency ω_f, the scattering process is inelastic and the associated energy transfer (E) is defined by **Equation 2.2.24** (where ν is the neutron frequency). However, the interaction between a neutron and nucleus may also occur without energy transfer, in which case $\omega_f = \omega_i$ and the scattering process is described as elastic.

Equation 2.2.24: $$E = \hbar(\omega_i - \omega_f) = \hbar\omega \qquad \text{where } \omega = 2\pi\nu$$

In the scattering experiment depicted in **Figure 2.2.23**, an incident neutron beam of wavevector $\boldsymbol{k_i}$ interacts with a single, fixed nucleus, and is scattered elastically with a wavevector $\boldsymbol{k_f}$.[101]

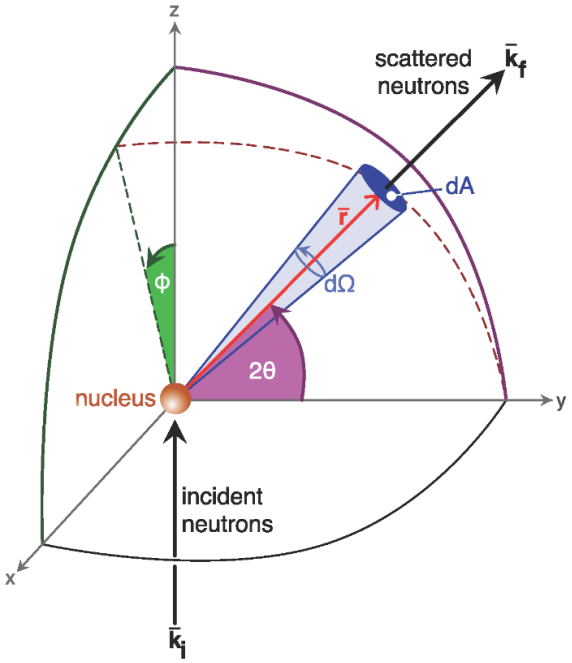

Figure 2.2.23: A diagram depicting the interaction of an incident neutron beam of wavevector $\boldsymbol{k_i}$ with a single nucleus. The neutrons are scattered with a wavevector $\boldsymbol{k_f}$, which lies along the position vector $\boldsymbol{r}$, described by the spherical polar coordinates (2θ, Φ). At a distance, $|\boldsymbol{r}|$, from the nucleus, scattered neutrons are incident on a small area of detector (dA) that subtends the solid angle $d\Omega$.[101]

To explain the scattering interaction, the incident neutrons that travel along the z-direction are represented as a plane wave, e^{ikz}, of unit amplitude.[102] When the neutron beam interacts with the nucleus, it is scattered isotropically, producing spherical wavefronts from the centre of the atom. These scattered wavefronts have the form $-\frac{b}{r}e^{ikr}$, where $r = |\boldsymbol{r}|$ and the position vector, $\boldsymbol{r}$, lies parallel to $\boldsymbol{k_f}$. The amplitude factor, $\frac{1}{r}$ accounts for the decrease in scattering

intensity as the wavefront radiates out from the nucleus, which follows an inverse square law.[99] The factor b is the empirical scattering length of the nucleus, which describes the strength of its interaction with a neutron.[102] The scattering length may have positive or negative value, depending on whether incident and scattered neutron-waves are in-phase or out-of-phase, respectively. In the case of a nucleus with non-zero spin, an average scattering length ($\langle b \rangle$) and a standard deviation (Δb) is specified.[102]

The scattering length is closely related to the nuclear cross section, σ, another empirical descriptor of the strength (i.e. likelihood) of a neutron-nucleus interaction. Essentially, σ describes the effective area that an atom presents to an incoming neutron, as though b was the nuclear radius (**Equation 2.2.25**).[99] Experimentally, σ is equal to the total number of neutrons scattered in all directions, per second, as a fraction of the incident flux.[101]

Equation 2.2.25: $\sigma = 4\pi|b|^2$

The nuclear cross-section is the sum of two components: a coherent cross-section (σ_{coh}) and an incoherent cross-section (σ_{incoh}). These quantities describe the probability that the phase relationship between incident and scattered neutrons will be preserved (coherent), or destroyed (incoherent) by interaction with the nucleus. The coherent and incoherent cross-sections of a nucleus are related to a coherent (b_{coh}) and incoherent (b_{incoh}) scattering length, respectively, which are defined by **Equation 2.2.26** and **Equation 2.2.27**.[98, 102]

Equation 2.2.26: $\sigma_{coh} = 4\pi\langle b \rangle^2 = 4\pi\langle b_{coh} \rangle^2$

Equation 2.2.27: $\sigma_{incoh} = 4\pi(\Delta b)^2 = 4\pi\langle b_{incoh} \rangle^2$

Coherent scattering occurs when a neutron wave interacts with multiple scattering centres simultaneously, and the wavefronts scattered by the different nuclei interfere.[98] As such, coherent scattering describes correlations between nuclei, and pertains to the sample as a whole.[99] On the other hand, incoherent scattering provides information about single-particle dynamics *via* self-correlations. In an incoherent scattering event, a single neutron interacts with a single nucleus, and the waves scattered from different nuclei do not interfere. Instead, the individual scattering intensities from each nucleus sum to give the total intensity.[99] The weight of the coherent and incoherent cross-sections varies randomly between nuclei but are

generally dominated the coherent interaction.[104] The exception is hydrogen, which is both an incoherent scatterer and also the nucleus with the largest total cross section.[104]

Thus, neutron scattering encompasses several types of nuclear interaction, each of which yields different information about the scattering system (**Figure 2.2.24**). For example, if neutron scattering is elastic and coherent (e.g. for a highly ordered sample) the result is a well-defined diffraction pattern of peak intensity *versus* scattering angle, which reflects the time-averaged structure of the lattice. However, any random spin or isotopic variations in the lattice can disrupt the short-range order, giving rise to an incoherent (elastic) background and reduced intensity in the diffraction pattern. If neutron scattering is coherent and inelastic, it provides information about excitations that involve the collective motion of nuclei in a lattice (e.g. phonons and magnons).[104] In contrast, incoherent, inelastic scattering is used to probe local dynamics and it can be used to track the motion of a single scattering centre over time.[100, 105] Also, a distinction is often made for quasi-elastic neutron scattering (QENS), which is associated with very small energy transfers due to interaction with 'dissipative excitations', such as the translational motion of diffusing nuclei.[104] Whilst coherent QENS is used to study the correlated diffusive motions of nuclei (transport diffusivity), incoherent QENS tracks the motion of a single scattering centre over time (self-diffusivity).[106]

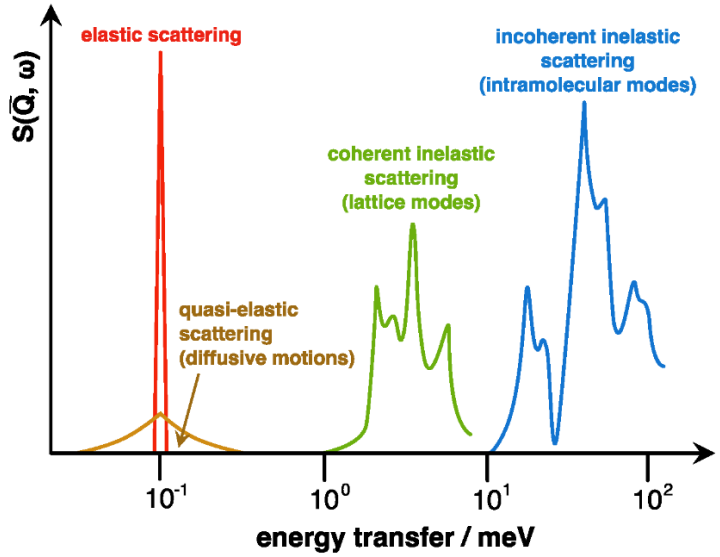

Figure 2.2.24: An illustrative spectrum showing the energy transfers associated with different types of neutron scattering interaction.

In general, atomistic information is obtained from the scattering experiment by measuring the intensity of neutrons scattered into a small solid angle, $d\Omega$, with a final energy between E_f and $(E_f + dE)$.[107] This measureable is known as the double differential cross section ($\frac{d^2\sigma}{d\Omega d\omega}$, **Equation 2.2.28**) and it is related to the dynamic structure factor, $S(\boldsymbol{Q}, \omega)$: the function that contains all the structural and dynamical information about the scattering system.[108]

Equation 2.2.28: $$\frac{d^2\sigma}{d\Omega dE_f} = \frac{\boldsymbol{k_f}}{\boldsymbol{k_i}}\frac{\sigma}{4\pi}S(\boldsymbol{Q},\omega)$$

For this reason, $S(\boldsymbol{Q}, \omega)$ is also known as the total dynamic structure factor. If a sample contains a mixture of different nuclei then $S(\boldsymbol{Q}, \omega)$ is the sum over all partial contributions from every scatterer, weighted for the strength of their neutron-nucleus interaction.[109] Since total measured intensity is the contribution of both coherent and incoherent scattering, $S(\boldsymbol{Q}, \omega)$ is also the sum of coherent ($S_{coh}(\boldsymbol{Q}, \omega)$) and incoherent ($S_{incoh}(\boldsymbol{Q}, \omega)$) parts, weighted by their respective cross-sections (**Equation 2.2.29**).[108]

Equation 2.2.29: $$\sigma_{total}\, S(\boldsymbol{Q},\omega) = \sigma_{coh}\, S_{coh}(\boldsymbol{Q},\omega) + \sigma_{incoh}\, S_{incoh}(\boldsymbol{Q},\omega)$$

Although the intensity measured in a neutron scattering experiment is directly proportional to the scattering function, it is convolved with the instrumental response.[110] Thus, raw neutron spectroscopic data (usually detector counts as a function of 2θ and time-of-flight) is reduced to $S(\boldsymbol{Q}, \omega)$, an instrument-independent function that is more readily analysed.[111]

2.2.8.2 Experimental methods & instrumentation

When using neutron spectroscopy to probe atomic-level structure and dynamics, an intense neutron source is advantageous. The ISIS Neutron and Muon Source in Oxfordshire (**Figure 2.2.25**) is a pulsed, spallation source.[112] At ISIS, the process of generating neutrons[98] begins at the injector, where hydride ions are produced from hydrogen gas and caesium vapour using an electrical discharge. The hydride ions are focussed into the radiofrequency quadrupole accelerator, which uses electrical fields to generate discrete bunches of H^- ions. The pulses of H^- are introduced into a linear accelerator, where a thin alumina foil strips the electrons from the hydride ions to produce protons. The protons are transferred into the synchrotron where they are maintained on a circular orbit by bending magnets. Following ~10,000 orbits of the synchrotron, the proton beam is separated into two, 100 ns bunches that are kicked into the extracted proton beamline. The acceleration process is repeated 50 times per second, generating a mean current of 200 μA. The protons are directed towards a tungsten plate in the target station, whereupon decay of the excited metal nuclei generates neutrons. The impact of each proton produces ~ 15 neutrons, and since evaporation occurs

within < 10^{-15} seconds of proton impact, the time distribution of the neutrons is determined by the time distribution of the proton pulse.[113]

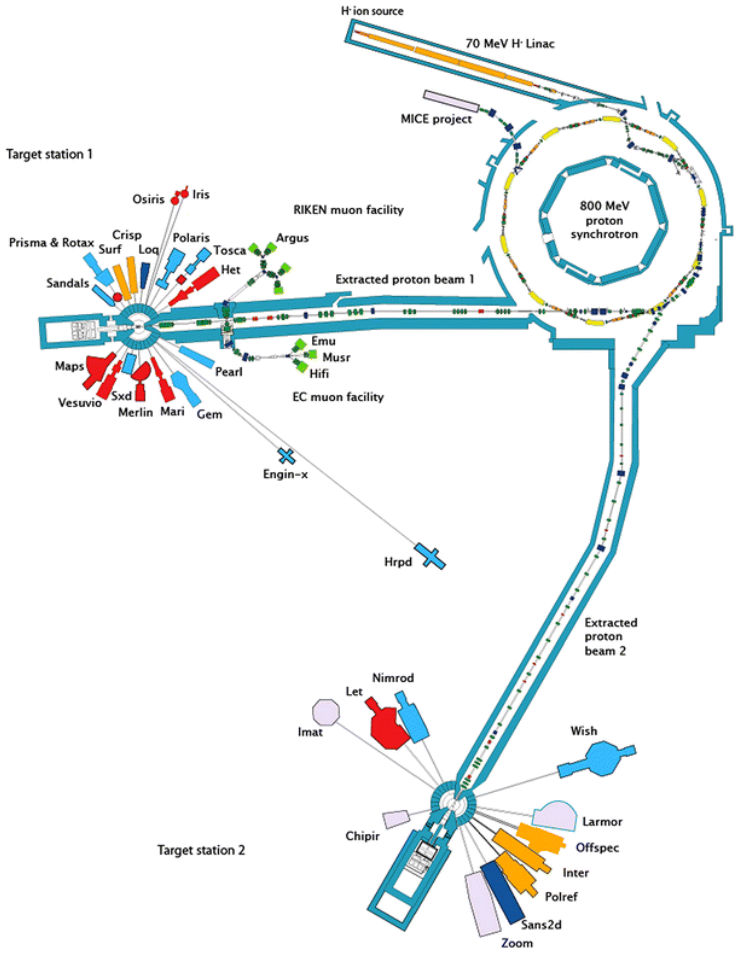

Figure 2.2.25: A schematic plan of the of the ISIS Neutron and Muon Source (Oxfordshire).[114]

The neutrons ejected from the target are fast neutrons, with wavelengths that are too short to be used for the study of molecular structure and dynamics. To slow the energetic neutrons, the source is surrounded by a moderator material with a large neutron cross-section (e.g. CH_4, H_2O, H_2).[98] During numerous, inelastic collisions the neutrons transfer energy to the moderator until a near thermal equilibrium is achieved.[98] The thermal neutrons emitted from the moderator have a Maxwell-Boltzmann distribution of energies, centred about an average value determined by the moderator temperature.[115] However, a significant number of higher energy, epithermal neutrons may also escape, particularly if the volume of the moderator is small (as is the case at many spallation sources).[98]

For neutron spectroscopy, the energy of the incident and scattered neutrons must be known. At a spallation source, neutrons emitted in a single pulse are produced at essentially the same time, so their energies can be determined by their time-of-flight (TOF) to a detector.[100] For TOF analyses, one of two types of experimental setup may be used (**Figure 2.2.26**). At a direct-geometry instrument, a monochromating device (such as a rotating chopper) is used to select the energy of the incident neutrons. If the neutrons undergo inelastic collisions with

the sample they become distributed in time and the final energy of the scattered neutrons is determined by their arrival time at the detector.[116] With an indirect-geometry setup, the sample is irradiated with a white neutron beam, such that the incidence time of a neutron depends on its wavelength. A monochromator selects the energy of the scattered neutrons, which travel from sample to detector with a known flight time. Typically, a direct-geometry instrument will have many detectors covering a large range of scattering angles (and hence $\boldsymbol{Q}$-range), allowing momentum and energy transfer to be measured independently. In contrast, the $\boldsymbol{Q}$-range of the indirect spectrometer is limited.[117] For an indirect setup $\boldsymbol{k_i} >> \boldsymbol{k_f}$ such that $\boldsymbol{Q} \approx \boldsymbol{k_i}$, and thus $\boldsymbol{Q}$ lies almost parallel to the incident neutron beam. Since $\boldsymbol{Q}$ is independent of $\boldsymbol{k_f}$, there is a fixed relationship between the energy and momentum transfer, such that $\boldsymbol{Q} \approx \sqrt{\frac{2m_n\omega}{\hbar}}$.[100, 118] For a direct geometry instrument, the energy of the incident neutrons places a limit on the largest transition that can be observed. However, indirect instruments are able to access the entire range of energy transfers.[98]

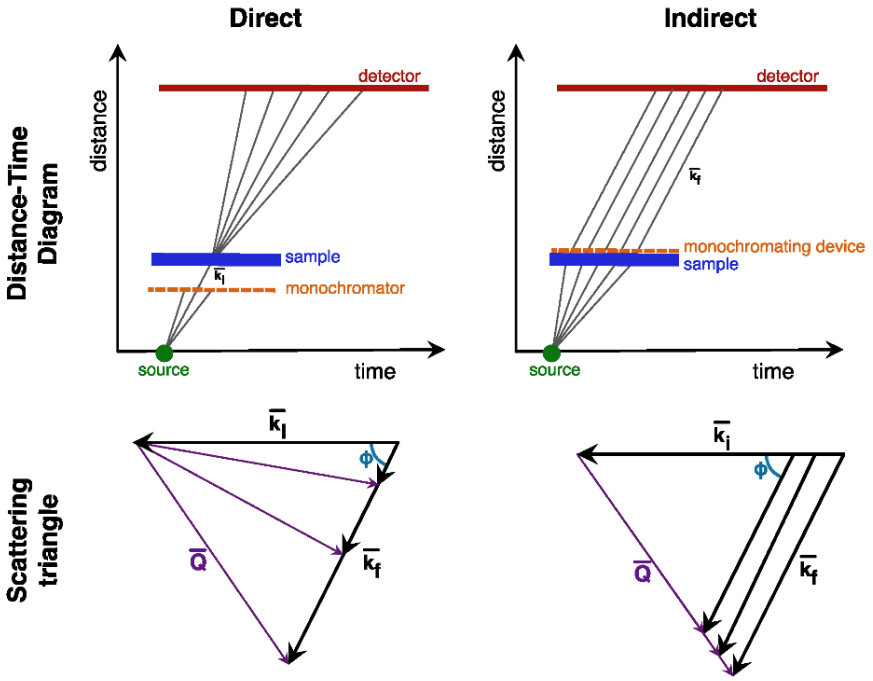

Figure 2.2.26: The distance-time time diagrams of a direct and indirect TOF spectrometer are depicted with the corresponding scattering triangle, which shows the wavevector transfer ($\boldsymbol{Q}$) when an incident neutron of wavevector $\boldsymbol{k_i}$ is scattered with a wavevector $\boldsymbol{k_f}$ at an angle Φ.

2.2.8.3 Inelastic neutron scattering

Inelastic neutron scattering (INS) is a vibrational technique that is used to study atomic and molecular dynamics in the condensed phases.[98] By using thermalised neutrons with wavelengths in the X-ray region (i.e. comparable to interatomic separations) and energies of the order of the spacing between vibrational energy levels (i.e. equivalent to mid-infrared

energies), INS can probe atomic-level structure and dynamics simultaneously. Whilst INS experiments are often more involved and costly than conventional vibrational spectroscopies (e.g. IR, Raman), neutron spectroscopy offers some unique capabilities.[100] For example, since neutrons (unlike photons) possess mass, their inelastic collisions are associated with both energy and momentum transfers. Consequently, all vibrational modes of the sample, including optically forbidden transitions, are allowed (and thus measurable) by INS. In contrast, spectroscopies that rely on photon scattering are subject to optical selection rules. It is also relatively straightforward to accurately model the position and intensity of INS bands using *ab initio* calculations in order to assign vibrational modes.[98]

Since the ^{1}H nucleus has the largest incoherent scattering cross-section of any nucleus, INS spectra are dominated by signals associated with hydrogen.[100] As such, INS is suited to the study of the dynamics and environment of individual protons or hydrogenous species, even in the presence of a non-hydrogenous matrix. Furthermore, where neutrons typically interact only weakly with heavy elements, INS measurements can be performed on samples within containers that accommodate forcing conditions.

Equation 2.2.30 is the scattering law for INS,[100] which gives the intensity (S) of the i^{th} mode at momentum transfer, $\boldsymbol{Q}$, and frequency, ω (n is the order of the oscillation, such that n = 1 is the fundamental, n = 2 is the first overtone, *etc.*). U_i is the root mean square displacement of the atoms (of inelastic scattering cross-section, σ) in the mode, and U_{Tot} is the total mean square displacement of all atoms in all internal and external modes.

Equation 2.2.30: $$S(\boldsymbol{Q}, n\omega_i) \propto \sigma \frac{[Q\ U_i]^{2n}}{n!} e^{-(Q\ U_{tot})^2}$$

The scattering law can be considered as comprising two key terms.[98] The pre-exponential term (indicated in red in **Equation 2.2.30**) increases with momentum transfer and also the displacement of the scattering atoms. Since $\boldsymbol{Q}$ is fixed by the spectrometer, determination of $S(\boldsymbol{Q}, \omega)$ can be used to extract atomic displacements. The exponential term (or Debye-Waller factor, indicated in blue in **Equation 2.2.30**) always decreases faster with $\boldsymbol{Q}$ than the pre-exponential factor increases (**Figure 2.2.27**). Since the magnitude of U_{Tot} is partly determined by the thermal motion of the sample, INS measurements are often performed at < 30 K to suppress the Debye-Waller factor and minimise damping of INS intensity.[100]

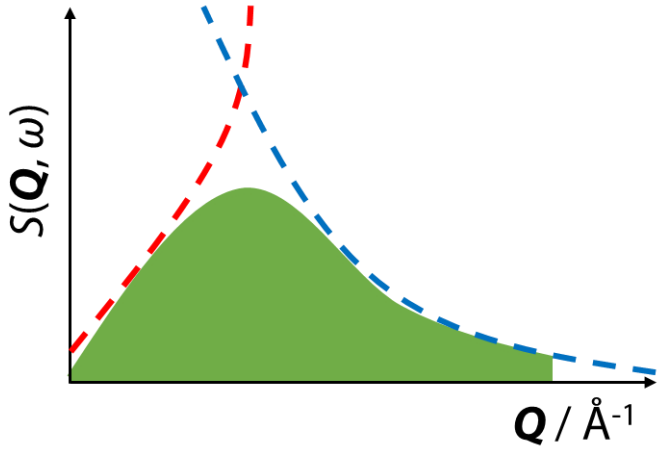

Figure 2.2.27: A representation of the variation of the scattering law ($S(\boldsymbol{Q}, \omega)$) with momentum transfer ($\boldsymbol{Q}$) for a given vibrational mode (**Equation 2.2.30**). At low $\boldsymbol{Q}$ the increase in INS intensity is driven by the pre-exponential factor (red line), but at higher $\boldsymbol{Q}$, intensity is damped by the Debye-Waller factor (blue line).[98]

2.2.8.4 Quasi-elastic neutron scattering

Quasi-elastic neutron scattering (QENS) is a limiting case of INS, where minute energy transfers (neV to μeV)[119] due to particle rotations and translations cause broadening of the elastic peak of scattered neutrons.[120] QENS provides information about the molecular dynamics occurring over time scales of 10^{-8} - 10^{-13} s and distances of 10^{-9} - 10^{-10} m.[106]

During a QENS experiment, motions in real space and time are measured in $\boldsymbol{Q}$-ω space *via* the scattering function $S(\boldsymbol{Q}, \omega)$.[121] As $S(\boldsymbol{Q}, \omega)$ is the four-dimensional Fourier transform of the van Hove correlation function, $G(\boldsymbol{r}, t)$, the variables $\boldsymbol{Q}$ and ω can be transformed into the displacement vector, $\boldsymbol{r}$, and time, t, respectively. In this case, motions that occur over large distances and time scales correspond to small $\boldsymbol{Q}$ and ω. If the scattering function is separated into its coherent and incoherent parts, $S_{incoh}(\boldsymbol{Q}, \omega)$ is related to the self-part of the van Hove correlation function $G_s(\boldsymbol{r}, t)$, which is the probability that a nucleus, starting at the origin, will be displaced by the vector $\boldsymbol{r}$ within a time, t.[119, 122] The coherent part of the scattering function, $S_{coh}(\boldsymbol{Q}, \omega)$, is the Fourier transform of the pair correlation function, $G_p(\boldsymbol{r}, t)$: the probability of any particle being displaced by $\boldsymbol{r}$, at time t, if any particle is at the origin at $t = 0$. Hence, the incoherent scattering from a nucleus can be used to calculate self-diffusivity (D_s) of a single scattering centre, whereas coherent scattering is used to obtain the (collective) transport diffusivity (D_t).[119, 121]

The scattering function measured by a QENS experiment comprises an elastic component and a quasi-elastic contribution. In order for quasi-elastic broadening to be detected, the time period of a dynamical process must be shorter than the inverse of the instrumental resolution ($\Delta\omega$).[119] In this case, $S(\boldsymbol{Q}, \omega)$ can be fit as a linear combination of a Gaussian instrumental-resolution function, and a Lorentzian function that describes the quasi-elastic component (**Figure 2.2.28 a**). The relationship between the Lorentzian broadening (measured as a half-width at half-maximum) and $\boldsymbol{Q}$ is then fit to theoretical models in order to characterise the time of the motions in the sample and to calculate diffusion coefficients.

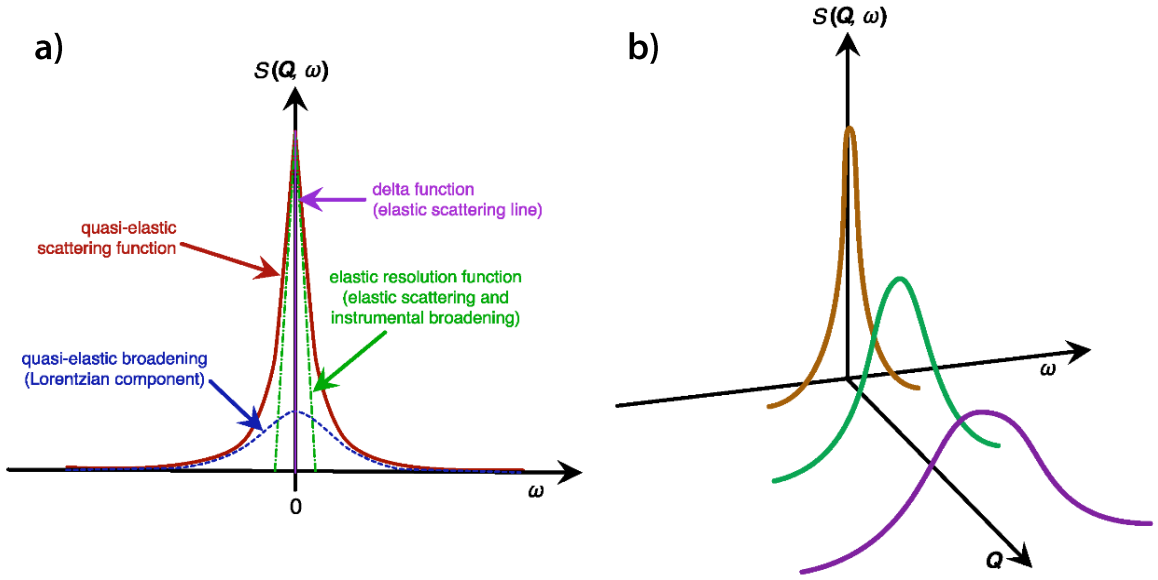

Figure 2.2.28: (a) A schematic of a quasi-elastic spectrum (red) showing the Lorentzian component that models quasi-elastic broadening (blue), and the elastic resolution function (green) that convolutes the elastic scattering (delta function, purple) at zero energy transfer (ω) and the instrumental broadening. **(b)** A depiction of broadening of the scattering function $S(\boldsymbol{Q}, \omega)$ as a function of $\boldsymbol{Q}$, due to quasi-elastic scattering.

Ideally, the elastic component of the QENS spectrum would be a delta function, however the resolution of the spectrometer gives rise to an experimental, finite linewidth.[106] Nonetheless, if the sharp, elastic component can be deconvoluted from the wider quasi-elastic part, an elastic incoherent structure factor (EISF) can be calculated from the ratio of the elastic intensity and the total intensity.[106] By evaluating the EISF of each scattering function over a range of $\boldsymbol{Q}$ values (**Figure 2.2.28 b**), it is possible to extract information about the geometry of the motion of the scattering nuclei by using models available in literature.[120, 123]

2.2.8.5 Total neutron scattering

Total neutron scattering is used in materials characterisation to access long- and short-range structural information.[124] It may be considered an extension of neutron powder diffraction as it considers not only Bragg scattering, but also the diffuse scattering that encodes short-range atomic structure and reveals disorder in a crystalline lattice.[125]

In neutron diffraction, neutrons scattered in accordance with Bragg's Law produce sharp peaks of intensity that contain the long-range structure as time-averaged, atomic positions.[124] Whilst Bragg scattering provides an adequate description of a crystalline material, real crystals exhibit both static and dynamic disorder. Any deviations from the perfect lattice leads to destructive interference between the scattered neutrons, reducing the intensity of the Bragg peaks and creating a background of diffuse scattering. Since diffraction experiments rely on the predominance of elastic scattering, they tend to lack energy transfer discrimination and any diffuse scattering or instrumental contributions are subsumed in a background that is discarded.[102] As such, diffraction techniques are largely uninformative when studying amorphous solids or liquids, as these materials have little or no long-range structure. However, local atomic correlations may be extracted from the diffuse scattering if the total neutron scattering (i.e. Bragg and diffuse scattering) is analysed.[124]

2.2.9 Positron annihilation lifetime spectroscopy

Over the last century, techniques that exploit the physical chemistry of positron annihilation have been used increasingly for materials characterisation.[126] Positron annihilation lifetime spectroscopy (PALS) is one technique that uses positron annihilation to characterise the electronic and structural properties of solid samples. A particular advantage of the positron probe is its tendency to localise in regions of low electron density, so that the dominant annihilation signals originate from sites such as vacancies, surfaces, pores, defects and voids.[127] It is for this reason that PALS finds application in porosimetry.[128]

2.2.9.1 Positron annihilation

Annihilation describes the transformation of the mass of a matter/anti-matter pair into energy. In condensed matter, an electron-positron pair will exist for only a few hundred picoseconds before annihilating with the release of gamma radiation.[126] Commonly,

annihilation occurs as either a two- or three-photon process, although the cross-section (i.e. the probability) of a three-photon annihilation is considerably smaller.

Before annihilation, a positron may be slowed sufficiently that it captures an electron from its surroundings and forms a bound, hydrogen-like species called a positronium (Ps).[129] The Ps is a neutral, metastable species that exists in one of two ground states, depending on the relative orientation of the electron and positron spins (**Figure 2.2.29**).[126] If electron and positron spins are aligned anti-parallel, a singlet-state, *para*-positronium (*p*-Ps) is produced. However, if the electron and positron spins are aligned in parallel, the result is a triplet-state, *ortho*-positronium (*o*-Ps).[127]

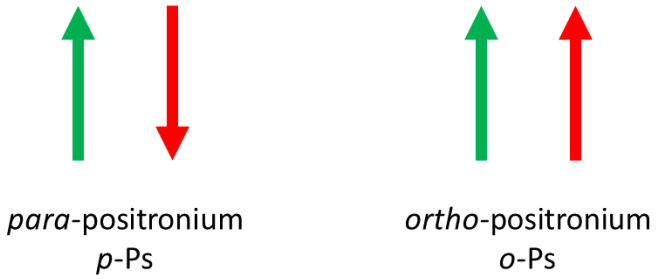

Figure 2.2.29: In a *para*-positronium, electron (green) and positron (red) spins are anti-parallel. In an *ortho*-positronium, the electron and positron spins are aligned in parallel.

Not only does the *p*-Ps have a shorter lifetime (0.125 ns) than the *o*-Ps (142 ns),[127] but also their annihilation behaviour is quite distinct. A *p*-Ps annihilates with the emission of two gamma photons, whereas an *o*-Ps undergoes three-photon annihilation.[127] As the triplet state population is three times that of the singlet state, Ps formation leads to an increase in three-photon annihilation *versus* random electron-positron annihilation.[129] A positronium in an insulating sample may also annihilate *via* the pick-off mechanism. During pick-off annihilation, a Ps interacting with its surroundings collects an electron with an anti-parallel spin to its positron. For *o*-Ps, pick-off annihilation occurs with a two-photon emission, and the lifetime of the *o*-Ps is decreased to 1 - 5 ns.[130] As a consequence, the *o*-Ps lifetime and the 3-to-2 gamma photon ratio are detectably modified by pick-off annihilation. Since the annihilation event will depend on the nature of the positron-electron interaction, the dominant annihilation pathway is determined by the electronic and structural properties of the annihilation site.[130] Variations in the gamma-photon emissions can be detected spectroscopically, and correlated with material characteristics such as defects and voids.

2.2.9.2 The PALS experiment

In a laboratory experiment (**Figure 2.2.30**), it is typical to exploit the natural decay process of a radioactive isotope in order to generate positrons. ^{22}Na is a common positron source, as it is relatively inexpensive and its long half-life (2.6 years) ensures that the positron flux is essentially constant for the duration of an experiment.[127] In addition, the decay of the ^{22}Na isotope is accompanied by the emission of a characteristic (1.274 MeV) gamma photon, which identifies the time of positron birth with high resolution. Such information is essential for PALS, since positron lifetime can be calculated if its time of death is determined from the annihilation gamma-photon emission.[126]

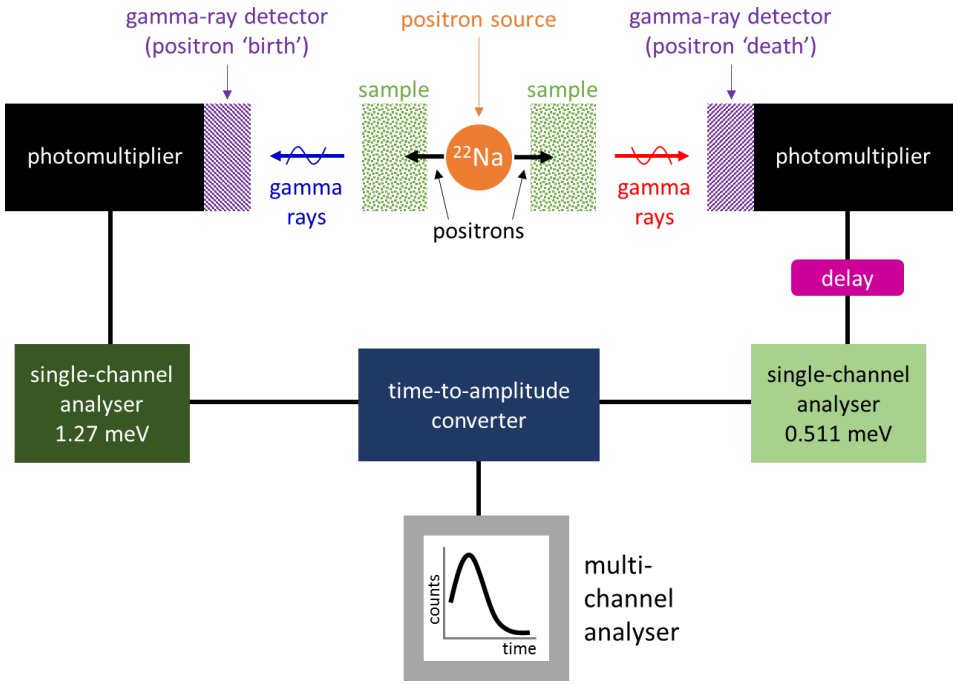

Figure 2.2.30: A schematic of the PALS spectrometer. Positron lifetime is measured as the time interval between detection of the 1.27 MeV gamma photon emitted during decay of the ^{22}Na positron source, and the gamma photon emitted during annihilation (0.511 MeV). The output spectrum is a histogram of the number of annihilation events *versus* lifetime.[126, 127]

In the PALS spectrometer, the positron source is inserted between two identical samples of sufficient thickness that any injected positrons are stopped. The source, however, has as little mass as possible in order to minimise its contribution to the measured positron lifetime.[126] The assembly of source and samples is positioned between two detectors,[127] one of which collects the 1.274 MeV gamma photons emitted by ^{22}Na during the birth of a positron, and the other of which monitors the gamma photons produced with annihilation. Gamma emissions may be collected using a scintillation detector, where the incident radiation excites a phosphor that relaxes with detectable photoemission. These photoemissions are then collected by a photomultiplier, which transforms the signal into a pulse of current.

2.2.9.3 Porosimetry with positrons and positronium

PALS is as a non-destructive technique that can be used to characterise porosity in the range 0.3–30 nm.[128] Both positrons and positronium are very sensitive to the open volume of a material and, in insulating samples, these species will tend to localise in electron-deficient voids and pores.[128] As a consequence, the gamma photons produced during annihilation can encode information about the structure and size of the pores.

The spectrum obtained by PALS is a lifetime histogram that contains information about the annihilation of all the positrons implanted in a sample.[128] However, this multi-component spectrum can be deconvoluted in order to extract the Ps lifetimes, which can be directly related to the size of the pore within which the Ps was trapped. In the quantum mechanical Tao-Eldrup model,[131, 132] a long-lived *o*-Ps is trapped in an infinite potential well that represents the pores. An *o*-Ps will only undergo pick-off annihilation when in proximity to a wall, and its lifetime will be reduced from that in vacuum (142 ns). Using the Tao-Eldrup model, the rate of *o*-Ps pick-off annihilation has been empirically related to the size and shape of the micropores. More recently, the model has been extended to allow PALS characterisation of mesoporous structures.[133-135] Typically, there is excellent agreement between the pore size distributions obtained by PALS and those measured by gas adsorption.[128] However, unlike BET, PALS can measure small pores that are inaccessible to gaseous probe molecules. Likewise, closed pores can also be measured using PALS.[127]

2.3 Molecular Modelling

Theoretical calculation of molecular structure and dynamics, although nontrivial, has advanced markedly in recent decades due to new computational methods and increased computing power.[98] With these developments, theoretical methods are providing greater insight into chemical phenomena that would be inaccessible by empirical study alone.[136] There are various computational techniques to study events occurring over length- and time-scales from the sub-nanoscale to the macroscale. By modelling systems at the electronic- and atomic-scale, it is possible to extract information about molecular geometry, reactivity, and physical properties, and to predict spectra.

In computational modelling, information about molecular properties and chemistry can be obtained by constructing a potential energy surface (PES), which describes the energy of the system in terms of certain parameters, such as molecular geometry.[98] For example, a chemical reaction may be described by locating the lowest energy path between (reactant and product) minima on a PES (**Figure 2.3.1 a**), whereas molecular vibrations correspond to

small nuclear motions about a minimum on a PES (**Figure 2.3.1 b**). Generally, the motion of atoms on a PES is solved using either classical or quantum mechanics.[137]

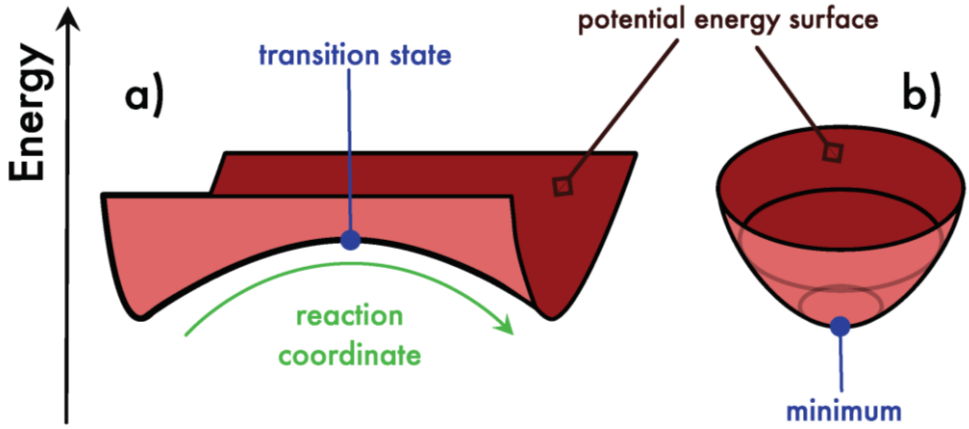

Figure 2.3.1: A depiction of potential energy surfaces showing **(a)** a transition state (or saddle point), which is a maximum along the reaction coordinate but a minimum in all other directions, and **(b)** a potential energy minimum that is a minimum in all directions.[138]

2.3.1 Molecular mechanics

Electronic structure calculations (which yield a PES by solving the electronic Schrödinger equation) are computationally expensive, especially for polyatomic systems.[137] In molecular mechanics (MM), explicit calculation of electronic energies is bypassed and instead, the PES is derived from force fields: mathematical constructs that describe the energy-dependence of a system in terms of atomic coordinates.

In MM, the electron is not considered explicitly, rather the fundamental units are atoms (i.e. the Born-Oppenheimer approximation[139] applies), and each atom-type is simulated as a particle of fixed radius, charge, and polarisability. Correspondingly, the MM molecule can be treated as a collection of 'atom particles', which are connected together by bonds that are modelled as springs of various length and stiffness.[138] If the atoms are characterised, and the bond lengths and angles, and stretching and bending energies are known, an interatomic potential energy function, or force field, can be defined. The MM force field energy, E_{FF} (**Equation 2.3.1**), is the sum of individual energy functions (i.e. bonded terms: E_{bond} for bond stretching, E_{angle} for bending an angle, $E_{dihedral}$ for (torsional) rotation about a bond, and non-bonded terms: $E_{electrostatic}$ for electrostatic atom-atom interactions, and $E_{van\ der\ Waals}$ for van der Waals interactions, **Figure 2.3.2**) that are derived from classical mechanics, and parametrised using empirical or quantum mechanical data.[140] By minimising E_{FF}, it is possible to optimise molecular energies and geometries, and hence characterise the stable molecules that correspond to minima on the PES.

Equation 2.3.1: $$E_{FF} = E_{bond} + E_{angle} + E_{dihedral} + E_{van\ der\ Waals} + E_{electrostatic}$$

Although MM is less accurate than quantum mechanical (QM) methods, MM calculations are relatively rapid and undemanding of computational resources.[138] As such, MM has proven well suited to the study of large systems, such as biomolecules. However, the quality of the MM model will depend on the force fields, and hence the availability and suitability of (empirical/QM) parameters. Consequently, predictions of molecular geometries and relative energies may be unreliable if the system is unusual, or if a lack of information necessitates the use of generic parameters. Furthermore, MM cannot describe chemical properties, such as bond cleavage, charge distribution, or electronically-excited states, which are related to the electronics of the system.[140]

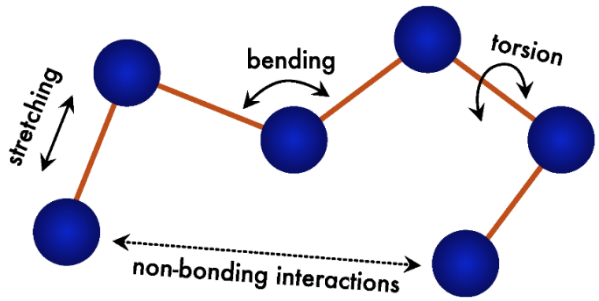

Figure 2.3.2: A representation of fundamental force field energy terms using the ball and stick model, where the atoms (blue) are connected *via* bonds (orange) modelled as springs.[137]

2.3.2 *Ab initio* calculations

An *ab initio* method is an approximate, quantum-mechanical approach that uses theoretical principles to describe the energy and distribution of electrons, without empirical data.[140] The *ab initio* approach uses the rationale that, if behaviour of the electrons in the atoms can be understood, then it is possible to use this information to evaluate molecular structure, properties, and reactivity.

Fundamentally, *ab initio* methods solve the Schrödinger equation in order to obtain an energy, and a wavefunction (Ψ) that describes the electron distribution. However, the Schrödinger equation can only be solved exactly for two bodies, and thus approximations must be used.[138] The Born– Oppenheimer approximation[139] is important in solving the Schrödinger equation for many-body systems, as it decouples nuclear and electronic motion, allowing the electronic part to be solved using the nuclear coordinates as parameters.[137] Then, by solving the Schrödinger equation for a number of nuclear geometries and electronic

states, a PES can be generated and used to evaluate nuclear motion. Nevertheless, solving the Schrödinger equation for polyatomic system is very complex and computationally demanding.[137] Therefore, to simplify the problem further, a many-body system may be transformed into a *pseudo*-one-particle system. In the Hartree-Fock (HF) method,[141, 142] the central field approximation is used to average particle-particle interactions, so that each electron is described by an orbital (a one-electron function), and the total wave function is a linear combination of the atomic orbitals.[140]

Although widely used, the HF method neglects electronic correlation, which limits the accuracy of the model because electron-electron repulsion (and hence energies) are overestimated.[136] Nonetheless, HF theory is considered the basis of all developments in *ab initio* studies, including methods that account for electron-electron interactions and the contributions of accessible electronic states. This includes semi-empirical methods, which are based on the Schrödinger equation but parameterised using empirical or high-level QM data.[138] Density functional theory (DFT) is also a development of HF theory, where electron correlation is modelled by an electron density function. Unlike HF theory, DFT does not calculate a wavefunction; instead it derives the electron density directly, and the energy of the system is estimated using an approximate functional.[136]

2.3.2.1 Density Functional Theory

Most modern DFT calculations are based on the Kohn-Sham approach,[143] which is derived from the theorems of Hohenberg and Kohn.[144] The first Hohenberg-Kohn theorem states that a property of a molecule in the ground electronic state is a functional (i.e. a rule that transforms a function into a value) of the ground-state electron density function, $\rho_0(x, y, z)$. Therefore, if $\rho_0(x, y, z)$ is known, any ground state property, such as energy (E_0), can be calculated. The second Hohenberg-Kohn theorem states that any trial electron density function will yield an E_0 higher than, or equal to, the true ground state energy. In principle, the Hohenberg-Kohn theorems provide access to all ground-state properties of a system, but the universal functional is unknown. However, Kohn and Sham later described a route to obtain a good approximation to the energy functional, which can be used to calculate molecular properties.[138]

Essentially, the Kohn-Sham approach[143] decomposes the molecular energy into a sum of energy terms of which only one (the exchange-correlation energy - a relatively small contribution of the total energy) involves an unknown functional.[138] It is possible to determine the unknown functional if the energy of the system is expressed as a deviation from the energy of an idealised system with non-interacting electrons. Since the energy of the

reference system can be calculated exactly, the small difference in energy *versus* the real system must contain the exchange-correlation functional. Thus, the target of DFT is the approximation of the unknown, exchange-correlation functional. An initial value of $\rho_0(x, y, z)$ can be input into Kohn-Sham equations in order to calculate a guess of the Kohn-Sham single-electron orbitals and energy levels. The final Kohn-Sham orbitals and energy levels are determined by iterative refinement, and these used to calculate the energy of the system.[138]

The simplest version of DFT is the local density approximation (LDA). In the LDA, electron density is assumed to vary slowly, so the exchange-correlation energy can be calculated on the assumption of uniform electron density.[136] However, LDA approaches have largely been superseded by more accurate gradient-corrected functionals, for example the general gradient approximation (GGA), which account for an electron-density gradient. The preeminent DFT methods use hybrid functionals that approximate the exchange-correlation energy functional using a combination of HF theory and *ab initio* or empirical data. One of the most popular gradient-corrected hybrid methods is the Becke three-parameter Lee-Yang-Parr (B3LYP) functional,[145] which calculates molecular properties with superior accuracy.[146]

In general, a*b initio* calculations are more accurate than MM methods, although this comes at the expense of time and computational resources. Therefore, a MM approach may be preferred when studying large, complex systems, but QM may be favoured for calculations of novel systems (since parameterisation in MM can lead to unreliable models). In some cases, a hybrid quantum-mechanics/molecular mechanics (QM/MM) approach[147] can offer a suitable compromise. In QM/MM, a finite 'quantum region' is simulated using an electronic structure technique and this is then embedded in a larger structure that is modelled using force field methods. By using QM to compute electronic phenomena in the quantum region, and exploiting the efficiency of MM to ascertain the geometry of the surrounding structure, it is possible to obtain electronic information about a chemically active region, simulated in a more representative local environment.

2.4 References

1. C. F. Poole, *Gas Chromatography*, Elsevier, Oxford, 2012.

2. H. M. McNair and J. M. Miller, *Basic Gas Chromatography*, John Wiley & Sons, New Jersey, USA, 2 edn., 2009.

3. *Practical Gas Chromatography: A Comprehensive Reference*, Springer, Berlin, 2014.

4. A. Braithwaite and F. J. Smith, *Chromatographic Methods*, Chapman and Hall, London, 4 edn., 1985.

5. J. Hagen, *Industrial Catalysis: A Practical Approach*, John Wiley & Sons, Weinheim, 3 edn., 2015.

6. E. J. Mittemeijer and U. Welzel, *Modern Diffraction Methods*, John Wiley & Sons, Inc., Weinheim, 2012.

7. J. K. Cockcroft, Advanced Certificate in Powder Diffraction on the Web, http://pd.chem.ucl.ac.uk/pdnn/pdindex.htm#inst1, (accessed August 2018).

8. *Powder Diffraction: Theory and Practice*, ed. R. E. Dinnebier and S. J. L. Billinge, Royal Society of Chemistry, Cambridge, 2008.

9. L. E. Smart and E. A. Moore, *Solid State Chemistry: An Introduction*, CRC Press, Boca Raton, 4 edn., 2012.

10. J. Als-Nielsen and D. McMorrow, *Elements of Modern X-Ray Physics*, John Wiley & Sons, Inc., New Jersey, 2011.

11. G. V. Pavlinsky, *Fundamentals of X-Ray Physics*, Cambridge International Science Publishing, Cambridge, 2007.

12. B. B. He, *Two-Dimensional X-Ray Diffraction*, John Wiley & Sons, Inc., New Jersey, 2009.

13. *Structure from Diffraction Methods*, ed. D. W. Bruce, D. O'Hare and R. I. Walton, John Wiley & Sons, Ltd., Chichester, 2014.

14. *Multi Length-Scale Characterisation*, ed. D. W. Bruce, D. O'Hare and R. I. Walton John Wiley & Sons, Chichester, 2014.

15. J. Rouquerol, F. Rouquerol, P. Llewellyn, G. Maurin and K. S. W. Sing, *Adsorption by Powders and Porous Solids : Principles, Methodology and Applications*, Elsevier Science & Technology, London, 2013.

16. K. S. W. Sing and R. T. Williams, *Adsorpt. Sci. Technol.*, 2004, **22**, 773-782.

17. K. S. Sing, *Pure Appl. Chem.*, 1985, **57**, 603-619.

18. K. Sing, *Colloids Surf., A*, 2001, **187-188**, 3-9.

19. M. Thommes, K. Kaneko, V. Neimark Alexander, P. Olivier James, F. Rodriguez-Reinoso, J. Rouquerol and S. W. Sing Kenneth, *Pure Appl. Chem.*, 2015, **87**, 1051-1069.

20. D. H. Everett and J. C. Powl, *J. Chem. Soc., Faraday Trans. 1*, 1976, **72**, 619-636.

21. S. Brunauer, P. H. Emmett and E. Teller, *J. Am. Chem. Soc.*, 1938, **60**, 309-319.

22. I. Langmuir, *J. Am. Chem. Soc.*, 1918, **40**, 1361-1403.

23. G. Barnes and I. Gentle, *Interfacial Science: An Introduction*, Oxford University Press, Oxford, 2 edn., 2011.

24. P. Haines, P. G. Laye, S. B. Warrington, G. Thermal Methods, G. R. Heal, D. M. Price and R. Wilson, *Principles of Thermal Analysis and Calorimetry*, Royal Society of Chemistry, Cambridge, 2002.

25. J. M. Thomas and W. J. Thomas, *Principles and Practice of Heterogeneous Catalysis*, John Wiley & Sons, Inc., Weinheim, 2014.

26. *Zeolite Characterization and Catalysis: A Tutorial*, ed. A. W. Chester, E. G. Dourane, Springer, Amsterdam, 2009.

27. R. I. Masel, *Principles of Adsorption and Reaction on Solid Surfaces*, John Wiley & Sons, Inc., New Jersey, 1996.

28. W. J. Kirsten, *Organic Elemental Analysis: Ultramicro, Micro, and Trace Methods*, Academic Press, New York, 1983.

29. CHN Elemental Microanalysis, https://www.ucl.ac.uk/pharmacy/facilities/research-services/chn-elemental-microanalysis, (accessed September 2018).

30. V. A. Fassel and R. N. Kniseley, *Anal. Chem.*, 1974, **46**, 1110A-1120A.

31. N. K. Aras and O. Y. Ataman, *Trace Element Analysis of Food and Diet*, Royal Society of Chemistry, Cambridge, UK, 2006.

32. J. W. Olesik, *Anal. Chem.*, 1991, **63**, 12A-21A.

33. J. Lynch, *Physico-chemical Analysis of Industrial Catalysts: A Practical Guide to Characterisation*, Editions Technip, Paris, France, 2003.

34. P. J. Goodhew, J. Humphreys and R. Beanland, *Electron Microscopy and Analysis*, CRC Press, Florida, 3 edn., 2001.

35. Y. Leng, *Materials Characterization: Introduction to Microscopic and Spectroscopic Methods*, John Wiley & Sons, Inc., Weinheim, 2013.

36. W. J. Croft, *Under the Microscope: A Brief History of Microscopy*, World Scientific Publishing Co. Pte. Ltd., Singapore, 2006.

37. D. B. Williams and C. B. Carter, *Transmission Electron Microscopy: A Textbook for Materials Science*, Springer, New York, 2009.

38. T. Oku, *Structure Analysis of Advanced Nanomaterials: Nanoworld by High-Resolution Electron Microscopy*, De Gruyter, Inc., Berlin, 2014.

39. P. Larkin, *IR and Raman Spectroscopy: Principles and Spectral Interpretation*, Elsevier, Massachusetts, 2011.

40. S. Duckett and B. Gilbert, *Foundations of Spectroscopy*, Oxford University Press, Oxford, 2000.

41. B. C. Smith, *Infrared Spectral Interpretation: A Systematic Approach*, CRC Press, Florida, 1998.

42. B. H. Stuart, *Infrared Spectroscopy: Fundamentals and Applications*, John Wiley & Sons Inc., Chichester, 2004.

43. A. K. Brisdon, *Inorganic Spectroscopic Methods*, Oxford University Press, Oxford, 1998.

44. *Introduction to Zeolite Science and Practice*, ed. H. van Bekkum, E. M. Flanigen, P. A. Jacobs, J. C. Jansen, Elsevier, Amsterdam, 2001.

45. E. M. Flanigen, H. Khatami and H. A. Szymanski, in *Molecular Sieve Zeolites-I*, ed. E. M. Flanigen and L. B. Sand, American Chemical Society, Washington D.C., 1974, vol. 101, ch. 16, pp. 201-229.

46. *Characterization of Solid Materials and Heterogeneous Catalysts: From Structure to Surface Reactivity*, ed. M. Che and J. C. Védrine, Wiley VCH, Weinheim, Germany, 2012.

47. W. J. Mortier and R. A. Schoonheydt, *Prog. Solid State Chem.*, 1985, **16**, 1-125.

48. *Handbook of Zeolite Science and Technology*, ed. S. M. Auerbach, K. A. Carrado and P. K. Dutta, Marcel Decker, New York, 2003.

49. L. M. Kustov, *Top. Catal.*, 1997, **4**, 131-144.

50. K. I. Hadjiivanov and G. N. Vayssilov, *Adv. Catal.*, 2002, **47**, 307-511.

51. A. Zecchina and C. O. Areán, *Chemical Society Reviews*, 1996, **25**, 187-197.

52. H. Knözinger and S. Huber, *J. Chem. Soc., Faraday Trans.*, 1998, **94**, 2047-2059.

53. R. Howe, in *Recent Advances and New Horizons in Zeolite Science and Technology*, ed. H. Chon, S. I. Woo and S.-E. Park, Elsevier, Amsterdam, 1996, vol. 102, ch. 4, pp 97-136.

54. J. A. Lercher, C. Gründling and G. Eder-Mirth, *Catal. Today*, 1996, **27**, 353-376.

55. D. W. Breck, *Zeolite Molecular Sieves: Structure, Chemistry, and Use*, John Wiley & Sons Inc., New York, 1974.

56. E. P. L. Hunter and S. G. Lias, *J. Phys. Chem. Ref. Data*, 1998, **27**, 413-656.

57. W. W. Porterfield, *Inorganic Chemistry: A Unified Approach*, Academic Press, London, 1993.

58. I. Miletto, G. Paul, S. Chapman, G. Gatti, L. Marchese, R. Raja and E. Gianotti, *Chem. – A Eur. J.*, 2017, **23**, 9952-9961.

59. F. Leydier, C. Chizallet, D. Costa and P. Raybaud, *Chem. Commun.*, 2012, **48**, 4076-4078.

60. M. S. Holm, S. Svelle, F. Joensen, P. Beato, C. H. Christensen, S. Bordiga and M. Bjørgen, *Appl. Catal. A: Gen.*, 2009, **356**, 23-30.

61. A. van Miltenburg, J. Pawlesa, A. M. Bouzga, N. Žilková, J. Čejka and M. Stöcker, *Top. Catal.*, 2009, **52**, 1190-1202.

62. *Ordered Porous Solids: Recent Advances and Prospects*, ed. V. Valtchev, S. Mintova and M. Tsapatsis, Elsevier, Oxford, 2009.

63. F. Thibault-Starzyk, A. Travert, J. Saussey and J.-C. Lavalley, *Top. Catal.*, 1998, **6**, 111-118.

64. A. G. Pelmenschikov, R. A. van Santen, J. Janchen and E. Meijer, *J. Phys. Chem.*, 1993, **97**, 11071-11074.

65. C. Flego, L. Galasso, R. Millini and I. Kiricsi, *Appl. Catal. A: Gen.*, 1998, **168**, 323-331.

66. E. P. Parry, *J. Catal.*, 1963, **2**, 371-379.

67. A. A. Tsyganenko, D. V. Pozdnyakov and V. N. Filimonov, *J. Mol. Struct.*, 1975, **29**, 299-318.

68. A. Zecchina, L. Marchese, S. Bordiga, C. Pazè and E. Gianotti, *J. Phys. Chem. B*, 1997, **101**, 10128-10135.

69. A. A. Davydov, *Molecular Spectroscopy of Oxide Catalyst Surfaces*, John Wiley & Sons Inc., Chichester, 2003.

70. G. I. Hawe, I. Alkorta and P. L. A. Popelier, *J. Chem. Inf. Model.*, 2010, **50**, 87-96.

71. C. H. K. Jr. and J. Turkevich, *J. Chem. Phys.*, 1944, **12**, 300-309.

72. M. I. Zaki, M. A. Hasan, F. A. Al-Sagheer and L. Pasupulety, *Colloids Surf., A*, 2001, **190**, 261-274.

73. F. Thibault-Starzyk, I. Stan, S. Abelló, A. Bonilla, K. Thomas, C. Fernandez, J.-P. Gilson and J. Pérez-Ramírez, *J. Catal.*, 2009, **264**, 11-14.

74. L. Oliviero, A. Vimont, J.-C. Lavalley, F. Romero Sarria, M. Gaillard and F. Maugé, *Phys. Chem. Chem. Phys.*, 2005, **7**, 1861-1869.

75. A. A. Tsyganenko, E. N. Storozheva, O. V. Manoilova, T. Lesage, M. Daturi and J.-C. Lavalley, *Catal. Lett.*, 2000, **70**, 159-163.

76. F. Thibault-Starzyk, A. Vimont and J.-P. Gilson, *Catal. Today*, 2001, **70**, 227-241.

77. A. Erigoni, S. H. Newland, G. Paul, L. Marchese, R. Raja and E. Gianotti, *ChemCatChem*, 2016, **8**, 3161-3169.

78. J. F. Arenas, I. López Tocón, J. C. Otero and J. I. Marcos, *J. Mol. Struct.*, 1999, **476**, 139-150.

79. M. Milina, S. Mitchell, N.-L. Michels, J. Kenvin and J. Pérez-Ramírez, *J. Catal.*, 2013, **308**, 398-407.

80. K. Góra-Marek, K. Tarach and M. Choi, *J. Phys. Chem. C*, 2014, **118**, 12266-12274.

81. A. Corma, V. Fornés, L. Forni, F. Márquez, J. Martínez-Triguero and D. Moscotti, *J. Catal.*, 1998, **179**, 451-458.

82. NIST Chemistry WebBook, https://webbook.nist.gov/cgi/cbook.cgi?ID=C585488&Units=SI&Mask=80#IR-Spec, (accessed November 2018).

83. D. C. Apperley, R. K. Harris and P. Hodgkinson, *Solid-State NMR: Basic Principles and Practice*, Momentum Press, New York, 2012.

84. D. W. Bruce, D. O'Hare and R. I. Walton, *Local Structural Characterisation: Inorganic Materials Series*, John Wiley & Sons Inc., New York, 2014.

85. T. L. James, *Nuclear Magnetic Resonance in Biochemistry: Principles and Applications*, Academic Press, New York, 197.

86. A. F. Ojo, J. Dwyer, J. Dewing and K. Karim, *J. Chem. Soc., Faraday Trans.*, 1991, **87**, 2679-2684.

87. R. B. Borade and A. Clearfield, *J. Mol. Catal.*, 1994, **88**, 249-265.

88. C. S. Blackwell and R. L. Patton, *J. Phys. Chem.*, 1988, **92**, 3965-3970.

89. A. Buchholz, W. Wang, A. Arnold, M. Xu and M. Hunger, *Micropor. Mesopor. Mater.*, 2003, **57**, 157-168.

90. J. A. Martens, C. Janssens, P. J. Grobet, H. K. Beyer and P. A. Jacobs, *Stud. Surf. Sci. Catal.*, 1989, **49**, 215-225.

91. M. J. Peltre, P. P. Man, M. Briend, M. Derewinski and D. Barthomeuf, *Catal. Lett.*, 1992, **16**, 123-128.

92. P. P. Man, M. Briend, M. J. Peltre, A. Lamy, P. Beaunier and D. Barthomeuf, *Zeolites*, 1991, **11**, 563-572.

93. J. A. Martens, P. J. Grobet and P. A. Jacobs, *J. Catal.*, 1990, **126**, 299-305.

94. B. Zibrowius, E. Löffler and M. Hunger, *Zeolites*, 1992, **12**, 167-174.

95. M. Hunger, M. W. Anderson, A. Ojo and H. Pfeifer, *Micropor. Mater.*, 1993, **1**, 17-32.

96. M. Hunger, *Catal. Rev.*, 1997, **39**, 345-393.

97. A. Buchholz, W. Wang, M. Xu, A. Arnold and M. Hunger, *Micropor. Mesopor. Mater.*, 2002, **56**, 267-278.

98. P. C. H. Mitchell, S. F. Parker and A. J. Ramirez-Cuesta, *Vibrational Spectroscopy with Neutrons: With Applications in Chemistry, Biology, Materials Science and Catalysis*, World Scientific Publishing, Singapore, 2005.

99. R. Pynn, *Los Alamos Science*, 1990, **19**, 1-31.

100. S. F. Parker, D. Lennon and P. W. Albers, *Appl. Spectrosc.*, 2011, **65**, 1325-1341.

101. B. T. M. Willis and C. J. Carlile, *Experimental Neutron Scattering*, Oxford University Press, New York, 2009.

102. D. S. Sivia, *Elementary Scattering Theory: For X-ray and Neutron Users*, Oxford University Press, Oxford, 2011.

103. *Neutron Scattering in Biology: Techniques and Applications*, ed. J. Fitter, T. Gutberlet and J. Katsaras, Springer, Berlin, 2006.

104. N. F. Berk, *J. Res. Natl. Inst. Stand. Technol.*, 1993, **98**, 15.

105. Neutrons for Society, https://www.ill.eu/neutrons-for-society/, (accessed November 2018).

106. H. Jobic and A. Méthivier, *Oil Gas Sci. Technol.*, 2005, **60**, 815-830.

107. *Diffusion in Condensed Matter: Methods, Materials, Models*, ed. P. Heitjans and J. Kärger, Springer, Berlin, 2005.

108. H. Schober, *Putting Neutron Scattering into Perspective*, Institut Laue-Langevin, Grenoble, 2003.

109. *Materials for Tomorrow: Theory, Experiments and Modelling*, ed. S. Gemming, M. Schreiber and J. -B. Suck, Springer, Berlin, 2007.

110. S. Mukhopadhyay, *How to use Mantid for Low Energy Inelastic Neutron Scattering Data Analysis on Indirect Geometry Instruments*, Technical Report RAL-TR-2014-005, Rutherford Appleton Laboratory, U.K., 2014.

111. *Neutron Scattering: Experiment Manuals of the JCNS Laboratory*, Report INIS-DE-1250, ed. T. Brückel, G. Heger, D. Richter, G. Roth and R. Zorn, Forschungszentrum Jülich, Germany, 2014.

112. ISIS Neutron and Muon Source, https://www.isis.stfc.ac.uk/Pages/home.aspx, (accessed October 2018).

113. G. S. Bauer, *Neutron Sources*, Paul Scerrer Institut, Switzerland, pp. 12-26.

114. M. O. Jones, A. D. Taylor and S. F. Parker, *Appl. Petrochem. Res.*, 2012, **2**, 97-104.

115. M. Arai and K. Crawford, in *Neutron Imaging and Applications*, ed. I. S. Anderson, R. L. McGreevy and H. Z. Bilheux, Springer, New York, 2009, ch. 2, pp. 13-30.

116. J. M. Carpenter and C.-K. Loong, *Elements of Slow-Neutron Scattering*, Cambridge University Press, Cambridge, 2015.

117. P. W. Albers, D. Lennon and S. F. Parker, *Neutron Scattering – Applications in Biology, Chemistry, and Materials Science*, ed. F. Fernandez-Alonso and D. L. Price, Elsevier, Cambridge, 2017.

118. D. Colognesi, M. Celli, F. Cilloco, R. J. Newport, S. F. Parker, V. Rossi-Albertini, F. Sacchetti, J. Tomkinson and M. Zoppi, *Appl. Phys. A*, 2002, **74**, 64-s66.

119. H. G. Karge and J. Weitkamp, *Adsorption and Diffusion*, Springer, Berlin, 2008.

120. M. Bée, *Quasielastic Neutron Scattering: Principles and Applications in Solid State Chemistry, Biology and Materials Science*, IOP Publishing Ltd., Bristol, 1988.

121. H. Jobic and D. N. Theodorou, *Micropor. Mesopor. Mater.*, 2007, **102**, 21-50.

122. A. J. O'Malley, S. F. Parker and C. R. A. Catlow, *Chem. Commun.*, 2017, **53**, 12164-12176.

123. M. Bée, *Phys. B: Condens. Matter*, 1992, **182**, 323-336.

124. M. H. Sørby, in *Neutron Scattering and Other Nuclear Techniques for Hydrogen in Materials*, eds. H. Fritzsche, J. Huot and D. Fruchart, Springer, Cham, 2016, ch. 4, pp. 91-113.

125. D. Keen, *J. Appl. Crystallogr.*, 2001, **34**, 172-177.

126. R. W. Siegel, *Annu. Rev. Mater. Sci.*, 1980, **10**, 393-425.

127. Y. C. Jean, P. E. Mallon and D. M. Schrader, *Principles and Applications of Positron and Positronium Chemistry*, World Scientific Publishing, Singapore, 2003.

128. D. W. Gidley, H.-G. Peng and R. S. Vallery, *Annu. Rev. Mater. Res.*, 2006, **36**, 49-79.

129. J. Green and J. C. Lee, *Positronium Chemistry*, Academic Press, New York, 1964.

130. O. E. Mogensen, *Positron Annihilation in Chemistry*, Springer, Berlin, 1995.

131. S. J. Tao, *J. Chem. Phys.*, 1972, **56**, 5499-5510.

132. M. Eldrup, D. Lightbody and J. N. Sherwood, *Chem. Phys.*, 1981, **63**, 51-58.

133. D. W. Gidley, W. E. Frieze, T. L. Dull, A. F. Yee, E. T. Ryan and H. M. Ho, *Phys. Rev. B*, 1999, **60**, R5157-R5160.

134. D. W. Gidley, W. E. Frieze, T. L. Dull, J. Sun, A. F. Yee, C. V. Nguyen and D. Y. Yoon, *Appl. Phys. Lett.*, 2000, **76**, 1282-1284.

135. T. L. Dull, W. E. Frieze, D. W. Gidley, J. N. Sun and A. F. Yee, *J. Phys. Chem. B*, 2001, **105**, 4657-4662.

136. O. Deutschmann, *Modeling and Simulation of Heterogeneous Catalytic Reactions: From the Molecular Process to the Technical System*, John Wiley & Sons Inc., Weinheim, 2011.

137. F. Jensen, *Introduction to Computational Chemistry*, John Wiley & Sons Inc., Chichester, 2017.

138. E. G. Lewars, *Computational Chemistry: Introduction to the Theory and Applications of Molecular and Quantum Mechanics*, Springer, Switzerland, 3 edn., 2016.

139. M. Born and R. Oppenheimer, *Ann. Phys.*, 1927, **389**, 457-484.

140. K. I. Ramachandran, G. Deepa and K. Namboori, *Computational Chemistry and Molecular Modeling: Principles and Applications*, Springer, Berlin, 2008.

141. D. R. Hartree, *Math. Proc. Cambridge Philos. Soc.*, 2008, **24**, 89-110.

142. V. Fock, *Zeitschrift für Physik*, 1930, **61**, 126-148.

143. W. Kohn and L. J. Sham, *Phys. Rev.*, 1965, **140**, A1133-A1138.

144. P. Hohenberg and W. Kohn, *Phys. Rev.*, 1964, **136**, B864-B871.

145. A. D. Becke, *J. Chem. Phys.*, 1993, **98**, 1372-1377.

146. P. J. Stephens, F. J. Devlin, C. F. Chabalowski and M. J. Frisch, *J. Phys. Chem.*, 1994, **98**, 11623-11627.

147. A. Warshel and M. Levitt, *J. Mol. Biol.*, 1976, **103**, 227-249.

Chapter 3 An integrated empirical and theoretical investigation of the role of secondary porosity in a hierarchical silicoaluminophosphate catalyst for the Beckmann rearrangement

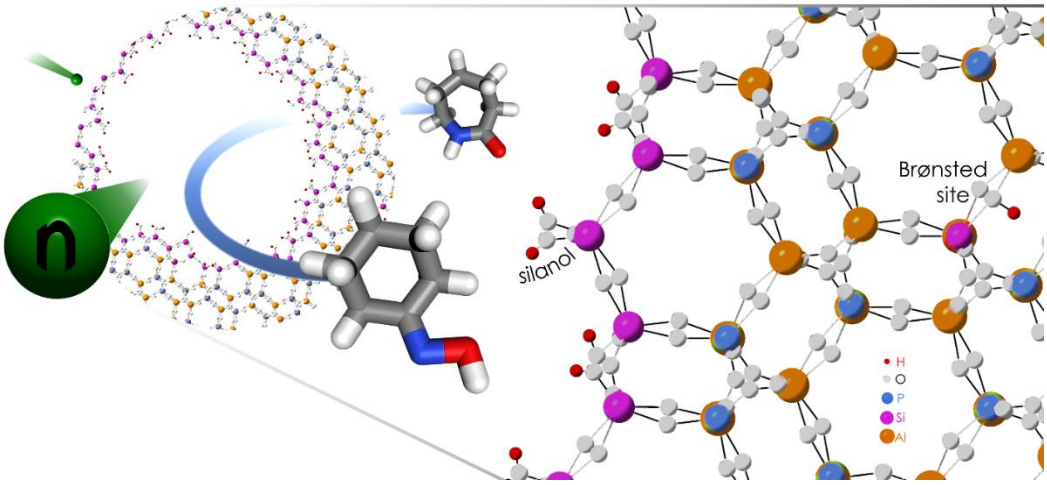

Publications

Parts of this chapter have been published as:

- Chapman, S; O'Malley, A. J.; Parker, S. F.; Raja, R., Comprehensive vibrational spectroscopic characterisation of nylon-6 precursors for precise tracking of the Beckmann rearrangement. *ChemPhysChem* **2018**, *19* (23), 3196–3203.
- Chapman, S.; Potter, M.; Raja, R., The molecular design of active sites in nanoporous materials for sustainable catalysis. *Molecules* **2017**, *22* (12), 2127.
- Chapman, S.; Raja, R., Expanding beyond the micropore: catalysis with hierarchical architectures. *Adv. Sci. Lett.* **2017**, *23* (6), 5995-5997.

Special Acknowledgements

Dr James Taylor and **Hannah Dixon**

ISIS Hydrogen and Catalysis Lab, Rutherford Appleton Laboratory, U.K.

For performing NH_3-TPD experiments.

Dr Alexander J. O'Malley

Department of Chemistry, University of Bath U.K.

For assistance in sample preparation and undertaking INS measurements.

Dr Stewart F. Parker

ISIS Pulsed Neutron and Muon Facility, Rutherford Appleton Laboratory, U.K.

For assistance and expertise as the local contact during INS beam times, and for undertaking computational analyses used in the assignment of INS spectra.

Dr Enrica Gianotti and **Dr Ivana Miletto**

Department of Science and Technological Innovation, Università del Piemonte Orientale, Italy.

For access to FTIR equipment, and assistance in acquiring FTIR data.

Dr Marina Carravetta

School of Chemistry, University of Southampton, U.K.

For assistance and expertise in performing MAS NMR experiments.

Dr Paul Cox

School of Pharmacy and Biomedical Sciences and Institute of Biomedical and Biomolecular Sciences, University of Portsmouth, U.K.

For undertaking the computational studies of catalyst-substrate interactions.

3.1 Introduction

3.1.1 Establishing a mechanism for the heterogeneously-catalysed Beckmann rearrangement

The acid-catalysed Beckmann rearrangement (BR) of cyclohexanone oxime is a fundamental step in the production of ε-caprolactam; a valuable bulk chemical and the precursor to nylon-6.[1] Conventionally, the industrial BR process uses a homogeneous, oleum catalyst to transform cyclohexanone oxime into caprolactam,[2, 3] albeit that this is both hazardous and uneconomical.[1] In 1941, Lazier and Rigby patented one of the earliest examples of a heterogeneous catalyst (silica gel) for the Beckmann rearrangement, which mitigated the use of mineral acid catalyst by operating under vapour-phase conditions (200 – 500 °C).[4] There has since been considerable development in benign, solid-acid catalysts for the vapour-phase Beckmann rearrangement - particularly in the form of zeotype materials,[5, 6] which have been implemented industrially.[3, 7, 8] Nonetheless, with the growing pressure to meet global sustainability targets,[9] catalyst research has become increasingly directed towards the liquid-phase Beckmann rearrangement, which can reduce energy requirements, enhance product selectivity, and extend catalyst lifetimes.[5, 10-14]

A variety of zeotypes have been investigated as solid-acid catalysts for the Beckmann rearrangement,[1, 5, 8, 15, 16] reflecting the structural and chemical diversity of these materials. In particular, the tuneable acidity and molecular-sieving properties of the zeotypes premise the design of active and selective catalysts for the BR,[17] provided the underlying structure-property relationships are understood. However, a holistic understanding of catalyst mechanism requires not only characterisation of the active site and its matrix, but also the chemical interactions and physical processes that facilitate catalysis. As empirical and computational techniques have evolved, it has been possible to probe in more detail the structure-activity relationships that allow zeolitic catalysts to operate effectively in the Beckmann rearrangement.[18]

3.1.1.1 The mechanism of the vapour-phase Beckmann rearrangement

In 1966, Landis and Venuto investigated the mechanism of the vapour-phase Beckmann rearrangement under zeolite catalysis.[18] In the transformation of (asymmetric) acetophenone oxime over H-Y zeolite, a high selectivity for *N*-phenylacetamide revealed that the BR proceeded with migration of the alkyl group *anti* to the hydroxyl (**Figure 3.1.1 a**). More

recently, the vapour-phase rearrangement of *anti*-2-methylcyclohexanone oxime over MFI-zeolite was found to produce 6- and 2-methyl-ε-caprolactam in a 11:1 molar ratio, due to migration of the *anti* methyl-group (**Figure 3.1.1 b**).[8] In both cases, the minor product (i.e. *N*-methylbenzamide or 2-methyl-ε-caprolactam) was produced following the isomerisation of the starting oxime, rather than catalytic *syn*-migration. Therefore, it was concluded that the zeolite-catalysed Beckmann rearrangement proceeds *via anti* alkyl migration, i.e. analogously to the homogeneously- (oleum-)catalysed process.[19]

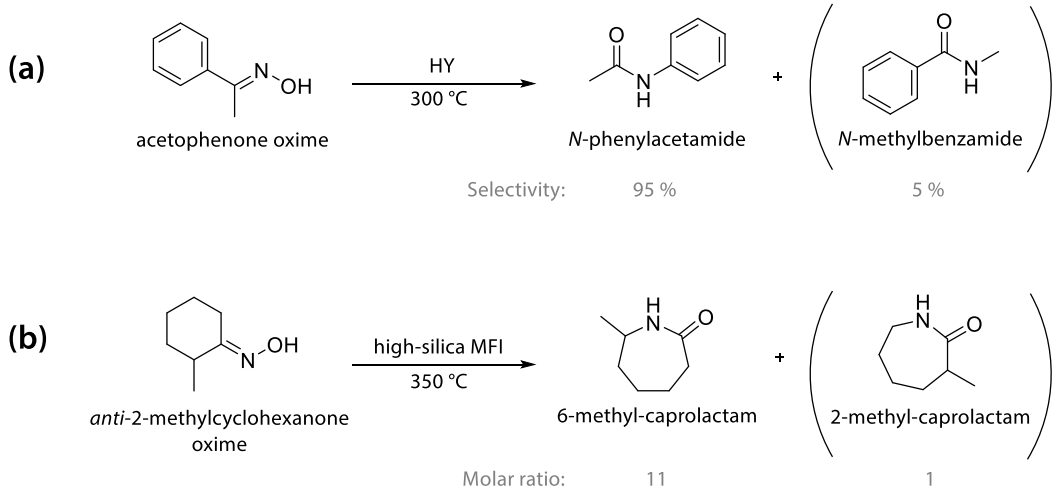

Figure 3.1.1: Schemes for the vapour-phase Beckmann rearrangement of asymmetric oxime over zeolite catalysts. **(a)** The rearrangement of acetophenone oxime over H-zeolite-Y (HY) achieved 93 % conversion of acetophenone oxime, with 95 % selectivity to *N*-phenylacetamide and 5 % to *N*-methylbenzamide.[18] **(b)** The rearrangement of *anti*-2-methylcyclohexanone oxime over MFI-zeolite produced 6- and 2-methyl-ε-caprolactam in a 11:1 molar ratio.[8] In both **(a)** and **(b)**, the small amount of '*syn*' product (in parentheses) was attributed to the isomerisation of the oxime prior to rearrangement, as opposed to *syn* alkyl-migration.

The mechanism of the BR with sulphuric acid catalyst (**Figure 3.1.2**) has been studied by Nguyen *et al.*, *via* an *ab initio* study of the isolated gas-phase system.[20] Their calculations indicated that the most favourable reaction pathway was initiated with *N*-protonation of the oxime, rather than *O*-protonation, and they proposed that the subsequent 1,2-hydride shift was the rate-limiting step.

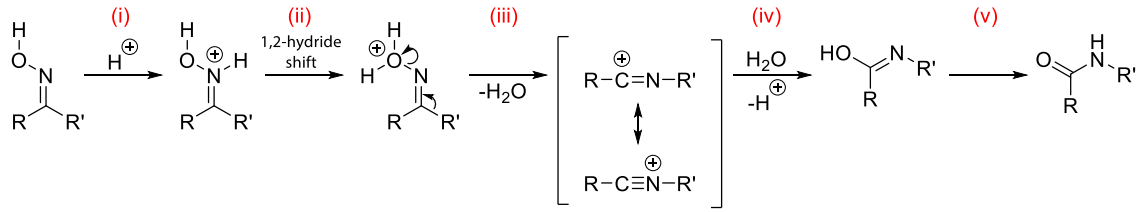

Figure 3.1.2: The general acid-catalysed Beckmann rearrangement mechanism begins with **(i)** *N*-protonation of the oxime, followed by **(ii)** a 1,2-hydride shift to give the *O*-protonated oxime. **(iii)** Migration of the alkyl group *anti* to the hydroxyl group proceeds with the loss of water and the formation of a nitrilium cation. **(iv)** Hydrolysis of the nitrilium cation gives an iminol, which **(v)** tautomerises to the corresponding amide.[19]

However, Shinohara *et al.* later disputed the validity of this mechanism for acidic, oxide catalysts, as their own quantum-chemical investigations indicated that the rate-determining step involved alkyl-group transfer with simultaneous liberation of the hydroxyl group.[21]

Thus, the general mechanism may systematise the BR, but it fails to address the more subtle variations in mechanism due to the nature of the catalyst. Such information is important in optimising zeotype catalysts for the BR, as the catalytic outcome is known to vary significantly with the properties of the framework, and the operating conditions. For example, it is well documented that both Brønsted sites and silanol sites can catalyse the BR, despite the considerable difference in their acid strength. Yet, under vapour-phase conditions, it is the most weakly acidic silanol sites that effect the BR with a high selectivity for caprolactam, whilst the stronger Brønsted sites tend to form by-products.[22-27] In contrast, stronger acidity is preferred under liquid-phase conditions if caprolactam is to be produced in significant yield.[11-14, 28] Consequently, a more detailed and targeted mechanism has been sought for the zeolite-catalysed BR. Due to the success of the industrial Sumitomo process,[8] many of these mechanistic studies focus on the catalysts (MFI-type) and the conditions of the vapour-phase BR.

Using *in situ* Fourier transform infrared (FTIR) spectroscopy, Flego and Dalloro studied the adsorption and transformation of cyclohexanone oxime over weakly acidic Silicalite-1 (MFI, Si >> Al).[29] Under ambient conditions (21 °C), the signal of the external framework silanols (3742 cm^{-1}) was rapidly diminished by interaction with cyclohexanone oxime, whereas the signals of the internal Si-OH groups (at 3730 and 3710 cm^{-1}) were only eroded gradually due to slow mass transfer into the pores. A corresponding blue-shift in the O-H stretching mode of cyclohexanone oxime (due to shortening of the O–H bond) revealed that the substrate-framework interactions (hydrogen bonding and van der Waals) occurred predominantly *via* the oxygen atom of the oxime. At room temperature, the C=N stretching mode of

cyclohexanone oxime (1668 cm^{-1}) remained largely unperturbed; only a shoulder at 1656 cm^{-1} revealed that a small fraction of the oxime molecules were weakly hydrogen bonded through nitrogen. On heating to 200 °C, the O-H stretch signals of the internal silanols were significantly diminished as the oxime diffused more readily into the MFI pores.[29] Simultaneously, a red-shift of the C=N stretching signal (to 1620 cm^{-1} ($\Delta\tilde{\upsilon}$ = -48 cm^{-1}), with shoulders at 1638 cm^{-1} ($\Delta\tilde{\upsilon}$ = -30 cm^{-1}) and 1656 cm^{-1} ($\Delta\tilde{\upsilon}$ = -12 cm^{-1}), and the development of an N-H stretching band (3391 cm^{-1}) revealed significant bonding interactions between the nitrogen atom of the oxime and the silanol sites of the catalyst. The authors proposed that bonding at the oxime nitrogen atom was favoured by both the higher temperature, and an increased interaction with the (more acidic) nest-silanols within the pores. Whilst the interaction at nitrogen was insufficient to transform cyclohexanone oxime to caprolactam, the partial positive charge on the oxime *N* atom was expected to activate the *O* atom of the OH group, and ensure that the oxime remained in proximity to the active sites of Silicalite-1. Thus, Flego and Dalloro proposed that the active sites for the Beckmann rearrangement in Silicalite-1 are the internal silanol nests, where multiple Si-OH sites can work co-operatively to activate the oxime, stabilise the reactive intermediates, and preserve a cyclic configuration during transformation to caprolactam.[29]

The efficacy of the hydrogen-bonded silanol nest was later substantiated in an *ab initio* study by Bucko *et al.*,[30] who compared the mechanism of the vapour-phase BR at a Brønsted acid site, a silanol nest, and a hydrogen-bonded terminal silanol site in mordenite (MOR). At the Brønsted acid site (Si-O(H)-Al, **Figure 3.1.3**), cyclohexanone oxime was preferentially adsorbed *via* nitrogen, forming an *N*-protonated species, stabilised by Coulomb interaction with the negatively charged framework (adsorption energy = -127 kJ mol^{-1}). Although the oxime was also found interact with the Brønsted site *via* oxygen (adsorption energy = - 49 kJ mol^{-1}), this did not facilitate protonation, only hydrogen bonding to the acid site. Thus, the BR proceeded with a 1,2-hydride shift of the *N*-protonated oxime to form the *O*-protonated oxime, with proton transfer facilitated by the framework (activation energy = +88 kJ mol^{-1}). In the subsequent *N*-insertion step (activation energy = +64 kJ mol^{-1}), loss of water and an alkyl-shift occurred simultaneously to produce a carbiminium ion, which was ultimately hydrolysed (activation energy = +40 kJ mol^{-1}) to *O*-protonated caprolactam.

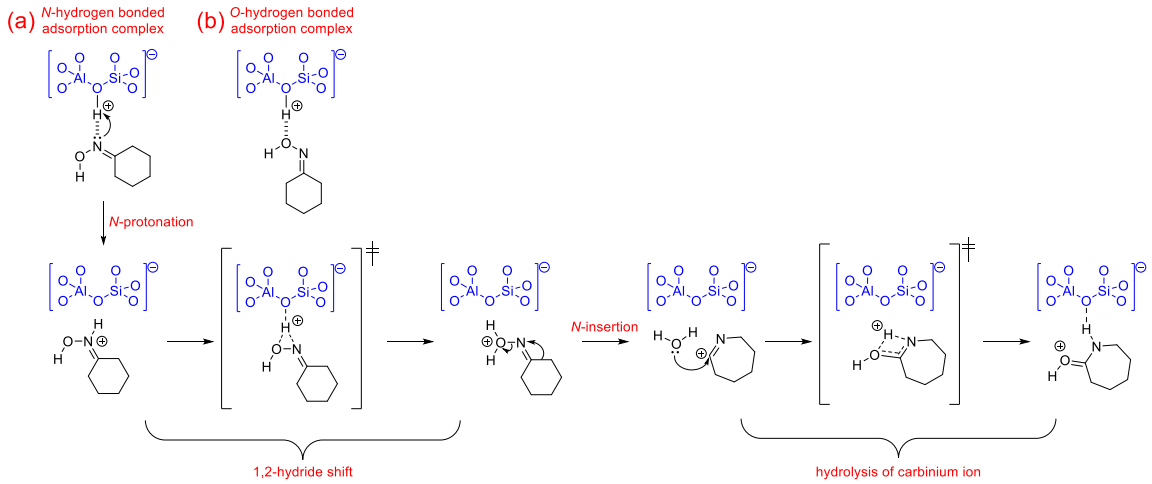

Figure 3.1.3: The mechanism of the Beckmann rearrangement at a Brønsted acid site, as determined by *ab initio* study.[30] Although cyclohexanone oxime may adsorb *via* **(a)** nitrogen or **(b)** oxygen, the BR is initiated from the *N*-protonated species. The mechanism proceeds as: *N*-protonation → 1,2-hydride shift → *N*-insertion → hydrolysis to form *O*-protonated caprolactam. The fragment of the zeolite framework containing a Brønsted acid site is depicted in blue.

As was reported for the gas-phase process,[20] the 1,2-hydride shift was calculated as the rate-limiting step of the BR at a Brønsted acid site.[30] However, the relatively high adsorption energy of caprolactam (-86 kJ mol^{-1}) indicated that product desorption would also contribute significantly to the overall rate of reaction. Indeed, a kinetic study by Komastu *et al.*,[31] reported the desorption of ε-caprolactam to be the slowest step in the BR of cyclohexanone oxime over the Brønsted sites of ZSM-5.

To model a silanol nest, Bucko *et al.* removed a T-atom from the mordenite framework and terminated the four, dangling Si-O bonds with hydrogen, so that every silanol was hydrogen-bonded to the adjacent Si-OH group (**Figure 3.1.4 a**).[30] As at the Brønsted site, a more stable adsorption complex was formed when the oxime interacted with the nest through nitrogen, rather than oxygen (adsorption energies of -56 and -21 kJ mol^{-1}, respectively). Furthermore, the formation of an *N*-hydrogen bonded complex led directly to *N*-protonated oxime (**Figure 3.1.4 b**), whereas the adsorption complex formed *via* the hydroxyl group remained neutral. Significantly, the siloxy group formed during oxime protonation was stabilised by hydrogen bonding with the adjacent silanols in the nest.

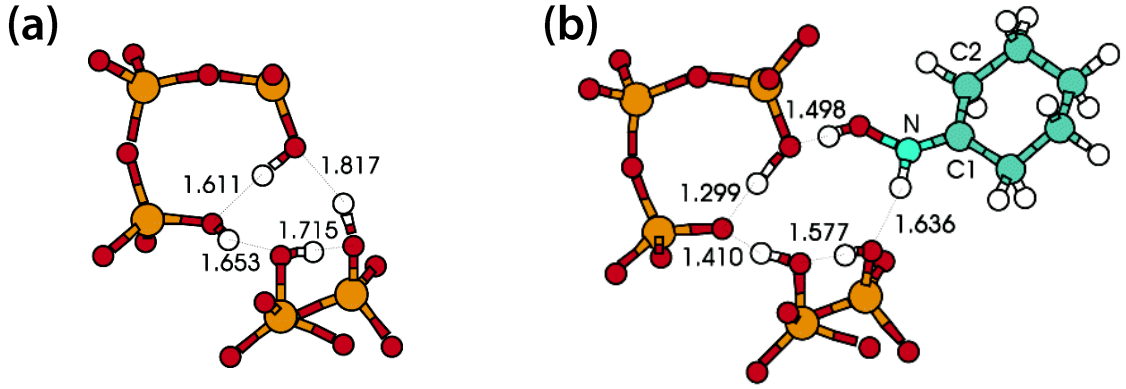

Figure 3.1.4: (a) A graphic showing the model of the silanol nest as reported by Bucko *et al.*.[30] **(b)** The model of the most stable adsorption state, *N*-protonated cyclohexanone oxime, shows the stabilisation of the framework siloxy group through hydrogen bonding interactions.[30] Key: red = oxygen; orange = silicon; white = hydrogen; green = carbon. The lengths of the hydrogen bonds (dashed lines) are reported in Å. Adapted with permission from the American Chemical Society.

Nonetheless, the neutral *O*-hydrogen bonded complex was subsequently formed by proton transfer from the *N*-protonated oxime, back to the framework (activation energy = +42 kJ mol^{-1}). *N*-insertion ensued from this neutral configuration, and the alkyl shift was accompanied by the liberation of water (**Figure 3.1.5**). Since the energetically unfavourable siloxy group was only partially stabilised by hydrogen bonding interactions, *N*-insertion was the rate-determining step of the BR (activation energy = +149 kJ mol^{-1}). Subsequently, the proton was transferred to the framework and the silanol nest was restored. In contrast with the Brønsted-site mechanism, a neutral molecule of ε-caprolactim was formed, and in the final step, intramolecular proton migration from OH to N yields ε-caprolactam (activation energy +72 kJ mol^{-1}). Since the adsorption energy of caprolactam is much lower at the silanol nest (-28 kJ mol^{-1}) than at the Brønsted site (-86 kJ mol^{-1}), product desorption was expected to proceed more readily from the nest site. The adsorption energy of cyclohexanone oxime at the weakly acidic silanol sites is much lower than the effective activation energy for the BR, which indicated that desorption of the substrate may retard the overall reaction rate. Moreover, if both Brønsted sites and silanol nests were to coexist within a zeolite, cyclohexanone oxime would adsorb preferentially to the former.

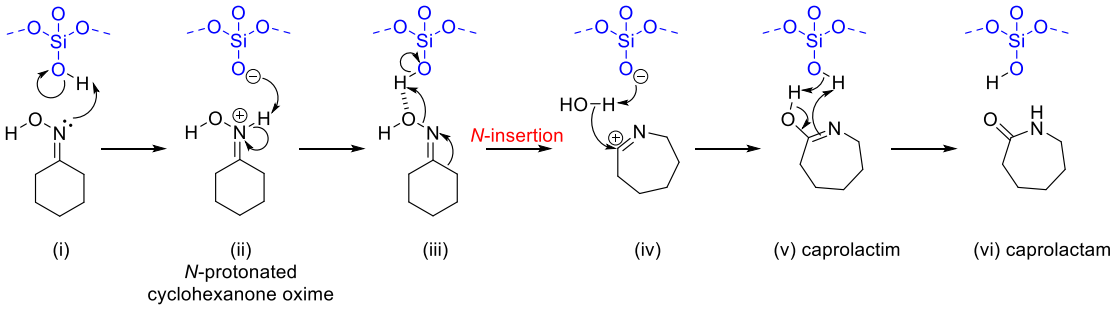

Figure 3.1.5: A mechanism of the Beckmann rearrangement at a silanol nest site, as determined by *ab initio* study.[30] *N*-protonated cyclohexanone oxime **(ii)** is the most stable adsorption complex at a silanol nest. However, the rearrangement proceeds from the *O*-hydrogen bonded configuration **(iii)**, *via N*-insertion, to form a neutral molecule of caprolactim **(v)**. In the final step, proton transfer yields caprolactam **(vi)**. For simplicity, the hydrogen-bonded network of the silanol nest has been abbreviated to the fragment depicted in blue.

Finally, the terminal silanol site was modelled as a hydrogen-bonded system at the mordenite surface. Consistent with the mechanism of the Brønsted and nest sites, reaction at the terminal silanol favoured the formation of an *N*-bonded oxime rather than an *O*-bonded species. However, as the terminal silanol was much less acidic than the Brønsted site, and lacked the stabilising, hydrogen-bonded configuration of the silanol nest, *N*-protonation of the oxime was not observed. Thus, the Beckmann rearrangement was progressed from an adsorption complex of the oxime and the terminal silanols (**Figure 3.1.6**). Two adsorption complexes were identified in which cyclohexanone oxime interacted *via* nitrogen: in one, both the oxygen and nitrogen atoms of the oxime accepted hydrogen bonds from the terminal silanol groups (adsorption energy = -76 kJ mol^{-1}). In the other, the oxime nitrogen atom accepted a hydrogen bond, whilst the OH group donated a hydrogen bond to the surface (-74 kJ mol^{-1}). A third adsorption complex was also identified, where the oxime interacted solely through its hydroxyl group to form a chain of four hydrogen bonds with the two terminal silanols (-77 kJ mol^{-1}). Due to the small difference in their adsorption energies, it was proposed that all three configurations would be equally populated. From the adsorption complex, the mechanism of the BR at a terminal silanol proceeded analogously to that at a silanol nest, except that the activation barriers were much higher due to poor stabilisation of the framework siloxy group. Thus, it was inferred that hydrogen-bonding interactions are key in stabilising the transition states of the BR at a weak acid site. Overall, Bucko *et al.* concluded that the effective activation energies for Beckmann rearrangement over mordenite increased in the order: Brønsted acid site (+142 kJ mol^{-1}: 1,2-hydride shift and *N*-insertion) < silanol

nest (+184 kJ mol^{-1}: 1,2-hydride shift and *N*-insertion) < hydrogen bonded terminal silanol (+223 kJ mol^{-1}: *N*-insertion).

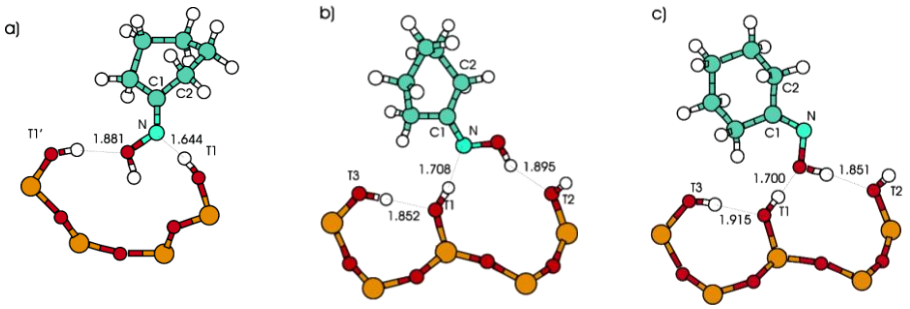

Adsorption energy: -76 kJ mol^{-1} -74 kJ mol^{-1} -77 kJ mol^{-1}

Figure 3.1.6: Models of the three adsorption complexes of cyclohexanone oxime at a surface of hydrogen-bonded terminal silanols.[30] **(a)** The nitrogen and oxygen atoms of the oxime both accept hydrogen bonds from the silanols. **(b)** The nitrogen and oxygen atoms of the oxime accept and donate a hydrogen bond, respectively. **(c)** The oxime both accepts and donates a hydrogen bond through its OH group. Key: red = oxygen; orange = silicon; white = hydrogen; green = carbon. The lengths of the hydrogen bonds (dashed lines) are reported in Å. Adapted with permission from the American Chemical Society.

The BR mechanism has also been evaluated experimentally, in particular by NMR spectroscopy. In a study by Fernández *et al.*, a combination of magic-angle spinning (MAS) NMR spectroscopy and theoretical calculations were used to study the BR of isotopically-labelled acetophenone oxime over beta-zeolites.[19] In particular, the authors contrasted the initial steps of BR at an isolated silanol site (Si-OH) *versus* a Brønsted acid site (Al-O(H)-Si). At the silanol site, theoretical calculations and experiment (^{15}N NMR) both evidenced the *N*- and *O*-hydrogen bonding interactions of acetophenone oxime, although the former was determined to be the more stable complex. Notwithstanding these hydrogen-bonding interactions, the oxime was not protonated by the silanol site at room temperature (although the rearrangement could be effected by heating to 473 K). In contrast, the exposure of acetophenone oxime to a Brønsted acid site at room temperature caused a large up-field shift of the ^{15}N NMR signal of the oxime ($\Delta\delta$ = - 113.8 ppm), consistent with *N*-protonation. Since both silanol and Brønsted acid sites were catalytically active in the BR, Fernández *et al.* concluded that the reaction pathway must vary with the strength of the acid site.[19]

Later, Marthala *et al.* used ^{15}N cross-polarisation (CP) MAS NMR spectroscopy,[32] and subsequently ^{1}H and high-speed ^{2}H MAS NMR spectroscopy,[33] to study the BR of cyclohexanone oxime over the MFI-type catalysts, Silicalite-1 and ZSM-5. By monitoring the stepwise conversion of cyclohexanone oxime to ε-caprolactam, the reaction intermediates

were characterised, and thus two mechanistic pathways were proposed, reflecting the different interactions at Brønsted and silanol sites (**Figure 3.1.7**). Whereas the BR over Silicalite-1 was found to be driven by hydrogen-bonding interactions, the MAS NMR spectra for the BR on ZSM-5 was dominated by signals of the protonated oxime and lactam.

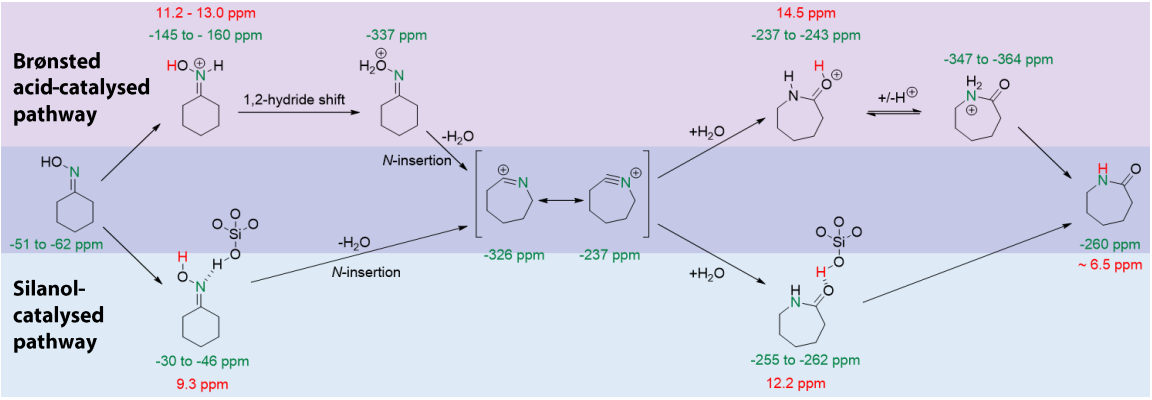

Figure 3.1.7: The mechanism of the Beckmann rearrangement determined by MAS NMR spectroscopy. Whilst the Brønsted acid-catalysed route (purple) is dominated by protonated intermediates, the silanol-catalysed pathway (blue) is driven by hydrogen-bonding interactions. Both pathways proceed *via* a nitrilium ion intermediate. The ^{15}N NMR chemical shifts of the highlighted nitrogen atom are reported in green, and the ^{1}H NMR chemical shifts of the highlighted hydrogen atom are reported in red.

There have been many theoretical[30, 34-37] and experimental[8, 18, 19, 29, 33, 38, 39] studies of the mechanism of the vapour-phase BR, and their conclusions are largely unified. Over zeolites, the BR can be catalysed by either Brønsted acid sites or weaker silanol sites. Whilst the oxime will preferentially adsorb to the stronger Brønsted sites, silanol nests are more active under vapour-phase conditions. At a Brønsted site, the BR proceeds from the *N*-protonated oxime *via* a 1,2-hydride shift (rate-determining step), *N*-insertion, and tautomerisation, ultimately producing the *O*-protonated ε-caprolactam. Due to strong retention of the protonated lactam, slow product desorption from a Brønsted site can retard reaction rate and facilitate by-product formation. At a silanol nest, the adsorption and transformation of cyclohexanone oxime is facilitated by an extensively hydrogen bonded network, which activates the substrate towards the BR and maintains intermediates in reactive conformation, close to the active site. The adsorption complexes of both oxime and lactam are relatively weakly bound at a silanol nest, and although poor retention of the oxime can reduce reaction rate, the facile desorption of product favours a high lactam selectivity.

3.1.1.2 The mechanism of the liquid-phase Beckmann rearrangement

The mechanism of the zeolite-catalysed Beckmann rearrangement has been less studied for liquid-phase conditions (130 °C) than the vapour-phase reaction. In general, the liquid-phase BR is presumed to proceed by those pathways identified for the gas-phase process,[11, 40, 41] albeit the nature of the most active catalysts differ significantly with the reaction conditions. In contrast to the vapour-phase BR,[8] it is widely reported that a zeotype catalyst requires relatively strong acid sites in order to be significantly active under the conditions of the liquid-phase BR. Several authors[10, 12, 41] have reported that the external silanols of purely siliceous zeolites are almost entirely inactive under liquid-phase conditions, and otherwise form the hydrolysis product, cyclohexanone. However, conversion and selectivity can be improved with the introduction of internal silanol defects (i.e. hydrogen-bonded silanol nests) and framework aluminium (i.e. Brønsted acid sites), which create stronger acidity. Seemingly, at the lower temperatures of the liquid-phase reaction, stronger acid sites are favoured in order to overcome the activation barrier to the BR. However, the nature of the acid site is also important: strong Lewis-acid sites (from extra-framework Al) are catalytically active under liquid-phase conditions, but promote the formation of the ketone by-product.[13, 14] Hence, moderate-strength Brønsted acid sites have been identified as the most effective active sites for the liquid-phase BR.

Zeolite pore structure can also have a significant impact on catalytic performance in the BR. In the vapour-phase, small pores may be favoured (despite the tendency to become coked) in order to restrict catalysis to the external surface of the zeolite and avoid the steric confinement of the pores (which can decrease reaction rates and encourage by-product formation).[42] However, in the liquid-phase, lower temperatures retard the diffusion of substrate to the active sites. As such, the accessibility of the internal pore surface becomes significant, as this increases the number of available active sites and hence the catalyst turnover. Accordingly, larger-pore and hierarchical (HP) zeotypes are being explored as catalysts for the liquid-phase BR.

The advantage of enhanced mass transport in the zeolite-catalysed, liquid-phase BR has been demonstrated by Botella *et al.*.[41] In their study, the performance of nanocrystalline beta-zeolite, mesoporous MCM-41, and delaminated ITQ-2 was compared for the liquid-phase BR of cyclododecanone oxime. All three catalysts gave 100 % selectivity to ω-laurolactam; however, the activity of ITQ-2 exceeded both beta-zeolite and MCM-41 by some margin (**Figure 3.1.8**). The lower activity of beta-zeolite was attributed to the diffusion constraints of the micropore, which expedites catalyst deactivation due to adsorbed species in the pores. In contrast, the delaminated structure of ITQ-2 increases the accessibility of the active sites and

reduces the diffusion path to the acid centres; hence, the oxime conversion was increased. Whilst the MCM-41 pore diameter (3.5 nm) was deemed large enough to avoid significant mass transport restrictions, its catalytic activity was curtailed by having fewer, and weaker, acid sites than the ITQ-2 zeolite.

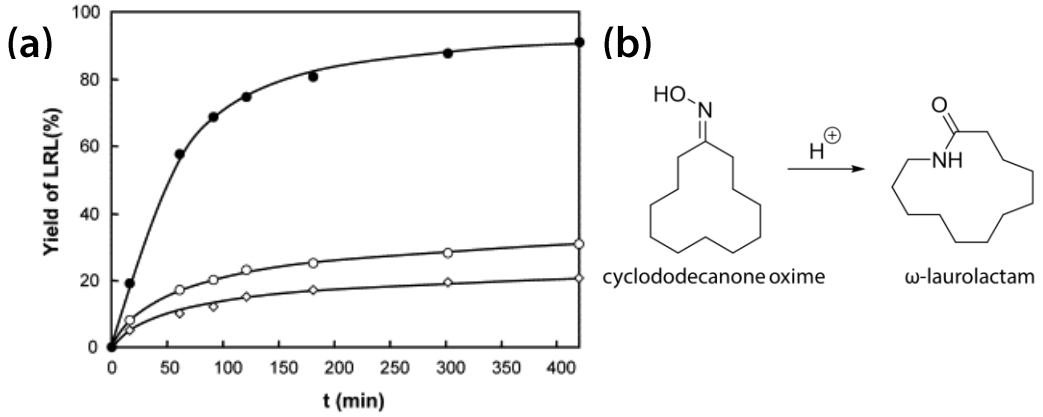

Figure 3.1.8: (a) The yield of ω-laurolactam obtained over ITQ-2 (●), MCM-41 (○), and beta-zeolite (◊) under liquid-phase conditions (130 °C, chlorobenzene solvent)[41] in **(b)** the Beckmann rearrangement of cyclododecanone oxime. Graph reproduced with the permission of Elsevier.

Recently, Linares *et al.* investigated an organosilane-templated, hierarchical beta-zeolite catalyst for the liquid-phase Beckmann rearrangement of cyclohexanone and cyclododecanone oximes.[40] With both substrates, the hierarchical zeolite achieved a higher oxime conversion than its microporous analogue, reflecting the improved mass transport of the mesoporous network. However, in the BR of cyclohexanone oxime, the Si/Al ratio of the zeolite was found to have greater influence on catalyst activity than the pore architecture, since the improved diffusion provided less benefit to the smaller substrate (kinetic diameter ~ 6 Å).[40] Nevertheless, the improved active-site accessibility in HP zeolite was evident in the BR of the cyclododecanone oxime substrate. Since cyclododecanone oxime (kinetic diameter ~ 9 Å)[40] is significantly larger than the pore diameter of the microporous BEA zeolite (5.6 – 7.7 Å),[43] the mesopore apertures in the HP zeolite provided a route for the bulky oxime to diffuse into the pores, and interact with the internal acid sites. Overall, both the conversion and reaction rate of the BR were improved with the introduction of hierarchical porosity, which the authors attributed to a combination of increased surface area, faster intracrystalline diffusion, reduced steric hindrance, and a better resistance to deactivation by pore blockage.[40]

3.1.1.3 Investigating the mechanism of the Beckmann rearrangement in organosilane-templated hierarchical SAPOs

Recently, Newland *et al.* recommended organosilane-templated hierarchical silicoaluminophosphates (HP SAPO) as highly-selective catalysts for the vapour-phase Beckmann rearrangement, with extended lifetimes on-stream.[44] These particular HP SAPO catalysts were prepared by a soft-templating approach, with an organosilane surfactant:[45] dimethyloctadecyl[3-(trimethoxysilyl)propyl]ammonium chloride (DMOD). In general, organosilanes have proven effective as mesoporogens for zeotype materials,[44-54] as the siliceous head-group of the surfactant is integrated within the crystallising microporous phase. Yet, as a result, the removal of the template leaves the internal surfaces of the mesopores terminated with a high concentration of silanol groups (Si-OH).[44, 49, 55] In their investigations, Newland *et al.*, found that the weakly-acidic silanols in HP SAPOs moderated the acidity of the bulk Brønsted acid sites (from the isomorphous substitution of Si into the aluminophosphate framework).[44] The authors proposed that both the silanols and the Brønsted sites were catalytically active in the vapour-phase BR, but that the presence of weakly acidic silanol sites favoured rapid desorption of the lactam, reducing consecutive reactions and coking.

Thus, the organosilane, soft-templating methodology creates HP SAPOs with a combination of active sites (silanols and Brønsted acid sites) and pore architectures (mesopores and micropores) (**Figure 3.1.9**). However, the influence of secondary mesoporosity in the BR has not been explored in detail; in particular, whether the mesopores play an active catalytic role, or simply improve mass transport to/from the Brønsted sites in the bulk.[56] Evidence of catalysis within the mesopores could have implications for the mechanism of the Beckmann rearrangement in HP SAPOs, since the reaction pathway is known to differ between silanols and Brønsted acid sites.[30, 39] Thus, information about the transformation of cyclohexanone oxime in HP SAPOs may provide a rationale of their activity the BR, and aid in the optimisation of acid strength for liquid- and vapour-phase reaction conditions.

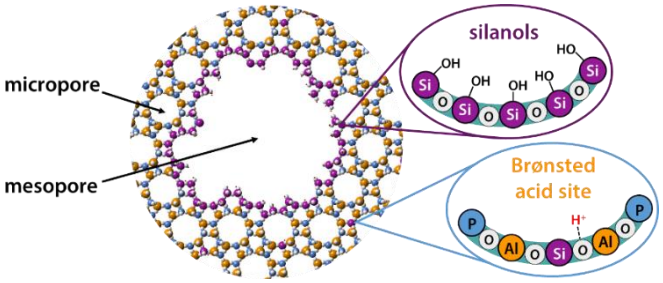

Figure 3.1.9: A depiction of the types of acid site and pore structures in organosilane-templated HP SAPOs. The walls of the mesopores present a high density of weakly acidic silanols, whilst the more acidic Brønsted sites are located within the smaller micropores.

3.2 Aims

Soft-templating with organosilane surfactant is an established protocol for the synthesis of hierarchically-porous silicoaluminophosphates (HP SAPOs) with improved mass transport properties. However, the nature of the siliceous mesoporogen is such that the HP SAPO is produced with a high density of weakly acidic silanols in the mesopores, in addition to the Brønsted sites in the micropores. Significantly, organosilane-templated HP SAPOs have shown enhanced activity in the acid-catalysed, vapour-phase Beckmann rearrangement (BR) *versus* their microporous analogues.[44] Whilst both silanol and Brønsted sites have the potential to catalyse the BR, the mode and degree to which they might facilitate this process is unknown. To this end, an integrated theoretical and empirical study was undertaken to establish whether the mesopores play an active role in catalysing the BR, or simply facilitate transport to the Brønsted acid sites in the micropores.

For these investigations, the interactions between cyclohexanone oxime and HP SAPO-34 were contrasted with those in microporous SAPO-34. Whilst both HP and microporous SAPO-34 have proven activity in the vapour-phase BR (> 300 °C),[44] the lower temperatures required for these fundamental studies were expected to accentuate the steric constraints of the CHA windows (3.8 Å). As such, structure-activity relationships were described in the context of the liquid-phase BR (130 °C), under which conditions the influence of pore dimensions on catalyst activity would also be emphasised. To deconvolute the catalytic contribution of the siliceous mesopore from its mass transport effects, the interaction between cyclohexanone oxime and HP AlPO-5 was also studied. Like HP SAPO-34, HP AlPO-5 possesses silanols from surfactant soft-templating, however the AlPO lacks the Brønsted sites developed by isomorphous substitution of Si into the framework. Importantly, the micropore apertures of AlPO-5 (7.3 Å) do not present the same size-constraints that inhibit the uptake of oxime into SAPO-34. Hence, any catalytic activity or substrate interactions in HP AlPO-5 can be attributed to the activity of the silanols, rather than the mass transport effects of the mesopores.

A variety of characterisation tools were employed in this study. First, the structural, textural, and acid characteristics of the frameworks were established using, XRD, gas adsorption, and NH_3-TPD, respectively. Then, a range of *in situ* techniques, with complementary computational studies, were used to probe the interactions between catalyst and substrate. In particular, inelastic neutron scattering (INS) was exploited for its particular suitability for studying hydrogenous species adsorbed within a zeolite matrix.[57-59] Recently, a detailed vibrational characterisation of the molecular species relevant to the BR was undertaken using

INS, Raman, and FTIR spectroscopies.[60] Building on these fundamental studies, INS is herein presented as a tool to probe molecular-level, substrate-framework interactions, with a view to obtain new insights into the mechanism of the BR in organosilane-templated HP SAPO catalysts.

3.3 Experimental

3.3.1 Catalyst synthesis

3.3.1.1 HP AlPO-5

Phosphoric acid (85 wt. % in H_2O, 18.2 mL, Sigma Aldrich) and deionised water (80 mL) were added to a Teflon beaker and stirred. Aluminium isopropoxide (54.5 g, Sigma Aldrich) was ground in a pestle and mortar before being added gradually to the reaction mixture. The gel was stirred for 1.5 hours. Dimethyloctadecyl[(3-(trimethoxysilyl)propyl] ammonium chloride ('DMOD', 72 wt. % in H_2O, 9.6 mL, Sigma Aldrich) was added dropwise to the gel, followed by triethylamine (29.8 mL, Sigma Aldrich), also dropwise. Finally, deionised water (160 mL) was added to the gel, which was stirred for 1 hour. The gel was transferred to a Teflon-lined, stainless steel reactor and crystallised at 200 °C for 24 hours. The reactor was allowed to cool to ambient temperature before its contents were removed and distributed between four 100 mL centrifuge tubes. The solid in each tube was washed 3 times with deionised water at 10,000 rpm and then dried overnight in an oven at 80 °C. The solid (~ 32 g) was calcined in batches (~ 2 g) by heating at 550 °C (ramp rate of 2 °C min^{-1}) under a flow of air for 16 hours.

Table 3.3.1: The synthesis gel ratio and the empirical elemental composition of the calcined HP AlPO-5 catalyst.

Catalyst	Gel Composition	ICP-OES elemental analysis
HP AlPO-5	1 Al: 1 P: 0.8 SDA: 0.05 DMOD: 50 H_2O	19.3 wt. % Al; 19.3 wt. % P; 1.3 wt. % Si

3.3.1.2 HP SAPO-34 and SAPO-34

The synthesis of HP SAPO-34 and SAPO-34 followed the same procedure, except that the latter did not include the addition of dimethyloctadecyl[(3-(trimethoxysilyl)propyl] ammonium chloride.

Aluminium isopropoxide (45.4 g, Sigma Aldrich) was ground in a pestle and mortar before being slowly added to a Teflon beaker containing tetraethylammonium hydroxide (35 wt. % in water, 91 mL, Sigma Aldrich), under stirring. After 1 hour, fumed silica (2.0 g, Sigma Aldrich) was added to the gel, followed by dimethyloctadecyl[(3-(trimethoxysilyl)propyl] ammonium chloride (72 wt. % in H_2O, 8 mL, Sigma Aldrich) which was stirred for a further 1

hour. Deionised water (140 mL) and phosphoric acid (85 wt. % in H_2O, 15 mL, Sigma Aldrich) were added sequentially, in a dropwise manner and the gel stirred for 2 hours. The gel was transferred to a Teflon-lined, stainless steel reactor and crystallised at 200 °C for 48 hours. The reactor was allowed to cool to ambient temperature before its contents were removed and distributed between four 100 mL centrifuge tubes. The solid in each tube was washed 3 times with deionised water at 10,000 rpm and then dried overnight in an oven at 80 °C. The solid (~ 32 g) was calcined in batches (2 g) by heating at 550 °C (ramp rate of 2 °C min^{-1}) under a flow of air for 16 hours.

Table 3.3.2: The synthesis gel ratio and empirical elemental composition of the calcined SAPO-34 and HP SAPO-34 catalysts.

Catalyst	Gel Composition	ICP-OES elemental analysis
SAPO-34	1 Al: 1 P: 0.15 Si : 1 SDA: 65 H_2O	18.8 wt. % Al; 14.8 wt. % P; 2.6 wt. % Si
HP SAPO-34	1 Al: 1 P: 0.15 Si : 1 SDA: 0.05 DMOD: 65 H_2O	21.6 wt. % Al; 11.3 wt. % P; 4.5 wt. % Si

3.3.2 Characterisation techniques

Powder X-ray diffraction patterns were acquired using a Bruker D2 diffractometer with Cu $K_{\alpha 1}$ radiation. Unit cell refinements were performed using the CelRef software.[61] Low-angle X-ray diffraction patterns were obtained using a Rigaku SmartLab diffractometer with Cu rotating anode source.

Nitrogen adsorption measurements were performed at 77K using the Micromeritics Gemini 2375 Surface Area Analyser. Samples were degassed, under vacuum, at 120 °C for 12 hours prior to measurement.

For ICP-OES elemental analysis, samples were subject to HNO_3/H_2O_2 digestion before analysis in the Varian Vista MPX CCD Simultaneous Axial ICP-OES.

NH_3-TPD measurements were performed using the Quantachrome Autosorb iQ-Chemi apparatus. Catalysts were pre-treated at 150 °C under a flow of helium gas for 2 hours. The samples were then dosed with ammonia gas for three hours at 100 °C, before desorption under a flow of helium gas, with a temperature ramp of 10 °C min^{-1} up to 600 °C.

Carbon, hydrogen, and nitrogen (CHN) elemental analysis was performed using the Thermo Carlo Erba Flash 2000 Elemental Analyser.

3.3.2.1 Inelastic neutron scattering studies

INS measurements were carried out using the high-resolution INS spectrometer TOSCA[62] at the ISIS Pulsed Neutron and Muon Source (Oxfordshire, UK).[63] Calcined catalysts were dried in an Inconel can at 350 °C, under a flow of helium gas. A mass spectrometer sampling the exhaust line was used to monitor the dehydration process in real time. The microporous SAPO-34 was dry after 2-3 hours, whilst the hierarchical catalysts required 8 - 12 hours under the same conditions. The sealed cans were transferred to a glove box under argon atmosphere. Cyclohexanone-d_{10} oxime : catalyst mixtures were prepared as a 1:10 solid-state mixture by mixing and mechanical grinding. The empty frameworks, catalyst-oxime mixtures, and reference compounds (cyclohexanone-d_{10} oxime (prepared in-house) and ε-caprolactam-d_{10} (QMX Laboratories Ltd.)) were each transferred to an aluminium foil sachet and sealed in a flat aluminium can. The sealed catalyst-oxime samples were heated in a fan-assisted oven at 50 °C for 2 hours for thermal mixing. The cans were placed in a top-loading closed cycle refrigerator cryostat and spectra collected at < 10 K to supress the Debye-Waller factor (line broadening due to thermal motion). Spectra were assigned using Jmol software[64] to visualise vibrational modes that were calculated using density-functional perturbation-theory-based[65] CASTEP calculations.[66]

3.3.2.1.1 Synthesis of cyclohexanone-d_{10} oxime for INS studies

In an ice bath, a 1:1 molar ratio of cyclohexanone-d_{10} (Sigma Aldrich) and hydroxylamine (50 wt. % in H_2O, Sigma Aldrich) were reacted under stirring. After 1 hour, the white solid was collected, washed with ice-cold water (200 mL), and then dried under vacuum.

3.3.2.2 MAS NMR

The calcined catalyst was packed in a 2.5 mm zirconium oxide rotor before drying overnight in a fan-assisted oven at 100 °C. Whilst still hot, the rotors were sealed by capping with a turbine. To prepare the catalyst-substrate samples, the dried catalysts, still sealed within the NMR rotors, were transferred to a glove box to be mixed with cyclohexanone oxime (Sigma

Aldrich) in a 10:1 ratio. Sealed rotors containing the catalyst-oxime mixtures were studied before and after heating to 50 °C to study the effect of the thermal mixing. MAS NMR spectra were acquired on a Bruker Avance-II spectrometer operating at 14.1 T, equipped with a Bruker 2.5 mm triple resonance MAS probe and tuned to ^{1}H (resonance frequency 600 MHz). The ^{1}H spectra were referenced against adamantane at 1.8 ppm.[67] Nitrogen boil-off gas was used for bearing and drive gases for magic-angle spinning (MAS).

3.3.2.3 Probe-based FTIR studies

FTIR spectra of self-supporting pellets were collected under vacuum (residual pressure < 10^{-5} mbar) using a Bruker Equinox 55 spectrometer equipped with a pyroelectric detector (DTGS type) with 4 cm^{-1} resolution. Calcined catalysts were ground in a pestle and mortar before pelletisation using a hydraulic press. The pellets were weighed and their surface area measured to ensure a density of 2 – 10 mg cm^{-2}. The pellet (~ 1 cm^{2}) was supported in a gold frame with a window to permit the transmission of IR radiation through the sample. The sample was then transferred to a specially designed quartz cell with potassium bromide window that was permanently connected to a vacuum line. The catalyst was pre-treated by heating to 300 °C under vacuum (ramp rate 5 °C min^{-1}). Once cooled to ambient temperature, the sample was isolated from the vacuum and an FTIR spectrum acquired. The catalyst was then exposed to a vapour pressure of cyclohexanone oxime for 10 minutes and another FTIR spectrum acquired. Finally, the oxime-dosed catalyst was heated to 130 °C (ramp rate 2 °C min^{-1}) for 30 minutes, cooled, and an IR spectrum acquired. FTIR spectra were normalised with respect to pellet weight and, whenever stated, difference-spectra show the subtraction of the pre-treated catalyst from the spectrum after oxime adsorption.

3.3.3 Computational studies

Density functional theory calculations were performed using the program DMol3.[68] All calculations were performed using double numerical plus polarisation basis sets with geometry optimisations carried out by treating the exchange-correlation interaction with the generalised gradient approximation using the Becke-Lee-Yang-Parr exchange-correlation functional.[69] Dispersion correction was applied using the method of Tkatchenko and Scheffler (TS).[70] Clusters of MCM-41 (447 atoms) and SAPO-34 (260 atoms) were generated from previously published structures[71, 72] and terminated with H atoms. Three convergence tolerances were set for the geometry optimisations, these were: energy change ≤ 2 x10^{-5} Ha, maximum force ≤ 0.004 Ha $Å^{-1}$, and maximum displacement ≤ 0.005 Å.

3.3.4 Catalysis: the liquid-phase Beckmann rearrangement

A portion of calcined catalyst was degassed by heating overnight at 120 °C, under vacuum. A 3-neck round bottom flask was charged with a stirrer bar, cyclohexanone oxime (0.1 g, Sigma Aldrich), anhydrous chlorobenzene (internal standard, 0.1 g, Sigma Aldrich), dried catalyst (0.1 g), and anhydrous benzonitrile (20 mL, Sigma Aldrich). The reaction vessel was sealed with a rubber septum, glass stopper, and reflux condenser. The reaction was transferred to a pre-heated oil bath at 130 °C and stirred under a constant nitrogen atmosphere. Aliquots of the reaction mixture were extracted hourly over a 6 hour reaction period, and analysed by gas chromatography using the Clarus 480 apparatus with flame ionisation detector and an Elite 5 column. Products were identified using authenticated standards, and quantified against the internal standard, chlorobenzene.

3.4 Results and discussion

3.4.1 Characterisation and catalytic testing

Soft-templating with siliceous surfactant is an established protocol for the synthesis of hierarchically-porous aluminophosphates (HP AlPOs) with improved mass transport properties.[44, 51, 53] Nonetheless, fundamental characterisation was undertaken in order to ascertain the structural and acidic properties of the calcined frameworks. First, the crystalline structure of the calcined HP AlPO-5 (AFI), SAPO-34 (CHA), and HP SAPO-34 (CHA) catalysts was examined by XRD (**Figure 3.4.1**).

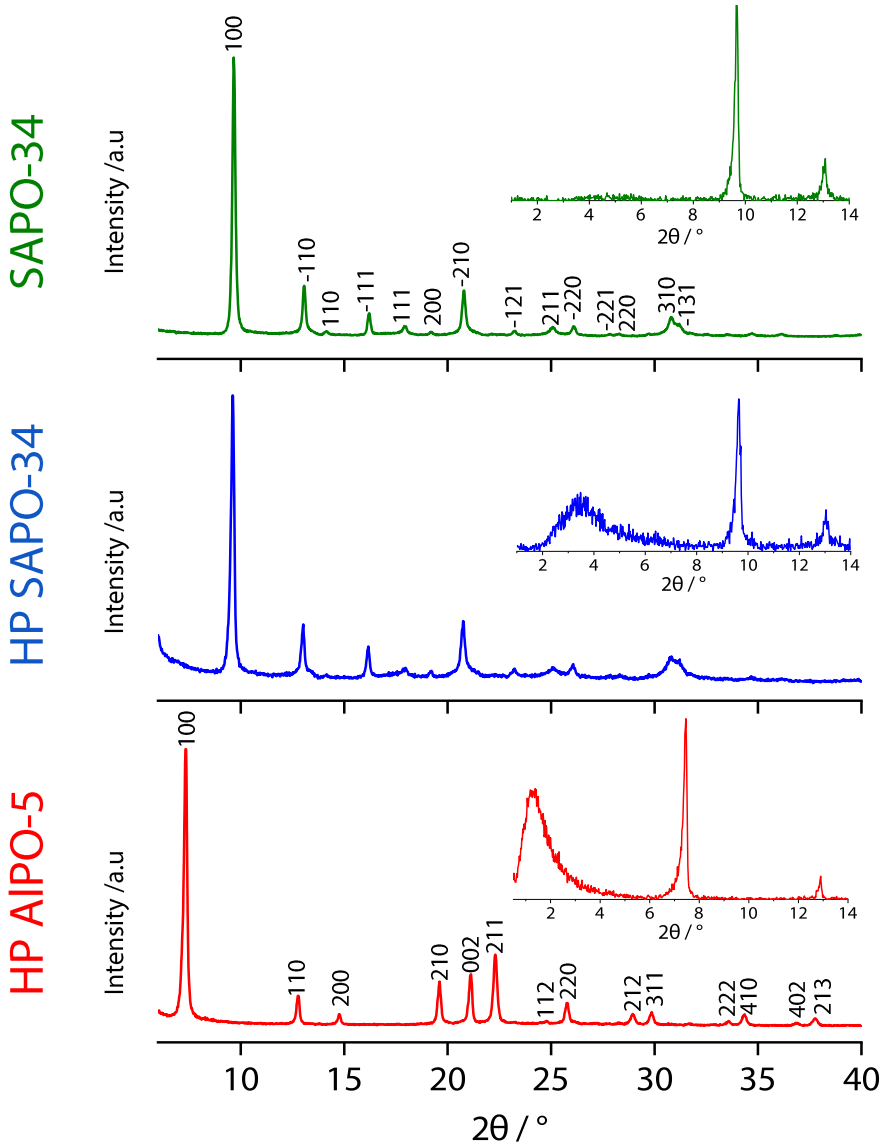

Figure 3.4.1: The indexed powder XRD patterns of SAPO-34 (top, green), HP SAPO-34 (middle, blue) and HP AlPO-5 (bottom, red) confirmed that the catalysts were phase pure. The respective low-angle XRD spectra (inset) revealed a low-angle peak in the HP catalysts, indicative of mesopores.

By comparing each experimental powder pattern with the theoretical spectrum for that framework-type,[43] the catalysts were confirmed to be phase-pure. When the XRD data for SAPO-34, HP SAPO-34, AlPO-5 and HP AlPO-5 were subject to structural refinement in the appropriate space group (**Table 3.4.1**, **Table 3.4.2**, **Table 3.4.3** and **Table 3.4.4**, respectively),[43] the soft-templating protocol was found to have a negligible effect on the unit cell parameters of the hierarchical frameworks (**Table 3.4.5**).

Table 3.4.1: Unit cell refinements for SAPO-34.

λ /Å	*a* / Å	*b* / Å	*c* / Å	α / °	β / °	γ / °	Volume / Å³
1.5406	13.6199	13.6199	14.846	90	90	120	2385
0	0.0375	0	0.0075	0	0	0	
h	***k***	***l***	**2θ(Obs) / °**	**2θ-Zero / °**	**2θ(Cal) / °**	**Dif. / °**	
1	0	1	9.661	9.661	9.5691	0.0919	
1	1	0	13.064	13.064	12.9897	0.0743	
0	1	2	14.179	14.179	14.0856	0.0934	
0	2	1	16.204	16.204	16.1583	0.0457	
0	0	3	17.906	17.906	17.9099	-0.0039	
2	0	2	19.202	19.202	19.2057	-0.0037	
2	1	1	20.803	20.803	20.7869	0.0161	
1	2	2	23.254	23.254	23.2554	-0.0014	
1	0	4	25.077	25.077	25.1334	-0.0564	
2	2	0	26.07	26.07	26.1502	-0.0802	

Table 3.4.2: Unit cell refinements for HP SAPO-34.

λ /Å	*a* / Å	*b* / Å	*c* / Å	α / °	β / °	γ / °	Volume / Å³
1.5406	13.6429	13.6429	14.8482	90	90	120	2393.4
0	0.0165	0	0.0056	0	0	0	
h	***k***	***l***	**2θ(Obs) / °**	**2θ-Zero / °**	**2θ(Cal) / °**	**Dif. / °**	
1	0	1	9.6	9.6	9.5586	0.0414	
1	1	0	13.024	13.024	12.9677	0.0563	
0	2	1	16.164	16.164	16.1343	0.0297	
0	0	3	17.967	17.967	17.9073	0.0597	
2	0	2	19.223	19.223	19.1846	0.0384	
2	1	1	20.742	20.742	20.7541	-0.0121	
1	2	2	23.234	23.234	23.2253	0.0087	
1	0	4	25.057	25.057	25.1261	-0.0691	
2	2	0	26.07	26.07	26.1053	-0.0353	
4	0	1	30.83	30.83	30.8403	-0.0103	

Table 3.4.3: Unit cell refinements for microporous AlPO-5.

λ /Å	*a* / Å	*b* / Å	*c* / Å	α / °	β / °	γ / °	Volume / Å³
1.5406	13.8038	13.8038	8.3948	90	90	120	1385.3
0	0.0164	0	0.0027	0	0	0	
h	***k***	***l***	**2θ(Obs) / °**	**2θ-Zero / °**	**2θ(Cal) / °**	**Dif. / °**	
0	1	0	7.33	7.33	7.389	-0.059	
1	1	0	12.82	12.82	12.816	0.004	
0	2	0	14.79	14.79	14.8089	-0.0189	
1	2	0	19.63	19.63	19.6318	-0.0018	
0	0	2	21.15	21.15	21.1495	0.0005	
1	2	1	22.34	22.34	22.3269	0.0131	
1	1	2	24.83	24.83	24.8065	0.0235	
2	2	0	25.8	25.8	25.7958	0.0042	
1	2	2	28.99	28.99	29.0126	-0.0226	
0	4	0	29.85	29.85	29.8727	-0.0227	

Table 3.4.4: Unit cell refinements for HP AlPO-5.

λ /Å	*a* / Å	*b* / Å	*c* / Å	α / °	β / °	γ / °	Volume / Å³
1.5406	13.8135	13.8135	8.4036	90	90	120	1388.7
0	0.0172	0	0.003	0	0	0	
h	***k***	***l***	**2θ(Obs) / °**	**2θ-Zero / °**	**2θ(Cal) / °**	**Dif. / °**	
0	1	0	7.332	7.332	7.3838	-0.0518	
1	1	0	12.781	12.781	12.8069	-0.0259	
0	2	0	14.746	14.746	14.7985	-0.0525	
1	2	0	19.608	19.608	19.6179	-0.0099	
0	0	2	21.127	21.127	21.1272	-0.0002	
1	2	1	22.302	22.302	22.3093	-0.0073	
1	1	2	24.793	24.793	24.7826	0.0104	
2	2	0	25.786	25.786	25.7774	0.0086	
1	3	1	28.946	28.946	28.9084	0.0376	
0	4	0	29.858	29.858	29.8512	0.0068	

Table 3.4.5: The optimised unit cell parameters for SAPO-34, HP SAPO-34, AlPO-5, and HP AlPO-5 catalysts.

Catalyst	Lattice Parameters				Space Group	Unit Cell Volume / Å³
	***a* = *b* / Å**	***c* / Å**	**α = β / °**	**ϒ / °**		
SAPO-34	13.62	14.85	90	120	R-3m	2385
HP SAPO-34	13.64	14.85	90	120	R-3m	2393
AlPO-5	13.80	8.39	90	120	P6cc	1385
HP AlPO-5	13.81	8.40	90	120	P6cc	1389

In addition, a low-angle XRD spectrum was recorded for all catalysts (**Figure 3.4.1**, inset). Due to the inverse relationship between lattice *d*-spacing and 2θ, low-angle XRD reveals larger structures, such as mesoporous networks, provided they exhibit some long-range order. Significantly, both HP SAPO-34 and HP AlPO-5 possessed a broad, low-angle peak (2$\theta \approx$ 3.5 ° and 2$\theta \approx$ 1.5 °, respectively), indicative of mesopores,[44, 45, 73] whereas the low-angle XRD spectrum of SAPO-34 was featureless in the same region.

To assess the textual properties of the calcined catalysts, nitrogen adsorption-desorption measurements were performed. As presented in **Figure 3.4.2**, SAPO-34 exhibited a Type I isotherm, which is typical for a microporous material.[74] In contrast, both hierarchical systems produced a Type IV isotherm with Type H4 hysteresis, which is consistent with the presence of narrow mesopores.[74] Further analysis of the N_2 sorption data indicated that both HP SAPO-34 and HP AlPO-5 contained small mesopores of ~ 3 nm diameter (which is typical for this surfactant template)[45] and returned a quantifiable mesopore volume for both HP systems (**Figure 3.4.2 d** and **Table 3.4.6**). Evidence that the HP catalysts have a larger BET surface area[44] and external (i.e. non-microporous) surface area[75] than their microporous counterparts provided further evidence that mesopore-templating was successful.

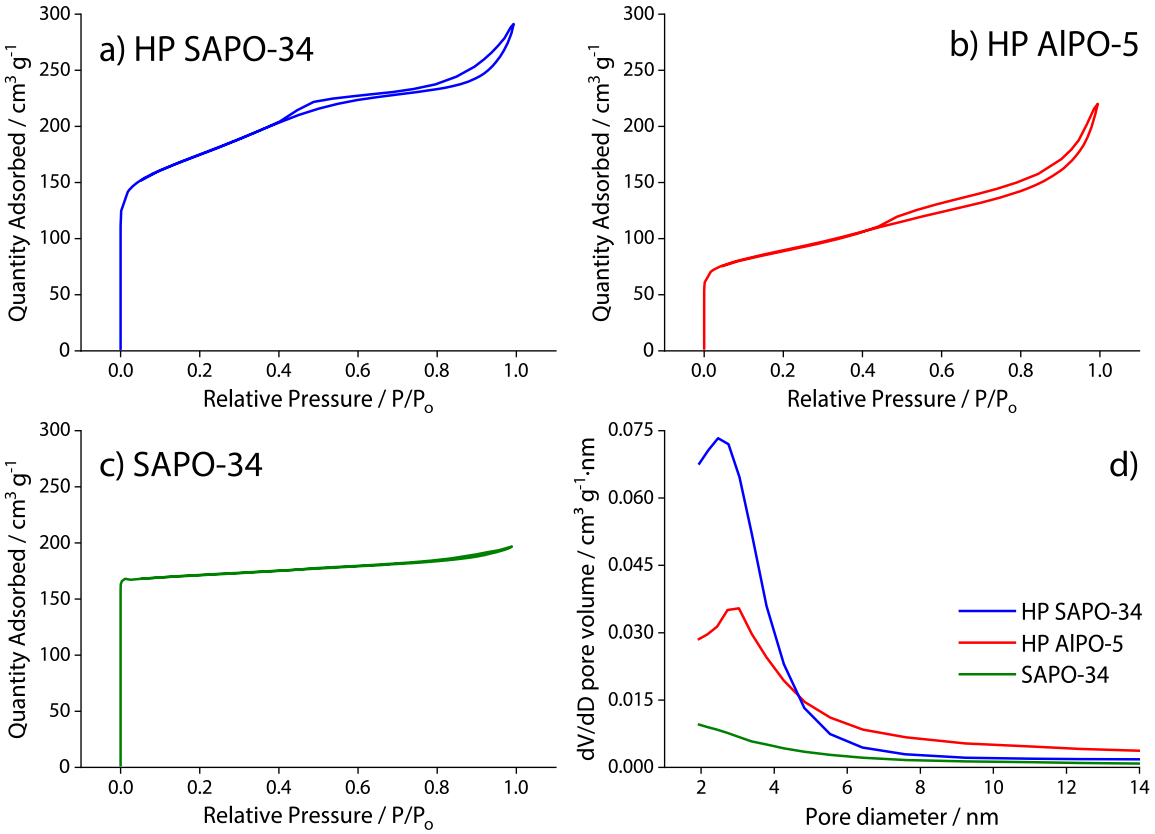

Figure 3.4.2: The N_2 gas adsorption-desorption isotherms of **(a)** SAPO-34 (Type I = micropores), **(b)** HP SAPO-34 (Type IV = mesopores) and **(c)** HP AlPO-5 (Type IV = mesopores), and **(d)** their respective BJH adsorption pore-size distribution.

Table 3.4.6: The textural properties of SAPO-34, HP SAPO-34, and HP AlPO-5 catalysts determined from N_2 adsorption-desorption studies.

Catalyst	BET surface area / $m^2\ g^{-1}$	Micropore volume / $cm^3\ g^{-1}$	Mesopore volume / $cm^3\ g^{-1}$	External surface area / $m^2\ g^{-1}$	BJH mesopore diameter / Å
SAPO-34	548	0.24	-	49	-
HP SAPO-34	589	0.13	0.14	319	26
AlPO-5	189	0.09	-	25	-
HP AlPO-5	323	0.06	0.20	180	30

To probe the acidity of the frameworks, the calcined samples were examined by temperature-programmed adsorption of ammonia (NH_3-TPD), a technique that provides information about the quantity and strength of the acid sites. Broadly, ammonia that is physisorbed or chemisorbed to weak acid sites, is removed below 250 °C.[76-78] At temperatures between 250 – 350 °C, ammonia that is bound to moderately-acidic sites will be lost,[79, 80] whilst temperatures > 350 °C are required to remove ammonia bound to strong acid sites (i.e. NH_4^+) .[78, 81, 82] The fitted spectra are reported in **Figure 3.4.3**.

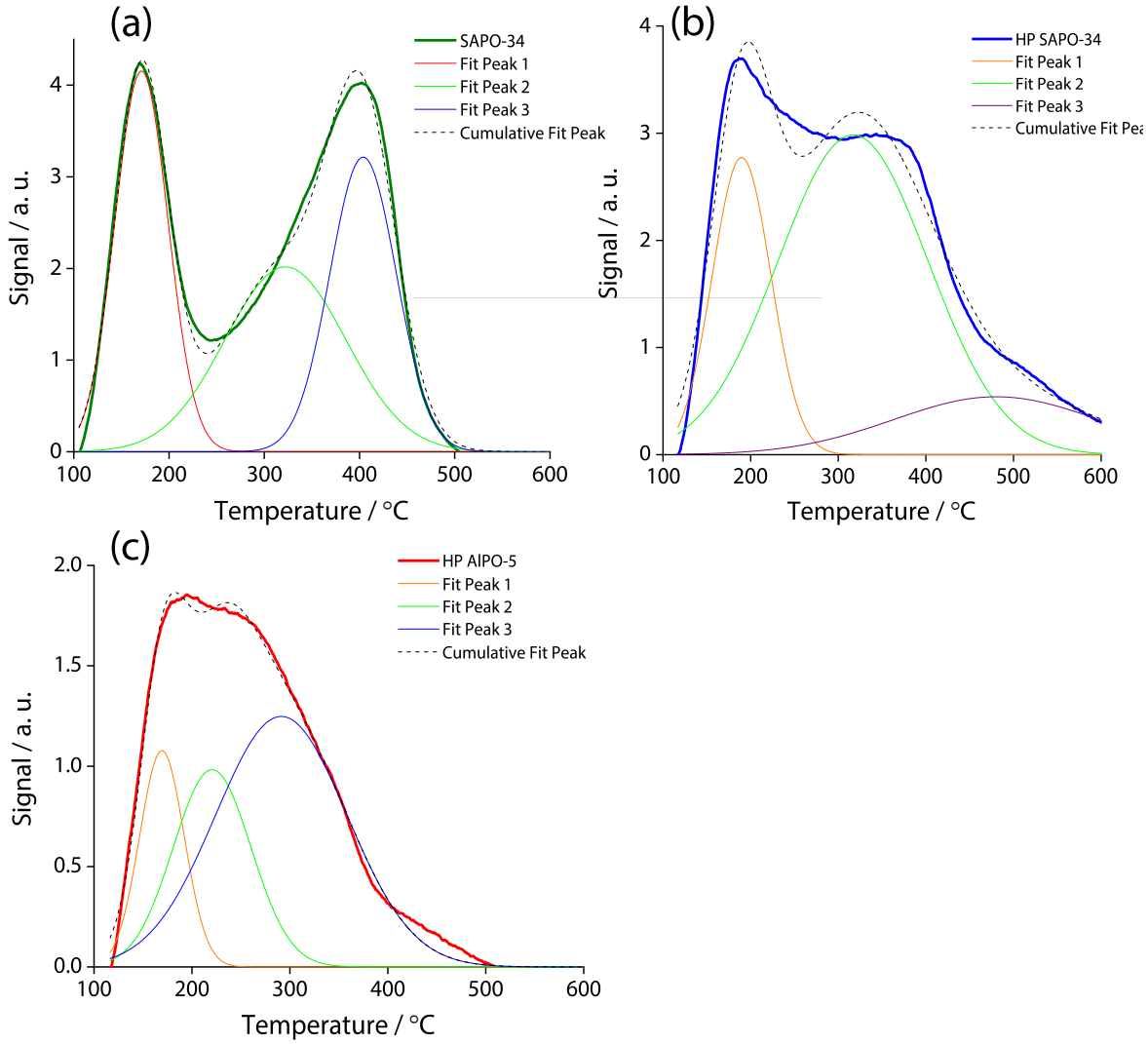

Figure 3.4.3: The peak fit for the NH_3-TPD data of **(a)** SAPO-34, **(b)** HP SAPO-34, and **(c)** HP AlPO-5. Spectra acquired at a ramp rate of 10 °C min^{-1}, after dosing with NH_3 gas at 100 °C for 3 hours.

From first inspection, the structure of the ammonia desorption profiles for SAPO-34,[53, 83] and the surfactant-templated HP AlPO-5[51] and HP SAPO-34,[53] (**Figure 3.4.4**) were in agreement with the literature. For SAPO-34, the thermodesorption of ammonia occurred in two distinct steps. The first desorption, centred around 170 °C, corresponded to the loss of ammonia that

was physisorbed within the SAPO pores, or bound to weakly acidic Brønsted sites and defects (e.g. P-OH, Al-OH).[84, 85] The second peak, centred at 400 °C, was associated with the desorption of ammonia from stronger Brønsted sites (of the type Si-O(H)-Al) created by the isomorphous substitution of silicon into the framework. The asymmetry of the higher temperature band also correlated with the desorption of ammonia from the distinct O(2) and O(4) bridging-hydroxyl proton sites in SAPO-34.[84, 86]

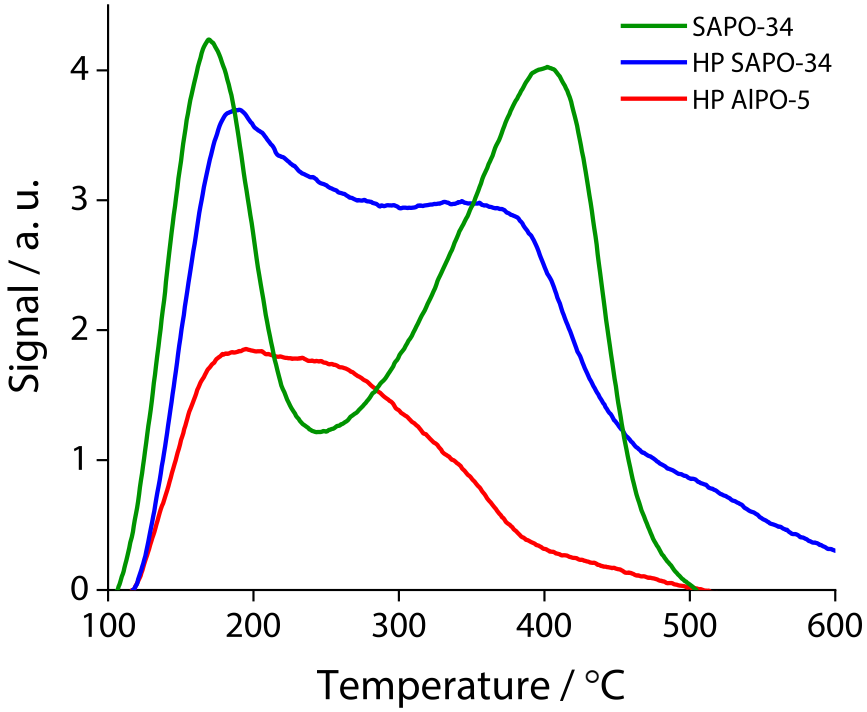

Figure 3.4.4: The NH_3-TPD profiles of SAPO-34 (green), HP SAPO-34 (blue) and HP AlPO-5 (red) acquired at a ramp rate of 10 °C min^{-1}, after dosing with NH_3 gas at 100 °C for 3 hours. Spectra not mass normalised.

Although HP AlPO-5 lacks the Brønsted acid sites from isomorphous substitution of Si, NH_3-TPD revealed significant acidity from the siliceous mesopores (with a small contribution from defect sites).[51] The TPD profile of HP AlPO-5 was a single, broad peak, although it was apparent that this was a convolution of several desorption processes. Such behaviour is consistent with the soft-templating protocol, which creates amorphous, Si-rich, mesopore-walls containing a range of hydroxyl sites.[46, 87] Since the majority of the TPD signal was observed between 190 – 300 °C, it was inferred that most of the silanols are of weak-to-moderate-acidity. However, as the TPD profile remained significantly elevated in excess of 350 °C, there was indication that local defects and aluminosilicate regions in the amorphous mesopore walls also created some strong acid sites.[51, 88]

Like SAPO-34, the TPD profile of HP SAPO-34 exhibited two predominant desorptions. However, the first of these peaks, which corresponds to the loss of weakly bound ammonia, was observed ~20 °C higher in HP SAPO-34 than SAPO-34. In fact, the lower-temperature desorption occurred at a similar temperature for both hierarchical catalysts, and was thus attributed to the interaction between ammonia and weakly-acidic silanols in the mesopores.[78] The availability of weak-interaction sites in the mesopores may also have been responsible for the delayed onset of ammonia desorption observed for the two HP frameworks. The influence of the mesopore network on the acidity of HP SAPO-34 was also apparent in the 200 – 350 °C range, where the desorption of ammonia from medium-strength silanol sites produced considerably more signal than observed for SAPO-34. In the high-temperature regime (> 350 °C), the second desorption peak of HP SAPO-34 occurred ~ 40 °C lower than the corresponding feature in the NH_3-TPD profile of SAPO-34. This phenomenon is well known[51, 53, 80, 89] and demonstrates how soft-templating with organosilane can moderate the acidity of the framework. Nonetheless, HP SAPO-34 was the only system in which ammonia desorption was incomplete by 500 °C. Thus, HP SAPO-34 also contained a number of very strong acid sites, which may be due to local distortions near to a Brønsted site, caused by proximity to a mesopore.

The total amount of ammonia desorbed from each catalyst was determined from the area under each NH_3-TPD curve (**Table 3.4.7**). For SAPO-34, the total amount of desorbed ammonia was 1.23 mmol NH_3 per gram of catalyst, which is in good agreement with the literature.[84, 85] By comparison, the total amount of ammonia desorbed from HP AlPO-5 was only 0.85 mmol g^{-1}. This is attributed to two factors: firstly, HP AlPO-5 presents a smaller surface area than SAPO-34 for the physisorption of ammonia (**Table 3.4.6**). Secondly, the total quantity of Si in HP AlPO-5 (1. 3 wt. %, **Table 3.3.1**) is less than in SAPO-34 (2.6 wt. %, **Table 3.3.2**), so the number of acidic adsorption sites is also fewer.[78] Hence, HP SAPO-34, which has both the highest surface area and Si content, was found to adsorb in excess of 1.45 mmol NH_3 per gram of catalyst.

Table 3.4.7: Quantitative analysis of NH_3-TPD data for SAPO-34, HP SAPO-34, and HP AlPO-5, including the onset of NH_3 desorption, the temperature of the peak corresponding to the loss of weakly and strongly bound NH_3, and the total quantity of ammonia desorbed between 100 – 600 °C.

Catalyst	Onset of ammonia desorption / °C	Peak maximum for loss of weakly-bound NH_3 / °C	Peak maximum for loss of strongly-bound NH_3 / °C	Total quantity of ammonia desorbed < 600 °C / (mmol NH_3) (g^{-1} catalyst)
SAPO-34	107	170	400	1.23
HP SAPO-34	120	187	~ 360	1.45
HP AlPO-5	120	190-250	-	0.85

To assess the reactive characteristics of the frameworks, the catalytic activity of SAPO-34, HP SAPO-34, and HP AlPO-5 was studied in the liquid-phase Beckmann rearrangement (**Figure 3.4.5**). Unlike the (industrial) vapour-phase process (> 300 °C), under the lower temperature (130 °C) conditions of the liquid-phase reaction, the improved mass transport conferred by the mesopores is more evident. For microporous SAPO-34, the 3.8 Å micropore windows preclude access to cyclohexanone oxime and as such, catalysis is restricted to external acid sites. Such pore-size restrictions are less problematic in the vapour-phase, as rapid diffusion allows high turnover at the active sites on the catalyst surface and pore mouths.[22, 44] However, in the liquid-phase, slow diffusion and limited access to the active sites curtails catalytic turnover; correspondingly, SAPO-34 achieved just 4.5 % conversion of oxime after 6 hours of reaction, whereas HP SAPO-34 achieved a conversion of 32 % over the same period. Thus, the difference in activity of hierarchical and microporous SAPO was attributed to the increased availability of active sites in HP SAPO-34, although there may have been some contribution from the increased polarity of the siliceous mesopores, which has been reported to encourage the uptake of oxime.[10]

Notably, the performance of HP SAPO-34 and HP AlPO-5 was comparable in the liquid-phase BR, despite the absence of Brønsted sites in the latter. Thus, the catalytic data indicates that the silanols in the organosilane-templated mesopores (identified subsequently, and in other reports[44, 51, 53, 78, 87]) are also active in the Beckmann rearrangement. The marginally higher yield of caprolactam for HP SAPO-34 *versus* HP AlPO-5 was attributed to the greater number of active sites (i.e. the additional Brønsted acid sites) available in HP SAPO-34. However, as the initial ($\leqslant$ 2 hours) lactam selectivity of HP SAPO-34 was lower than HP AlPO-5, it is likely

the strongest Brønsted sites in HP SAPO-34 facilitated oxime hydrolysis. Nonetheless, the strongest acid sites are also more susceptible to deactivation through the adsorption of substrate, product, and other organic by-products, and by 3 hours, the selectivity of HP SAPO-34 was in line with HP AlPO-5 (> 70 %). Therefore, the most selective active sites for the liquid-phase Beckmann rearrangement were identified as the weak-to-moderately acidic sites.

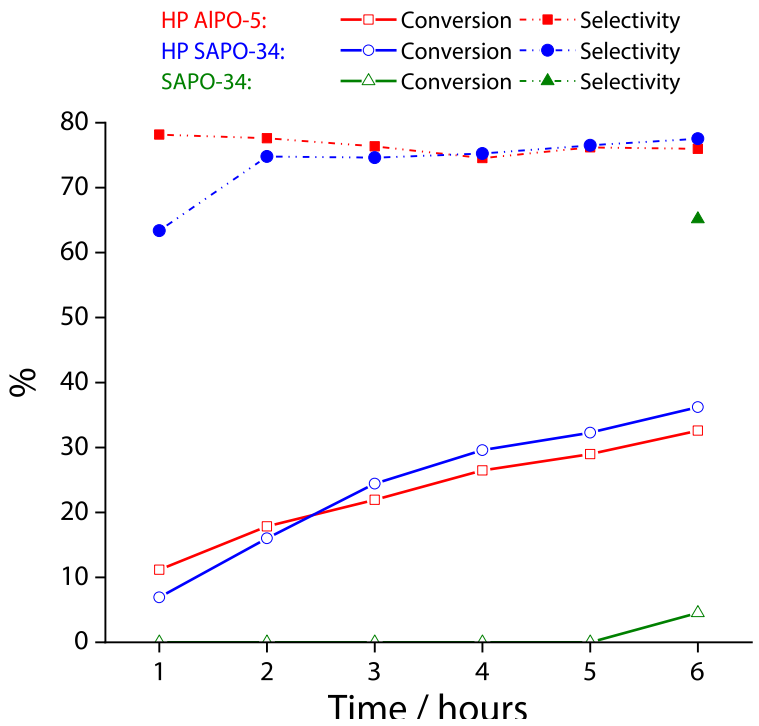

Figure 3.4.5: The conversion of cyclohexanone oxime (solid line) and selectivity towards ε-caprolactam product (dashed line) in the liquid-phase Beckmann rearrangement (130 °C, benzonitrile solvent) catalysed by HP AlPO-5 (red), HP SAPO-34 (blue) and SAPO-34 (green). Cyclohexanone was the only by-product.

3.4.2 Inelastic neutron scattering studies

To probe the interactions that drive the transformation of cyclohexanone oxime in HP (Si)AlPOs, inelastic neutron scattering (INS) experiments were undertaken. For reference purposes, the INS spectrum of cyclohexanone oxime was first acquired (**Figure 3.4.6 a**). Crystallographic studies indicate that cyclohexanone oxime crystallises in the $P\bar{3}$ space group, with asymmetric units that comprise a hydrogen-bonded trimer, where the individual oxime molecules both accept and donate hydrogen bonds (**Figure 3.4.6 b**).[90] As there is minimal interaction between the oxime trimers, the system was modelled as a single

asymmetric unit, and the INS spectrum assigned by correlating experimental modes with computed vibrations.[60]

Notably, heating the pure oxime in excess of its melting point (359 K) did not modify the appearance of its INS vibrational spectrum. The indication was that the intermolecular hydrogen bonding interactions within the oxime trimer were not irreversibly modified by thermal treatment; hence, the crystal structure of the substrate was retained.

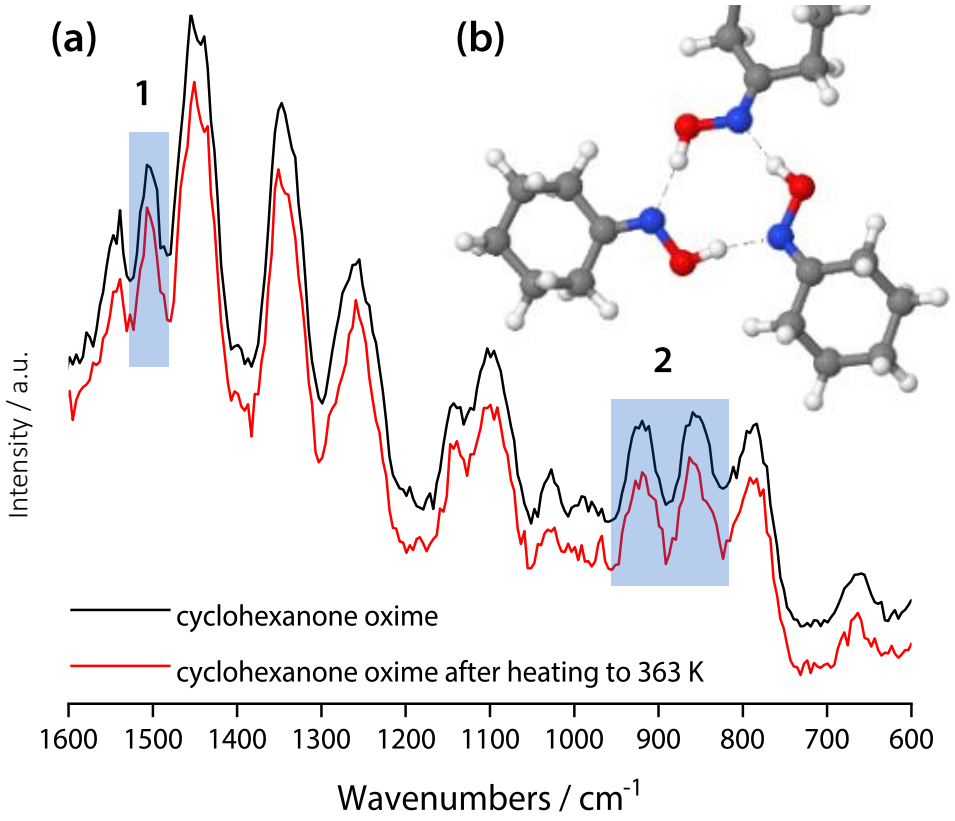

Figure 3.4.6: (a) The INS vibrational spectrum of cyclohexanone oxime before (black) and after heating to 363 K (red). Key vibrational modes are identified as **(1)** the in-plane N-O-H bend and **(2)** the out-of-plane N-O-H bend**. (b)** A depiction of the hydrogen-bonding interaction within a trimeric unit of crystalline cyclohexanone oxime. Spectra acquired on the TOSCA spectrometer.[62]

In the INS experiments reported subsequently, deuterated cyclohexanone-D_{10} oxime (CDO, $C_6D_{10}NOH$) was used as the substrate in order to remove the dominant vibrational modes of the ring protons, and allow the oxime functional group to be targeted spectroscopically (**Figure 3.4.7**).[60]

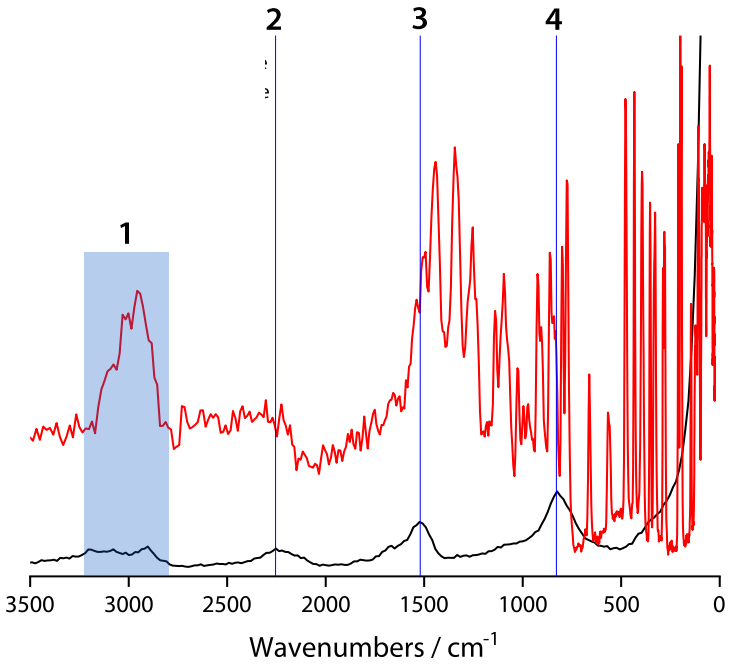

Figure 3.4.7: The INS spectrum of hydrogenous cyclohexanone oxime (red) is dominated by vibrations associated with the ring methylene groups, which give rise to many intense bands. The vibrational spectrum of cyclohexanone-D_{10} oxime (black) is simplified, allowing for identification of oxime O-H stretching modes **(1)**, the O-H in-plane **(3)** and out-of-plane **(4)** bending modes, and a combination band arising from these two bending modes **(2)**.[1]

Gas chromatography (GC) indicated that cyclohexanone-D_{10} oxime was eluted with the same retention time as its hydrogenous analogue (**Figure 3.4.8**), and in the liquid-phase BR catalysed by HP AlPO-5, the transformation of CDO was comparable to the hydrogenous oxime (**Figure 3.4.9** and **Figure 3.4.10**).

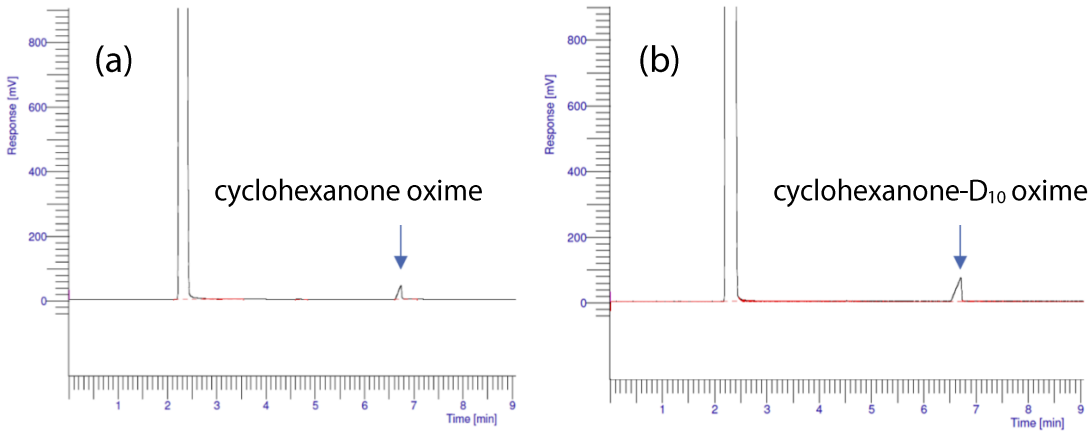

Figure 3.4.8: When analysed using the same GC method, **(a)** hydrogenous cyclohexanone oxime and **(b)** deuterated cyclohexanone-D_{10} oxime dissolved in ethanol, both compounds are detected at the same retention time

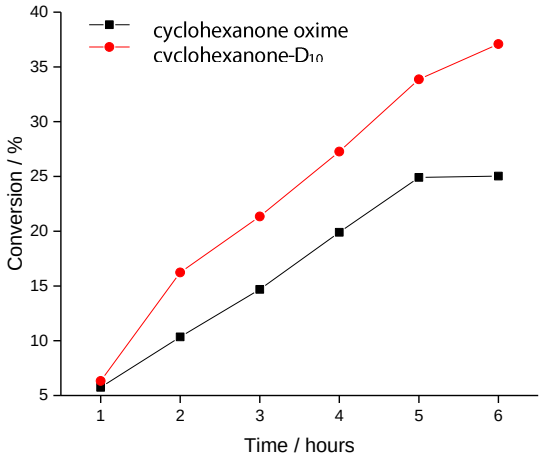

Figure 3.4.9: Conversion of hydrogenous (black line) and D_{10}-deuterated (red line) cyclohexanone oxime in the liquid-phase Beckmann rearrangement with HP AlPO-5 catalyst. Due to the limited quantity of D_{10}-oxime, the GC data was not calibrated for the deuterated substrate and products, which may explain the difference in catalytic activity when using hydrogenous and deuterated oxime.

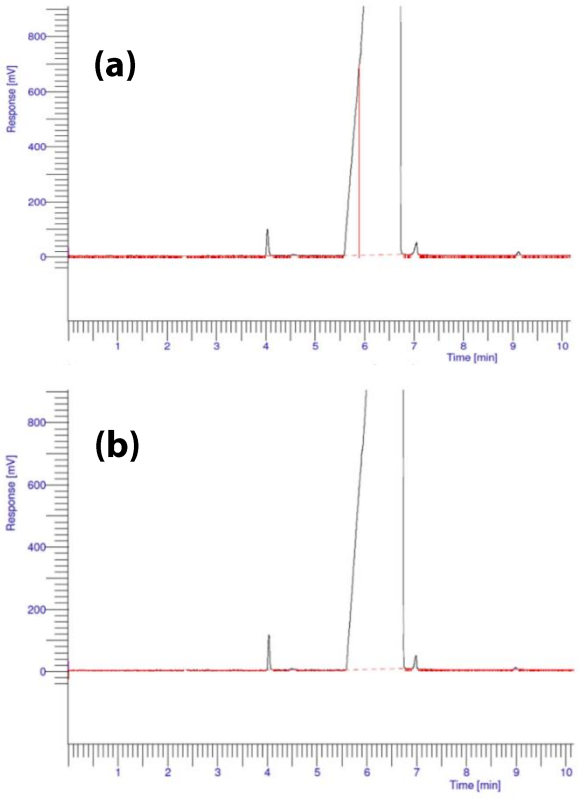

Figure 3.4.10: GC trace after 6 hours of liquid-phase Beckmann rearrangement with HP AlPO-5 catalyst using **(a)** hydrogenous cyclohexanone oxime and **(b)** cyclohexanone-D10 oxime substrates. The peak at ~ 4 ppm is due the internal standard, chlorobenzene. The peak at ~4.6 ppm is due to the by-product cyclohexanone. The broad peak centred at ~ 6.3 ppm is due to the benzonitrile solvent. The peak at ~7.1 ppm is the oxime substrate. The peak at ~ 9.2 ppm is due to formation of ε-caprolactam. The GC analysis of the reaction mixtures at 6 hours show a similar product distribution for both substrates.

The INS spectra of the catalyst frameworks are presented in **Figure 3.4.11**. Since the main components of the HP AlPO-5 framework (Al, P, O) have a relatively low scattering cross-section for neutrons, the INS spectrum of the empty framework was largely featureless. The exceptions were those framework modes made detectable by their association with hydrogen (a strong neutron scatterer). Therefore, the peak at 1125 cm^{-1} was assigned to the O-H bending mode of the pendant silanol sites in the mesopores, with possible contribution from P-OH or Al-OH defect sites. The corresponding O-H stretching mode was visible as a low intensity peak in the characteristic 3000-4000 cm^{-1} range.

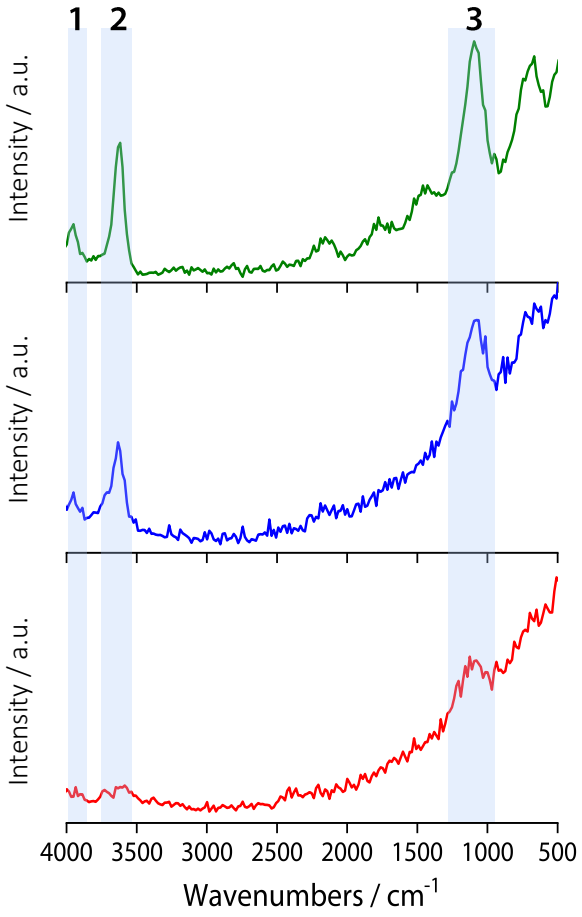

Figure 3.4.11: INS vibrational spectra of SAPO-34 (top, green), HP SAPO-34 (middle, blue) and HP AlPO-5 (bottom, red), with **(1)** the combination band of the O-H stretching and out-of-plane O-H bending modes, **(2)** O-H stretching, and **(3)** O-H bending modes highlighted. Spectra acquired on the TOSCA spectrometer.[62]

The INS spectrum of SAPO-34 revealed more, intense O-H vibrational modes than HP AlPO-5 due to a greater quantity and variety of acid sites from Type II and Type III substitution of Si. The band at 3625 cm^{-1} has been observed by diffuse-reflectance IR spectroscopy of SAPO-34,[91] and was assigned as the fundamental stretching vibration of Si-O(H)-Al groups. The corresponding bending mode was observed at 1100 cm^{-1},[92] and a combination band of

the stretching and out-of-plane bending modes of the OH groups was detected at 3900-4000 cm^{-1}.[93] The vibrational INS spectrum of HP SAPO-34 was largely comparable to that of SAPO-34, with a few distinctions. Firstly, the O-H stretching band of the bulk Brønsted sites (3650 cm^{-1}) possessed a high energy shoulder, which revealed its superposition with the broad, low-intensity stretching mode of the pendant silanols (identified in HP AlPO-5). Moreover, the HP SAPO-34 hydroxyl bands were, in general, broader than those in the microporous framework. This is likely due to structural disorder in the local environment of the Brønsted sites, caused by the mesoporous network.

Physical mixtures of CDO with each framework were analysed by INS (**Figure 3.4.12**). For SAPO-34/CDO, there was no significant interaction between the catalyst and substrate. As well as retention of the SAPO-34 framework bands, both the out-of-plane (OOP) and in-plane (IP) N-O-H bending modes (at 825 and 1600 cm^{-1}, respectively), and O-H stretching modes (2750-3250 cm^{-1}) of the oxime were identifiable. The lack of substrate-framework interactions was attributed to the inaccessibility of the active sites within the SAPO-34 framework, reflecting its catalytic performance in the liquid-phase Beckmann rearrangement (**Figure 3.4.5**).

Contrastingly, for HP AlPO-5/CDO, key vibrational modes of the substrate were altered. In the NO-H stretching region, peak intensity in the range 2750-3250 cm^{-1} was lost, and the remaining NO-H stretching bands were shifted ($\Delta\nu \approx +50$ cm^{-1}) relative to the pure substrate. These observations were consistent with the loss of oxime-oxime hydrogen bonding (resulting in a stronger and shorter NO-H bond), probably driven by (multiple) interactions with the accessible silanols. Given the tendency of the oxime to retain its crystalline structure after heating, the disruption of the trimer at room temperature, in a physical mixture with HP AlPO-5 was significant, and had implications for substrate activation. In the O-H bending region, the discrete OOP and IP N-O-H bending modes of cyclohexanone oxime (at 825 and ~1600 cm^{-1}, respectively) were lost and instead, a broad peak spanning 500-1500 cm^{-1} was observed. The broad peak may be a convolution of the discrete bending modes, where molecular vibration has become constrained by hydrogen bonding to a variety of silanol sites. However, a discussion of the modifications to the HP AlPO-5 framework modes was limited by the low intensity of these bands, although the SiO-H stretching mode appeared to be absent in the HP AlPO-5/CDO mixture.

Despite the different constitution of their frameworks, the vibrational spectrum of HP SAPO-34/CDO bore close resemblance to that of HP AlPO-5/CDO, reinforcing the hypothesis that the mesopore-based silanols (common to both HP catalysts) are involved in ambient-temperature interactions with CDO. As in HP AlPO-5, there was evidence for the loss of oxime NO-H stretching modes, and a blue-shift of the residual NO-H band on exposure to HP SAPO-34. Again, this suggested that the silanols in the mesopores of the HP catalyst interacted with cyclohexanone oxime, disrupting the intermolecular hydrogen bonding interactions in the solid state. It is also feasible that the interaction between cyclohexanone oxime and the mesopore silanols would facilitate the Beckmann rearrangement (once energetic requirements are met) by isolating the individual molecules and binding them in a reactive conformation, close to the active sites. In HP SAPO-34, a loss of intensity at 3630 cm^{-1} (the region associated with framework Brønsted acid sites) was also notable, as this suggested that some of the Brønsted acid sites were accessible to the substrate *via* the mesopores.

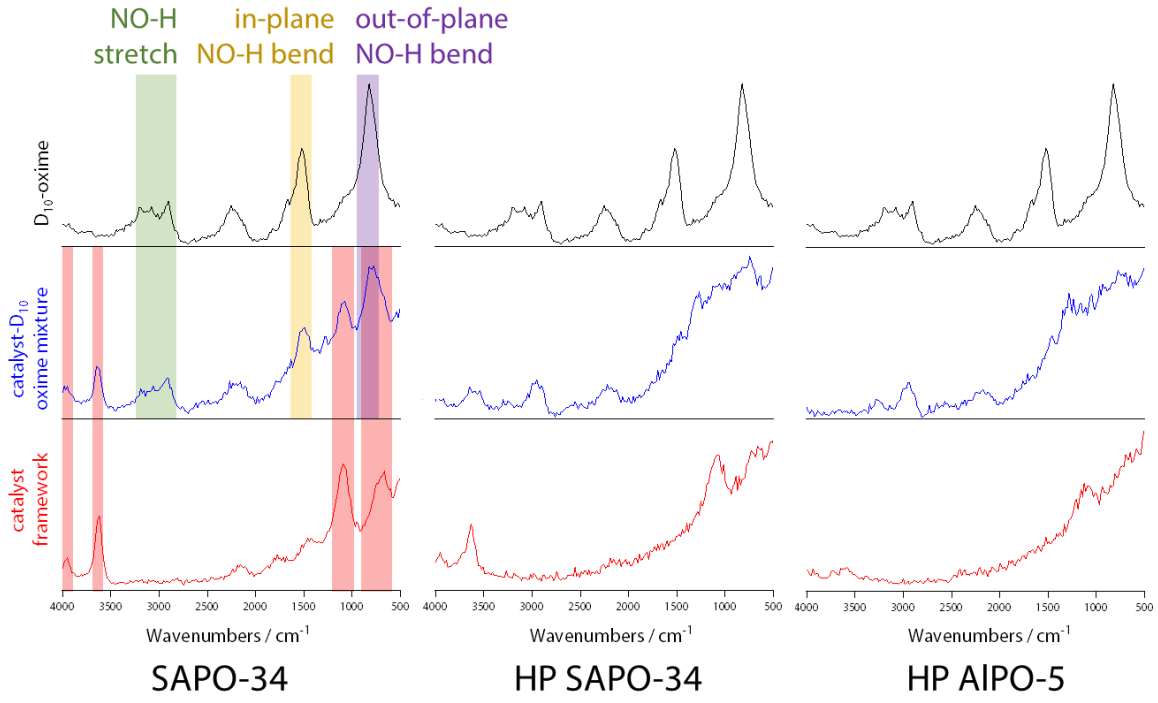

Figure 3.4.12: The INS vibrational spectrum of cyclohexanone-D10 oxime (top, black line), the empty frameworks (bottom, red line) and a physical mixture of the substrate and framework (middle, blue line) for SAPO-34 (left), HP SAPO-34 (middle) and HP AlPO-5 (right). Key framework and substrate bands are highlighted. Y-axes show intensity in arbitrary units. Spectra acquired on the TOSCA spectrometer.[62]

3.4.3 FTIR studies

Further insight into the interaction between the soft-templated catalysts and cyclohexanone oxime was achieved through probe-based infrared (FTIR) spectroscopy. Complementary to INS, FTIR is sensitive to non-hydrogenous functional group vibrations, allowing characteristic modes (such as the C=N bond of the oxime, and the C=O functionality in ε-caprolactam) to be identified.[60]

The SAPO-34, HP SAPO-34 and HP AlPO-5 catalysts were outgassed at 300°C to remove adsorbed water and allow framework O-H stretching modes to be characterised (**Figure 3.4.13**). In the O-H stretch region, microporous SAPO-34 exhibited two characteristic bands (at 3630 and 3600 cm^{-1}), which were attributed to Si-O(H)-Al Brønsted sites in the O(4) and O(2) framework positions, respectively.[86, 94] These Brønsted sites were also present, but less defined, in HP SAPO-34 where the mesoporous network introduced structural disorder. In addition, the silanols in HP SAPO-34 and HP AlPO-5 were identified by the SiO-H stretching mode at ~ 3745 cm^{-1}. A weak PO-H stretching band at ~ 3678 cm^{-1} (from defect sites) was observed for all catalysts.[83, 95]

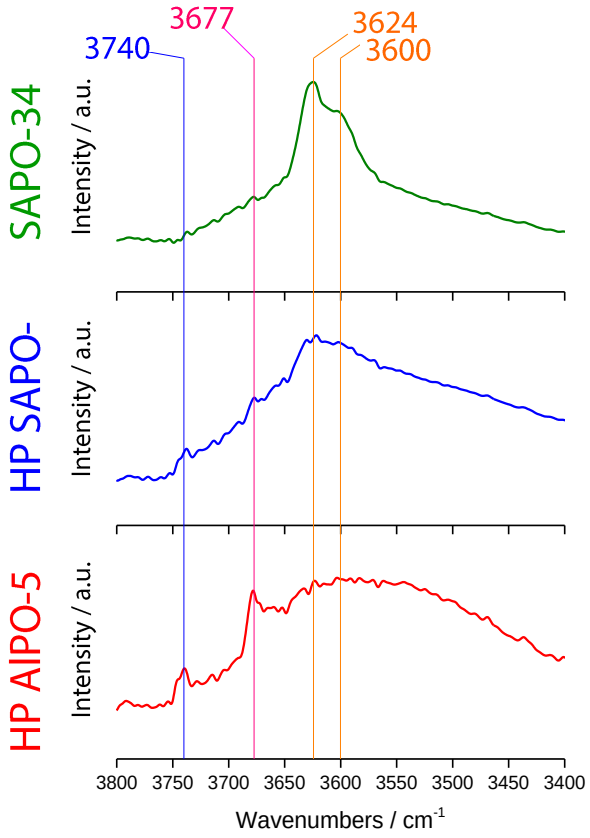

Figure 3.4.13: FTIR absorbance spectra of the O-H stretching region of HP AlPO-5 (red line), HP SAPO-34 (blue line) and SAPO-34 (green line), labelled with the modes associated with Brønsted acid sites (orange), P-OH sites (pink) and Si-OH sites (blue).

On exposing the three catalysts to cyclohexanone oxime, the O-H stretch region revealed that substrate-framework interactions had occurred under ambient conditions (**Figure 3.4.14**). For example, a 'negative' peak in the difference spectra at 3630-3600 cm^{-1} for the SAPO frameworks indicated a loss of intensity in the Brønsted acid, O-H stretching modes. On inspection of the corresponding absorbance spectra, it was revealed that although the adsorption of oxime eliminated the Brønsted O-H bands in HP SAPO-34, some intensity was retained in the microporous analogue. The implication was that in microporous SAPO-34, only a fraction of the Brønsted sites (i.e. those accessible at the surface and pore mouths) interacted with cyclohexanone oxime. Significantly, the loss of the SiO-H stretch mode (3742 cm^{-1}) from the FTIR spectra of the HP catalysts evidenced ambient-temperature interactions between the oxime and silanols, consistent with the observations of INS.

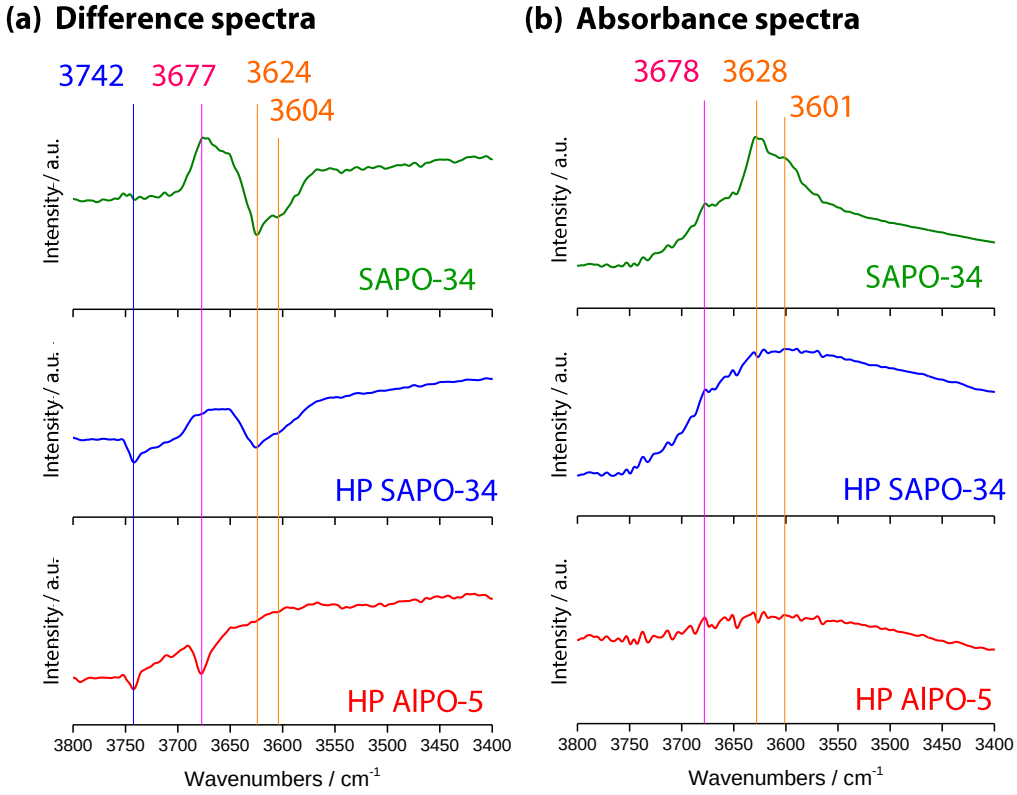

Figure 3.4.14: The FTIR **(a)** difference and **(b)** absorbance spectra in the O-H stretching region of HP AlPO-5 (red line), HP SAPO-34 (blue line) and SAPO-34 (green line) after adsorption of cyclohexanone oxime at room temperature. Modes associated with Brønsted acid sites (orange), P-OH sites (pink) and Si-OH (blue) are labelled.

In the lower energy region of the FTIR spectra (**Figure 3.4.15 a**), the asymmetric and symmetric CH_2 stretching modes (2861 and 2933 cm^{-1}), and the C=N stretch (1638 cm^{-1}) of cyclohexanone oxime were identified.[29] Significantly, in HP SAPO-34, an additional shoulder (1688 cm^{-1}) was assigned to the $C=N^+$ stretch of *N*-protonated oxime.[96] Therefore, in HP

SAPO-34, the enhanced accessibility of the Brønsted sites, and the substrate-activating effect of the silanols in the mesopores (identified by INS) appear to facilitate oxime protonation under ambient conditions. Moreover, *N*-protonation is consistent with the mechanism of the Beckmann rearrangement at a Brønsted acid site, which has been reported to occur with formation of *N*-protonated oxime, prior to the rate-determining step.[30]

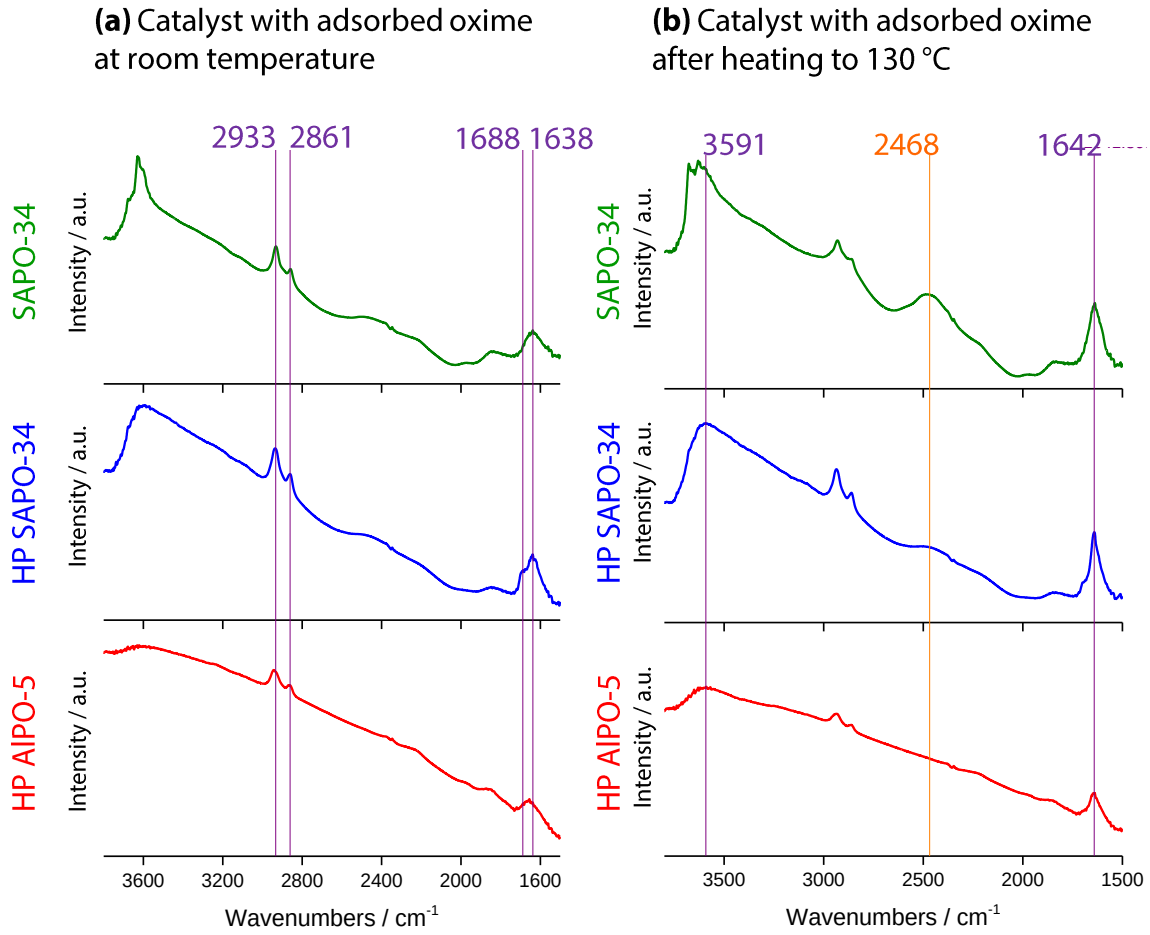

Figure 3.4.15: The FTIR absorbance spectra of HP AlPO-5 (red line), HP SAPO-34 (blue line), and SAPO-34 (green line) after **(a)** adsorption of cyclohexanone oxime at room temperature. The oxime CH_2 stretch modes are observed between 2935 – 2860 cm^{-1}, and the C=N stretch at 1838 cm^{-1}. Only the spectrum of the HP SAPO-34 catalyst shows evidence of oxime protonation by the $C=N^+$ stretch at 1688 cm^{-1}. **(b)** The FTIR absorbance spectra of the same systems are shown after heating to 130 °C for 30 minutes. Some Brønsted acid sites remain in SAPO-34 (> 3500cm^{-1}). Caprolactam is identified in all systems by the C=O stretch at 1642 cm^{-1}. The broad peak at 2486 cm^{-1} (in orange) is due to admission of water.[97] Y-axes show intensity in arbitrary units.

On heating the oxime-dosed samples to 130 °C (**Figure 3.4.15 b**) all three catalysts facilitated the BR, as indicated by the appearance of the C=O stretching mode of ε-caprolactam at 1642 cm^{-1}.[6] Due to the inaccessibility of the internal Brønsted acid sites, microporous

SAPO-34 was found to retain features in the region >3500 cm^{-1} after heating. Nonetheless, the formation of caprolactam on SAPO-34 suggested that the elevated temperature might have facilitated substrate turnover at active sites on the surface and at the pore mouths.

3.4.4 MAS NMR experiments

To further probe the ambient-temperature, silanol-substrate interactions identified by INS and FTIR, magic-angle spinning nuclear magnetic resonance (MAS NMR) studies were undertaken. In the ^{1}H MAS NMR spectra of the calcined catalysts shown in **Figure 3.4.16**, the structure of the spectrum produced by SAPO-34 was consistent with that in the literature.[91] Thus, peak intensity in the region of 1.2 - 2.3 ppm was attributed to the hydroxyl groups of framework defect sites and terminal silanols, whilst resonances between 3.6 - 4.4 ppm, were assigned to bridging OH groups (Si-O(H)-Al).[33, 95, 98]

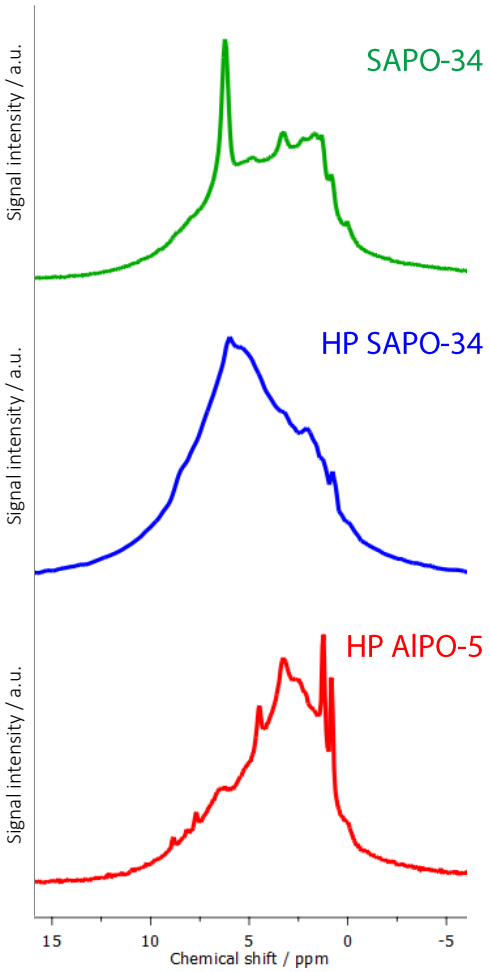

Figure 3.4.16: ^{1}H MAS NMR spectrum of HP AlPO-5 (red), HP SAPO-34 (blue), and SAPO-34 (green) acquired at 600 MHz under a N_2 atmosphere and ambient temperature. The spinning speed was 30 kHz.

Compared to SAPO-34 (and HP SAPO-34), the ^{1}H MAS NMR spectrum of HP AlPO-5 lacked the relatively intense peak at 6.2 ppm, which was thus attributed to the Brønsted acid sites in the SAPO frameworks. The assignment was also consistent with the O-H proton acidity, since proton deshielding (and hence acid strength) correlates with positive chemical shift.[99] HP AlPO-5 presented two sharp bands between 0 - 2 ppm, which were assigned to the weaker defect P-OH and Al-OH groups.[100] These were resolved in HP AlPO-5, where they were not masked by the bridging hydroxyl resonances. The broad signal observed in the HP systems, covering a chemical shift range of 0 - 5 ppm, was associated with the pendant silanols - the amorphous nature of the mesopores yielding a relatively ill-defined proton environment. Finally, the proton spectrum of HP SAPO-34 appeared as a convolution of the spectra obtained for SAPO-34 and HP AlPO-5, reflecting the presence of both Brønsted sites in the bulk framework, and pendant silanols in the mesopores.

The proton spectrum of the substrate, cyclohexanone oxime, revealed two intense peaks: a broad resonance centred at 1.8 ppm, due to the ring methylene protons, and a peak at 11.1 ppm from the oxime NOH functionality (**Figure 3.4.17**).[33] More specifically, the downfield resonance was attributed to the oxime in the hydrogen-bonded trimer of the crystalline phase, since the associated intermolecular interactions caused a downfield shift in the NOH resonance, relative to the isolated oxime molecules in solution (9 - 10 ppm).[99]

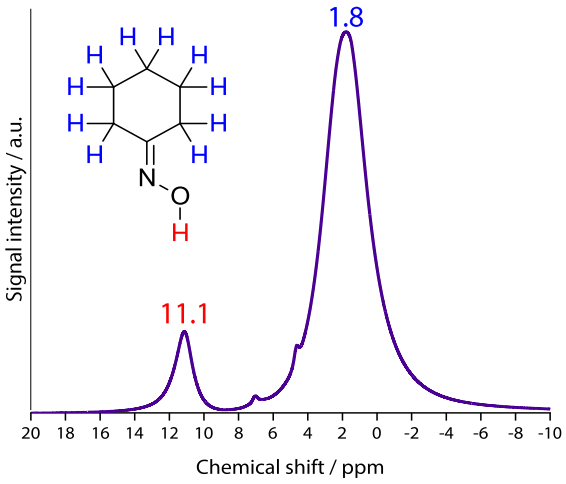

Figure 3.4.17: The ^{1}H MAS NMR spectrum of cyclohexanone oxime (structure inset) acquired at 600 MHz and a spinning speed of 27 kHz. The ring methylene protons (blue) contribute to an intense signal centred at 1.8 ppm, and a proton resonance from the NOH functionality is observed at 11.1 ppm. Small peaks at 7.1 and 4.6 ppm are attributed to impurities.

Focussing on the downfield region, in a physical mixture of SAPO-34 and cyclohexanone oxime, two resonances were identified by ^{1}H MAS NMR (**Figure 3.4.18 a**). As well as the NOH resonance of crystalline oxime (11.1 ppm, **Figure 3.4.18 d(i)**), an additional resonance was detected at 10.1 ppm. The latter was assigned to the NOH proton of a small fraction of oxime

molecules that were isolated form the crystalline trimer and hydrogen bonded to an external Brønsted acid site on SAPO-34 (**Figure 3.4.18 d(ii)**). In this case, the loss of the (deshielding) oxime-oxime hydrogen bonds would cause the NOH proton resonance to shift upfield, towards that of solution-phase oxime.[99] In addition, a simultaneous downfield shift of the framework Brønsted-acid proton resonance from 6.2 ppm to 6.4 ppm identified the corresponding hydrogen-bond acceptor interaction of the framework, as it interacted with the NOH group of the oxime (**Figure 3.4.18 d(iii)**).

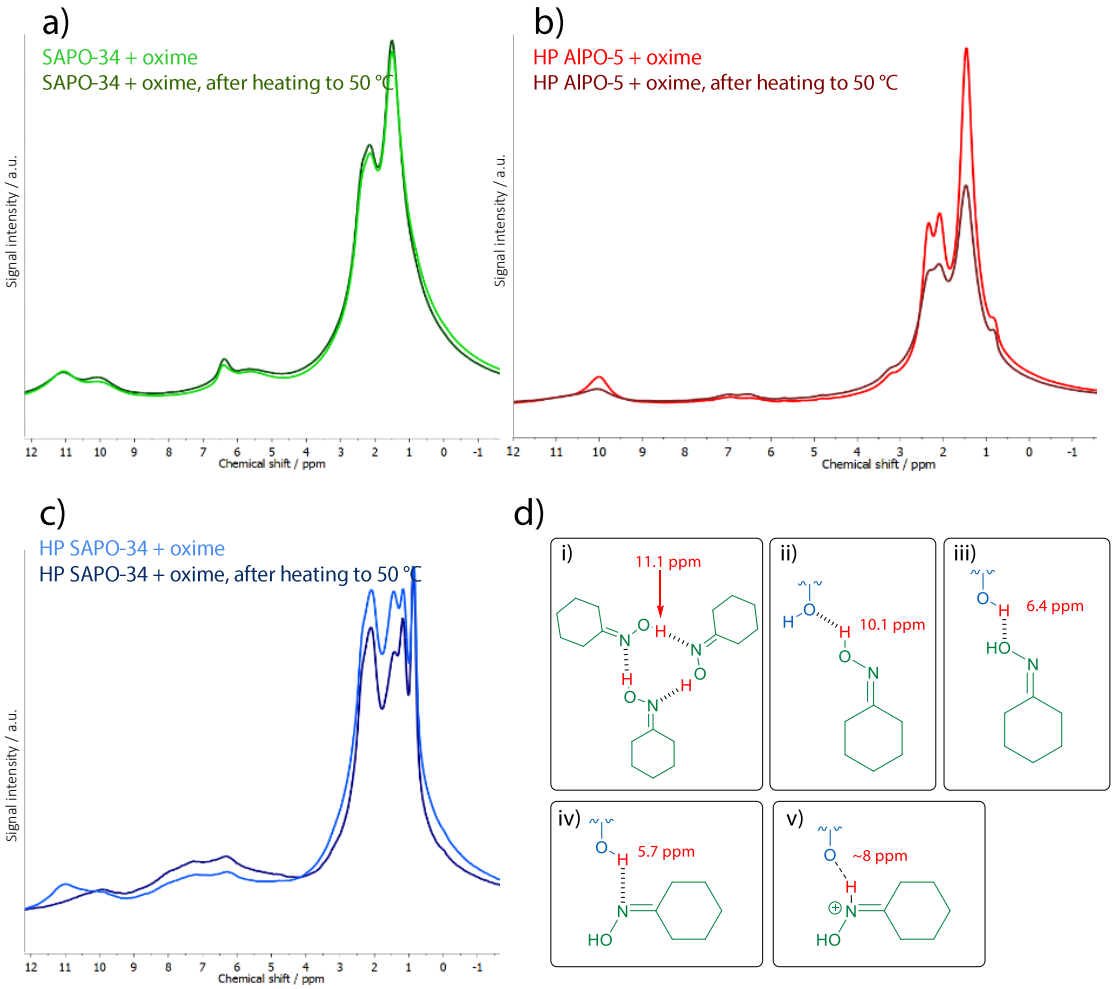

Figure 3.4.18: (a) The ^{1}H NMR of SAPO-34, **(b)** HP AlPO-5, and **(c)** HP SAPO-34 in a physical mixture with cyclohexanone oxime, before and after heating to 50 °C for 2 hours. Spectra acquired at 600 MHz and a spinning frequency of 30 kHz. **(d)** Proposed substrate-framework interactions identified in the ^{1}H NMR spectra **(a-c)** are shown with the resonance of the proton identified in red, cyclohexanone oxime in green, and the framework in blue. The interactions include: **(i)** hydrogen bonding within the solid oxime trimer, **(ii)** hydrogen bonding with proton-donation from the isolated oxime molecule. **(iii)** Hydrogen bonding with proton-acceptance from the oxygen atom of an isolated oxime molecule, **(iv)** hydrogen bonding with proton-acceptance from the nitrogen atom of an isolated oxime molecule, and **(v)** *N*-protonation of cyclohexanone oxime by the framework.

The broad, low intensity peak developed at 5.7 ppm was assigned to *N*-hydrogen bonding between the oxime and an acid site of SAPO-34, with the Brønsted sites (previously at 6.2 ppm) shielded on accepting electron density from the nitrogen lone pair (**Figure 3.4.18 d(iv)**). This interaction is consistent with the FTIR data, and the proposed mechanism of the Beckmann rearrangement, which is initiated by *N*-protonation of the oxime. On heating the SAPO-34/oxime sample to 50 °C, there was negligible change in the ^{1}H NMR spectrum, and overall retention of the peak at 11.1 ppm indicated that a significant proportion of the oxime molecules remained in the crystalline state. Thus, INS, FTIR, and ^{1}H MAS NMR characterised a limited interaction between cyclohexanone oxime and SAPO-34, which was consistent with the low catalytic activity of SAPO-34 in the liquid-phase BR.

When cyclohexanone oxime was combined with the hierarchically-porous catalysts, distinct modifications were observed in the ^{1}H NMR spectrum of the oxime. Firstly, considering the downfield region of the HP AlPO-5/oxime mixture (**Figure 3.4.18 b**), a single peak at 10.0 ppm revealed complete disruption of the solid oxime structure due to interaction with the mesopore-based silanols. In HP SAPO-34 (**Figure 3.4.18 c**), both crystalline (11.0 ppm) and *O*-hydrogen-bonded oxime (9.9 ppm) were identified at room temperature, but on heating to 50 °C, only the latter was observed. Thus, at room temperature, the transfer of oxime into the mesopores was incomplete because (unlike the AFI structure of AlPO-5) the CHA structure offers no possibility of oxime ingress *via* the micropores. Nonetheless, the peak at 9.9 ppm indicated that some of the oxime substrate was interacting with the framework silanols, made accessible by their location in the mesopores.

Both HP catalysts exhibited two peaks in the 5-8 ppm region on combination with cyclohexanone oxime. These peaks were attributed to development of N-H interactions between the framework hydroxyls and the nitrogen atom of the oxime. Similar N-H species are known to produce ^{1}H resonances in this region (~ 6.5 ppm),[33] and additional hydrogen bonding and protonation may cause downfield shifts.[33] N-H resonances are also consistent with the Beckmann rearrangement mechanism, and align with the earlier assignment of the SAPO-34/oxime ^{1}H NMR spectrum. For HP SAPO-34, the extent of the resonances observed in the 5-8 ppm region may be indicative of a range of N-H bond strengths, from weak hydrogen bonding (6.3 ppm), through to complete *N*-protonation (8 ppm), as identified by FTIR studies (**Figure 3.4.18 d(iv)** and **(v)**).

3.4.5 Computational studies

To reinforce the spectroscopic assignments, computational modelling was used to assess the binding and protonation energies of cyclohexanone oxime at Brønsted and silanol acid sites. First, the energy of a hydrogen bonded, trimeric oxime unit was compared to three isolated oxime molecules, and found to be 181 kJ mol^{-1} more stable. A single molecule of cyclohexanone oxime was then docked on the surface of a silanol-terminated mesopore, emulating the soft-templated structures of the HP catalysts. As indicated in **Figure 3.4.19**, of the two principal hydrogen-bonded configurations available at the silanol surface, the *N*-acceptor interaction (**Figure 3.4.19 a**) of the oxime was most stable (-184 kJ mol^{-1}), which is consistent with the rearrangement mechanism.[30] The *O*-acceptor interaction (**Figure 3.4.19 b**) was also stabilising (-165 kJ mol^{-1}), which is consistent with the previous ^{1}H MAS NMR assignments. Importantly, the interaction energy of three isolated oxime molecules *via* an *N*-acceptor interaction with the siliceous surface (3 x -184 kJ mol^{-1} = -552 kJ mol^{-1}) was significantly larger than the stabilisation energy for the oxime trimer (-181 kJ mol^{-1}), providing an energetic driving force for the separation of the trimer within the mesopores.

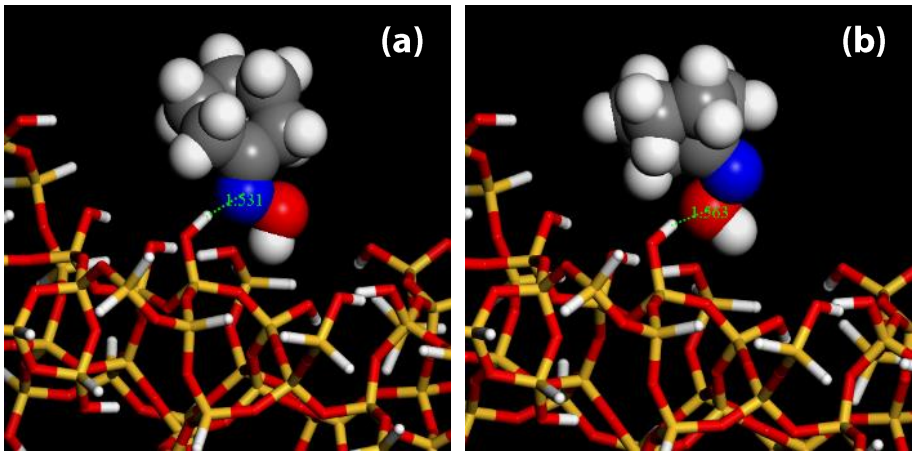

Figure 3.4.19: Cyclohexanone oxime hydrogen-bonded to the surface of an MCM-41 cluster *via* **(a)** a hydrogen bond-acceptor interaction at the oxime nitrogen atom (N-H distance = 1.531 Å) and **(b)** a hydrogen bond-acceptor interaction at the oxime oxygen atom (O-H distance = 1.563 Å).

The binding energy of cyclohexanone oxime at a Brønsted site on the surface of a SAPO-34 crystallite was also calculated with optimised geometries (**Figure 3.4.20**). Given the low loading of Si in the SAPO catalysts (**Table 3.3.2**), the bridging acid sites were treated as spatially isolated. Although the binding energies *via N*-acceptor interaction (-242 kJ mol^{-1}) and *O*-acceptor interaction (-238.9 kJ mol^{-1}) were similar, again the *N*-acceptor configuration was (marginally) more favourable. Notably, the calculations revealed that the oxime molecule

was more strongly bound by a Brønsted site than a silanol site. Furthermore, the deprotonation energy at a Brønsted site in SAPO-34 (+1242 kJ mol^{-1}) was lower than at a silanol site in the mesopore (+1371 kJ mol^{-1}), which correlated with the protonation of oxime observed spectroscopically.

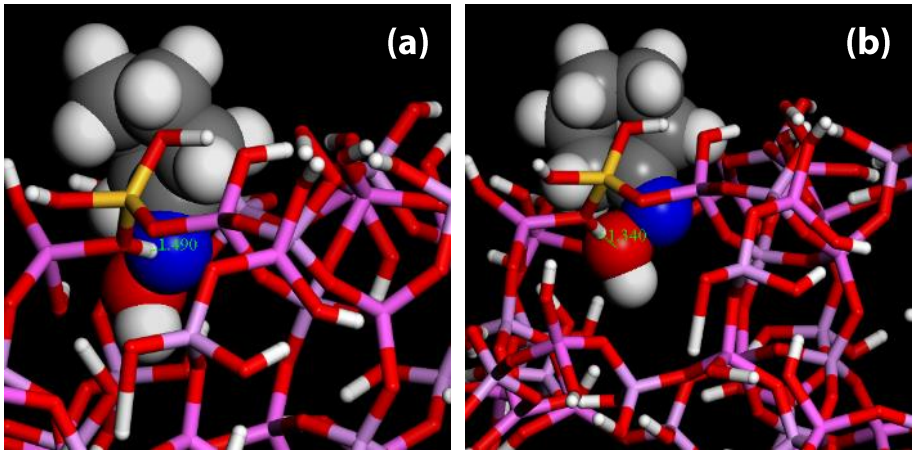

Figure 3.4.20: Cyclohexanone oxime hydrogen-bonded to the surface of a SAPO-34 cluster via **(a)** a hydrogen bond-acceptor interaction at the oxime nitrogen atom (N-H distance = 1.490 Å) and **(b)** a hydrogen bond-acceptor interaction at the oxime oxygen atom (O-H distance = 1.340 Å).

Based on a consideration of both the spectroscopic and computational findings, a mechanism was thus proposed for the adsorption and interaction of cyclohexanone oxime in the hierarchical catalysts. First, the solid oxime trimer is separated into isolated molecules by hydrogen bonding with silanol sites that are accessed within mesopores. Interaction with the silanols activates the oxime molecules, predominantly through *N*-hydrogen bonding interactions, with some contribution from *O*-hydrogen bonding. In the case that a Brønsted acid site is also available (as in HP SAPO-34), there is an energetic driving force for the transfer of oxime from the weak silanol sites in the mesopores to a stronger Brønsted site in the micropores, where protonation proceeds more readily.

3.5 Conclusions and future work

Motivated by the enhanced performance of organosilane-templated HP (Si)AlPOs in the Beckmann rearrangement of cyclohexanone oxime,[44] an integrated theoretical-empirical study was undertaken to ascertain the role of the siliceous mesopore network. In this investigation, the activity of HP SAPO-34 was compared with its microporous analogue under the conditions of the liquid-phase Beckmann rearrangement (BR), in order to accentuate the steric constraints of the CHA pores (3.8 Å). Moreover, to deconvolute the catalytic and mass transport effects of the siliceous mesopores, the HP AlPO-5 framework (AFI, 7.3 Å pores) was studied. In the liquid-phase BR, microporous SAPO-34 achieved negligible conversion (< 5 %) of cyclohexanone oxime after 6 hours due to the restricted access to acids sites. Under the same conditions, the activities of HP SAPO-34 and HP AlPO-5 were comparable (35 and 33 % conversion, respectively), indicating the catalytic role of the silanols in the mesopores.

INS, MAS NMR, and FTIR spectroscopies were used to study the interaction of cyclohexanone oxime with the SAPO-34, HP SAPO-34, and HP AlPO-5 frameworks. Universally, the spectral features attributed to the Brønsted sites of SAPO-34 were largely retained on exposure to cyclohexanone oxime at ambient temperature, which characterised the limited interaction with cyclohexanone oxime. In contrast, when cyclohexanone oxime was combined with the HP catalysts, significant substrate-framework interactions were identified. INS spectroscopy indicated that the stable, hydrogen-bonded trimer of the solid oxime was disrupted by exposure to the weakly acidic silanol sites within the mesopores, and DFT calculations determined this to be an energetically favourable process. Notably, HP SAPO-34 was the only system where there was (MAS NMR and FTIR) evidence for the formation of the *N*-protonated oxime at ambient temperature. Since cyclohexanone oxime was not protonated by HP AlPO-5 under the same conditions, the weakly acidic silanols were not implicated in oxime protonation. Equally, in the (limited) interaction between SAPO-34 and cyclohexanone oxime there was no evidence of substrate protonation by the external Brønsted acid sites. Therefore, in a physical mixture at ambient temperature, neither Brønsted sites, nor silanols alone, were found to effect the protonation of cyclohexanone oxime.

Thus, it has been proposed that the activity of HP SAPO-34 in the liquid and vapour-phase[44] BR is due to a co-operative effect, arising from the proximity of silanol and Brønsted acid sites. Based on computational and spectroscopic analyses of HP (Si)AlPO, the uptake of substrate occurs *via* the mesopores, where hydrogen-bonding interactions at the silanol sites cause disintegration of the trimeric oxime structure. The isolated oxime molecules then engage in activating interactions, predominantly through *N*-hydrogen bonding (and some

O-hydrogen bonding) to the silanols. If a Brønsted acid site is made accessible by the interconnectivity of micro- and meso-pores (as in HP SAPO-34), there is an energetic driving force for the oxime to bind to the stronger Brønsted site, with the lower deprotonation energy facilitating *N*-protonation of the oxime at ambient temperature. With sufficient energetic input, the Beckmann rearrangement to ε-caprolactam will then occur.

In conclusion, the organosilane mesoporogen generates siliceous mesopores in HP (Si)AlPO that modify both the catalytic and mass transport properties of the microporous framework. The secondary mesoporosity has been found to improve the uptake of oxime into the microporous framework, and the silanols elicit catalytic activity in the HP AlPO framework. Crucially, where accessible silanols can work in synergy with Brønsted sites (as in HP SAPO), the BR proceeds *via* a hybrid mechanism, where the formation of a hydrogen bonded complex at the silanols, facilitates the protonation of oxime at a stronger Brønsted site.

Nevertheless, there are aspects of the interaction between cyclohexanone oxime and soft-templated (Si)AlPOs that would benefit from further investigation. For example, the assignment of the ^{1}H MAS NMR spectra proved challenging due to the scope of substrate-framework interactions and the potential chemical shift range of the framework hydroxyls on interaction with the oxime.[101, 102] It might be possible to clarify the MAS NMR spectra with isotope labelling. For instance, selective deuteration of either the oxime or framework might be used to 'damp' the resonances of one component of the mixture, allowing the ^{1}H MAS NMR to be assigned more readily to the hydrogenous component.[103] Also, ^{15}N MAS NMR with ^{15}N-cyclohexanone oxime has proven invaluable in deducing the BR mechanism in zeolites,[32, 39] and might be used to probe the hydrogen bonding and protonation of oxime in HP SAPO-34. Otherwise, the ^{1}H MAS NMR spectra might be assigned with the aid of theoretical studies to predict the chemical shifts of oxime and framework.[104, 105]

Moreover, the studies in this Chapter have focussed solely on the interaction of the BR substrate, cyclohexanone oxime, with HP (Si)AlPO. However, the reported oxime-framework interactions also have implications for the adsorption of the BR product, ε-caprolactam. Various studies have indicated that the slow desorption and diffusion of caprolactam (especially *via* a protonated complex) can encourage the formation of by-products.[22, 32, 39] However, the catalytic studies of HP SAPO in both the liquid- and vapour-[44] phase BR, suggest that the siliceous mesopores do not have a detrimental impact on the catalyst selectivity. Thus, it might be inferred that if the lactam-silanol interactions are active in the HP SAPO, these are much weaker than those with the oxime, or otherwise outweighed by the enhanced mass transport properties of the mesopores. The preliminary vibrational characterisation of ε-caprolactam is in place to facilitate a study akin to that reported in this Chapter.[60]

3.6 References

1. G. Dahlhoff, J. P. M. Niederer and W. F. Hoelderich, *Catal. Rev.*, 2001, **43**, 381-441.

2. R. A. Sheldon and R. S. Downing, *Appl. Catal. A: Gen.*, 1999, **189**, 163-183.

3. B. Zong, B. Sun, S. Cheng, X. Mu, K. Yang, J. Zhao, X. Zhang and W. Wu, *Engineering*, 2017, **3**, 379-384.

4. US Pat. 2234566 A, 1941.

5. S. Chapman, M. Potter and R. Raja, *Molecules*, 2017, **22**, 2127.

6. H. Ichihashi and H. Sato, *Appl. Catal. A: Gen.*, 2001, **221**, 359-366.

7. US Pat. 4709024 A, 1987.

8. Y. Izumi, H. Ichihashi, Y. Shimazu, M. Kitamura and H. Sato, *Bull. Chem. Soc. Jpn*, 2007, **80**, 1280-1287.

9. Sustainability - Our contribution: providing solutions, https://www.cia.org.uk/Sustainability-Our-contribution/Providing-solutions, (accessed January 2019).

10. M. A. Camblor, A. Corma, H. García, V. Semmer-Herlédan and S. Valencia, *J. Catal.*, 1998, **177**, 267-272.

11. X. Wang, C.-C. Chen, S.-Y. Chen, Y. Mou and S. Cheng, *Appl. Catal. A: Gen.*, 2005, **281**, 47-54.

12. C. Ngamcharussrivichai, P. Wu and T. Tatsumi, *J. Catal.*, 2004, **227**, 448-458.

13. C. Ngamcharussrivichai, P. Wu and T. Tatsumi, *J. Catal.*, 2005, **235**, 139-149.

14. C. Ngamcharussrivichai, P. Wu and T. Tatsumi, *Appl. Catal. A: Gen.*, 2005, **288**, 158-168.

15. R. Raja, M. E. Potter and S. H. Newland, *Chem. Commun.*, 2014, **50**, 5940-5957.

16. R. Kumar and B. Chowdhury, *Ind. Eng. Chem. Res.*, 2014, **53**, 16587-16599.

17. *Zeolites and Catalysis: Synthesis, Reactions and Applications*, Wiley-VCH, Germany, 2010.

18. P. S. Landis and P. B. Venuto, *J. Catal.*, 1966, **6**, 245-252.

19. A. B. Fernández, M. Boronat, T. Blasco and A. Corma, *Angew. Chem.*, 2005, **117**, 2422-2425.

20. M. Nguyen, G. Raspoet and L. Vanquickenborne, *J. Chem. Soc., Perkin Trans.*, 1997, DOI: 10.1039/A604240F, 821-826.

21. Y. Shinohara, S. Mae, D. Shouro and T. Nakajima, *J. Mol. Struct.: THEOCHEM*, 2000, **497**, 1-9.

22. T. Takahashi, M. N. A. Nasution and T. Kai, *Appl. Catal. A: Gen.*, 2001, **210**, 339-344.

23. T. Yashima, N. Oka and T. Komatsu, *Catal. Today*, 1997, **38**, 249-253.

24. W. F. Hölderich, J. Röseler, G. Heitmann and A. T. Liebens, *Catal. Today*, 1997, **37**, 353-366.

25. H. Ichihashi, M. Ishida, A. Shiga, M. Kitamura, T. Suzuki, K. Suenobu and K. Sugita, *Catal. Surv. Asia*, 2003, **7**, 261-270.

26. H. Sato, K. Hirose, M. Kitamura and Y. Nakamura, *Stud. Surf. Sci. Catal.*, 1989, **49**, 1213-1222.

27. H. Ichihashi and M. Kitamura, *Catal. Today*, 2002, **73**, 23-28.

28. A. Corma, H. Garcia, J. Primo and E. Sastre, *Zeolites*, 1991, **11**, 593-597.

29. C. Flego and L. Dalloro, *Micropor. Mesopor. Mater.*, 2003, **60**, 263-271.

30. T. Bucko, J. Hafner and L. Benco, *J. Phys. Chem. A*, 2004, **108**, 11388-11397.

31. T. Komatsu, T. Maeda and T. Yashima, *Micropor. Mesopor. Mater.*, 2000, **35-36**, 173-180.

32. V. R. R. Marthala, Y. Jiang, J. Huang, W. Wang, R. Gläser and M. Hunger, *J. Am. Chem. Soc.*, 2006, **128**, 14812-14813.

33. V. R. Reddy Marthala, J. Frey and M. Hunger, *Catal. Lett.*, 2010, **135**, 91-97.

34. J. Sirijaraensre and J. Limtrakul, *Phys. Chem. Chem. Phys.*, 2009, **11**, 578-585.

35. J. Sirijaraensre, T. N. Truong and J. Limtrakul, *J. Phys. Chem. B*, 2005, **109**, 12099-12106.

36. M. Ishida, T. Suzuki, H. Ichihashi and A. Shiga, *Catal. Today*, 2003, **87**, 187-194.

37. J. Sirijaraensre and J. Limtrakul, *ChemPhysChem*, 2006, **7**, 2424-2432.

38. A. B. Fernández, I. Lezcano-Gonzalez, M. Boronat, T. Blasco and A. Corma, *J. Catal.*, 2007, **249**, 116-119.

39. V. R. Reddy Marthala, S. Rabl, J. Huang, S. A. S. Rezai, B. Thomas and M. Hunger, *J. Catal.*, 2008, **257**, 134-141.

40. M. Linares, C. Vargas, A. García, C. Ochoa-Hernández, J. Čejka, R. A. García-Muñoz and D. P. Serrano, *Catal. Sci. Tech.*, 2017, **7**, 181-190.

41. P. Botella, A. Corma, S. Iborra, R. Montón, I. Rodríguez and V. Costa, *J. Catal.*, 2007, **250**, 161-170.

42. T. Yashima, K. Miura and T. Komatsu, *Stud. Surf. Sci. Catal.*, 1994, **84**, 1897-1904.

43. Database of Zeolite Structures, https://www.iza-structure.org/databases, (accessed January 2019)

44. S. H. Newland, W. Sinkler, T. Mezza, S. R. Bare, M. Carravetta, I. M. Haies, A. Levy, S. Keenan and R. Raja, *ACS Catal.*, 2015, **5**, 6587-6593.

45. M. Choi, H. S. Cho, R. Srivastava, C. Venkatesan, D.-H. Choi and R. Ryoo, *Nat. Mater.*, 2006, **5**, 718.

46. A. J. J. Koekkoek, C. H. L. Tempelman, V. Degirmenci, M. Guo, Z. Feng, C. Li and E. J. M. Hensen, *Catal. Today*, 2011, **168**, 96-111.

47. V. N. Shetti, J. Kim, R. Srivastava, M. Choi and R. Ryoo, *J. Catal.*, 2008, **254**, 296-303.

48. M. Choi, D.-H. Lee, K. Na, B.-W. Yu and R. Ryoo, *Angew. Chem. Int. Ed.*, 2009, **48**, 3673-3676.

49. D.-H. Lee, M. Choi, B.-W. Yu and R. Ryoo, *Chem. Commun.*, 2009, 74-76.

50. A. Inayat, I. Knoke, E. Spiecker and W. Schwieger, *Angew. Chem. Int. Ed.*, 2012, **51**, 1962-1965.

51. M. Choi, R. Srivastava and R. Ryoo, *Chem. Commun.*, 2006, 4380–4382.

52. N. Danilina, F. Krumeich and J. A. van Bokhoven, *J. Catal,*, 2010, **272**, 37-43.

53. Q. Sun, N. Wang, D. Xi, M. Yang and J. Yu, *Chem, Commun,*, 2014, **50**, 6502-6505.

54. S. Tao, X. Li, G. Lv, C. Wang, R. Xu, H. Ma and Z. Tian, *Catal. Sci. Tech.*, 2017, **7**, 5775-5784.

55. M.-J. Jin, A. Taher, H.-J. Kang, M. Choi and R. Ryoo, *Green Chem.*, 2009, **11**, 309-313.

56. C. Yin, R. Ni, X. Bao and Y. Chen, *Micropor. Mesopor. Mater.*, 2015, **202**, 133-137.

57. M. O. Jones, A. D. Taylor and S. F. Parker, *Appl. Petrochem. Res.*, 2012, **2**, 97-104.

58. A. J. O'Malley, S. F. Parker and C. R. A. Catlow, *Chem. Commun.*, 2017, **53**, 12164-12176.

59. S. F. Parker, D. Lennon and P. W. Albers, *Appl. Spectrosc.*, 2011, **65**, 1325-1341.

60. S. Chapman, A. J. O'Malley, S. F. Parker and R. Raja, *ChemPhysChem*, 2018, **19**, 3196-3203.

61. J. Laugier and B. Bochu, CelRef Version 3, http://www.ccp14.ac.uk/tutorial/lmgp/celref.htm).

62. S. F. Parker, F. Fernandez-Alonso, A. J. Ramirez-Cuesta, J. Tomkinson, S. Rudic, R. S. Pinna, G. Gorini and J. F. Castañon, *J. Phys. Conf. Ser.*, 2014, **554**, 012003.

63. ISIS Neutron and Muon Source, https://www.isis.stfc.ac.uk/Pages/home.aspx, (accessed October 2018).

64. Jmol: an open-source Java viewer for chemical structures in 3D, http://www.jmol.org/, (accessed January 2019).

65. V. Milman, A. Perlov, K. Refson, S. J. Clark, J. Gavartin and B. Winkler, *J. Phys.: Condens. Matt.*, 2009, **21**, 485404.

66. K. Refson, P. R. Tulip and S. J. Clark, *Phys. Rev. B*, 2006, **73**, 155114.

67. H. Shigenobu and H. Kikuko, *Bull. Chem. Soc. Jpn.*, 1991, **64**, 685-687.

68. B. Delley, *J. Chem. Phys.*, 2000, **113**, 7756-7764.

69. A. D. Becke, *Phys. Rev. A*, 1988, **38**, 3098-3100.

70. A. Tkatchenko and M. Scheffler, *Phys. Rev. Lett.*, 2009, **102**, 073005.

71. P. Ugliengo, M. Sodupe, F. Musso, I. J. Bush, R. Orlando and R. Dovesi, *Adv. Mater.*, 2008, **20**, 4579-4583.

72. L. S. Dent and J. V. Smith, *Nature*, 1958, **181**, 1794-1796.

73. K. Na, C. Jo, J. Kim, K. Cho, J. Jung, Y. Seo, R. J. Messinger, B. F. Chmelka and R. Ryoo, *Science*, 2011, **333**, 328.

74. M. Thommes, K. Kaneko, V. Neimark Alexander, P. Olivier James, F. Rodriguez-Reinoso, J. Rouquerol and S. W. Sing Kenneth, *Pure Appl. Chem.*, 2015, **87**, 1051-1069.

75. M. Hartmann, *Angew. Chem. Int. Ed.*, 2004, **43**, 5880-5882.

76. Y. K. Park, K. Y. Park and S. I. Woo, *Catal. Lett.*, 1994, **26**, 169-180.

77. X. Niu, J. Gao, Q. Miao, M. Dong, G. Wang, W. Fan, Z. Qin and J. Wang, *Micropor. Mesopor. Mater.*, 2014, **197**, 252-261.

78. C. Wang, M. Yang, P. Tian, S. Xu, Y. Yang, D. Wang, Y. Yuan and Z. Liu, *J. Mater. Chem. A*, 2015, **3**, 5608-5616.

79. M. Du, Z. Qin, H. Ge, X. Li, Z. Lü and J. Wang, *Fuel Process. Technol.*, 2010, **91**, 1655-1661.

80. K. T. G. Carvalho and E. A. Urquieta-Gonzalez, *Catal. Today*, 2015, **243**, 92-102.

81. D. Liu, P. Yuan, H. Liu, J. Cai, D. Tan, H. He, J. Zhu and T. Chen, *Appl. Clay Sci.*, 2013, **80-81**, 407-412.

82. G. R. Moradi, F. Yaripour and P. Vale-Sheyda, *Fuel Process. Technol.*, 2010, **91**, 461-468.

83. G. V. A. Martins, G. Berlier, C. Bisio, S. Coluccia, H. O. Pastore and L. Marchese, *J. Phys. Chem. C*, 2008, **112**, 7193-7200.

84. L. Marchese, A. Frache, G. Gatti, S. Coluccia, L. Lisi, G. Ruoppolo, G. Russo and H. O. Pastore, *J. Catal.*, 2002, **208**, 479-484.

85. M. Popova, C. Minchev and V. Kanazirev, *Appl. Catal. A: Gen.*, 1998, **169**, 227-235.

86. L. Smith, A. K. Cheetham, L. Marchese, J. M. Thomas, P. A. Wright, J. Chen and E. Gianotti, *Catal. Lett.*, 1996, **41**, 13-16.

87. H. Xin, X. Li, L. Chen, Y. Huang, G. Zhu and X. Li, *Energy Environm. Focus*, 2013, **2**, 18-40.

88. M. E. Potter, A. J. O'Malley, S. Chapman, J. Kezina, S. H. Newland, I. P. Silverwood, S. Mukhopadhyay, M. Carravetta, T. M. Mezza, S. F. Parker, C. R. A. Catlow and R. Raja, *ACS Catal.*, 2017, **7**, 2926-2934.

89. S.-T. Yang, J.-Y. Kim, H.-J. Chae, M. Kim, S.-Y. Jeong and W.-S. Ahn, *Mater. Res. Bull.*, 2012, **47**, 3888-3892.

90. M. Lutz, A. L. Spek, R. Dabirian, C. A. van Walree and L. W. Jenneskens, *Acta Crystallogr. Sect. C: Cryst. Struct. Commun.*, 2004, **60**, 127-129.

91. B. Zibrowius, E. Löffler and M. Hunger, *Zeolites*, 1992, **12**, 167-174.

92. S. Coluccia, L. Marchese and G. Martra, *Micropor. Mesopor. Mater.*, 1999, **30**, 43-56.

93. S. A. Zubkov, L. M. Kustov, V. B. Kazansky, I. Girnus and R. Fricke, *J. Chem. Soc., Faraday Trans.*, 1991, **87**, 897-900.

94. I. Miletto, G. Paul, S. Chapman, G. Gatti, L. Marchese, R. Raja and E. Gianotti, *Chem. - A Eur. J.*, 2017, **23**, 9952-9961.

95. I. Miletto, C. Ivaldi, G. Paul, S. Chapman, L. Marchese, R. Raja and E. Gianotti, *ChemistryOpen*, 2018, **7**, 297-301.

96. Y.-M. Chung and H.-K. Rhee, *J. Mol. Catal. A: Chem.*, 2001, **175**, 249-257.

97. L. M. Kustov, *Top. Catal.*, 1997, **4**, 131-144.

98. D. Freude, M. Hunger and H. Pfeifer, *Zeitschrift für Phys. Chem.*, 1987, **152**, 171-182.

99. D. Freude, *Adv. Colloid Interface Sci.*, 1985, **23**, 21-43.

100. D. Freude, H. Ernst, M. Hunger, H. Pfeifer and E. Jahn, *Chem. Phys. Lett.*, 1988, **143**, 477-481.

101. B. Zibrowius, E. Löffler and M. Hunger, *Zeolites*, 1992, **12**, 167-174.

102. M. Hunger, D. Freude, T. Fröhlich, H. Pfeifer and W. Schwieger, *Zeolites*, 1987, **7**, 108-110.

103. H. Ernst, D. Freude and I. Wolf, *Chem. Phys. Lett.*, 1993, **212**, 588-596.

104. A. Simperler, R. G. Bell and M. W. Anderson, *J. Phys. Chem. B*, 2004, **108**, 7142-7151.

105. A. Zheng, H. Zhang, L. Chen, Y. Yue, C. Ye and F. Deng, *J. Phys. Chem. B*, 2007, **111**, 3085-3089.

Chapter 4 Investigating diffusion in hierarchical silicoaluminophosphates: a neutron scattering study in the context of the Beckmann rearrangement

Special Acknowledgments

Dr James Taylor and **Hannah Dixon**

ISIS Hydrogen and Catalysis Lab, Rutherford Appleton Laboratory, U.K.

For acquiring NH_3-TPD data.

Dr Alexander J. O'Malley

Department of Chemistry, University of Bath U.K.,

For assistance in sample preparation and undertaking QENS measurements, and for performing the analysis of QENS data.

Dr Ian Silverwood

ISIS Pulsed Neutron and Muon Facility, Rutherford Appleton Laboratory, U.K.

For assistance and expertise as the local contact during QENS experiments, and for useful discussions when undertaking total neutron scattering experiments.

Dr Tristan Youngs

ISIS Pulsed Neutron and Muon Facility, Rutherford Appleton Laboratory, U.K.

For assistance and expertise as the local contact during total neutron scattering experiments.

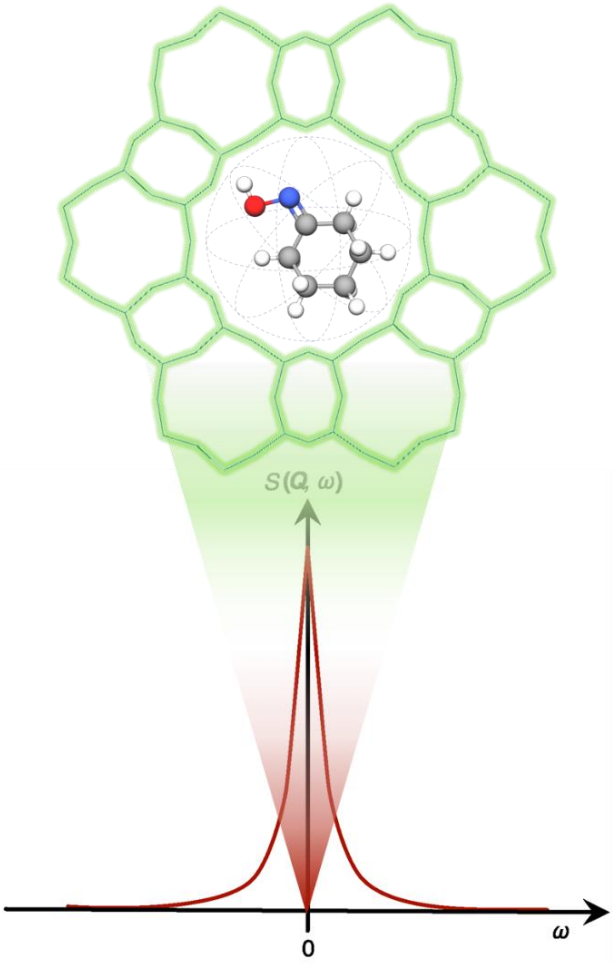

4.1 Introduction

4.1.1 Probing molecular motions in zeotype materials

Diffusion plays a fundamental role in catalysis, since mass transport to and from the active site is essential for catalytic turnover.[1] For porous, zeotype catalysts, a large proportion of the active sites are distributed across the internal surfaces of nanosized channels and cavities. Whilst the geometric constraints of nanoporous structures are often exploited for shape-selective transformations (**Figure 4.1.1**),[2] molecular diffusion may be hindered by physical and chemical interactions with the pore walls.[3] At an extreme, a catalytic transformation may become diffusion-limited if the rate of diffusion is much slower than the rate of reaction at the active site.[4] As such, an evaluation of molecular dynamics can provide an important insight into catalyst mechanism and reaction kinetics.

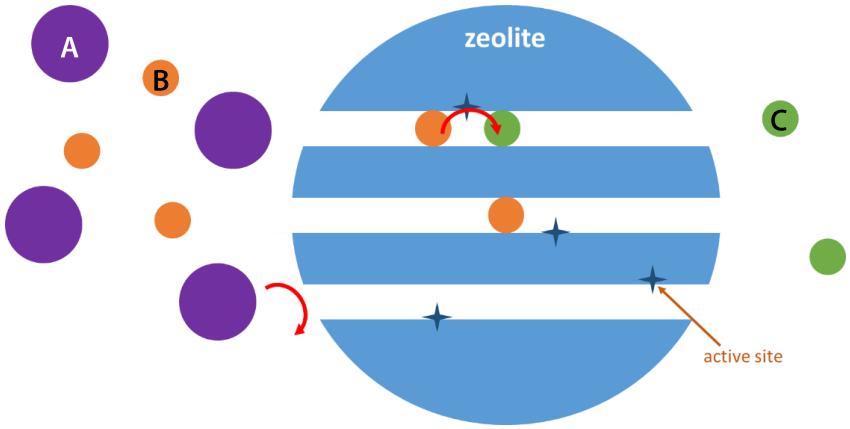

Figure 4.1.1: A schematic depicting a shape-selective transformation using a porous zeolite catalyst (blue). In a mixture of molecules **A** (purple) and **B** (orange), reactant selectivity favours the transformation of **B** into **C** (green), as the smaller reactant molecule can access the internal active sites located within the zeolite pores.

Diffusion is a mass transfer process, driven by the spontaneous flux of material down its local concentration gradient ($\frac{\partial C}{\partial x}$).[3] At a microscopic level, the process of diffusion is a result of stochastic motion and the tendency for molecules to disperse homogeneously in space. The diffusional characteristics of a molecule are described by its diffusivity (D): a constant of proportionality that relates the rate of molecular flux (J) to the concentration gradient, as expressed by Fick's First Law (**Equation 4.1.1**).[5]

Equation 4.1.1: $$J = -D\frac{\partial C}{\partial x}$$

Fick's Law can be used to describe the molecular diffusion in a porous material, provided the flux is defined relative to a fixed frame of reference (i.e. the pore walls). In this case, the mass transport is more accurately specified by the transport diffusivity (D_t), and the presence of a concentration gradient is implicit (**Figure 4.1.2 a**).[3] However, diffusion phenomena can also be described by a self-diffusivity coefficient (D_s), which is the rate of diffusion of a particle under equilibrium conditions (**Figure 4.1.2 b**).[6] Whilst transport and self-diffusion occur *via* the same fundamental mechanism (i.e. stochastic motion) the D_t and D_s for diffusion in a porous adsorbate are rarely the same.[3] However, D_t and D_s will converge at the limit of infinite dilution, under which conditions the sorbate molecules are insensitive to each other's presence, and the molecular flux is determined by the host-guest interaction only.[7]

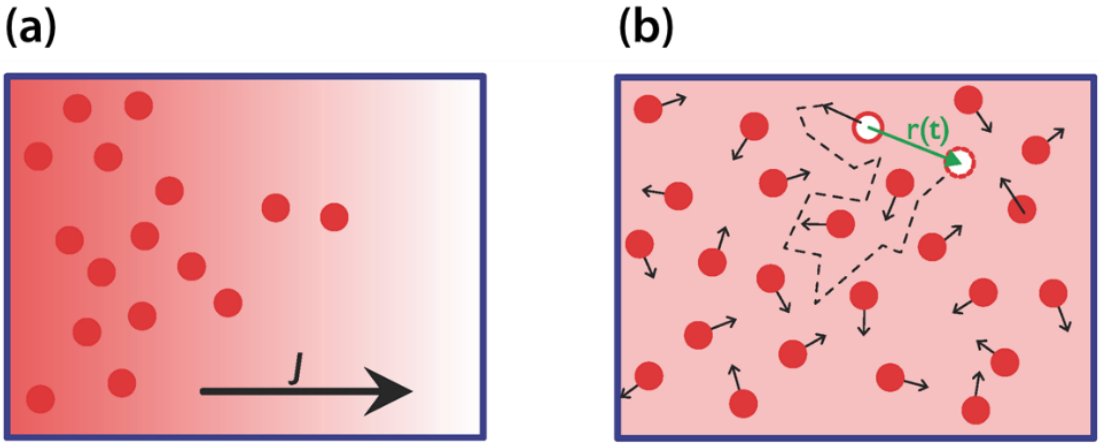

Figure 4.1.2: A microscopic depiction of **(a)** transport diffusion and **(b)** self-diffusion.[6, 8] **(a)** shows the direction of flux (J) of molecules (red spheres) down their concentration gradient, which can be described by Fick's Law. **(b)** shows molecular diffusion at equilibrium. White and red spheres represent the same type of molecule. Self-diffusion can be measured by following the displacement of individual diffusant molecules over time ($r(t)$).

A variety of techniques have been used to quantify diffusion phenomena in porous materials, each accessing a particular diffusivity range based on the time and length scale of the measurements (**Table 4.1.1**).[6] However, diffusion experiments are largely divided into two classes. Macroscopic methods are usually steady-state or transient techniques that invoke Fick's Law to interpret changes in sorbate concentration across a collection of porous crystals (or a membrane).[3, 8] As a result, macroscopic methods generally yield transport diffusivities (D_t). In contrast, microscopic methods can directly probe the mechanism of diffusion in a single, porous crystal by monitoring molecular displacements over short intervals of time and space.[3, 9] Such methods, which include pulsed-field gradient (PFG) NMR and quasi-elastic neutron scattering (QENS), are more often used to obtain self-diffusivities (D_s).

Table 4.1.1: An overview of some macroscopic and microscopic techniques used to study diffusion in porous materials.[3, 9]

	Technique	Overview
Macroscopic	**Membrane permeation (steady-state)**	A known pressure of sorbate gas is applied to one side of a zeolite membrane and the rate of pressure increase on the other side of the membrane is monitored.
	Uptake rate methods (transient)	A zeolite under vacuum is exposed to a pressure of sorbate gas and the time-dependent response is measured as a change in weight (gravimetric method), or the change the amount of gas in the surrounding container (volumetric method).
	Chromatography (transient)	A chromatographic column of zeolite crystals is subject to a perturbation in the sorbate concentration at the inlet feed. The diffusive and absorptive properties of the zeolite are quantified by monitoring the time lag and broadening of the response curve measured at the column outlet.
Microscopic	**Pulsed-field gradient NMR**	Two temporally isolated radiofrequency pulses are applied to a magnetised sample. Following each radiofrequency pulse, an inhomogeneous magnetic field pulse is applied. Under the magnetic field gradient, nuclear spins relax at different rates, depending on their in position in the field. If nuclear spins maintain their spatial position for the duration of the experiment, the NMR signal is completely refocussed, generating a 'spin echo'. However, if the nuclear spins migrate in the period between RF pulses, their precession rates are modified and signal refocussing is incomplete. As a result, the amplitude of the spin echo undergoes a diffusion-dependent dampening.
	***Quasi*-elastic neutron scattering**	The diffusion of a sorbate within a zeolite is determined from the energy distribution of a scattered neutron beam. Minute energy transfers between diffusing sorbate and impinging neutrons leads to *quasi*-elastic broadening of the elastic peak. The resulting profile can be used to characterise the mechanism of diffusion.
	Interference microscopy	A microscope is used to measure the change in the optical density of a zeolite during a sorption process.

4.1.1.1 Diffusion mechanisms in porous materials

Sorbate-sorbate and host-sorbate interactions can give rise to complex diffusional behaviour in porous materials. Yet, at a fundamental level the diffusion mechanism can be predisposed by the relative dimensions of the sorbate and the pore.[6] As depicted in **Figure 4.1.3 (a)**, the relationship between molecular diffusivity and the pore diameter is divided into three regimes.[3]

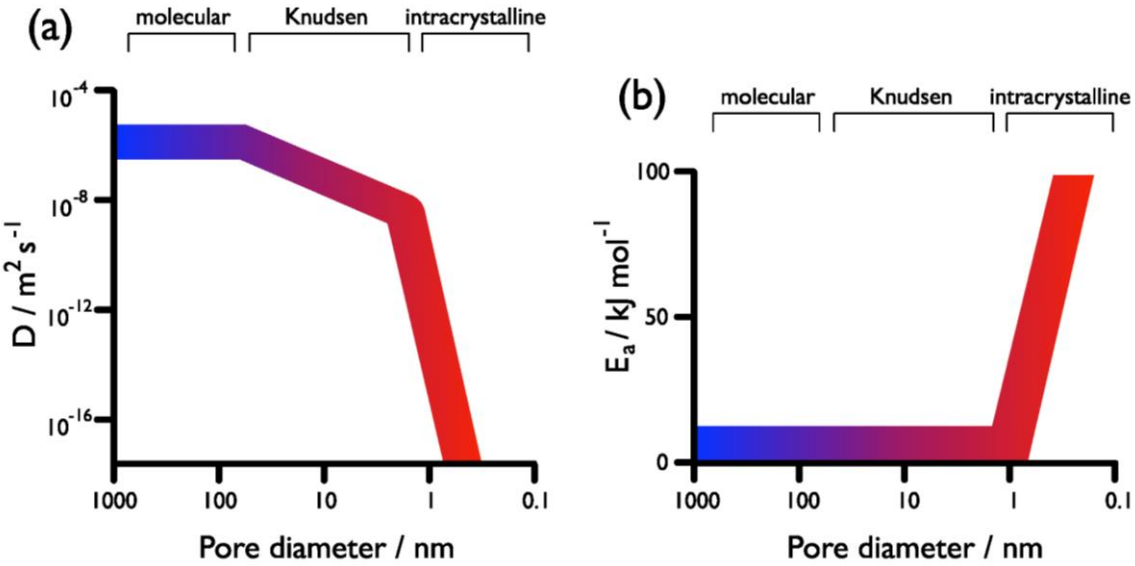

Figure 4.1.3: The influence of pore diameter on **(a)** diffusivity and **(b)** diffusional activation energy, E_a (373 K and 1 bar), with three diffusion regimes highlighted.[10]

In the molecular regime, the pore diameter is much larger than the mean free path of the sorbate, so collisions between the sorbate occur much more frequently than collisions with the pore walls. As in the case of a macroporous material, the interactions with the pore wall may become so infrequent as to be negligible, and the sorbate diffusivity can be approximated by Fick's Law.[6, 8] By extension, collisions between the sorbate and the pore wall can be increased if the pore size is decreased. In the Knudsen regime, the mean free path of the sorbate is comparable to (or larger than) the pore diameter, such that sorbate-pore interactions occur much more often than intermolecular collisions.[6] Ultimately, interactions between sorbate are neglected in the Knudsen regime, and the molecules are considered to move autonomously, with a diffusivity that is independent of the concentration gradient.[8] However, if the molecular environment is constricted to the order of molecular dimensions, steric hindrance becomes significant and there is a rapid drop in diffusivity with increasing sorbate size. In the intracrystalline regime, the close confinement means that the sorbate cannot escape the force field exerted by the pore walls. Consequently, intracrystalline (or configurational) diffusion is an activated process (**Figure 4.1.3 b**), akin to the diffusion of molecules adsorbed on a surface.

In a microporous material, mass transport can be considered bounded by two limiting types of molecular motion:[11]

- gas-translation (or activated Knudsen diffusion), where sorbate molecules retain their gaseous character but movement is hindered by the potential field of the pore walls;

- solid vibration (or activated jump diffusion), where the sorbate loses its gaseous character due to the strong interaction with the pore walls. The sorbate molecules oscillate with the adsorbent until they acquire sufficient energy to jump to another adsorption site on the host.

In reality, both activated translation and surface diffusion will contribute to the overall intracrystalline diffusivity;[8] their relative contributions dependent on steric effects and the nature of the sorbate-framework interaction.[9] For example, in the central region of a micropore, sorbate diffusion may occur *via* activated gas translation. However, with a close size-match between sorbate and pore, or a strong host-guest interaction, the sorbate may become increasingly adsorbed to the walls.[11] Molecular adsorption is an exothermic and competitive process,[10] and the adsorbed molecules must overcome an energy barrier in order to travel along the pore.[12] If the adsorbate-adsorbent interaction is strong, mass transport is facilitated by surface diffusion, and molecular displacement occurs by jumping between adsorption sites on the pore wall.[13] However, as the strength of the surface interaction decreases, molecular desorption occurs more frequently, and the sorbate increasingly propagates *via* the pore-gas phase.

In larger micropores and mesopores, diffusion behaviour may be complicated by the accumulation of a multilayer of adsorbate at the pore walls. (**Figure 4.1.4**).[13] At low concentration, the sorbate will be adsorbed at the surface sites of highest binding energy, and will propagate *via* surface diffusion. However, as the sorbate concentration is increased, the weaker surface sites will be increasingly occupied, and a multilayer of adsorbate may accumulate at the pore walls. Within the liquid-like multilayer, mass transport may occur *via* molecular rearrangements, but since the intermolecular interactions in the multilayer are often weaker than the adsorbate-adsorbent interactions at the pore wall, gas-translation can also make a significant contribution. If the sorbate concentration is increased sufficiently that capillary condensation occurs (**Section 2.2.2**), gas-phase diffusion can become restricted by the capillary-condensed liquid, leading to a significant decrease in sorbate diffusivity.

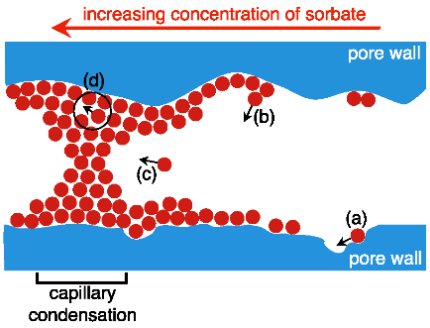

Figure 4.1.4: A depiction of molecular mass transport mechanisms in a mesopore as sorbate concentration is increased.[13] **(a)** At low sorbate concentration, molecular adsorption occurs at the surface sites of highest binding energy, and mass transport occurs predominantly *via* surface diffusion. As the concentration of sorbate increases, weaker adsorption sites may be occupied, and a multilayer may form. **(b)** The more weakly-bound molecules will desorb from their adsorption sites more frequently, leading to increased **(c)** translation *via* the gas phase in the pore. **(d)** Mass transport may also occur by molecular rearrangement in the multilayer. If capillary-condensed liquid is formed in the pore, gas-translation of the sorbate is hindered.

Thus, many variables can influence the intracrystalline diffusivity, including the diameter of the pore, the concentration, molecular weight, and kinetic diameter of the sorbate, the enthalpy of adsorption, and the activation barrier to diffusion.[9] Also, the nature of the interaction between the pore wall and the diffusant can play a critical role, as do interactions between the sorbate molecules, which can lead to correlation effects. Moreover, transport barriers, such as surface inhomogeneities, pore connectivity, and surface layers, can add further complexity.[14] As a consequence, the diffusional behaviour of a confined molecule can differ vastly from the same species moving in the bulk,[15] and the diffusivity of molecules in a microporous framework tend to be much more variable (e.g. from 10^{-19} m^2 s^{-1} for the diffusion of benzene in Ca Zeolite-Y,[16] to 10^{-8} m^2 s^{-1} for methane diffusing in Silicalite-1[17])[18] than molecular liquids (~ 10^{-9} m^2 s^{-1}) and gases (~10^{-5} m^2 s^{-1}).[19] Whilst this provides scope to regulate the mass transport in microporous materials (e.g. *via* framework topology or composition), intracrystalline diffusion phenomena can be challenging to characterise.[10]

There has been considerable development of methodologies to improve the understanding of mass transport in zeolites. Sophisticated experiments, such as PFG-NMR,[20] interference microscopy,[21] and QENS,[22] can be used to measure microscopic diffusivity in zeolites directly.[14] Theoretical models (such as Monte Carlo methods[23-25] and molecular dynamics simulations[26, 27]) are providing detailed insights into diffusion phenomena, providing a means to rationalise and predict experimental data, and to derive mass transport properties.[14, 26, 27] In turn, experimental studies provide a means to evaluate the reliability of the molecular models, demonstrating the reciprocity of theoretical and empirical analyses.[14, 28]

4.1.1.2 Quasi-elastic neutron scattering

The phenomenon of quasi-elastic neutron scattering (QENS) has been harnessed as a spectroscopic technique to study microscopic diffusion processes.[3] QENS arises due to minute energy transfers between low-energy neutrons and mobile particles reorienting or diffusing on a timescale of 10^{-10} – 10^{-12} s.[22] These interactions give rise to quasi-elastic broadening (of neV to meV) of the elastic peak of the scattered neutrons, and an energy profile that encodes sub-nanoscale molecular dynamics (e.g. rotations, vibrations, and diffusion).[3] QENS is often used to study proton dynamics as the ^{1}H incoherent scattering cross-section for neutrons exceeds nearly all other nuclei. Since hydrogen is a predominantly incoherent scatterer, QENS studies of hydrogenous molecules are best suited to the analysis of self-diffusion, which can be accessed at diffusivities as low as 10^{-14} m^2 s^{-1}.[3, 6]

Quasi-elastic broadening is typically described by a Lorentzian profile. For isotropic, Fickian diffusion over long distances, the self-diffusivity (D_s) is related to the half-width at half-maximum (HWHM) ($\Delta\omega(Q)_{\text{inc}}$) of the Lorentzian by **Equation 4.1.2**, where Q and $\Delta\omega$ are the momentum and energy transfers, respectively.[3]

Equation 4.1.2: $$\Delta\omega(\mathrm{Q})_{inc} = D_s Q^2$$

However, the space- and time-resolution of the QENS technique also permits the study of complex, microscopic diffusion phenomena not predicted on the basis of Fick's Law.[29] In fact, over shorter distances (probed at large Q), the relationship between $\Delta\omega$ and Q^2 often deviates from linearity; this behaviour is quite typical for intracrystalline diffusion in zeotypes, which is probed over the distance of a few unit cells.[3] Various models have been developed to describe the systematic deviations from Fick's Law, revealing details of elementary diffusive steps. These include a number of models of translation *via* jump-diffusion, where the diffusant resides at a particular site before making a short jump to another site (**Table 4.1.2**). QENS can also be used to characterise localised molecular motions, such as rotations and confined translations (**Table 4.1.3**), by deconvolution from the translational motion. (It is typical to assume that the long-range translations, rotations, and vibrations of a molecule are uncoupled).[30]

In the quasi-elastic regime, the incoherent scattering function, $S_{incoh}(\boldsymbol{Q}, \omega)$ (which is proportional to the incoherent scattering intensity (**Chapter 2.2.8**)) can be considered a

superposition of elastic and quasi-elastic components (**Equation 4.1.3**, highlighted in blue and red, respectively).[31]

Equation 4.1.3: $$S_{incoh}(\boldsymbol{Q},\omega) = A(\boldsymbol{Q})\delta(\omega) + S_{quasi-elastic}(\boldsymbol{Q},\omega)$$

In **Equation 4.1.3**, the coefficient of the delta function, $A(\boldsymbol{Q})$, is the elastic incoherent structure factor (EISF), which describes the fraction of the total quasi-elastic intensity contained in the elastic peak (i.e. the ratio of the integrals of the elastic intensity to the total intensity (elastic and quasi-elastic)).[32] Provided the sharp elastic component can be separated from the broad quasi-elastic part, the EISF is quantifiable.[28] Then, the variation of the experimental EISF can be studied as a function of Q, and compared to various models to determine the nature and geometry of the localised motion.[33]

So whilst the total scattering intensity is independent of the nature of the motion in a sample, the ratio of elastic and inelastic intensities provides information on the rate of motion, and the Q-dependence of this ratio is related to the geometry of motion.[31, 33]

Table 4.1.2: Some examples of models used to describe translational diffusion. These models can be characterised by the relationship between the momentum transfer, Q, and the half width at half maximum (HWHM) of the Lorentzian component of the QENS peak.[3, 22]

Model	Description	Relationship between HWHM ($\Delta\omega(Q)$) and Q	Example
Fickian[22]	A particle undergoing continuous, stochastic motion is described by the probability of a particle at the origin being found at position *r*, at time *t*. The particle is assumed to diffuse by infinitesimally small jumps.	$\Delta\omega(Q) = D_s Q^2$	QENS analysis of methanol diffusion in H-Y zeolite revealed Fickian diffusion.[34] A higher diffusivity in H-Y *versus* Na-X zeolite was attributed to a smaller concentration of extra-framework cations in H-Y.
Chudley and Elliott[35]	A particle remains at a site for a residence time, τ. Spontaneous thermal fluctuations allow the particle to jump a distance, d, to the nearest-neighbour site on the host lattice. **Fixed jump length.**	$\Delta\omega(Q) = \frac{1}{\tau}\left(1 - \frac{\sin(Qd)}{Qd}\right)$	The diffusion of cyclohexane in MCM-41 was best fit to the Chudley and Elliott model. The diffusivity of sorbed cyclohexane was higher than the bulk liquid. On excluding sorbate-framework bonding, it was proposed that cyclohexane in MCM-41 exists in a metastable state between liquid and vapour.[36]
Hall and Ross[37]	A particle resides at a site for a time, τ, before making a random jump in three dimensions, within a confined region. The jump length varies as the particle vibrates around a fixed point on the lattice. **Accounts for a fixed distribution of jump-lengths.**	$\Delta\omega(Q) = \frac{1}{\tau}\left(1 - e^{-\frac{Q^2\langle r^2\rangle}{6}}\right)$ <r^2> is the mean square jump length.	The diffusion of acetylene[38] and propane[39] in Na-Y zeolite was consistent with the Hall and Ross model, where the sorbate undergoes random diffusion within the zeolite cages, with a Gaussian distribution of jump-lengths.

Table 4.1.2 continued: Some examples of models used to describe translational diffusion. These models can be characterised by the relationship between the momentum transfer, Q, and the half width at half maximum (HWHM) of the Lorentzian component of the QENS peak.[3, 22]

Model	Description	Relationship between HWHM ($\Delta\omega(Q)$) and Q	Example
Singwi and Sjölander[40]	The particle is assumed to oscillate about the origin, r = 0, for a mean time, τ_0. It then jumps to a point at distance r, for the duration, τ_1, before resuming fixed oscillation. The particle can arrive at point r after 2N steps (of oscillation and then translation). It is assumed that the particle spends more time oscillating than diffusing. **Accounts for a fixed distribution of jump-lengths.**	$\Delta\omega(Q) = \frac{1}{6\tau}\left(\frac{Q^2\langle r^2\rangle}{1+\frac{Q^2\langle r^2\rangle}{6}}\right)$ <r^2> is the mean square jump length.	The Singwi and Sjölander model was fit to the diffusion of benzene in Na-X and Na-Y zeolites.[41] Two mean square jump lengths were calculated (2.9 and 6 Å) but as these were smaller than the distance between adjacent supercages, the jumps were confined within the supercage (r < 6 Å).
Jobic[42]	An extension of the Chudley and Elliott model. A particle is assumed to jump between two sites separated by a distance, d_0. However, when the particle occupies a site, it is considered to be delocalised over a length r_0. **Accounts for a variable distribution of jump-lengths.**	$\Delta\omega(Q) = \frac{1}{\tau}\left[1-\frac{\sin(Qd_0)}{Qd_0}e^{-\frac{Q^2r_0^2}{2}}\right]$	A mixture of n-butane and methane in silicalite-1 was fit to the Jobic model with d_0 = 9.57 Å and r_0 = 2.5 Å.[43] Molecular dynamics studies indicated that the molecular displacements occurred with short oscillations at an energetically favourable site, and infrequent, rapid, jump-like translations.

Table 4.1.3: Some examples of models for localised molecular motions detected by QENS. The confined motions are usually characterised by the Q-dependence of the elastic incoherent structure factor (EISF, $A_0(Q)$).[3, 22, 44]

Model	Description	EISF [a]	Example
Isotropic rotation[45]	Continuous rotation on the surface of a sphere. Molecular reorientation occurs *via* random, small-angle rotations.	$A_0(Q) = j_0^2(Qr)$	The rotational motion of methane sorbed in Na ZSM-5 was best fit to an isotropic rotation model. The rotational motion in Na ZSM-5 was found to be much slower that in bulk, solid methane.[46]
Free diffusion inside a sphere[47]	Diffusion is confined within an impermeable sphere of radius *r*. The molecule rotates as it molecule undergoing translational motions in a confined spherical volume	$A_0(Q) = \left[\frac{3j_1(Qr)}{Qr}\right]^2$	QENS was used to investigate the mechanism of proton conductivity in the phosphonate-based metal–organic framework, MFM-500(Ni). QENS analysis indicated that proton diffusion occurred by 'free diffusion inside a sphere' *via* the hydrogen-bonded networks at the metal centres.[48]
Jump rotation among N equivalent sites, equally spaced on a circle[49]	Rotation occurs *via* instantaneous jump to a neighbouring site at a distance *d*. There are N equivalent sites, distributed at equidistance on the circumference of a circle, radius *r*. The average residence time at each site is described by τ.	For N = 2 (two-site jump rotation): $A_0(Q) = \frac{1}{2}[1 + j_0(Qd)]$	Benzene sorbed in H-ZSM-5 and Ca-ZSM-5 zeolites was found to undergo a six-site jump rotation about the C_6 molecular axis, perpendicular the plane of the ring.[50] On loading the zeolite to near-saturation, the amplitude of rotation was restricted by benzene-benzene interactions.

Table 4.1.3 continued: Some examples of models for localised molecular motions detected by QENS. The confined motions are usually characterised by the Q-dependence of the elastic incoherent structure factor (EISF, $A_0(Q)$).[3, 22, 44]

Model	Description	EISF [a]	Example
Uniaxial rotation[51]	Rotational motion about a single molecular axis. This model cannot be applied directly to a polycrystalline sample, since there is no expression for the average angle (θ) between the axis of rotation and the direction of Q. However, the approximation of jump rotation over N sites can be used, since at large N (> 10), the scattering function does not change as N is increased further, and is near identical to that of continuous rotation.	$A_0(Q) = \frac{1}{N}\sum_{n=1}^{N} j_0\left[2Qr_u \sin\left(\frac{n\pi}{N}\right)\right]$	QENS was used to study the mobility of ethane and propane in ZSM-5. As well as identifying jump-diffusion (best fit to the Singwi and Sjölander model), the QENS analyses revealed uniaxial rotation of the sorbate molecules about their principle molecular axis.[52]

[a] Due to the spherical symmetry of rotation, the structure factor is expressed as a Bessel function, j_n of the nth order.

4.1.1.3 QENS for catalysis: diffusion in porous zeotype catalysts

An understanding of elementary transport mechanisms in porous media can be a powerful tool in heterogeneous catalysis, as it provides a means to rationalise and optimise catalyst properties based on fundamental adsorption and diffusion characteristics. Among the various techniques that are available for the study of mass transfer phenomena in microporous zeotypes (**Table 4.1.1**), QENS is well suited to probing both dynamical and geometrical aspects of microscopic molecular motion.

In the context of catalysis, one of foremost applications of QENS is for the study of hydrocarbon dynamics. The predominance of QENS studies in this field reflects both the unique capabilities of the neutron scattering technique (especially the dominant incoherent scattering cross-section of the hydrogen nucleus), and the relevance of these studies to the petrochemical industry.[53] For example, QENS has been used to quantify the diffusivity of *n*-alkanes in the MFI-type frameworks of ZSM-5[54] and silicalite-1,[55, 56] as a function of the hydrocarbon chain length.[57] In both frameworks, the jump-diffusion model of Singwi and Sjölander gave the best fit to the QENS spectra of the *n*-alkanes (300 K, < 1 molecule per unit cell).[54, 55] The diffusion coefficient was universally diminished with increasing hydrocarbon chain length, although a large drop in *n*-alkane diffusivity from $n = 6$ to $n = 8$ in ZSM-5 (**Figure 4.1.5 a**)[54] was not observed in silicalite-1.[55] Nonetheless, in both frameworks the diffusivity the longer *n*-alkanes ($n \geqslant 8$), decreased near-linearly with an increasing number of carbon atoms (**Figure 4.1.5 b**).[54, 55]

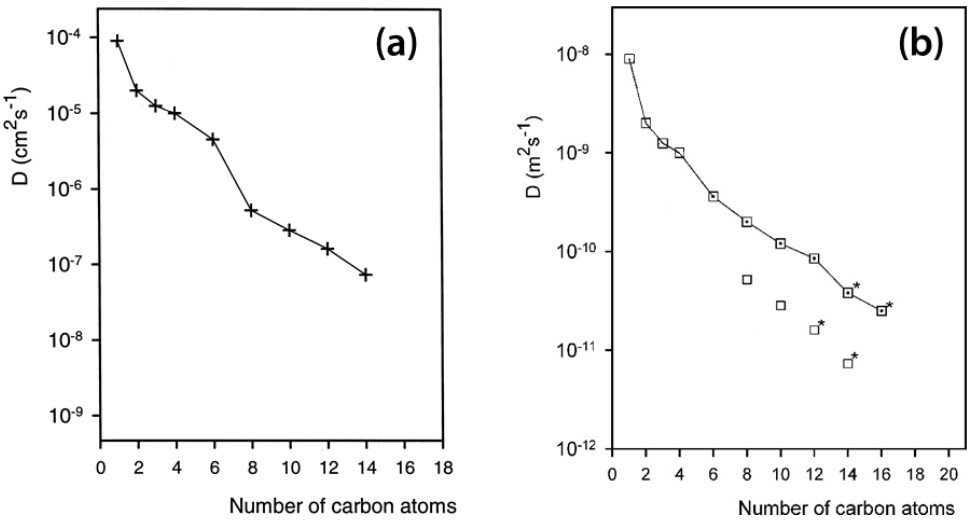

Figure 4.1.5: (a) Self-diffusion coefficients of *n*-alkanes in Na-ZSM-5 obtained from QENS measurements at 300 K.[54] Figure adapted from with permission of Elsevier. **(b)** Self-diffusion coefficients of *n*-alkanes in (□) Na-ZSM-5 and (⊡) silicalite-1 obtained from QENS measurements at 300 K.[55] Asterixed points correspond to extrapolation to 300 K. Figure adapted with permission of The American Chemical Society.

The QENS analyses indicated that the self-diffusivities of the longer hydrocarbons (n = 8 - 14) were 4 – 5 times lower in Na-ZSM-5 than in silicalite-1, which was attributed to Na^+ in the MFI channels hindering the movement of the alkanes.[28, 56] The increased sterics of branched alkanes has also been evidenced by QENS studies, namely the diffusion coefficient of *n*-butane in ZSM-5 was calculated to be 3 orders of magnitude larger than for isobutane sorbed in the same framework.[54, 58]

Recently, QENS has been used to probe the diffusion of methanol in H-ZSM-5 zeolite in the context of the methanol-to-hydrocarbon (MTH) process.[59, 60] Interestingly, QENS analysis indicated that the methanol adsorbed in H-ZSM-5 was completely immobilised (on the time-scale of the spectrometer) at 298 K.[60] A complementary inelastic neutron scattering (INS) experiment revealed that when the methanol was adsorbed in H-ZSM-5, the vibrational modes of the hydroxyl group were eliminated, whilst the deformation of the methyl group was retained. It was thus concluded that the methanol adsorbate had effected near-instantaneous methylation of the framework Brønsted acid sites at room temperature (**Figure 4.1.6**).

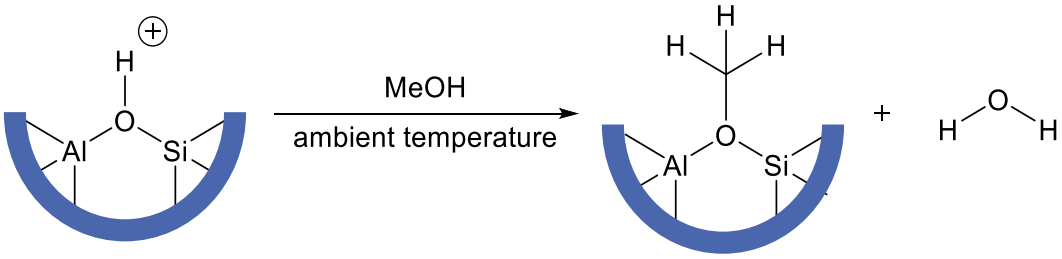

Figure 4.1.6: A scheme for the room temperature methoxylation of a Brønsted acid site of the H-ZSM-5 framework (represented in blue).

A subsequent investigation was undertaken to investigate the mass transport characteristics of the H-ZSM-5 catalyst after its application in the MTH reaction. When methanol was adsorbed in ZSM-5 after it had catalysed the MTH reaction for 72 hours at 623 K, the QENS spectrum at 325 K showed no quasi-elastic broadening. Although the immobility of methanol was consistent with the framework methylation observed in fresh ZSM-5, the reduced pore volume and methanol uptake at room temperature indicated partial (~ 30 %) blockage of the micropores due to coking. In contrast, QENS revealed significant methanol dynamics in ZSM-5 after 72 hours in the MTH reaction at 673 K. Specifically, localised motion of methanol was characterised as a mobile fraction (42 %) undergoing isotropic rotation with a rotational diffusion coefficient of 3×10^{10} s^{-1}. In this case, the increased mobility of methanol was attributed to the development of mesoporosity in the ZSM-5 catalyst (caused by dealumination under the higher-temperature MTH conditions), which created sufficient space for the mobile fraction to rotate freely.

QENS has also been used to investigate the role of diffusion in other industrially significant catalytic processes, including the production of *para*-xylene - an important feedstock in polymer industry.[28, 61] Typically, high purity *p*-xylene is produced by a combination of selective isomerisation and efficient separation from the mixture of C_8 aromatics. The separation of *p*-xylene has been achieved by selective adsorption into cation-exchanged zeolites X and Y, with an appropriate counter-cation.[62, 63] For example, Ba-X zeolite will preferentially adsorb *p*-xylene from a mixture of C_8 aromatics, whereas Na-X zeolite shows no such selectivity. It was proposed that the mobility of the sorbate was a factor in the zeolite selectivity, and so to investigate the role of the counter-cation, Jobic *et al.* used QENS to study the dynamics of *para*- and *meta*-xylene in Na-X and Ba-X zeolites.[30] The authors reported that on the time-scales of localised motion, the aromatic ring of *p*-xylene was immobile in the Ba-X zeolite, and only methyl rotation (*via* three-site jump rotation) was detected at 460 K. However, in the same zeolite, *m*-xylene exhibited not only methyl rotation, but also rotation about the *pseudo*-C_6 molecular axis (**Figure 4.1.7**). The same rotational behaviour was also observed for *p*- and *m*- xylenes in Na-X, although the amplitude of their rotations was larger than in Ba-X, indicating that the π-electron density interacted more strongly with Ba^+ than Na^+. However, unlike in Ba-X, in the Na-X zeolite *p*-xylene was more mobile than *m*-xylene.

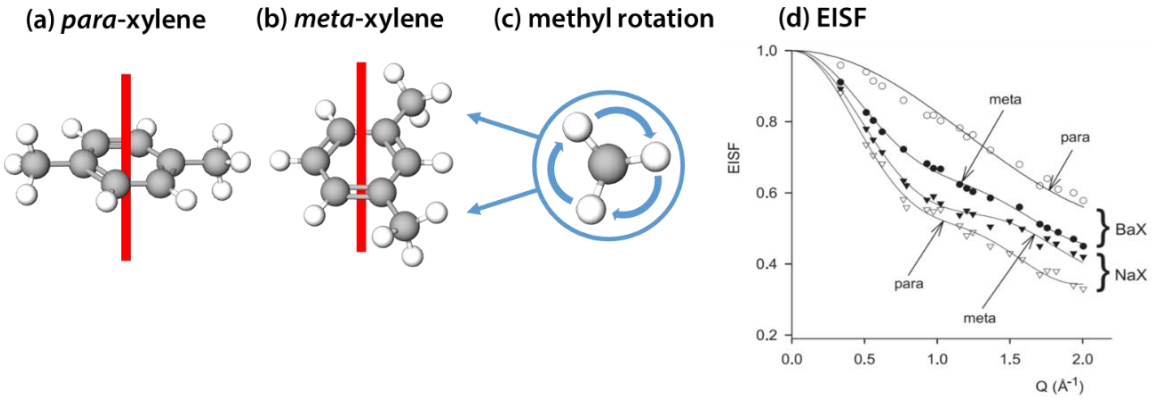

Figure 4.1.7: A depiction of the *pseudo*-C_6 axis of **(a)** *para*-xylene and **(b)** *meta*-xylene, and **(c)** the three-site jump rotation of their methyl groups. **(d)** The experimental (points) and calculated (solid lines) EISFs of (○) *p*-xylene in Ba-X (●) *m*-xylene in Ba-X, (▼) *m*-xylene in Na-X, and (▽) *p*-xylene in Na-X zeolites at 460 K.[30] The EISF of *p*-xylene in Ba-X was simulated using a three-site jump rotation model for both methyl groups. The EISFs of *m*-xylene in Ba-X, *m*-xylene in Na-X, and *p*-xylene in Na-X were simulated with rotation about the *pseudo*-C_6 molecular axis, superimposed on the three-site jump rotation of the methyl groups. Figure reproduced with permission from Elsevier.

At a longer time-scale, the translation of the xylenes in Na-X zeolite was characterised by jump diffusion (Singwi-Sjölander) between the zeolite supercages. In this case, the calculated

diffusivity of *p*-xylene in Na-X was higher than for the *m*-xylene isomer. In contrast, the long-range mobility of the xylenes was so restricted in the Ba-X zeolite that any inter-cage diffusion was too slow to be measured (> 10 ns). Thus, it was concluded that the interaction of *p*- and *m*-xylenes was stronger with the Ba^{+} than Na^{+}, and that the selectivity of Ba-X zeolite was due to stronger interaction with the aromatic ring of the *para*-isomer.

4.1.1.4 QENS studies of hierarchical zeotypes

The strong interdependence of zeolite topology and adsorbate dynamics plays an important role in determining the nature and rate of reactions that occur within a molecular sieve catalyst. Whilst it is possible to effect highly-selective transformations by employing a microporous catalyst, this is typically at the expense of molecular flux.[18] Here, a hierarchically-porous (HP) zeotype, possessing both micro- and meso-pores, may provide a balance between increased mass transport and high reaction selectivity.[64] Despite their increasing prevalence in catalysis, to the best of our knowledge, there has been no direct observation of microscopic, mass transport phenomena in a templated, hierarchically-porous zeotype.

4.2 Aims

Hierarchical porosity has been shown to improve the activity and lifetime of SAPO catalysts in the Beckmann rearrangement.[65-67] In many cases, the superior performance of the HP SAPO has been attributed to enhanced mass transport, in particular the improved access to internal active sites, and the increased resistance to deactivation by coking. However, a recent spectroscopic and computational study of organosilane-templated HP SAPO-34 has revealed the catalytic potential of the siliceous mesopore network (**Chapter 3**). In this case, the role of the mesopores was proposed to be two-fold, as both the acidic and mass transport properties of the microporous framework were modified by soft-templating. Under ambient-to-low temperature conditions, the weakly acidic silanol sites in the siliceous mesopores were found to activate the oxime substrate *via* hydrogen bonding interactions, whilst the larger mesopore network improved access to the stronger Brønsted sites in the micropores.

In the earlier investigation of HP SAPO-34, the improved mass transport properties of the hierarchical pore network were inferred on the basis of the substrate-framework interactions; specifically the interaction of cyclohexanone oxime with otherwise inaccessible Brønsted sites in the micropores. However, a more targeted study of oxime mobility was proposed, seeking a better insight into the mass transport properties of the HP framework, and further evidence of substrate-framework interactions. It was considered that the mobility of the rearrangement product, ε-caprolactam, was also crucial in understanding the role of mass transport in the BR , since the selectivity of porous, acid catalysts has often been linked to the ease of desorption and diffusion of the product.[68-71] Hence, the mobility of both cyclohexanone oxime and caprolactam were investigated by QENS; a technique well-suited to studying the motion of hydrogenous sorbates confined within porous matrices.[53]

For this undertaking, the one-dimensional AFI framework[72] of SAPO-5 was chosen as the 7.3 Å diameter micropores were expected to allow intracrystalline diffusion of both oxime and lactam (kinetic diameter ~ 6 Å).[70] As well as assessing the temperature-dependence of the sorbate mobility *via* an elastic window scan, detailed QENS analyses were performed at 373 K to characterise and quantify the motions of both sorbates. Some preliminary total neutron scattering experiments were also undertaken (exploiting the neutron contrast between the pore walls and a filled *versus* an empty pore space) to investigate the uptake of cyclohexanone oxime in MP and HP SAPO-5. Specifically, the total scattering studies aimed to establish whether the adsorption of oxime from the ambient-temperature, physical mixture (**Chapter 3**) occurred for both MP and HP SAPO-5 (which might be expected on the basis of

the micropore diameter), or whether this process was driven by interaction with the silanols in the organosilane-templated mesopores.

4.3 Experimental

4.3.1 HP SAPO-5 synthesis

The synthesis of HP SAPO-5 and MP SAPO-5 followed the same procedure, except that the latter did not include the addition of dimethyloctadecyl[(3-(trimethoxysilyl)propyl] ammonium chloride.

Phosphoric acid (85 wt. % in H_2O, 11.4 mL, Sigma Aldrich) and deionised water (50 mL) were added to a Teflon beaker and stirred. Aluminium isopropoxide (34.0 g, Sigma Aldrich) was ground in a pestle and mortar, before being added gradually to the reaction mixture. The gel was stirred for 1.5 hours. Dimethyloctadecyl[(3-(trimethoxysilyl)propyl] ammonium chloride (DMOD, 72 wt. % in H_2O, 6.0 mL, Sigma Aldrich) was added dropwise to the gel, followed by triethylamine (TEA, 18.5 mL, Sigma Aldrich), also dropwise. Deionised water (100 mL) was added to the gel, which was then stirred for 1 hour. Ludox AS-40 colloidal silica (40 wt. % suspension in H_2O, 3.86 mL, Sigma Aldrich) was added dropwise to the gel, before 1.5 hours of stirring.

The gel was transferred to a Teflon-lined, stainless steel reactor and crystallised at 200 °C for 24 hours. The reactor was allowed to cool to ambient temperature before its contents were removed and distributed between 4 x 100 mL centrifuge tubes. The solid in each tube was washed 3 times with deionized water at 10,000 rpm, and then dried overnight in an oven at 80 °C. The solid (~ 32 g) was calcined in batches (~ 2 g) by heating to 550 °C (ramp rate of 2 °C min^{-1}) for 16 hours.

Table 4.3.1: The synthesis gel ratio and empirical elemental composition of the calcined MP SAPO-5 and HP SAPO-5 catalysts.

Catalyst	Gel Composition	ICP-OES elemental analysis
HP SAPO-5	1 Al: 1 P: 0.15 Si : 0.8 TEA : 0.05 DMOD : 55 H_2O	16.76 wt. % Al; 17.45 wt. % P; 5.8 wt. % Si
MP SAPO-5	1 Al: 1 P: 0.15 Si : 0.8 TEA : 55 H_2O	18.43 wt. % Al; 19.30 wt. % P; 1.45 wt. % Si

4.3.2 Characterisation

Powder X-ray diffraction patterns were acquired using a Bruker D2 diffractometer with Cu $K_{\alpha 1}$ radiation. Unit cell refinements were performed using the CelRef software.[73]

Nitrogen adsorption measurements were performed at 77K using the Micromeritics Gemini 2375 Surface Area Analyser. Samples were degassed, under vacuum, at 120 °C for 12 hours prior to measurement.

For ICP-OES elemental analysis, samples were subject to HNO_3/H_2O_2 digestion before analysis in the Varian Vista MPX CCD Simultaneous Axial ICP-OES.

NH_3-TPD measurements were performed using the Quantachrome Autosorb iQ-Chemi apparatus. Catalysts were pre-treated at 150 °C under a flow of helium gas for 2 hours. The samples were then dosed with ammonia gas for three hours at 100 °C, before desorption under a flow of helium gas, with a temperature ramp of 10 °C min^{-1} up to 600 °C.

SEM images were acquired on the JEOL JSM-6500F field-emission gun SEM, which operates at 0.5 - 30 kV with resolution of 1.5 nm, and a magnification of 10 - 400,000x.

4.3.2.1 Quasi-elastic neutron scattering (QENS) experiments

QENS experiments were performed with the time-of-flight backscattering neutron spectrometer OSIRIS[74] at the ISIS Pulsed Neutron and Muon Source.[75] Pyrolitic graphite 002 analyser crystals were used giving an energy resolution of 24.5 μeV, and energy transfers were measured in a window of ±0.55 meV. The detector *Q*-range was 0.2–1.7 $Å^{-1}$. The diffraction detector bank on OSIRIS was used for simultaneous diffraction measurements during QENS experiments.

The calcined catalysts were dried in an Inconel can at 250 °C under a flow of He gas. In a glove box under Ar atmosphere, the empty SAPOs and SAPO-sorbate mixtures (prepared in the glove box as a 1:10 physical mixture by mechanical mixing) were transferred to an annular, Al can. In turn, each cell was placed in the top-loading closed cycle refrigerator. In the case of a catalyst-sorbate mixture, the sample was heated to 363 K *in situ* to melt the sorbate and encourage its uptake into the SAPO pores. (The melting point of cyclohexanone oxime was 86 - 89 °C,[76] and ε-caprolactam was 68 - 71 °C).[77] All samples were cooled to < 10 K for a resolution measurement, and then heated to 373 K in step of 10 K. At each step, a short, signal measurement was collected for an elastic window scan. Longer measurements were acquired

at 10 K and 373 K with sufficient statistics for full QENS analyses. In the analysis of the QENS data, the measurement of the empty SAPO framework was subtracted from the corresponding loaded-SAPO, so that the signal from the sorbate could be extracted and any scattering from the aluminium container was removed. QENS spectra were fitted using the neutron scattering analysis software DAVE[78] and MANTID[79].

4.3.2.2 Total neutron scattering experiments

Total neutron scattering experiments were performed on the time-of-flight spectrometer NIMROD,[80] at the ISIS Pulsed Neutron and Muon Source.[75] NIMROD uses wavelengths in the range 0.04 - 12 Å to measure over a continuous length scale from < 1 to > 300 Å, with a resolution of the order of ~0.1 Å. A *Q*-range of 0.02– 50.0 $Å^{-1}$ is probed at ~ 4 % resolution.

The calcined catalysts were dried in an Inconel can at 250 °C under a flow of He gas. In a glove box under Ar atmosphere, the empty SAPOs, and the SAPO-cyclohexanone oxime mixtures (prepared in the glove box as a 1:10 physical mixture by mechanical mixing) were transferred to a flat-plate, thin-walled titanium-zirconium alloy pressure-cell. The cell was attached to a centre-stick and transferred to the closed-cycle refrigerator (CCR). In the case of the empty framework, scattering measurements were performed at 150, 300, and 373 K. For the catalyst-oxime mixtures, a preliminary measurement was performed at 300 K, before the sample was heated to 373 K to melt the oxime. Measurements were then acquired as the samples were cooled gradually to 150 K. For data correction, neutron scattering spectra were also collected for the empty instrument, the empty sample can, and a vanadium standard. Data processing was performed using the Gudrun program.[81]

4.3.3 Catalysis

4.3.3.1 The liquid-phase Beckmann rearrangement

A portion of calcined catalyst was degassed by heating overnight at 120 °C, under vacuum. A 3-neck round bottom flask was charged with a stirrer bar, cyclohexanone oxime (0.1 g, Sigma Aldrich), anhydrous chlorobenzene (internal standard, 0.1 g, Sigma Aldrich), dried catalyst (0.1 g), and anhydrous benzonitrile (20 mL, Sigma Aldrich). The reaction vessel was sealed with a rubber septum, glass stopper, and reflux condenser. The reaction was transferred to a pre-heated oil bath at 130 °C and stirred under a constant nitrogen atmosphere. Aliquots of

the reaction mixture were extracted hourly over a 6 hour reaction period, and analysed by gas chromatography using the Clarus 480 apparatus with flame ionisation detector and an Elite 5 column. Products were identified using authenticated standards, and quantified against the internal standard, chlorobenzene.

4.4 Results and discussion

4.4.1 Catalyst characterisation

SAPO-5 catalysts were synthesised using the protocol described by Newland *et al.*,[65] with an amphiphilic organosilane[82] used to template the mesopores of the hierarchical sample. Powder XRD analyses confirmed that hierarchical (HP) and microporous (MP) SAPO-5 were phase-pure after calcination, and that both materials retained the AFI structure in the bulk (**Figure 4.4.1**).

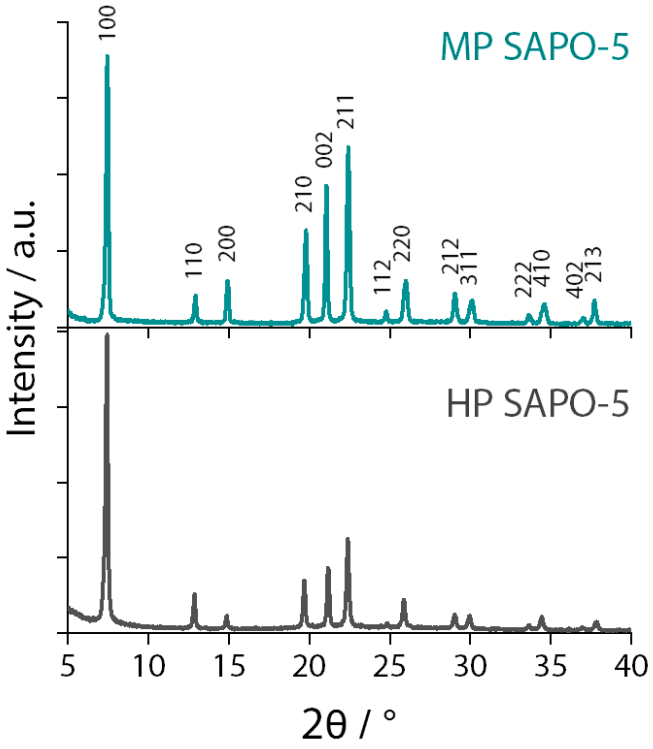

Figure 4.4.1: The indexed powder XRD patterns of MP SAPO-5 and HP SAPO-5 were consistent with an AFI structure and confirmed that the catalysts were phase-pure.

Subsequent refinement of the hexagonal lattice parameters indicated that the mesopore-templating protocol had negligible impact on the dimensions of the SAPO-5 unit cell (**Table 4.4.1**, **Table 4.4.2** and **Table 4.4.3**). In addition, the characteristic, hexagonal morphology of SAPO-5[83-85] was visualised in HP SAPO-5[65] by scanning electron microscopy (SEM, **Figure 4.4.2**).

Table 4.4.1: Unit cell refinements for MP SAPO-5.

λ /Å	*a* / Å	*b* / Å	*c* / Å	α / °	β / °	γ / °	Volume / Å³
1.5406	13.7151	13.7151	8.4338	90	90	120	1373.9
0	0.0188	0	0.0016	0	0	0	
h	***k***	***l***	**2θ(Obs) / °**	**2θ-Zero / °**	**2θ(Cal) / °**	**Dif. / °**	
0	1	0	7.453	7.453	7.4368	0.0162	
1	1	0	12.923	12.923	12.8992	0.0238	
0	2	0	14.908	14.908	14.9052	0.0028	
1	2	0	19.79	19.79	19.76	0.03	
0	0	2	21.046	21.046	21.0507	-0.0047	
1	2	1	22.403	22.403	22.417	-0.014	
1	1	2	24.773	24.773	24.7658	0.0072	
2	2	0	25.968	25.968	25.9655	0.0025	
1	2	2	29.047	29.047	29.0283	0.0187	
0	4	0	30.121	30.121	30.0704	0.0506	

Table 4.4.2: Unit cell refinements for HP SAPO-5.

λ /Å	*a* / Å	*b* / Å	*c* / Å	α / °	β / °	γ / °	Volume / Å³
1.5406	13.7651	13.7651	8.3894	90	90	120	1376.6
0	0.0135	0	0.0013	0	0	0	
h	***k***	***l***	**2θ(Obs) / °**	**2θ-Zero / °**	**2θ(Cal) / °**	**Dif. / °**	
0	1	0	7.433	7.433	7.4098	0.0232	
1	1	0	12.862	12.862	12.8521	0.0099	
0	2	0	14.867	14.867	14.8508	0.0162	
1	2	0	19.668	19.668	19.6875	-0.0195	
0	0	2	21.147	21.147	21.1634	-0.0164	
1	2	1	22.383	22.383	22.3794	0.0036	
1	1	2	24.854	24.854	24.8376	0.0164	
2	2	0	25.887	25.887	25.8695	0.0175	
1	3	1	29.027	29.027	29.005	0.022	
0	4	0	29.939	29.939	29.9586	-0.0196	

Table 4.4.3: The optimised unit cell parameters for MP SAPO-37 and HP SAPO-37 catalysts.

Catalyst	Lattice Parameters				Space Group	Unit Cell Volume / Å³
	***a* = *b* / Å**	***c* / Å**	**α = β / °**	**γ / °**		
MP SAPO-5	13.72	8.43	90	120	P6cc	1374
HP SAPO-5	13.76	8.39	90	120		1377

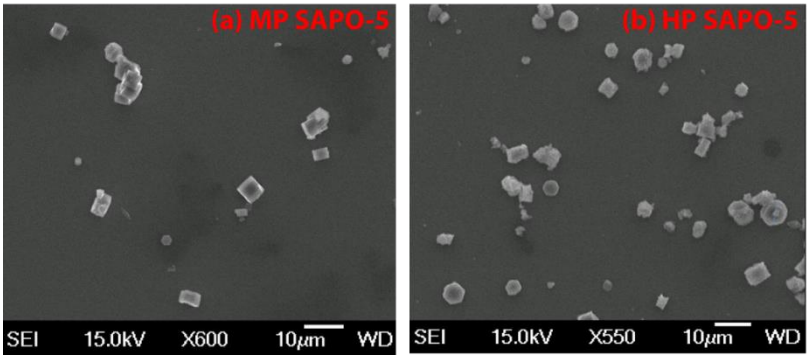

Figure 4.4.2: SEM images of **(a)** MP SAPO-5 and **(b)** HP SAPO-5.

Nitrogen adsorption-desorption measurements revealed some significant differences in the textural properties of the HP and MP SAPO-5 catalysts (**Figure 4.4.3**). The Type IV isotherm of HP SAPO-5 gave an indication of its mesoporosity, since the Type H4 hysteresis was consistent with the presence of narrow mesopores.[86] Subsequent BJH analysis of the adsorption branch of HP SAPO-5 yielded a narrow pore size-distribution, centred at 3.5 nm, which is typical for mesopores templated by the DMOD organosilane.[82] Whilst the N_2 isotherm of MP SAPO-5 was slightly hysteretic (Type H3),[86] this was attributed to intercrystalline mesoporosity (i.e. gas adsorption between aggregates of MP SAPO-3 crystallites).[65] Otherwise, the sharp uptake of gas at low partial pressure (due to micropore filling), followed by a long plateau (due to limited multi-layer adsorption) characterised the Type I isotherm of a microporous material.[86]

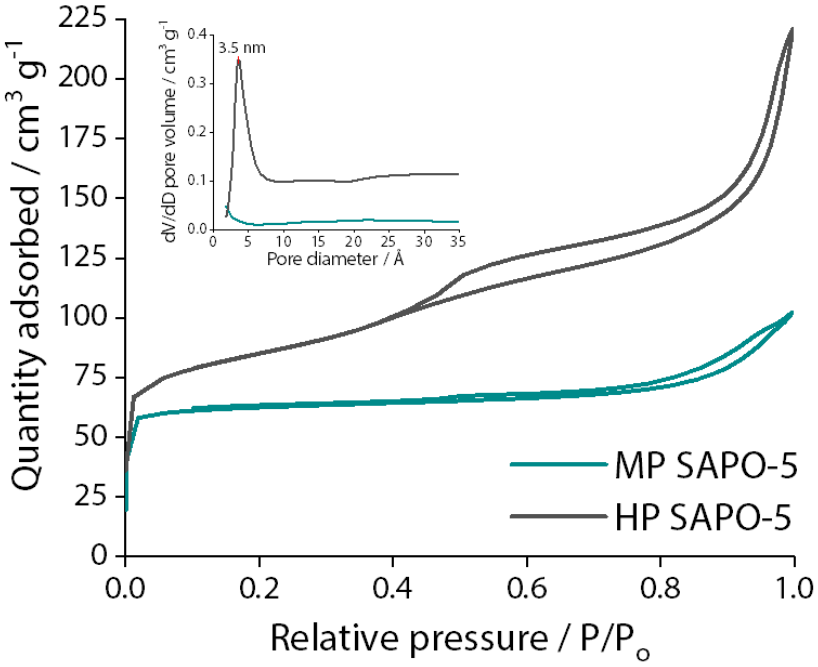

Figure 4.4.3: The N_2 gas adsorption-desorption isotherms of MP SAPO-5 (Type I isotherm, Type H3 hysteresis) and HP SAPO-5 (Type IV isotherm, Type H4 hysteresis), with their respective BJH adsorption pore-size distributions, inset.

Quantitative analysis of the N_2 sorption data (**Table 4.4.4**) returned a BET surface area of 259 $m^2\ g^{-1}$ for MP SAPO-5 and 283 $m^2\ g^{-1}$ for HP SAPO-5. The higher surface area of HP *versus* MP SAPO-5 was consistent with the reported trend for organosilane-templated zeotypes.[65, 82, 87-91] Furthermore, a quantifiable mesopore volume and relatively large external (i.e. non-microporous)[86] surface area provided additional evidence of mesoporosity in HP SAPO-5.[91]

Table 4.4.4: The textural properties of MP SAPO-5 and HP SAPO-5 determined by N_2 adsorption-desorption studies.

Catalyst	BET surface area / $m^2\ g^{-1}$	Micropore volume / $cm^3\ g^{-1}$	Mesopore volume / $cm^3\ g^{-1}$	External surface area / $m^2\ g^{-1}$	BJH mesopore diameter / Å
MP SAPO-5	259	0.11	-	33	-
HP SAPO-5	283	0.07	0.20	111	35

The acid characteristics of the SAPO catalysts were assessed by the temperature-programmed desorption of ammonia (NH_3-TPD) The fitted spectra are reported in **Figure 4.4.4**.

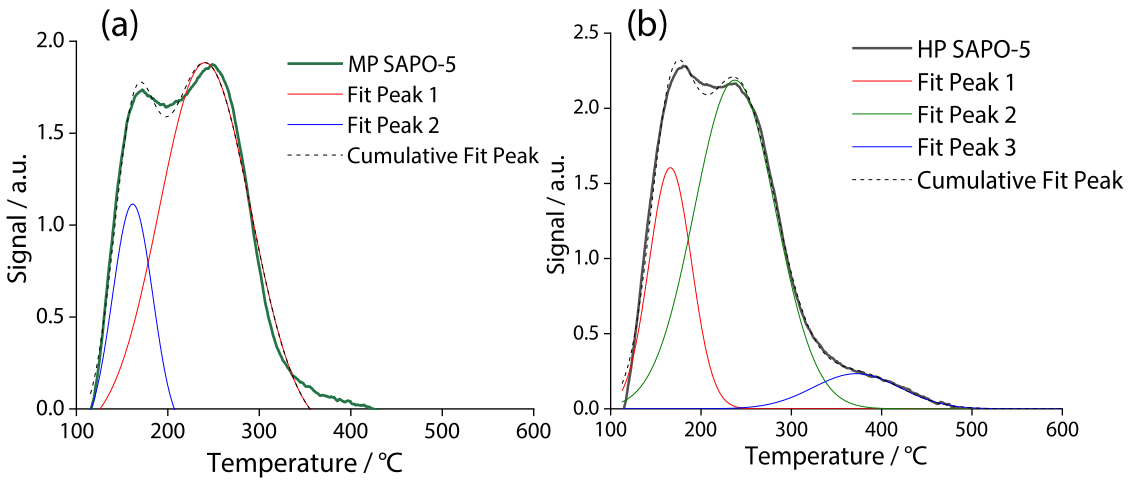

Figure 4.4.4: The fitted NH_3-TPD profiles of **(a)** MP SAPO-5 and **(b)** HP SAPO-5, acquired at a ramp rate of 10 °C min^{-1}, after dosing with NH_3 gas at 100 °C for 3 hours.

The NH_3-TPD profiles of MP and HP SAPO-5 were quite alike, with two desorption maxima occurring at a similar temperature for both frameworks (**Figure 4.4.5**).

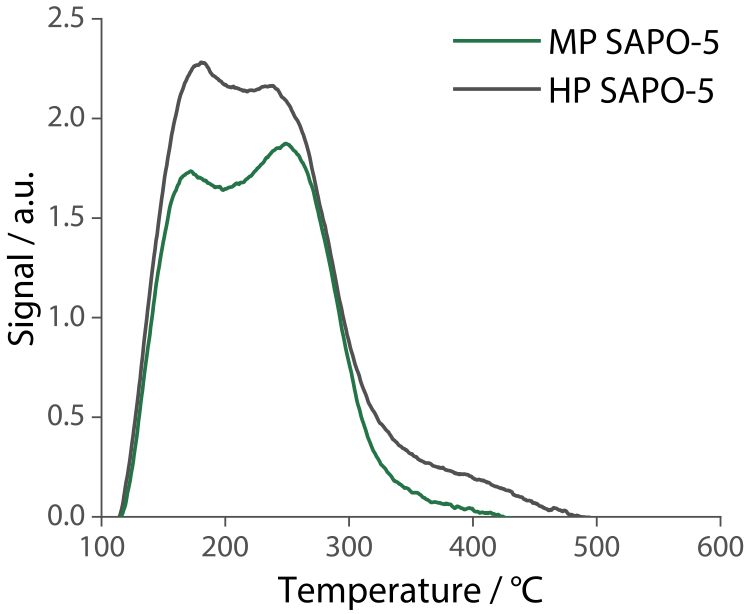

Figure 4.4.5: The NH_3-TPD profiles of MP SAPO-5 and HP SAPO-5, acquired at a ramp rate of 10 °C min^{-1}, after dosing with NH_3 gas at 100 °C for 3 hours. Spectra not mass normalised.

The first peak, observed at 170-180 °C, was assigned to the loss of ammonia that was physisorbed within the SAPO pores, or weakly bound to defect sites (e.g. P-OH, Al-OH, Si-OH).[92, 93] The second desorption (with a maximum at 248 °C in MP SAPO-5 and 237°C in HP SAPO-5) was attributed to the loss of ammonia from moderately acidic, bridging Brønsted sites in the bulk (i.e. from Type II and Type III substitution of Si(IV)).[65] In this case, the slightly lower desorption temperature of HP SAPO-5 identified the acid-strength moderation caused by the siliceous mesopores.[94-96] However, HP SAPO-5 also contained a small number of strong acid sites, which were identified by the elevated temperature for complete ammonia desorption *versus* MP SAPO-5 (**Table 4.4.5**). This strong acidity in HP SAPO-5 was attributed to the mesopore-templating process, where this causes structural distortions or defect sites in proximity to a Brønsted centre.[97]

Table 4.4.5: Quantitative analysis of NH_3-TPD data for MP and HP SAPO-5, including temperatures for the onset of NH_3 desorption and the loss of weakly and more strongly bound NH_3, and the total quantity of ammonia desorbed between 100 – 600 °C.

Catalyst	Onset of ammonia desorption / °C	Peak maximum for loss of weakly-bound NH_3 / °C	Peak maximum for loss of more strongly-bound NH_3 / °C	Completion of NH_3 desorption / °C	Total quantity of NH_3 desorbed < 600 °C / (mmol NH_3) (g^{-1} catalyst)
MP SAPO-5	115	172	248	430	0.42
HP SAPO-5	115	178	237	495	0.41

Catalytic testing was also employed for materials characterisation, where it was used to assess the impact of the auxiliary mesopore network on the mass transport and acidic properties of SAPO-5. Previous studies have revealed that organosilane-templated mesopores in SAPO-5 improve catalytic activity in the vapour-phase Beckmann rearrangement (BR) of cyclohexanone oxime at 325 °C.[65] It was reported that the reactive characteristics of the SAPO-5 catalyst were retained, but the mesopore network improved resistance to deactivation by coking. In this investigation, the vapour-phase activity of MP and HP SAPO-5 was not considered representative of the mass transport effects that would be active at the temperatures (< 373 K) used for the QENS study. Illustratively, microporous SAPO-34 is a highly active catalyst in the vapour-phase BR (325 °C),[65, 66] even though cyclohexanone oxime cannot access the active sites within the micropores. However, in the liquid-phase BR (130 °C, **Chapter 3**) oxime conversion is severely retarded by slow diffusion to/from the limited number of active sites on the surfaces of the MP SAPO-34 crystallites. It was thus proposed that the liquid-phase BR would provide a better insight into the relationship between pore-structure and catalyst activity for subsequent diffusion studies.

The influence of the mesopores was evident in the liquid-phase Beckmann rearrangement of cyclohexanone oxime (**Figure 4.4.6**), with HP SAPO-5 achieving 54 % conversion by six hours, *versus* the 34 % conversion of its microporous analogue. The increased activity of HP SAPO-5 alluded to increased intracrystalline diffusion in the HP catalyst, and an increased turnover at the internal active sites.[98] In addition, HP SAPO-5 sustained a considerably higher selectivity (86 - 90 %) for ε-caprolactam than MP SAPO-5 (65 – 72 %). However, under liquid-phase conditions, silanol sites (such as those in the mesopores) have been found to be too weakly acidic to catalyse the BR, instead promoting the formation of hydrolysis product (cyclohexanone).[99-101] It was thus proposed that the increased selectivity of HP SAPO-5 *versus* MP SAPO-5 was due to the few, strong acid sites that were identified by NH_3-TPD. Previous computational studies (**Chapter 3**) have revealed an energetic driving force for the cyclohexanone oxime molecule to desorb from a weakly acidic silanol site (such as those in the HP SAPO-5 mesopore) in favour of interaction with a stronger, Brønsted acid site (such as those in the SAPO-5 micropore).

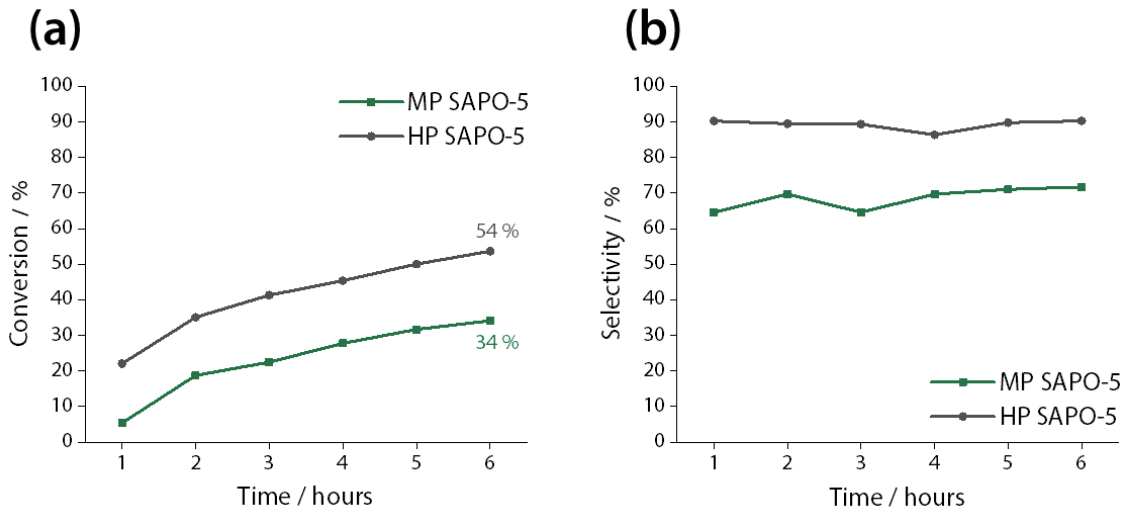

Figure 4.4.6: (a) The conversion of cyclohexanone oxime and **(b)** selectivity towards ε-caprolactam in the liquid-phase Beckmann rearrangement (130 °C, benzonitrile solvent) catalysed by MP SAPO-5 and HP SAPO-5. Cyclohexanone was the only by-product.

4.4.2 Neutron scattering studies

4.4.2.1 The diffusion of cyclohexanone oxime in hierarchical and microporous SAPO-5

To reliably quantify the diffusive behaviour of cyclohexanone oxime by QENS, it was important that the substrate remained unreacted over the temperature range of the experiment. However, at the elevated temperatures required to melt cyclohexanone oxime into the SAPO framework (< 373 K), there was potential for a catalytic transformation. As such, the activity of HP SAPO-5 was investigated under conditions for the liquid-phase BR at 100 °C. Since no substrate was converted within 5 hours at 100 °C, the molecular motion detected by QENS was attributed to the oxime.

To study the temperature-dependent mobility of cyclohexanone oxime in HP and MP SAPO-5, an elastic window scan (elwin) was performed. The elwins in **Figure 4.4.7** show how the elastic scattering intensity changed as a function of temperature in the range of 40 - 373 K. Since an increase in molecular motion causes a decrease in the elastic intensity of the QENS peak, this can be detected as a downward gradient in the elwin.

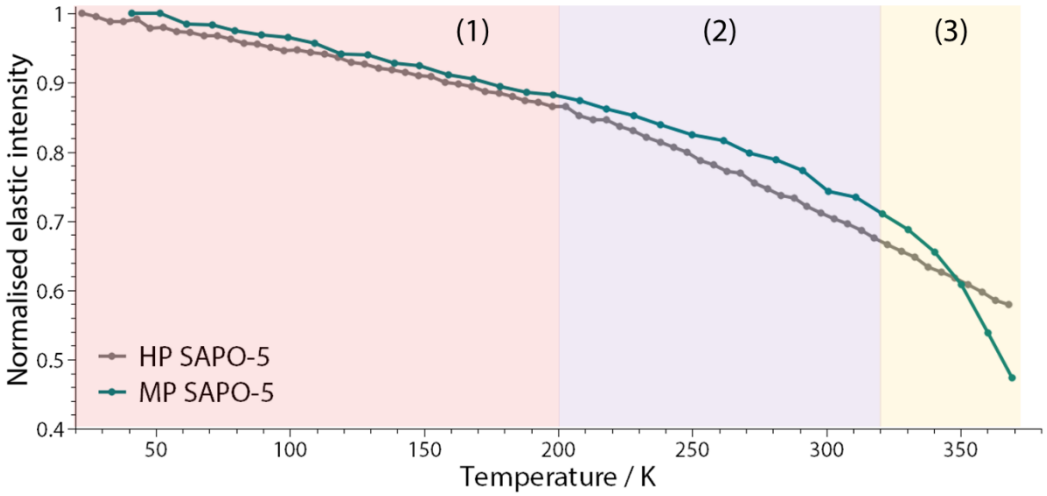

Figure 4.4.7: The elastic window scans (averaged over all *Q*-values) of cyclohexanone oxime sorbed in MP SAPO-5 (blue line) and HP SAPO-5 (grey line) in the temperature range of 40 - 373 K. Three regimes are highlighted: **(1)** the freedom of motion of the oxime is comparable in MP and HP SAPO-5; **(2)** the freedom of motion of the oxime is higher in HP SAPO-5 than MP SAPO-5; **(3)** the freedom of motion of the oxime is higher in MP SAPO-5 than HP SAPO-5. Data acquired on the OSIRIS spectrometer.[74]

To differentiate the motion of oxime in HP and MP SAPO-5 three temperature regimes were defined. At < 200 K (**Figure 4.4.7 (1)**), the mobility of cyclohexanone oxime was largely comparable in MP and HP SAPO-5, which reflected the limited movement of sorbate in a system with low thermal energy. However, as the temperature was increased from 200 – 320 K (**Figure 4.4.7 (2)**) the oxime was more mobile in HP SAPO-5 relative to MP SAPO-5, which was consistent with a greater freedom of mobility for oxime sorbed within a mesopore. Significantly, at temperatures in excess of 320 K (**Figure 4.4.7 (3)**) the trend was reversed, and the oxime became more mobile in MP SAPO-5 than HP SAPO-5. In fact, the sharp decline in the MP SAPO-5 elwin at ~ 340 K was indicative of bulk substrate melting, which suggested that at least a fraction of the oxime was outside the micropores.

To gain further insight into the oxime dynamics, the elwins were studied at various momentum transfers (Q), in order to probe the freedom of movement over different spatial-length scales. In particular, elwins at Q = 0.54, 1.21, and 1.68 Å^{-1} were used to study larger (~ 10 Å), intermediate (~ 5 Å), and localised oxime motions, respectively (**Figure 4.4.8**).

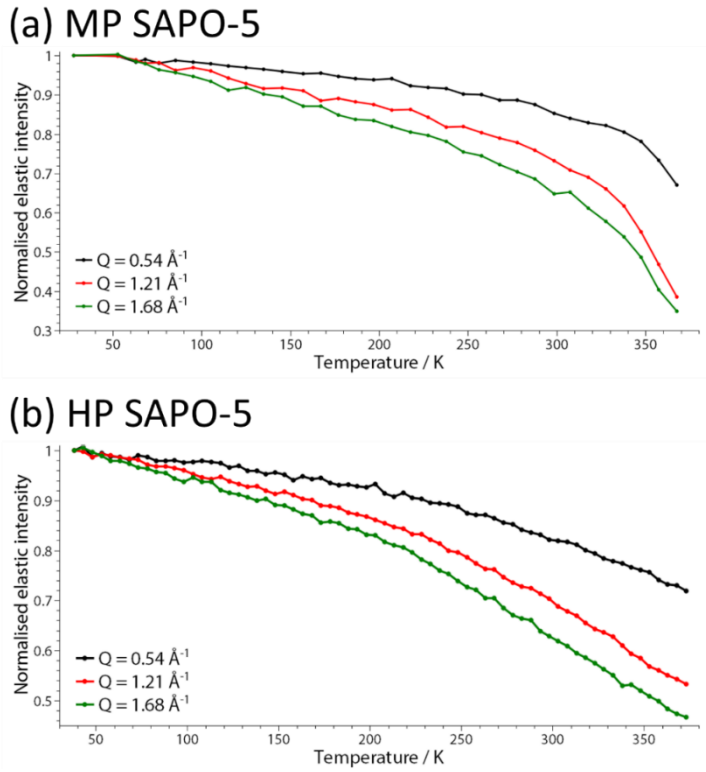

Figure 4.4.8: The elastic window scans of cyclohexanone oxime sorbed in **(a)** MP SAPO-5 and **(b)** HP SAPO-5 for Q = 0.54 Å^{-1} (black line), Q = 1.21 Å^{-1} (red line), and Q = 1.68 Å^{-1} (green line), in the temperature range of 40 - 373 K. Data acquired on the OSIRIS spectrometer.[74]

In both HP and MP SAPO-5, the proportion of mobile protons increased in the order: Q = 0.54 Å^{-1} < Q = 1.21 Å^{-1} < Q = 1.68 Å^{-1}, which indicated that localised motions made the largest contribution to the total oxime mobility. For MP SAPO-5 in particular, the steep increase in mobile oxime at > 300 K was more significant for Q = 1.21 and 1.68 Å^{-1} than Q = 0.54 Å^{-1}, revealing the predominance of mid-range and localised motions at higher temperature.

The crossover point of the HP and MP SAPO 5 elwins was also of significance, as it marked the temperature at which cyclohexanone oxime transitioned from being more mobile in HP SAPO-5, to being more mobile in MP SAPO-5. As depicted in **Figure 4.4.9**, the temperature of the crossover point occurred at 353 K for Q = 0.54 Å^{-1}, but at 338 K for Q = 1.21 and 1.68 Å^{-1}. The higher crossover temperature at low-Q indicated that more thermal energy was needed to increase the amount of long-range motion in MP SAPO-5 to match that in HP SAPO-5. The larger fraction of long-range translation in HP SAPO-5 was thought to reflect the less

restricted diffusion of oxime within the mesopores of HP SAPO-5, relative to the micropores of MP SAPO-5. Noticeably less thermal energy was required to equalise the fraction of oxime molecules undergoing intermediate-length or local motions in MP and HP SAPO-5.

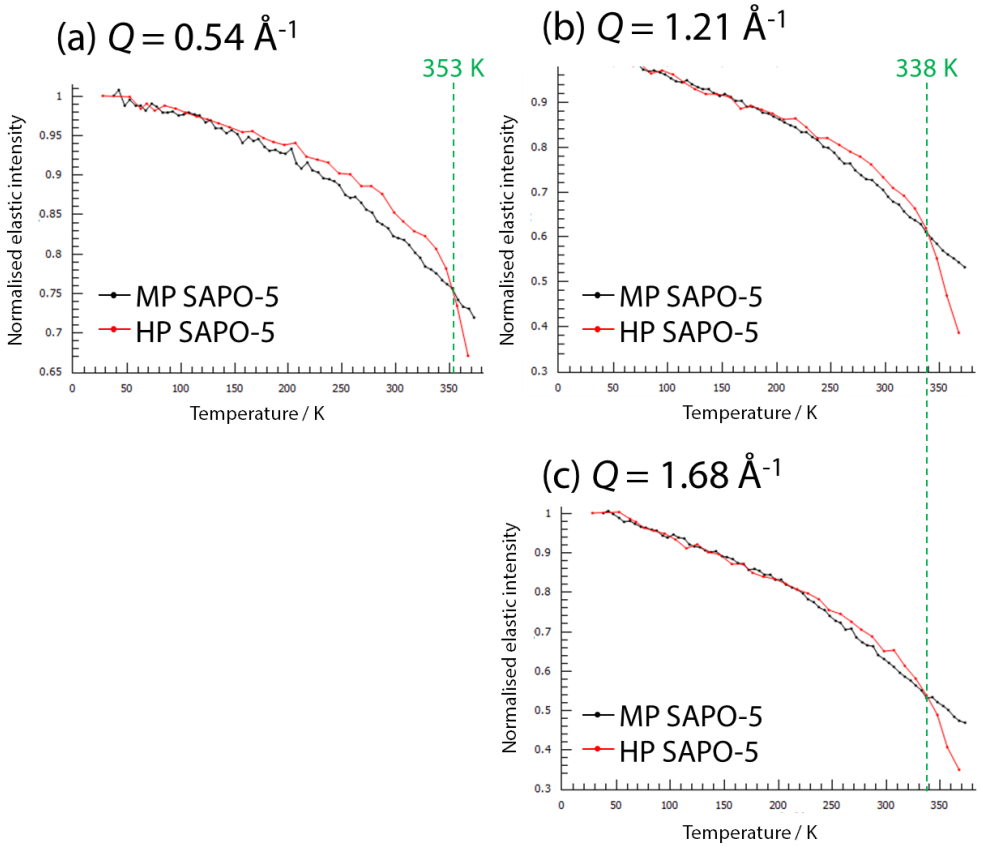

Figure 4.4.9: The elastic window scans of cyclohexanone oxime sorbed in MP SAPO-5 (black line) and HP SAPO-5 (red line) for **(a)** Q = 0.54 Å^{-1}, **(b)** Q = 1.21 Å^{-1}, and **(c)** Q = 1.68 Å^{-1}, in the temperature range of 40 - 373 K. The crossover point indicates the temperature at which the total mobility of the oxime was the same for both frameworks. Data acquired on the OSIRIS spectrometer.[74]

When the improved mass transport properties of the hierarchical pore network were considered, it was noteworthy that the short-range motion of cyclohexanone oxime was relatively curtailed in HP SAPO-5 at higher temperature. Nonetheless, a rationalisation was made on the basis of the previous spectroscopic study of cyclohexanone oxime adsorbed in organosilane-templated SAPO-34 (**Chapter 3**). In this earlier study, hydrogen bonding between cyclohexanone oxime and the siliceous mesopores of HP (Si)AlPO was implicated in the activation of substrate towards the Beckmann rearrangement. Thus, it was proposed that at > 320 K, the reduced mobility of oxime in HP SAPO-5 *versus* MP SAPO-5 was due to the adsorption of sorbate at silanol sites in the mesopores. The same investigations had also identified the oxime-silanol interactions to disrupt the hydrogen-bonded structure of the crystalline substrate, leading to the isolation of individual oxime molecules.[102] Since neutron

diffraction data was acquired simultaneously with QENS,[74] it was possible to seek further evidence of sorbate-framework interactions by examining the long-range order of the oxime.

Prior to the QENS measurements, the solid oxime was melted in the presence of the SAPO framework to encourage its adsorption into the pores. Nevertheless, diffraction data revealed that when the MP SAPO-5 sample was subsequently cooled to <20 K, some of the crystalline oxime was reformed (**Figure 4.4.10 a**). Given the extensive hydrogen bonding available in the crystalline substrate, sparse interactions with the isolated Brønsted sites in MP SAPO-5 may have been insufficient to the retain the oxime within the micropores on cooling.

As the temperature was increased for the elwin, the diffraction pattern of the MP SAPO-5 framework was largely unchanged (**Figure 4.4.10 b**). However, the diffraction peaks associated with the oxime were broadened and shifted towards significantly larger *d*-spacings, in a similar manner to that observed for the pure substrate (**Figure 4.4.11**). Since the diffraction maxima of the oxime were shifted to varying extents, it was proposed that the intermolecular oxime-oxime hydrogen bonds (that maintained the long-range order) were elongated asymmetrically by heating. However, at ~65 °C the diffraction peaks of the oxime were lost, which correlated with the substrate melting detected in the elwin (**Figure 4.4.7**).

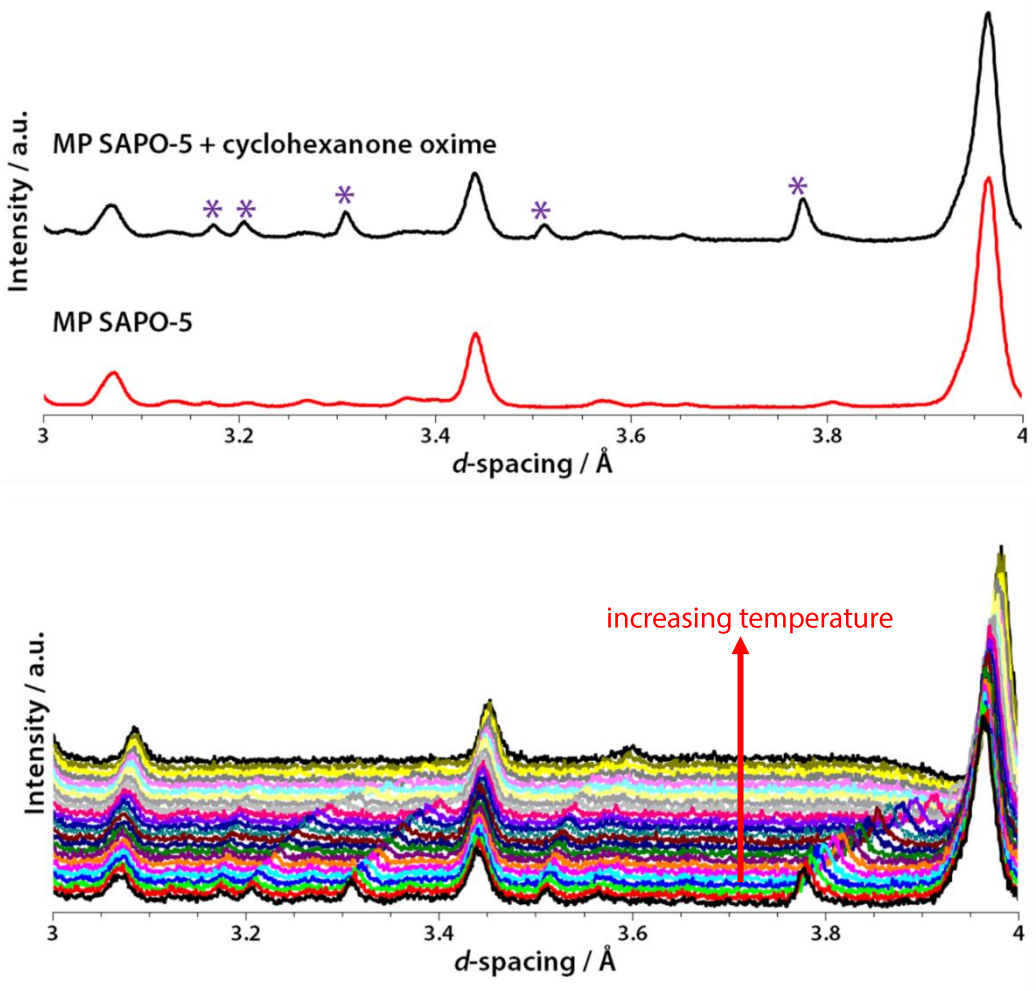

Figure 4.4.10: (a) The neutron diffraction patterns of MP SAPO-5 before (red line) and after cyclohexanone oxime was sorbed at 363 K (black line). Diffraction data is reported at < 20 K. Peaks due to cyclohexanone oxime are highlighted by *. **(b)** The neutron diffraction pattern of cyclohexanone oxime sorbed in MP SAPO-5 as the temperature was increased from 30 K to 360 K. Data acquired on the OSIRIS spectrometer.[74]

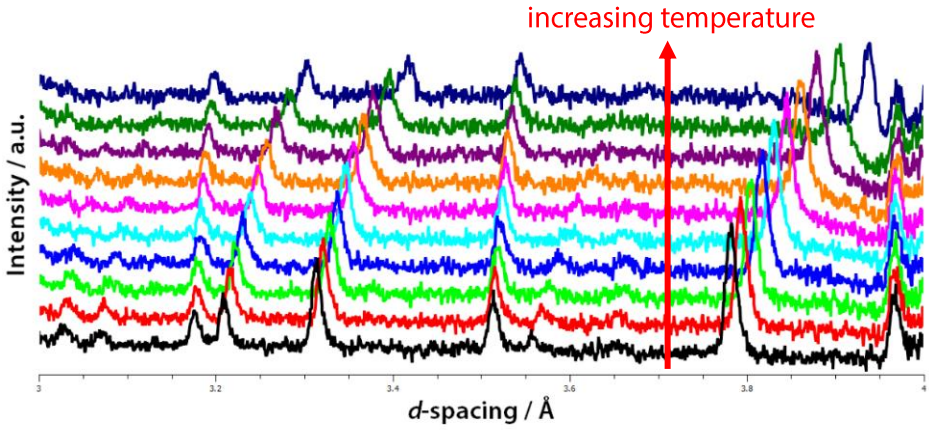

Figure 4.4.11: The neutron diffraction pattern of cyclohexanone oxime as temperature is increased in the range 40 K to 250 K. Data acquired on the OSIRIS spectrometer.[74]

In marked contrast, the diffraction pattern of HP SAPO-5 changed negligibly following the sorption of cyclohexanone oxime. Only the diffraction peaks of the HP SAPO-5 framework were observed, but an increased incoherent background was indicative of the disordered, sorbed oxime (**Figure 4.4.12**).

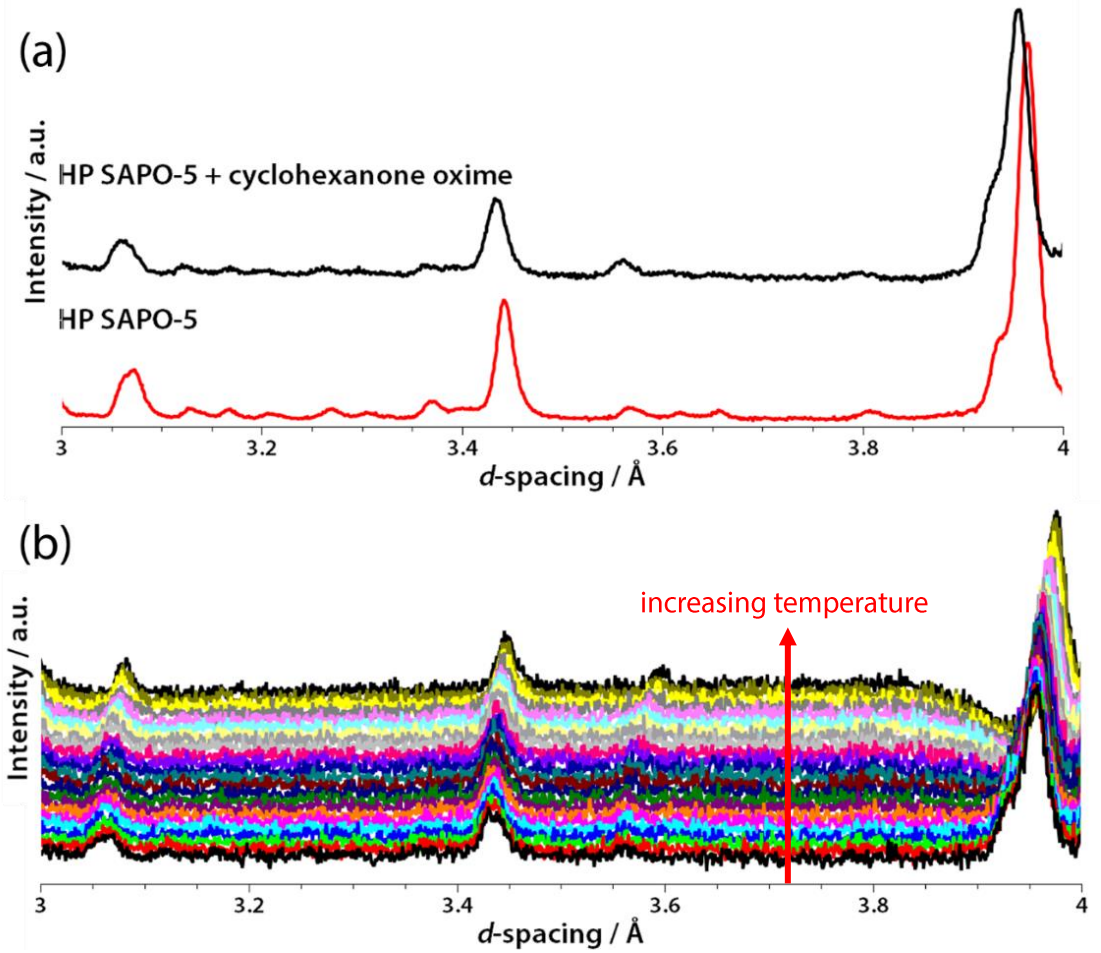

Figure 4.4.12: (a) The neutron diffraction patterns of HP SAPO-5 before (red line) and after cyclohexanone oxime was sorbed at 363 K (black line). Diffraction data reported at < 20 K. **(b)** The neutron diffraction pattern of cyclohexanone oxime sorbed in HP SAPO-5 as the temperature was increased from 30 K to 360 K. Data acquired on the OSIRIS spectrometer.[74]

Significantly, the lack of crystalline oxime in the presence of HP SAPO-5 proved consistent with the earlier spectroscopic findings, where substrate-mesopore interactions were evidenced to disintegrate the hydrogen-bonded trimers of the crystalline state (**Chapter 3**). Such consistency provided further evidence that the reduced motion of the oxime in HP SAPO-5 *versus* MP SAPO-5 at > 320 K was due to the immobilisation of the sorbate caused by hydrogen bonding to the mesopores.

The QENS spectra of cyclohexanone oxime in MP and HP SAPO-5 at 373 K are shown in **Figure 4.4.13 (a)** and **(b)**, respectively.

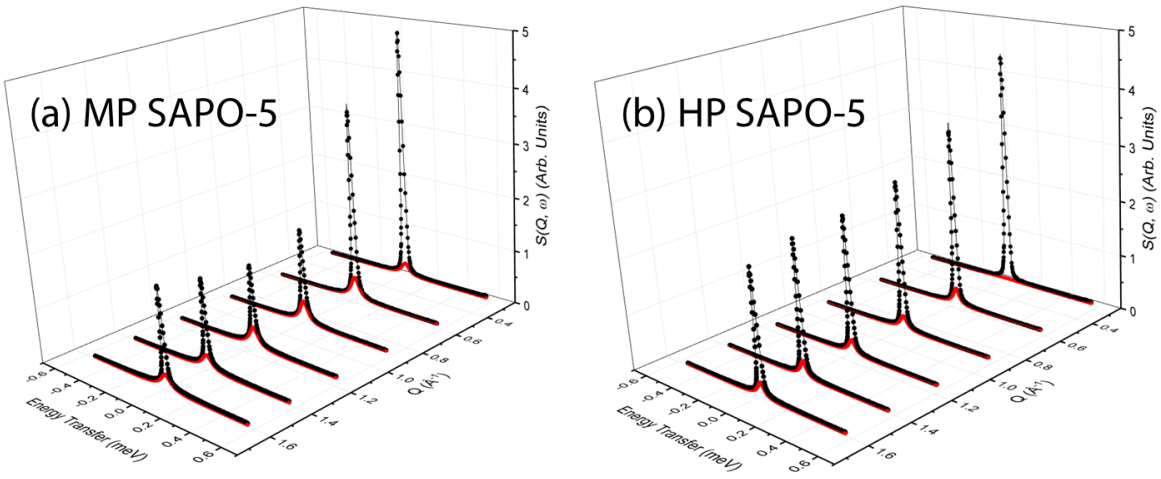

Figure 4.4.13: The QENS spectra for cyclohexanone oxime sorbed in **(a)** MP SAPO-5 and **(b)** HP SAPO-5 at 373 K, shown at a range of *Q*-values. The black line shows the total fit, which is a convolution of a delta function and the resolution measurement at 10 K (which account for elastic contributions from the substrate and framework), a single Lorentzian function that describes the data, and a flat background function that represents fast motions, outside the dynamic window of the instrument. The red line shows the Lorentzian function that describes the quasi-elastic broadening. Data acquired on the OSIRIS spectrometer.[74]

For the HP SAPO-5 system, at all *Q*-values the Lorentzian component of the QENS peaks was very small, whilst the elastic component was considerably larger. The small degree of quasi-elastic broadening suggested that a large fraction of oxime molecules sorbed in HP SAPO-5 were either static on the timescale of the instrument, or underwent localised motions. Whilst the quasi-elastic broadening was also small for the MP SAPO-5 sample, at all *Q* the Lorentzian component made a larger contribution to the total fit of the QENS spectra than for HP SAPO-5. Therefore, the oxime was identified to be more mobile in MP SAPO-5 than HP SAPO-5 at 373 K, which was consistent with their elwins (**Figure 4.4.7**). As a single Lorentzian function was sufficient to fit the broadening of both the HP and MP SAPO-5 QENS spectra, this indicated that only one mode of motion was observed.

To investigate the geometry of the localised motions in MP and HP SAPO-5, the elastic incoherent structure factor (EISF, $A_0(Q)$)[32] was calculated for various *Q*, using **Equation 4.4.1**, where $I_{elastic}(Q)$ is the elastic intensity, and $I_{QENS}(Q)$ is the inelastic intensity of the QENS peak.

Equation 4.4.1:
$$A_0(Q) = \frac{I_{elastic}(Q)}{I_{elastic}(Q)+I_{QENS}(Q)}$$

As shown in **Figure 4.4.14**, the EISFs of MP SAPO-5 were lower than those of HP SAPO-5 over the entire *Q*-range, which was consistent with the greater mobility of cyclohexanone oxime in MP SAPO-5.

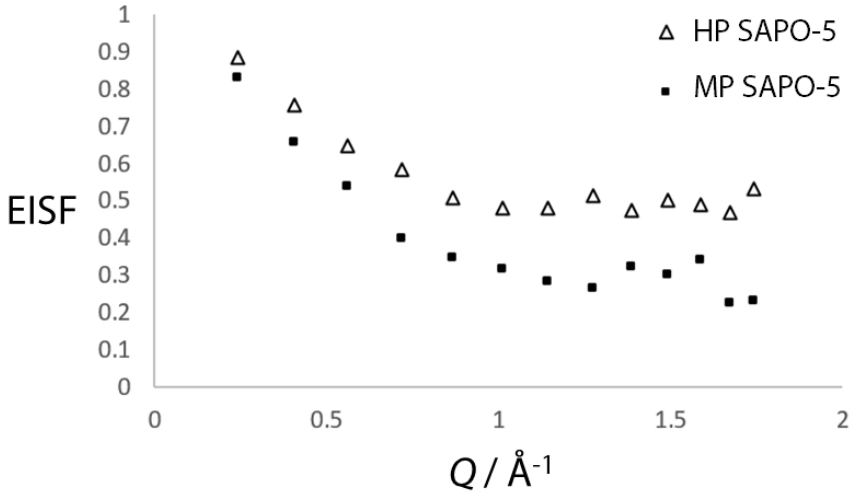

Figure 4.4.14: The experimental elastic incoherent structure factor (EISF) *versus Q* for cyclohexanone oxime sorbed in HP SAPO-5 (Δ) and MP SAPO-5 (■) at 373 K.

The experimental EISF was fit to a variety of models, including isotropic rotation, continuous uniaxial rotation around a circle, a two-site jump rotation model, and translational motion in a confined volume (**Figure 4.4.15** and **Table 4.4.6**).

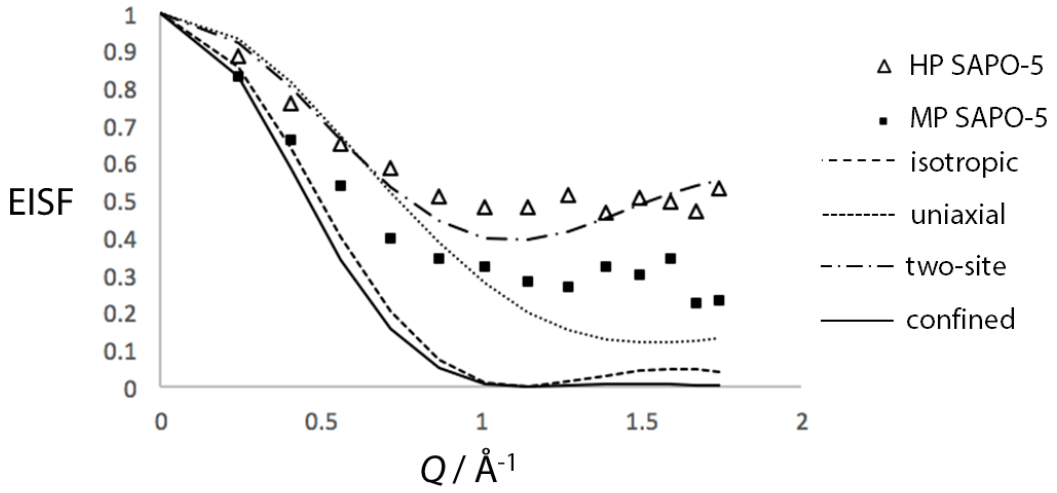

Figure 4.4.15: The experimental elastic incoherent structure factor (EISF) *versus Q* for cyclohexanone oxime sorbed in HP SAPO-5 (Δ) and MP SAPO-5 (■) at 373 K, showing theoretical EISF models for isotropic rotation, continuous uniaxial rotation around a circle, a two-site jump rotation model, and translation in a confined volume.

Table 4.4.6: A summary of the models and parameters used to generate the theoretical EISFs for cyclohexanone oxime in SAPO-5 presented in **Figure 4.4.14**.

Model	Description	Graphical Description	EISF	Parameters
Isotropic rotation[45]	Reorientation through random small angle rotations, with radius of rotation, *r*.	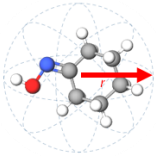	$A_0(Q) = j_0^2(Qr)$	r = 2.52 Å
Two-site jump rotation[49]	The ring protons (having two-fold rotational symmetry) jumping between equivalent ring sites. *d* is the distance between symmetrically equivalent protons (*).	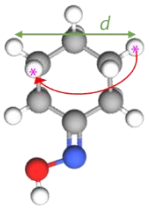	$A_0(Q) = \frac{1}{2}[1 + j_0(Qd)]$	d = 4.1 Å
Uniaxial rotation[51]	Uniaxial rotation of the ring protons about the C_1-C_4 axis at a rotational radius of r_u.	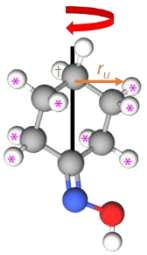	$A_0(Q) = \frac{1}{N}\sum_{n=1}^{N} j_0\left[2Qr_u \sin\left(\frac{n\pi}{N}\right)\right]$	EISF weighted for the 8 protons marked * of $r_u \approx 2.05$ Å, and 1 proton marked † of $r_u \approx 1$ Å.
Translation inside a sphere[47]	The localised motion of the cyclohexanone oxime was modelled as translation confined within a spherical volume of radius *r*.	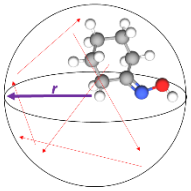	$A_0(Q) = \left[\frac{3j_1(Qr_{conf})}{Qr_{conf}}\right]^2$	r = 3.65 Å

Since none of the models provided a good fit to the empirical data, it was considered that only a fraction of the oxime molecules might be mobile on the instrument timescale, and thus the remainder could be treated as static. To account for static oxime, an effective EISF ($A(Q)_{eff}$) was calculated using **Equation 4.4.2**, where p_x is the fraction of mobile oxime.

Equation 4.4.2: $$A_0(Q)_{eff} = p_x\,[A_0(Q)] + (1 - p_x)$$

The effective EISF was applied to all of the aforementioned models and fit to the experimental EISF using a least-squares method. Of the various models, the best fit to the experimental EISF was found for isotropic rotation (i.e. random, small-angle rotations, with no preferred orientation on time-average),[103] with a mobile fraction (p_x) of 0.46 for HP SAPO-5 and 0.77 for MP SAPO-5 (**Figure 4.4.16**).

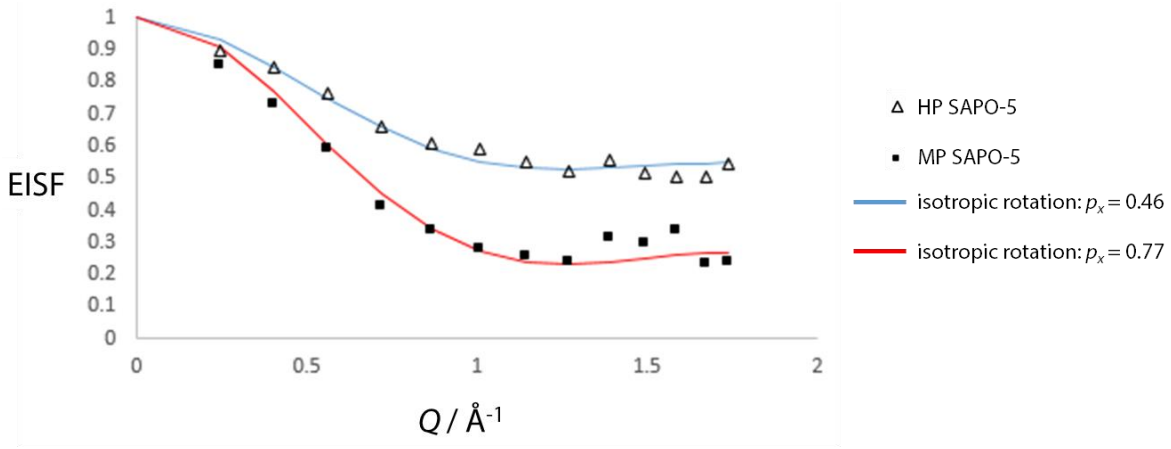

Figure 4.4.16: The experimental elastic incoherent structure factor (EISF) *versus* Q for cyclohexanone oxime sorbed in HP SAPO-5 (Δ) and MP SAPO-5 (■) at 373 K. The EISF model of isotropic rotation is shown for a mobile fraction (p_x) of 0.46 (blue line) and 0.77 (red line).

Thus, the data fit revealed that a larger proportion of oxime molecules were static in HP SAPO-5 *versus* MP-SAPO-5 at 373 K (p_x = 0.77 and 0.46, respectively). The larger mobile fraction in MP SAPO-5 was consistent with the relatively large decrease in elastic intensity in the elwins at Q = 1.21 and 1.68 Å^{-1} at 373 K (**Figure 4.4.8 a**), which had indicated that oxime motions over smaller distances (e.g. the rotational domain) made the largest contribution to the QENS signal. However, the evidence of some static oxime in MP SAPO-5 suggested that although crystalline oxime was present at < 338 K, by 373 K oxime, ~ 33 % of the oxime was adsorbed to the framework Brønsted acid sites.

Analysis of the Lorentzian components of the QENS spectra at 373 K provided further evidence of the rotational motion of cyclohexanone oxime in HP and MP SAPO-5, as the Lorentzian broadening was found to be independent of Q (**Figure 4.4.17**). To determine the rotational diffusion coefficient (D_{rot}) of the oxime, the rotational radius of the oxime (r = 2.52 Å) was used to calculate the quasi-elastic structure factor, $A_l(Q)$, using **Equation 4.4.3** (where j_l is the spherical Bessel function of the l^{th} order). Then, the $A_l(Q)$ was substituted into

the total incoherent scattering law for isotropic rotation diffusion (**Equation 4.4.4**),[59] yielding a D_{rot} of 2.64 x10^{10} s^{-1} in MP SAPO-5, and 2.62 x10^{10} s^{-1} in HP SAPO-5.

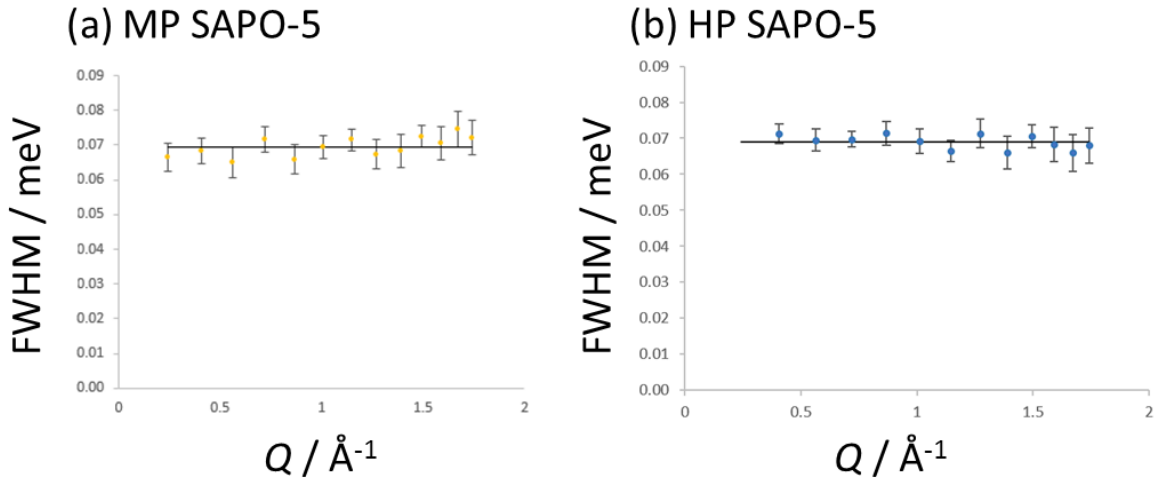

Figure 4.4.17: The Q-dependence of the FWHM broadening of the Lorentzian components of the QENS spectra of cyclohexanone oxime in **(a)** MP SAPO-5 and **(b)** HP SAPO-5 at 373 K.

Equation 4.4.3: $$A_l(Q) = (2l + 1)\, j_l^2(Qr)$$

Equation 4.4.4: $$S(Q,\omega) = A_0(Q)\delta(\omega) + \sum_1^\infty A_l \frac{l(l+1)D_{rot}}{[l(l+1)D_{rot}] + \omega^2}$$

Thus, the QENS studies indicated that the rotational motion of cyclohexanone oxime in HP SAPO-5 and MP SAPO-5 was identical in both geometry (i.e. isotropic) and rate (~ 2.6 x10^{10} s^{-1}). For this reason, it was proposed that mobile oxime was located within the SAPO micropores, these structures being found in both the MP and HP frameworks. Then, the larger fraction of immobile oxime in HP SAPO-5 was attributed to the presence of the mesopores, or more specifically, the immobilisation of oxime by hydrogen-bonding interactions with the silanol sites in the mesopore walls.

4.4.2.2 Total neutron scattering: neutron diffraction

Total neutron scattering experiments were undertaken to investigate the uptake of cyclohexanone oxime in MP and HP SAPO-5, exploiting the detectable change in framework scattering that can occur when the neutron contrast between the pore and the pore walls is modified. **Figure 4.4.18** shows the neutron scattering from MP SAPO-5 on forming a physical mixture with cyclohexanone oxime at 300K, and then on heating the mixture at 373 K.

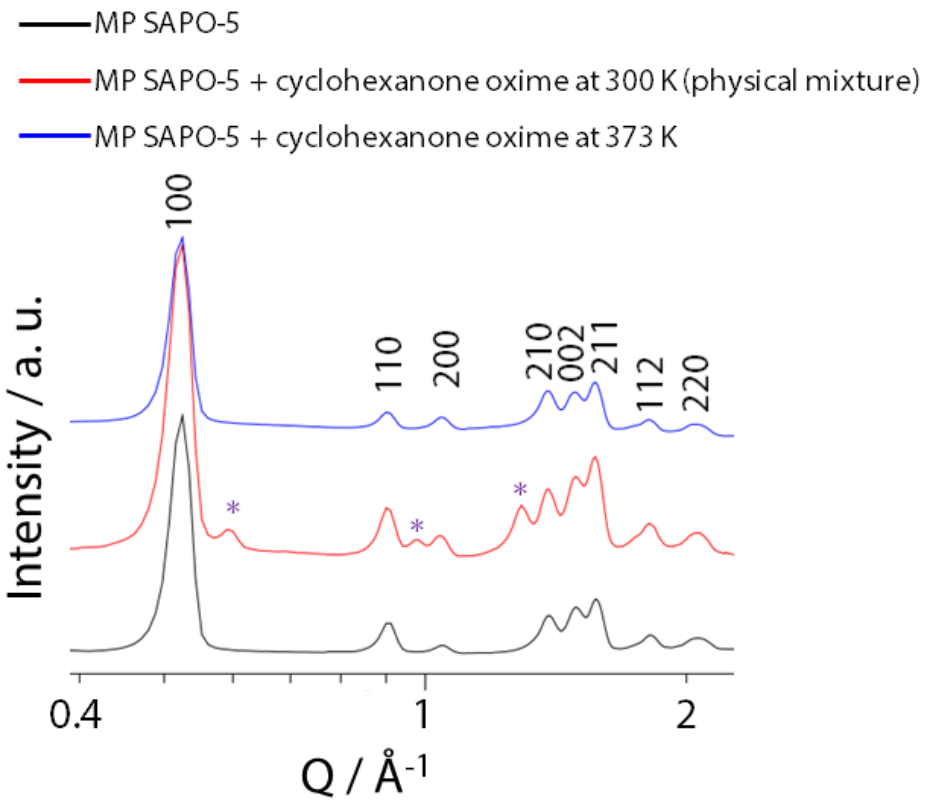

Figure 4.4.18: The neutron scattering spectrum showing diffraction from the empty MP SAPO-5 (black line), a physical mixture of MP SAPO-5 and cyclohexanone oxime at 300 K (red line), and the same physical mixture after heating to 373 K. *Q* is reported on a log scale. Peaks due to cyclohexanone oxime are highlighted with *. Data acquired on the NIMROD spectrometer.[80]

In the neutron scattering spectrum, intensity in the region $Q > 0.4$ Å^{-1} was associated with scattering from nanoscale, ordered structures e.g. the micropores of SAPO-5.[104] For MP SAPO-5, a number of Bragg peaks were observed that, by correlation with the powder XRD (**Figure 4.4.1**), identified the crystalline, microporous framework. However, in the physical mixture with cyclohexanone oxime, diffraction peaks due to solid oxime were developed, as was the case in the QENS experiment. Significantly, the increased scattering intensity from the framework suggested that the crystalline oxime was located at the exterior of the catalyst

particles, with this accentuating the neutron contrast between the framework and the empty pores.[104, 105 106]

On heating to 373 K, the oxime was melted, and the peaks due to the crystalline oxime were lost. At the same time, the Bragg scattering from the framework was decreased in intensity relative to both the physical mixture and the empty framework. These observations appeared to be consistent with the uptake of oxime into the micropores of MP SAPO-5, as this would reduce the scattering contrast with the framework, relative to an evacuated pore.[107] Thus, it was plausible that the rotational motion detected by QENS at 373 K, was due to oxime sorbed within the micropores of MP SAPO-5.

In the neutron scattering spectra of HP SAPO-5, no crystalline oxime was detected in the physical mixture, nor was the scattering from the framework significantly modified on heating to 373 K (**Figure 4.4.19**). However, the scattering intensity from the framework was reduced on introduction of cyclohexanone oxime, which suggested that the oxime was already sorbed into the SAPO pores from the physical mixture.

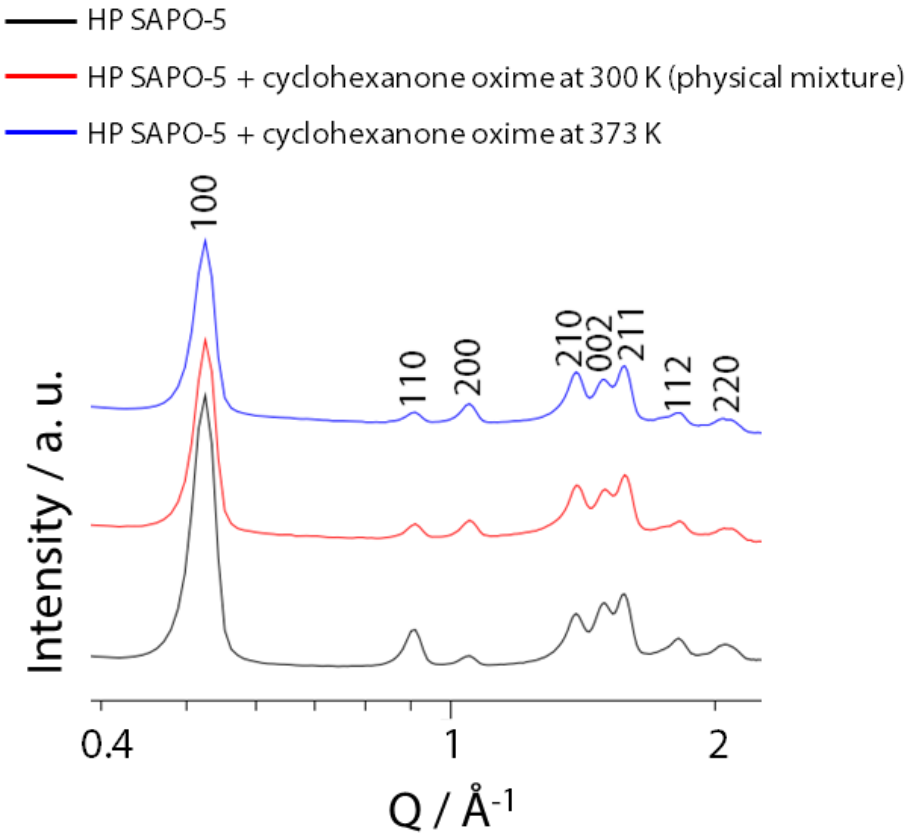

Figure 4.4.19: The neutron scattering spectrum showing diffraction from the empty HP SAPO-5 (black line), a physical mixture of HP SAPO-5 and cyclohexanone oxime (red line), and the same physical mixture after heating to 373 K. All spectra were recorded at 300 K. *Q* is reported on a log scale. Data acquired on the NIMROD spectrometer.[80]

The lack of crystalline oxime in the physical mixture with HP SAPO-5 at ambient temperature was significant, as it correlated with the QENS diffraction data, and the earlier INS studies of cyclohexanone oxime in HP SAPO-34 (**Chapter 3**). It was postulated that the loss of long-range order in the oxime was due to disintegration of the hydrogen-bonded solid, in favour of hydrogen-bonding interactions with the silanols in the soft-templated mesopores. By association, the lack of crystalline oxime observed during diffraction analysis of the HP SAPO-5 samples supported the rationale that the lower sorbate mobility at 373 K (relative to MP SAPO-5) was due to adsorption of the oxime at silanols sites in the mesopores.

4.4.2.3 The diffusion of ε-caprolactam in hierarchical and microporous SAPO-5

To investigate the desorption and diffusion of the BR product, the mobility of ε-caprolactam in HP and MP SAPO-5 was studied by QENS. The *Q*-averaged elwins showed no significant crossover or deviations between HP and MP SAPO-5, which indicated that the temperature-dependent mobility of that lactam was similar in both frameworks (**Figure 4.4.20 a**). When the elwins were studied as a function of *Q* (**Figure 4.4.20 b-c**), the proportion mobile lactam increased in the order: $Q = 0.54$ Å^{-1} < $Q = 1.21$ Å^{-1} < $Q = 1.68$ Å^{-1} in both samples, which revealed the predominance of localised motion at all temperatures. Whilst the lactam motion increased over all spatial-length scales at higher thermal energy, the medium- and short-range motions made an increasing contribution to the total lactam mobility at higher temperature. Since the mobility of the lactam was similar in both frameworks, and dominated by short-range motion, it was proposed that (like cyclohexanone oxime) the mobile lactam was confined within the SAPO-5 micropores.

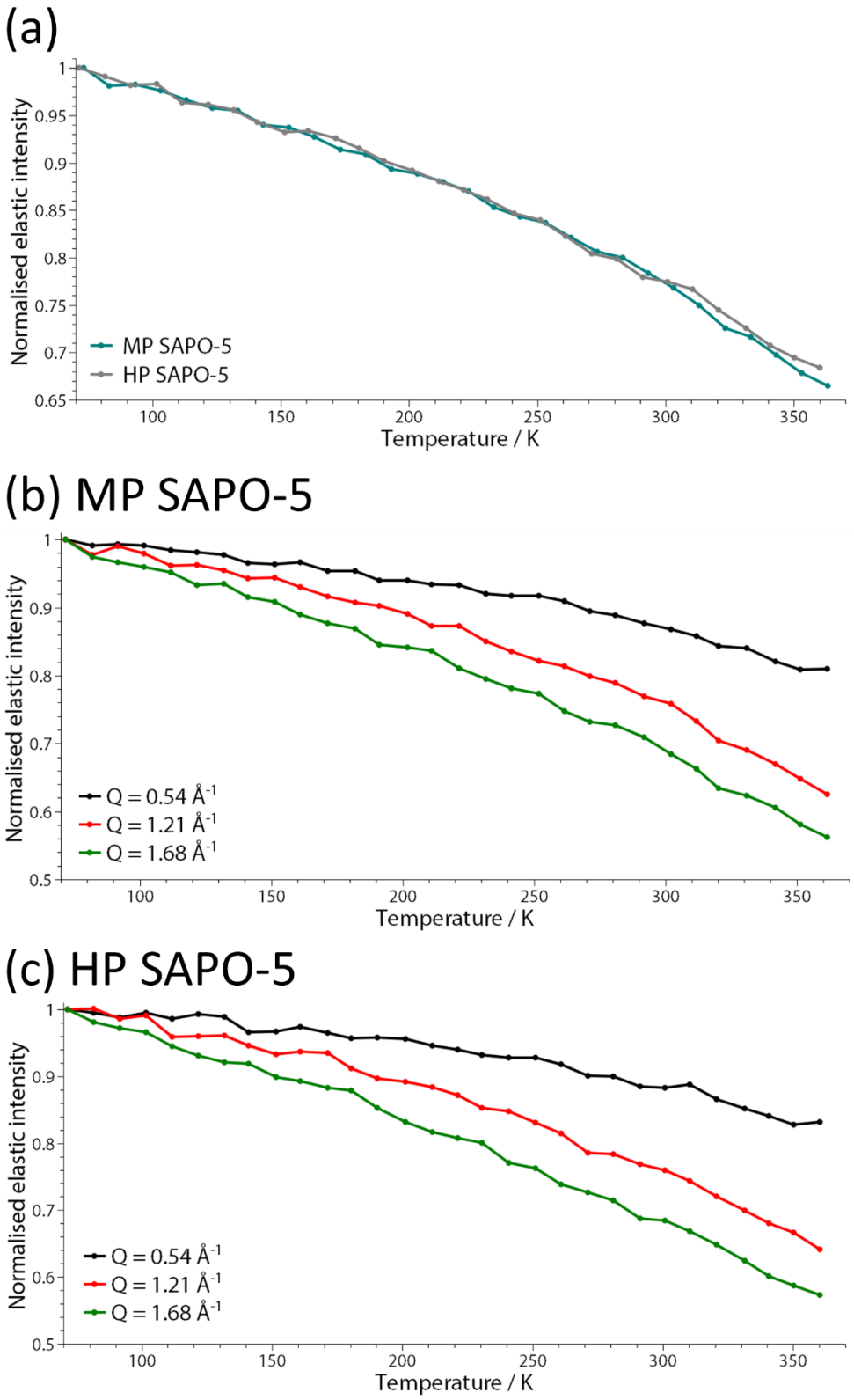

Figure 4.4.20: (a) The elastic window scans (averaged over all Q-values) of ε-caprolactam sorbed in MP SAPO-5 (blue line) and HP SAPO-5 (grey line) in the temperature range of 70 - 363 K. The elastic window scans of caprolactam sorbed in **(b)** MP SAPO-5 and **(c)** HP SAPO-5 for Q = 0.54 Å^{-1} (black line), Q = 1.21 Å^{-1} (red line), and Q = 1.68 Å^{-1} (green line), in the temperature range of 70 - 373 K. Data acquired on the OSIRIS spectrometer.[74]

Since neutron diffraction had proven informative in the study of cyclohexanone oxime mobility, the diffraction data from the lactam QENS experiment was also analysed. At base temperature, the diffraction pattern of the MP SAPO-5 sample contained several diffraction maxima originating from the lactam (**Figure 4.4.21 a**). However, as the temperature was increased for the elwin, the sorbate peaks were broadened and shifted to higher *d*-spacing, indicating an increase in lactam motion and a larger separation between the hydrogen-bonded dimers of the solid lactam (**Figure 4.4.21 b**).[108] Beyond ~ 323 K the long-range order of the lactam was lost due to melting.

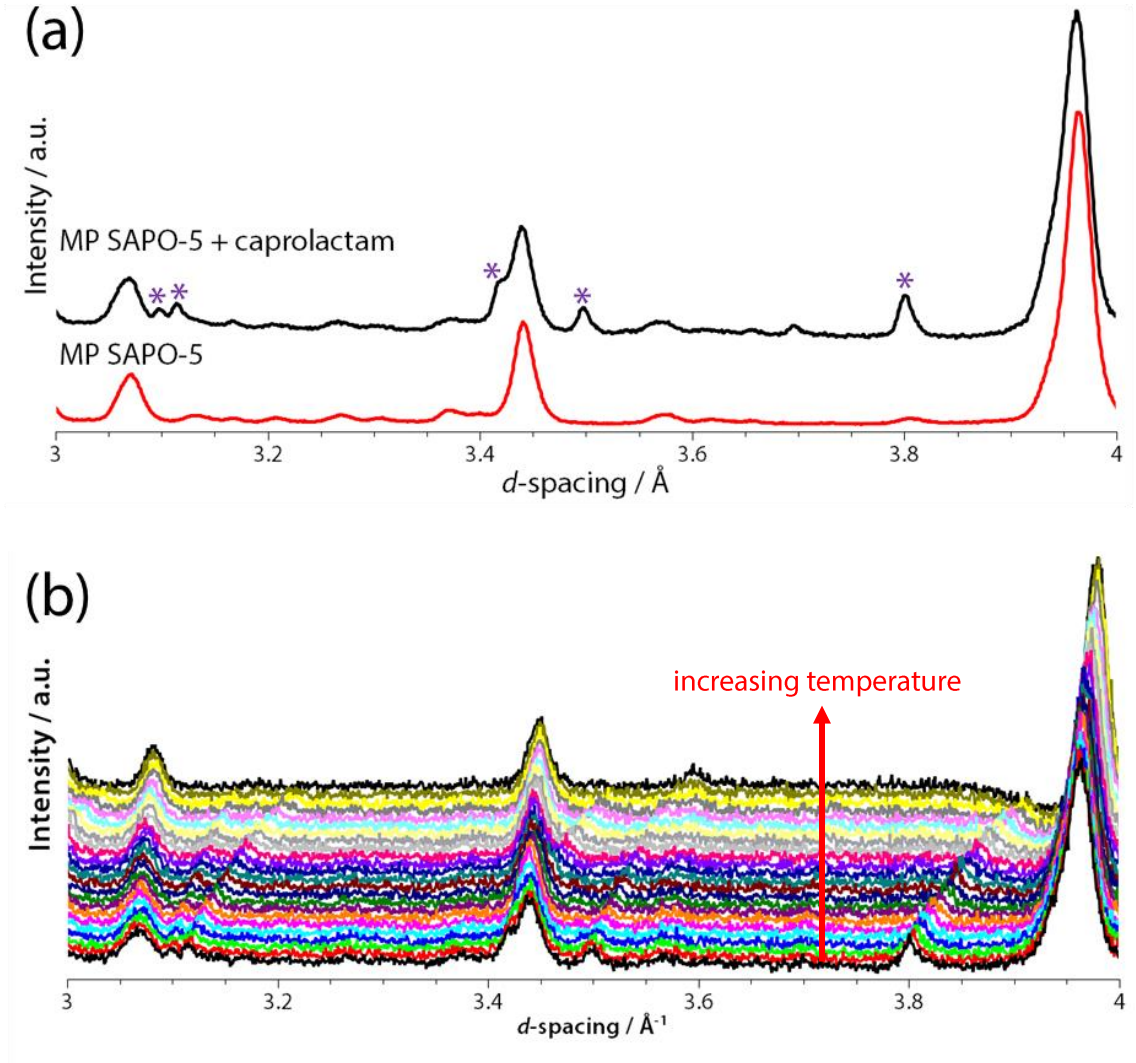

Figure 4.4.21: (a) The neutron diffraction pattern of MP SAPO-5 before (red line) and after ε-caprolactam was sorbed at 363 K (black line). Diffraction data was acquired at < 20 K. Peaks attributed to caprolactam are highlighted by *. **(b)** The neutron diffraction pattern of ε-caprolactam sorbed in MP SAPO-5 as the temperature was increased from 70 K to 363 K. Data acquired on the OSIRIS spectrometer.[74]

In contrast, no crystalline lactam was observed in the diffraction pattern of the HP SAPO-5 sample, although an increased incoherent background and broadened framework peaks suggested that the lactam was adsorbed into the pores (**Figure 4.4.22 a**). When the HP SAPO-5/lactam mixture was heated for the QENS experiment, there was no significant change in the diffraction pattern of the framework.

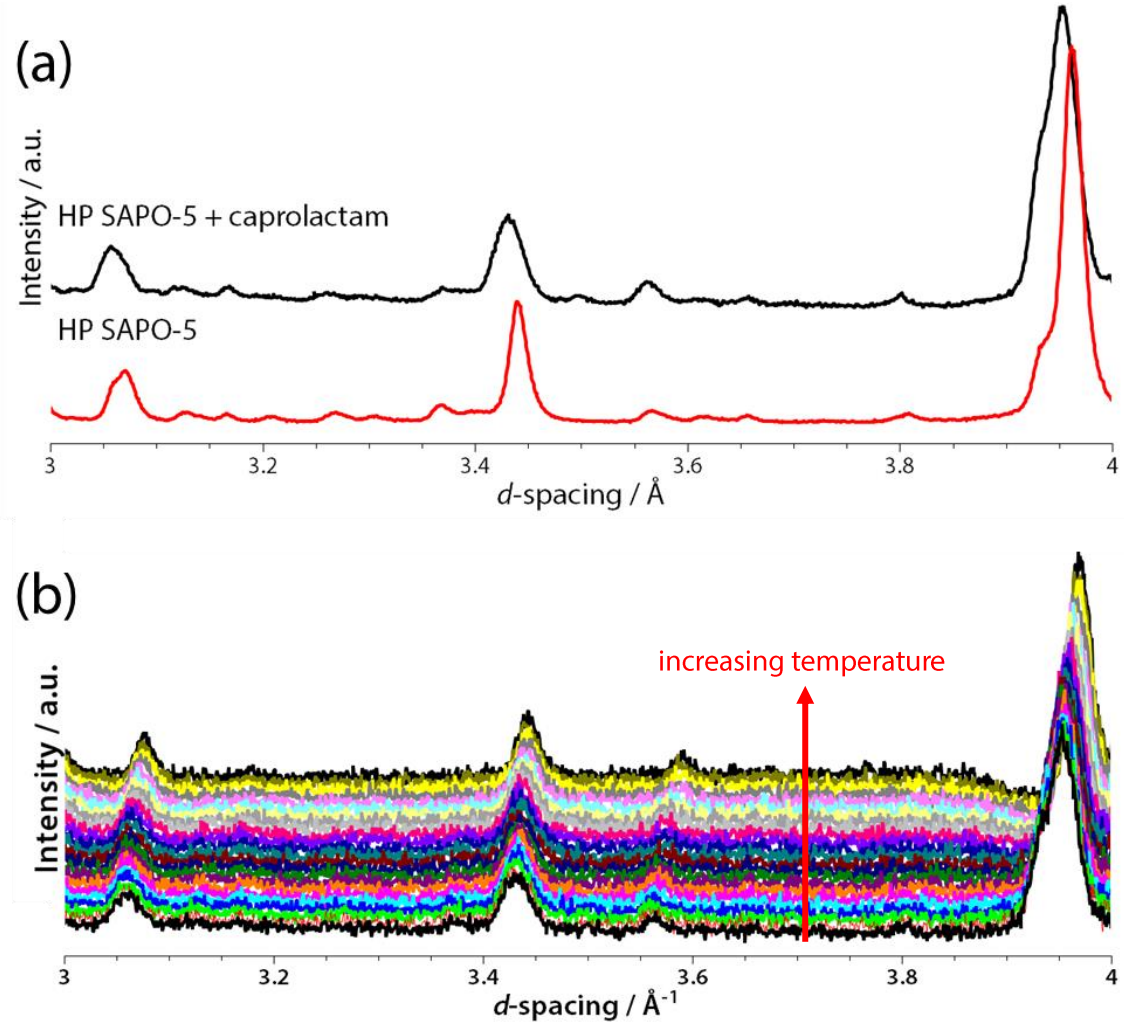

Figure 4.4.22: (a) The neutron diffraction pattern of HP SAPO-5 before (red line) and after ε-caprolactam was sorbed at 363 K (black line). Diffraction data was acquired at < 20 K. **(b)** The neutron diffraction pattern of ε-caprolactam sorbed in HP SAPO-5 as the temperature was increased from 70 K to 363 K. Data acquired on the OSIRIS spectrometer.[74]

Thus, the diffraction analyses revealed that the long-range order of the lactam differed significantly with HP and MP SAPO-5 at < 323 K, even though the elwins had indicated that the motion of the lactam was similar in both frameworks across the entire temperature range. In fact, the diffraction data suggested that the sorbate-silanol interactions inferred for cyclohexanone oxime in HP SAPO-5, were also active with ε-caprolactam sorbate.

Further evidence for the lactam-silanol interactions was extracted from the QENS spectra of caprolactam sorbed in MP and HP SAPO-5 at 373 K (**Figure 4.4.23**). In analogy to the QENS spectra of the sorbed oxime, the Lorentzian components of the lactam spectra were small at all *Q*, with the elastic component being dominant. Hence, it was proposed that the motion of the lactam in HP and MP SAPO-5 was localised, or a significant fraction of the lactam molecules were static. In addition, a single Lorentzian function was sufficient to fit the quasi-elastic broadening, which indicated that a single mode of motion was observed in the lactam. However, unlike the oxime analyses, the magnitude of the Lorentzian function was essentially the same for HP and MP SAPO-5, which suggested that the nature/degree of lactam motion was similar in both frameworks.

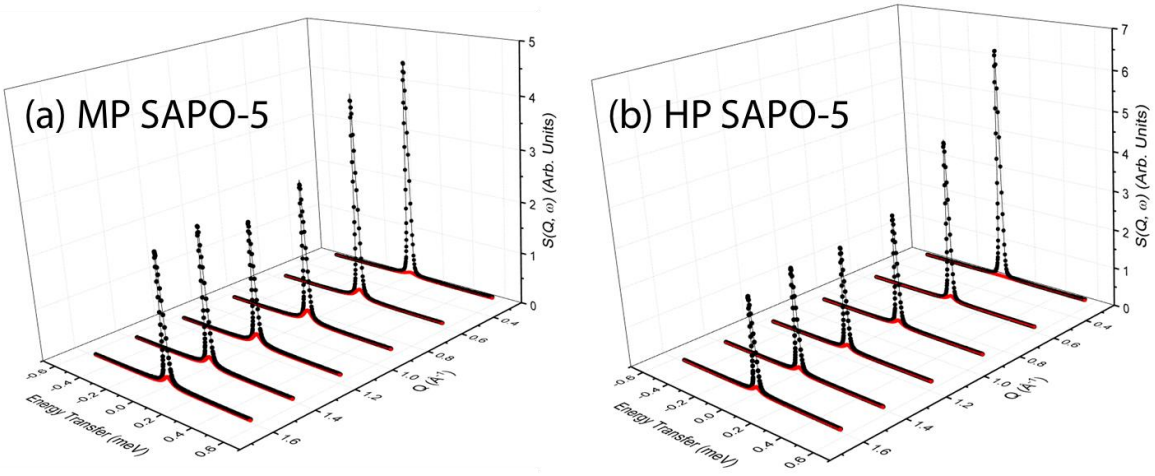

Figure 4.4.23: The QENS spectra for ε-caprolactam sorbed in **(a)** MP SAPO-5 and **(b)** HP SAPO-5 at 373 K, shown at a range of *Q*-values. The black line shows the total fit, which is a convolution of a delta function and the resolution measurement at 10 K (which account for elastic contributions from the substrate and framework), a single Lorentzian function that describes the data, and a flat background function that represents fast motions, outside the dynamic window of the instrument. The red line shows the Lorentzian function that describes the quasi-elastic broadening. Data acquired on the OSIRIS spectrometer.[74]

However, the experimental EISFs afforded better clarity on the relative motion of caprolactam in MP and HP SAPO-5, revealing that the lactam was, in fact, slightly more mobile in MP SAPO-5 at all temperatures (**Figure 4.4.24**). Various models were trialled in characterising the EISF of caprolactam in HP and MP SAPO-5 (**Figure 4.4.24** and **Table 4.4.7**), yet none provided a satisfactory fit to the experimental data.

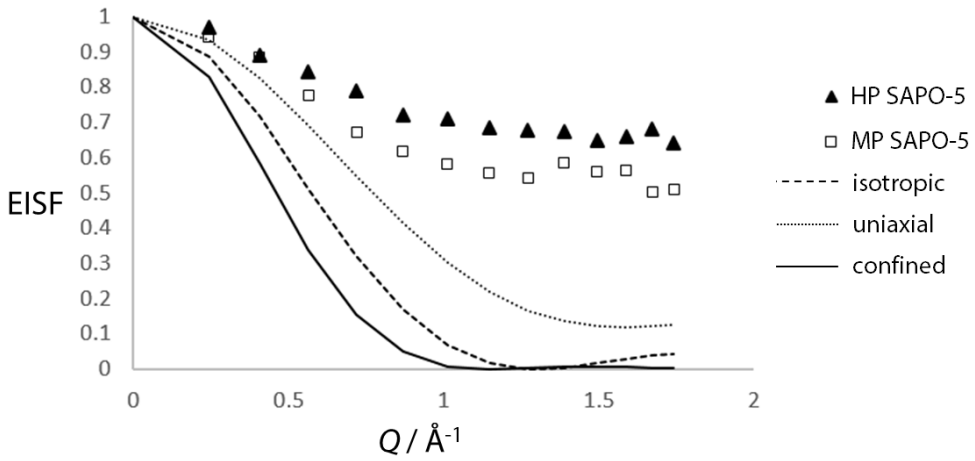

Figure 4.4.24: The experimental elastic incoherent structure factor (EISF) *versus* Q for ε-caprolactam sorbed in HP SAPO-5 (▲) and MP SAPO-5 (□) at 373 K, showing theoretical EISF models for isotropic rotation, continuous uniaxial rotation around a circle, and translation in a confined volume.

Table 4.4.7: The models and parameters used to generate the theoretical EISFs for ε-caprolactam in SAPO-5 presented in **Figure 4.4.23**.

Model	Description	Graphical Description	EISF	Parameters
Isotropic rotation[45]	Reorientation through random small angle rotations, with radius of rotation, *r*.	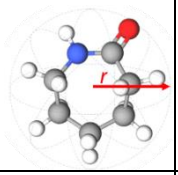	$A_0(Q) = j_0^2(Qr)$	r = 2.42 Å
Uniaxial rotation[51]	Uniaxial rotation of the ring protons about the axis along the C=O bond, at a rotational radius of r_u (the average radius of all ring protons from the C=O axis).	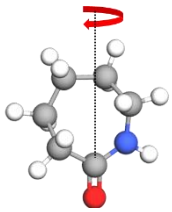	$A_0(Q) = \frac{1}{N}\sum_{n=1}^{N} j_0\left[2Qr_u \sin\left(\frac{n\pi}{N}\right)\right]$	r_u = 1.85 Å
Translation inside a sphere[47]	The localised motion of the caprolactam was modelled as translation confined within a spherical volume of radius *r*.	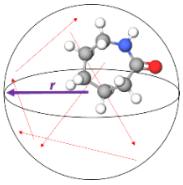	$A_0(Q) = \left[\frac{3j_1(Qr_{conf})}{Qr_{conf}}\right]^2$	r = 3.65 Å

As such, an immobile population of lactam molecules was considered by applying **Equation 4.4.2**. The isotropic rotation model gave the best fit to the experimental EISF (as with cyclohexanone oxime) when the mobile fraction of lactam was 0.34 for HP SAPO-5 and 0.45 for MP SAPO-5 (**Figure 4.4.25**).

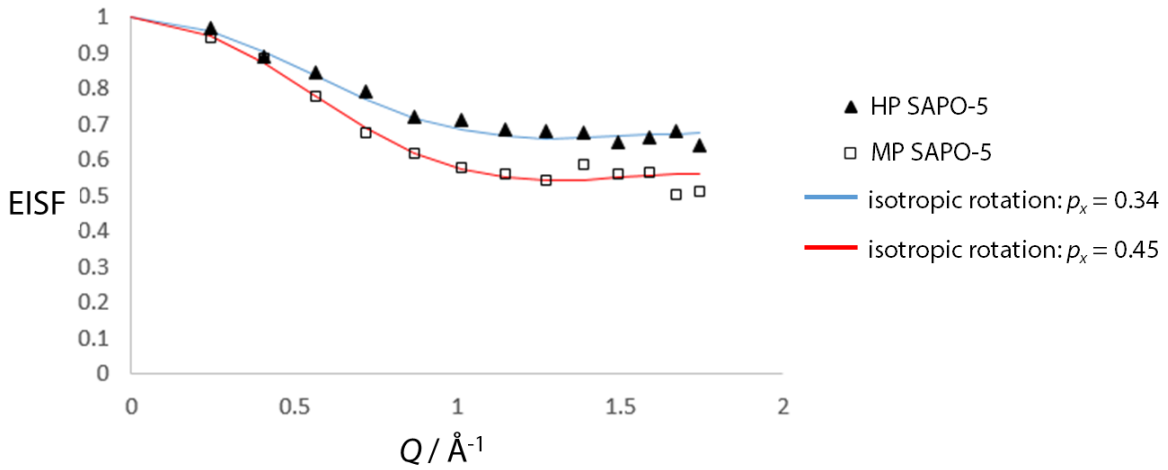

Figure 4.4.25: The experimental elastic incoherent structure factor (EISF) *versus Q* for cyclohexanone oxime sorbed in HP SAPO-5 (▲) and MP SAPO-5 (□) at 373 K. The EISF model of isotropic rotation is shown for a mobile-lactam fraction of 0.34 (blue line) and 0.45 (red line).

In light of the diffraction data (i.e. the lack of crystalline sorbate) and the slightly larger immobile fraction in HP SAPO-5, there was evidence to suggest that the silanols in the mesopores engaged in hydrogen bonding interactions with caprolactam, as was identified for cyclohexanone oxime. However, the adsorption of sorbate to the silanols in HP SAPO-5 had a smaller impact on the total mobility of the lactam, than on the total mobility of the oxime. (For example, difference in the mobile fraction of sorbate in MP *versus* HP SAPO-5 was 11 % for caprolactam, but 31 % for cyclohexanone oxime). In addition, the mobile fraction of caprolactam in MP SAPO-5 at 373 K (p_x = 0.34; lactam dimensions: 5.82 x 5.96 Å)[109] was much smaller than the mobile fraction of cyclohexanone oxime in the same framework (p_x = 0.77; oxime dimensions: 5.43 x 8.25 Å)[109]. This suggested that steric hindrance in the AFI micropores (7.3 Å diameter) was more detrimental to overall lactam mobility than the hydrogen bonding interactions in the HP SAPO-5 mesopores.

Analysis of the Lorentzian components of the QENS spectra at 373 K revealed the quasi-elastic broadening to be independent of *Q*, which was consistent with the rotational motion of the lactam (**Figure 4.4.26**). From the FWHMs of the Lorentzian components, D_{rot} values of 2.34 x10^{10} and 2.33 x10^{10} s^{-1} were extracted for HP and MP SAPO-5, respectively. So whilst there was a larger fraction of static molecules in HP SAPO-5 than MP SAPO-5, the rate of

isotropic rotation of the mobile fraction was identical in both frameworks. As the nature and rate of lactam rotation was identical in both HP and MP SAPO-5, this suggested that the mobile fraction was located in the AFI micropores.

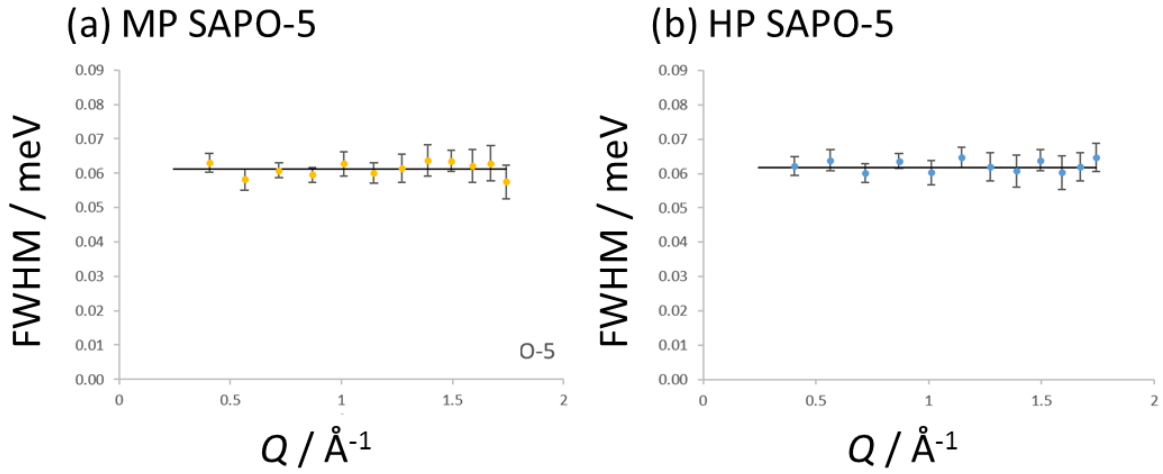

Figure 4.4.26: The *Q*-dependence of the FWHM broadening of the Lorentzian components of the QENS spectra of ε-caprolactam in **(a)** MP SAPO-5 and **(b)** HP SAPO-5 at 373 K.

4.5 Conclusions and future work

As part of an ongoing investigation into the mechanism of the Beckmann rearrangement in organosilane-templated SAPOs, the intracrystalline diffusion of cyclohexanone oxime and ε-caprolactam was probed by quasi-elastic neutron scattering. These studies elaborated on an earlier investigation, which had revealed the potential dual role of the mesopores in the BR: namely, substrate activation, and improved mass transport to the micropores. For the study of intracrystalline diffusion, the AFI-type framework of SAPO-5 (7.3 Å micropore diameter) was selected, since the micropores should be accessible to both cyclohexanone oxime and caprolactam (kinetic diameter ~ 6 Å).[110] Therefore, any variations in sorbate mobility in MP and HP SAPO-5 were linked to the presence of mesopores.

The MP and HP SAPO-5 catalysts were first characterised using powder XRD, which confirmed their phase-pure, crystalline AFI structure. Although refinement of the unit cell parameters indicated that the SAPO-5 unit cell was unperturbed by soft-templating, N_2 gas adsorption identified significant mesoporosity in HP SAPO-5. The acid characteristics of HP SAPO-5 were also subtly modified by soft-templating, with NH_3-TPD revealing slightly weaker framework Brønsted acid sites than in MP SAPO-5. However, HP SAPO-5 was also found to contain a small number of strong acid sites that were not detected in MP SAPO-5. The strong acid sites in HP SAPO-5 were later credited for an improved selectivity towards

ε-caprolactam in the liquid-phase Beckmann rearrangement (130 °C). As well as an increased lactam selectivity, HP SAPO-5 also achieved a higher conversion of cyclohexanone oxime within 6 hours than MP SAPO-5 (54 % and 34 %, respectively). The increased activity of HP SAPO-5 alluded to the enhanced accessibility of the Brønsted sites in the micropores and, potentially, the substrate-activating effect of the siliceous mesopores. Since weakly acidic silanols tend to favour the hydrolysis by-product under liquid-phase conditions,[99-101] it was unlikely that the mesopores were the site of the BR.

Initially, the dynamics of cyclohexanone oxime in MP and HP SAPO-5 were monitored *via* elastic window scans in the temperature range < 50 to 373 K. The elwins revealed that while heating to 200 K, the mobility of cyclohexanone oxime increased to a similar extent with both frameworks. However, in the range 200 - 320 K, the oxime became more mobile in HP SAPO-5 than MP SAPO-5, which reflected an increased freedom of movement inside the hierarchical framework. Notably, at temperatures > 320 K the trend in oxime mobility was reversed, with greater proton dynamics detected in MP SAPO-5 than HP SAPO-5. Neutron diffraction data (acquired during the QENS measurements and in a separate total scattering experiment) provided further insight into the varying oxime mobility in MP and HP SAPO-5. In the MP SAPO-5 sample, the sorbed oxime exhibited long-range order up to 338 K, producing a diffraction pattern akin to the pure substrate. However, the HP SAPO-5 sample showed no evidence for crystalline oxime, even at < 50 K. On the basis of earlier INS studies, it was proposed that the hydrogen-bonded structure of the crystalline oxime was disintegrated in favour of multiple hydrogen bonding interactions with the silanols in the mesopores of HP SAPO-5. (Whilst notable that oxime-silanol interactions were established in the physical mixture at room temperature, this was observed previously.) Therefore, the reduced mobility of cyclohexanone oxime in HP SAPO-5 at > 320 K was attributed to a fraction of the oxime molecules being immobilised on the walls of the mesopores by hydrogen bonding to silanol sites. For MP SAPO-5, the crystalline oxime identified a preference for the hydrogen-bonded network of the pure solid, over a more sparse interaction with the isolated framework acid sites. However, by increasing the thermal energy of the system, the intermolecular oxime-oxime hydrogen bonds were disrupted, whereupon the individual molecules may have been sorbed into the micropores.

On studying the elwins of MP and HP SAPO-5 at various Q, it was determined that the proton dynamics detected by QENS was predominantly due to localised motion of the oxime. Subsequent fitting of the QENS spectra and experimental EISFs (at 373 K) revealed that an isotropic rotation model best described the movement of oxime in HP and MP SAPO-5. Since the motion of the oxime in HP and MP SAPO-5 was identical in both geometry and rate

(~ 2.6 x10^{10} s^{-1}), the mobile oxime was thought to be located in their common pore structure: the micropores. The data fitting also quantified a larger fraction of immobile oxime in HP SAPO-5 (0.54) than MP SAPO-5 (0.23), which was consistent with the adsorption of some oxime within the siliceous mesopores.

In contrast to the oxime sorbate, the *Q*-averaged elwins for ε-caprolactam sorbed in HP and MP SAPO-5 were near-identical across the entire temperature range (70 – 373 K), indicating that the lactam mobility increased in a similar manner in both frameworks. However, the corresponding neutron diffraction data was quite dissimilar for the two adsorbents, with crystalline lactam observed up to ~ 323 K with MP SAPO-5, but no long-range order observed in the lactam with HP SAPO-5. Elwins at low-, medium-, and high-*Q* revealed that the motion of the lactam increased over all spatial-length scales with thermal energy, although medium- and short-range motions were increasingly dominant in both MP and HP SAPO-5. Correspondingly, analysis of QENS spectra and experimental EISFs at 373 K identified localised, isotropic rotation of lactam in MP and HP SAPO-5, with a mobile fraction of 0.45 and 0.34, respectively. Again, the nature and rate of lactam rotation (2.3 x10^{10} s^{-1}) was essentially identical in MP and HP SAPO-5, which suggested that mobile fraction was located in the micropores.

Given the increased immobility of caprolactam in HP SAPO-5 *versus* MP SAPO-5, as well as the lack of crystalline sorbate observed in the diffraction spectra, it was proposed that caprolactam interacted with the silanols in the mesopores in a manner similar to cyclohexanone oxime. Nevertheless, compared to cyclohexanone oxime, the sorbate-silanol hydrogen bonding interactions were less detrimental to the total mobility of caprolactam than the steric confinement of the micropores. **Table 4.5.1** summarises the key results from the QENS analysis of cyclohexanone oxime and ε-caprolactam sorbed in HP and MP SAPO-5.

Table 4.5.1: A summary of the rotational diffusion coefficients (D_{rot}) of the mobile fractions (p_x) of cyclohexanone oxime and caprolactam sorbed in MP and HP SAPO-5.

Sorbate	Catalyst	Nature of sorbate motion	p_x	D_{rot} / 10^{10} s^{-1}
cyclohexanone oxime	MP SAPO-5	Isotropic rotation	0.77	2.64
	HP SAPO-5		0.46	2.62
ε-caprolactam	MP SAPO-5		0.45	2.33
	HP SAPO-5		0.34	2.34

Thus, QENS analysis and diffraction data have provided further evidence that the hydrogen-bonded structure of crystalline cyclohexanone oxime is disrupted in favour of hydrogen bonding interactions with the mesopores of organosilane-templated HP SAPOs. Whilst substrate-silanol interactions were found to significantly curtail oxime mobility in HP SAPO-5, previous spectroscopic studies have alluded to their substrate activating effect in the Beckmann rearrangement. In addition, the neutron scattering experiments indicated that ε-caprolactam is also susceptible to hydrogen bonding with the silanols in the organosilane-templated mesopores. Significantly, the mobility of the lactam was largely unaffected by any interaction with silanols, as the hindered diffusion of caprolactam has been associated with reduced catalyst selectivity in the heterogeneously catalysed BR.

To complement the QENS studies, the mobility of cyclohexanone oxime in HP SAPO-5 was more recently probed *via* PFG-NMR. However, the proton spectrum of the oxime was not readily deconvoluted from that of the SAPO framework, and the oxime was insufficiently mobile to be detected at the resolution of the spectrometer. Therefore, further investigation of the mobility of cyclohexanone oxime in HP SAPO-5 might involve molecular dynamics simulations, which have previously been used to calculate the rotational coefficient of mobile sorbates in porous matrices,[103] and to investigate the configuration of adsorbed species.[34] One of the main challenges in any computational analysis involving the HP SAPO framework is the lack of a well-defined model pore structure that incorporates both micro- and meso-pores in a single system. Extracting detailed information about the degree of pore interconnectivity, and the length and distribution of the secondary mesoporosity remains a challenge in the characterisation of hierarchical pore architectures.

There is also an opportunity to build on the total neutron scattering studies with a contrast variation study of $C_6H_{10}NOH$ and $C_6D_{10}NOD$, exploiting the different coherent scattering lengths of the ^1H and ^2H isotopes (-3.74×10^{-15} and 6.67×10^{-15} m, respectively).[111] In this case, changes in the intensity of the diffraction from the framework, with analysis of the low-Q region (associated with larger structures, such as mesopores) might provide additional insight into the location of the adsorbate within the framework.[112]

4.6 References

1. J. Kärger and S. Vasenkov, *Micropor. Mesopor. Mater.*, 2005, **85**, 195-206.
2. S. M. Csicsery, *Zeolites*, 1984, **4**, 202-213.
3. H. G. Karge and J. Weitkamp, *Adsorption and Diffusion*, Springer, Berlin, 2008.
4. R. A. van Santen, *Modern Heterogeneous Catalysis: An Introduction*, John Wiley & Sons, Incorporated, Weinheim, GERMANY, 2017.
5. A. Fick, *Annalen der Physik*, 1855, **170**, 59-86.
6. J. Kärger, D. M. Ruthven and D. N. Theodorou, *Diffusion in Nanoporous Materials*, Wiley, Germany, 2012.
7. C. Chmelik, H. Bux, J. Caro, L. Heinke, F. Hibbe, T. Titze and J. Kärger, *Phys. Rev. Lett.*, 2010, **104**, 085902.
8. R. M. Roque-Malherbe, *Adsorption and Diffusion in Nanoporous Materials*, CRC press, Boca Raton, 2018.
9. D. Schuring, Doctor of Philosophy, Technische Universiteit Eindhoven, 2002.
10. D. M. Ruthven, in *Introduction to Zeolite Science and Practice*, eds. J. Cejka, H. van Bekkum, A. Corma and F. Schüth, Elsevier Science, Amsterdam, 3 edn., 2007, vol. 168.
11. J. Xiao and J. Wei, *Chem. Eng. Sci.*, 1992, **47**, 1123-1141.
12. H. Nagasawa, T. Niimi, M. Kanezashi, T. Yoshioka and T. Tsuru, *AIChE J.*, 2014, **60**, 4199-4210.
13. J. Kärger and R. Valiullin, *Encyclopedia of Magnetic Resonance*, 2011, DOI: 10.1002/9780470034590.emrstm0121.pub2.
14. J. Kärger and D. M. Ruthven, *New J. Chem.*, 2016, **40**, 4027-4048.
15. N. Y. Chen, T. F. Degnan and C. M. Smith, *Molecular Transport and Reaction in Zeolites: Design and Application of Shape Selective Catalysis*, John Wiley & Sons, New York, 1994.
16. D. E. Favre, D. J. Schaefer, S. M. Auerbach and B. F. Chmelka, *Phys. Rev. Lett.*, 1998, **81**, 5852-5855.
17. J. Caro, M. Bülow, W. Schirmer, J. Kärger, W. Heink, H. Pfeifer and S. P. Ždanov, *J. Chem. Soc., Faraday Trans. 1*, 1985, **81**, 2541-2550.
18. J. Kärger and S. Vasenkov, in *Handbook of Zeolite Science and Technology*, eds. S. M. Auerbach, K. A. Carrado and P. K. Dutta, Marcel Dekker, Inc., New York, 2003, ch. 10.
19. H. W. Georgii and P. Warneck in *Global Aspects of Atmospheric Chemistry*, ed. R. Zellner, H. Baumgärtel, W. Grünbein and F. Hesel, Springer, Berlin 1999, ch.3 pp 128.
20. J. Kärger and J. Caro, *J. Chem. Soc., Faraday Trans. 1.*, 1977, **73**, 1363-1376.
21. U. Schemmert, J. Kärger and J. Weitkamp, *Micropor. Mesopor. Mater.*, 1999, **32**, 101-110.

22. M. Bée, *Quasielastic Neutron Scattering: Principles and Applications in Solid State Chemistry, Biology and Materials Science*, IOP Publishing Ltd, Bristol, U.K., 1988.

23. R. Q. Snurr, A. T. Bell and D. N. Theodorou, *J. Phys. Chem.*, 1993, **97**, 13742-13752.

24. S. M. Auerbach, N. J. Henson, A. K. Cheetham and H. I. Metiu, *J. Phys. Chem.*, 1995, **99**, 10600-10608.

25. J. G. Tsikoyiannis and J. Wei, *Chem. Eng. Sci.*, 1991, **46**, 233-253.

26. E. A. Pidko and R. A. van Santen, in *Zeolite Characterization and Catalysis: A Tutorial*, eds. A. W. Chester and E. G. Derouane, Springer, Netherlands, 2009.

27. B. Smit and T. L. M. Maesen, *Chem. Rev.*, 2008, **108**, 4125-4184.

28. H. Jobic and D. N. Theodorou, *Micropor. Mesopor. Mater.*, 2007, **102**, 21-50.

29. M. Bée, *Chem. Phys.*, 2003, **292**, 121-141.

30. H. Jobic, M. Bée, A. Méthivier and J. Combet, *Micropor. Mesopor. Mater.*, 2001, **42**, 135-155.

31. H. Jobic, A. Renouprez, M. Bee and C. Poinsignon, *J. Phys. Chem.*, 1986, **90**, 1059-1065.

32. M. Bée, *Physica B: Condens. Matt.*, 1992, **182**, 323-336.

33. H. Jobic, M. Bée and A. J. Dianoux, *J. Chem. Soc., Faraday Trans.*, 1989, **85**, 2525-2534.

34. A. J. O'Malley, V. García Sakai, I. P. Silverwood, N. Dimitratos, S. F. Parker and C. R. A. Catlow, *Phys. Chem. Chem. Phys.*, 2016, **18**, 17294-17302.

35. C. T. Chudley and R. J. Elliott, *Proc. Phys. Soc.*, 1961, **77**, 353-361.

36. A. Sahasrabudhe, S. Mitra, A. K. Tripathi, R. Mukhopadhyay and N. M. Gupta, *Phys. Chem. Chem. Phys.*, 2003, **5**, 3066-3075.

37. P. L. Hall and D. K. Ross, *Mol. Phys.*, 1981, **42**, 673-682.

38. S. Mitra, S. Sumitra, A. M. Umarji, R. Mukhopadhyay, S. Yashonath and S. L. Chaplot, *Pramana*, 2004, **63**, 449-453.

39. S. Mitra, R. Mukhopadhyay, A. Sayeed, S. Yashonath and S. L. Chaplot, *Appl. Phys. A*, 2002, **74**, s1317-s1319.

40. K. S. Singwi and A. Sjölander, *Phys. Rev.*, 1960, **119**, 863-871.

41. H. Jobic, A. N. Fitch and J. Combet, *J. Phys. Chem. B*, 2000, **104**, 8491-8497.

42. H. Jobic, in *Recent Advances in Gas Separation by Microporous Ceramic Membranes*, ed. N. K. Kanellopoulos, Elsevier, The Netherlands, 2000, ch. 1.5.

43. L. N. Gergidis, D. N. Theodorou and H. Jobic, *J. Phys. Chem. B*, 2000, **104**, 5541-5552.

44. A. J. O'Malley and C. R. A. Catlow, in *Neutron Scattering - Applications in Biology, Chemistry, and Materials Science*, eds. F. Fernandez-Alonso and D. L. Price, Elsevier, USA, 2017.

45. V. F. Sears, *Can. J. Phys.*, 1966, **44**, 1279-1297.

46. H. Jobic, M. Bée and G. J. Kearley, *Zeolites*, 1989, **9**, 312-317.

47. F. Volino and A. J. Dianoux, *Mol. Phys.*, 1980, **41**, 271-279.

48. S. Pili, S. P. Argent, C. G. Morris, P. Rought, V. García-Sakai, I. P. Silverwood, T. L. Easun, M. Li, M. R. Warren, C. A. Murray, C. C. Tang, S. Yang and M. Schröder, *J. Am. Chem. Soc.*, 2016, **138**, 6352-6355.

49. J. D. Barnes, *J. Chem. Phys.*, 1973, **58**, 5193-5201.

50. S. Mitra, A. K. Tripathy, N. M. Gupta and R. Mukhopadhyay, *Appl. Phys. A*, 2002, **74**, s1308-s1310.

51. H. Hervet, F. Volino, A. J. Dianoux and R. E. Lechner, *J. Phys. Lett.*, 1974, **35**, 151-155.

52. H. Jobic, M. Bée and G. J. Kearley, *Zeolites*, 1992, **12**, 146-151.

53. A. J. O'Malley, S. F. Parker and C. R. A. Catlow, *Chem. Commun.*, 2017, **53**, 12164-12176.

54. H. Jobic, *J. Mol. Catal. A: Chem.*, 2000, **158**, 135-142.

55. H. Jobic and D. N. Theodorou, *J. Phys. Chem. B*, 2006, **110**, 1964-1967.

56. F. Leroy and H. Jobic, *Chem. Phys. Lett.*, 2005, **406**, 375-380.

57. H. Jobic, W. Schmidt, C. B. Krause and J. Kärger, *Micropor. Mesopor. Mater.*, 2006, **90**, 299-306.

58. B. Millot, A. Méthivier, H. Jobic, H. Moueddeb and M. Bée, *J. Phys. Chem. B*, 1999, **103**, 1096-1101.

59. S. K. Matam, A. J. O'Malley, C. R. A. Catlow, Suwardiyanto, P. Collier, A. P. Hawkins, A. Zachariou, D. Lennon, I. Silverwood, S. F. Parker and R. F. Howe, *Catal. Sci. Technol.*, 2018, **8**, 3304-3312.

60. A. J. O'Malley, S. F. Parker, A. Chutia, M. R. Farrow, I. P. Silverwood, V. García-Sakai and C. R. A. Catlow, *Chem. Commun.*, 2016, **52**, 2897-2900.

61. H. Jobic and A. Méthivier, *Oil Gas Sci. Technol.*, 2005, **60**, 815-830.

62. US Pat. 3558730 A, 1971.

63. US Pat. 3636121, 1972.

64. M. Hartmann, *Angew. Chem. Int. Ed.*, 2004, **43**, 5880-5882.

65. S. H. Newland, W. Sinkler, T. Mezza, S. R. Bare, M. Carravetta, I. M. Haies, A. Levy, S. Keenan and R. Raja, *ACS Catal.*, 2015, **5**, 6587-6593.

66. I. Miletto, G. Paul, S. Chapman, G. Gatti, L. Marchese, R. Raja and E. Gianotti, *Chem.– A Eur. J.*, 2017, **23**, 9952-9961.

67. I. Miletto, C. Ivaldi, G. Paul, S. Chapman, L. Marchese, R. Raja and E. Gianotti, *ChemistryOpen*, 2018, **7**, 297-301.

68. G. P. Heitmann, G. Dahlhoff and W. F. Hölderich, *J. Catal.*, 1999, **186**, 12-19.

69. V. R. R. Marthala, Y. Jiang, J. Huang, W. Wang, R. Gläser and M. Hunger, *J. Am. Chem. Soc.*, 2006, **128**, 14812-14813.

70. Y. Izumi, H. Ichihashi, Y. Shimazu, M. Kitamura and H. Sato, *Bull. Chem. Soc. Jpn.*, 2007, **80**, 1280-1287.

71. H. Sato, K. Hirose, M. Kitamura and Y. Nakamura, *Stud. Surf. Sci. Catal.*, 1989, **49**, 1213-1222.

72. Database of Zeolite Structures, https://www.iza-structure.org/databases, (accessed January 2019).

73. J. Laugier and B. Bochu, CelRef Version 3, http://www.ccp14.ac.uk/tutorial/lmgp/celref.htm).

74. M. T. F. Telling and K. H. Andersen, *Phys. Chem. Chem. Phys.*, 2005, **7**, 1255-1261.

75. ISIS Neutron and Muon Source, https://www.isis.stfc.ac.uk/Pages/home.aspx, (accessed October 2018).

76. C102202: cyclohexanone oxime, https://www.sigmaaldrich.com/catalog/product/aldrich/c102202?lang=en&region=GB, (accessed March 2019).

77. C2204: ε-caprolactam, https://www.sigmaaldrich.com/catalog/product/aldrich/c2204?lang=en&region=GB, (accessed March 2019).

78. R. T. Azuah, L. R. Kneller, Y. Qiu, P. L. Tregenna-Piggott, C. M. Brown, J. R. Copley and R. M. Dimeo, *J. Res. Nat. Inst. Stand. Technol.*, 2009, **114**, 341.

79. O. Arnold, J.-C. Bilheux, J. Borreguero, A. Buts, S. I. Campbell, L. Chapon, M. Doucet, N. Draper, R. F. Leal and M. Gigg, *Nucl. Instrum. Methods Phys. Res. Sect. A*, 2014, **764**, 156-166.

80. D. T. Bowron, A. K. Soper, K. Jones, S. Ansell, S. Birch, J. Norris, L. Perrott, D. Riedel, N. J. Rhodes, S. R. Wakefield, A. Botti, M.-A. Ricci, F. Grazzi and M. Zoppi, *Rev. Sci. Instrum.*, 2010, **81**, 033905.

81. S. McLain, D. B. A. Hannon and A. Soper, *Gudrun: a computer program developed for analysis of neturon diffraction data*, ISIS Facility, Rutherford Appleton Laboratory, U.K., 2012.

82. M. Choi, H. S. Cho, R. Srivastava, C. Venkatesan, D.-H. Choi and R. Ryoo, *Nat. Mater.* 2006, **5**, 718.

83. T. T. H. Dang, H.-L. Zubowa, U. Bentrup, M. Richter and A. Martin, *Micropor. Mesopor. Mater.*, 2009, **123**, 209-220.

84. L. Wang, C. Guo, S. Yan, X. Huang and Q. Li, *Micropor. Mesopor. Mater.*, 2003, **64**, 63-68.

85. S. H. Jhung, J.-S. Chang, J. S. Hwang and S.-E. Park, *Micropor. Mesopor. Mater.*, 2003, **64**, 33-39.

86. M. Thommes, K. Kaneko, V. Neimark Alexander, P. Olivier James, F. Rodriguez-Reinoso, J. Rouquerol and S. W. Sing Kenneth, *Pure Appl. Chem.*, 2015, **87**, 1051-1069.

87. K. Cho, H. S. Cho, L.-C. de Ménorval and R. Ryoo, *Chem. Mater.*, 2009, **21**, 5664-5673.

88. Y.-P. Guo, H.-J. Wang, Y.-J. Guo, L.-H. Guo, L.-F. Chu and C.-X. Guo, *Chem. Eng. J.*, 2011, **166**, 391-400.

89. M. Choi, R. Srivastava and R. Ryoo, *Chem. Commun.*, 2006, DOI: 10.1039/B612265E, 4380-4382.

90. Y. Cheneviere, F. Chieux, V. Caps and A. Tuel, *J. Catal.*, 2010, **269**, 161-168.

91. K. Qiao, F. Zhou, Z. Han, J. Fu, H. Ma and G. Wu, *Micropor. Mesopor. Mater.*, 2019, **274**, 190-197.

92. L. Marchese, A. Frache, G. Gatti, S. Coluccia, L. Lisi, G. Ruoppolo, G. Russo and H. O. Pastore, *J. Catal.*, 2002, **208**, 479-484.

93. M. Popova, C. Minchev and V. Kanazirev, *Appl. Catal. A: Gen.*, 1998, **169**, 227-235.

94. S.-T. Yang, J.-Y. Kim, H.-J. Chae, M. Kim, S.-Y. Jeong and W.-S. Ahn, *Mater. Res.Bull.*, 2012, **47**, 3888-3892.

95. S. Tao, X. Li, G. Lv, C. Wang, R. Xu, H. Ma and Z. Tian, *Catal. Sci. Technol.*, 2017, **7**, 5775-5784.

96. C. Wang, M. Yang, P. Tian, S. Xu, Y. Yang, D. Wang, Y. Yuan and Z. Liu, *J. Mater. Chem. A*, 2015, **3**, 5608-5616.

97. K. Suzuki, Y. Aoyagi, N. Katada, M. Choi, R. Ryoo and M. Niwa, *Catal. Today*, 2008, **132**, 38-45.

98. P. Botella, A. Corma, S. Iborra, R. Montón, I. Rodríguez and V. Costa, *J. Catal.*, 2007, **250**, 161-170.

99. M. A. Camblor, A. Corma, H. García, V. Semmer-Herlédan and S. Valencia, *J. Catal.*, 1998, **177**, 267-272.

100. C. Ngamcharussrivichai, P. Wu and T. Tatsumi, *J. Catal.*, 2004, **227**, 448-458.

101. C. Ngamcharussrivichai, P. Wu and T. Tatsumi, *J. Catal.*, 2005, **235**, 139-149.

102. M. Lutz, A. L. Spek, R. Dabirian, C. A. van Walree and L. W. Jenneskens, *Acta Crystallogr. Sect. C: Cryst. Struct. Commun.*, 2004, **60**, 127-129.

103. R. Mukhopadhyay, A. Sayeed, S. Mitra, A. V. Anil Kumar, M. N. Rao, S. Yashonath and S. L. Chaplot, *Phys. Rev. E*, 2002, **66**, 061201.

104. M. Leutzsch, M. Falkowska, T.-L. Hughes, A. J. Sederman, L. F. Gladden, M. D. Mantle, T. G. A. Youngs, D. Bowron, H. Manyar and C. Hardacre, *Chem. Commun.*, 2018, **54**, 10191-10194.

105. K. L. Stefanopoulos, F. K. Katsaros, T. A. Steriotis, A. A. Sapalidis, M. Thommes, D. T. Bowron and T. G. A. Youngs, *Phys. Rev. Lett.*, 2016, **116**, 025502.

106. S. Mascotto, D. Wallacher, A. Brandt, T. Hauss, M. Thommes, G. A. Zickler, S. S. Funari, A. Timmann and B. M. Smarsly, *Langmuir*, 2009, **25**, 12670-12681.

107. T. G. A. Youngs, H. Manyar, D. T. Bowron, L. F. Gladden and C. Hardacre, *Chem. Sci.*, 2013, **4**, 3484-3489.

108. F. t. Winkler and J. Dunitz, *Acta Crystallogr. Sect. B: Struct. Crystallogr. Cryst. Chem.*, 1975, **31**, 268-269.

109. C. Flego and L. Dalloro, *Micropor. Mesopor. Mater.*, 2003, **60**, 263-271.

110. M. Linares, C. Vargas, A. García, C. Ochoa-Hernández, J. Čejka, R. A. García-Muñoz and D. P. Serrano, *Catal. Sci. Technol.*, 2017, **7**, 181-190.

111. W. T. Heller, *Acta Crystallogr. Sect. D: Biol. Crystallogr.*, 2010, **66**, 1213-1217.

112. J. D. F. Ramsay, *Adv. Colloid Interface Sci.*, 1998, **76-77**, 13-37.

Chapter 5 The synthesis and characterisation of an organosilane-templated hierarchical SAPO-37 catalyst for the Beckmann rearrangement

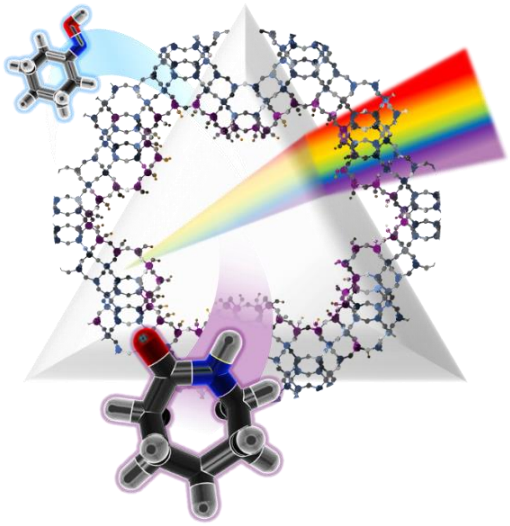

Special Acknowledgements

Dr James Taylor and **Hannah Dixon**

ISIS Hydrogen and Catalysis Lab, Rutherford Appleton Laboratory, U.K.

For acquiring NH_3-TPD data.

Dr Cara Doherty

The Commonwealth Scientific and Industrial Research Organisation, Australia.

For acquiring and processing PALS data.

Dr Enrica Gianotti and **Dr Ivana Miletto**

Department of Science and Technological Innovation, Università del Piemonte Orientale, Italy.

For acquiring FTIR data.

Dr Marina Carravetta

School of Chemistry, University of Southampton, U.K.

For assistance and expertise in performing MAS NMR experiments.

5.1 Introduction

The development of zeotype catalysts for the Beckmann rearrangement (BR) has motivated an extensive investigation of the underlying structure-activity relationships. In particular, physicochemical characterisation has highlighted the influential role of framework architecture[1-7] and acid-site strength.[6-13] Probe-based techniques are providing increasingly detailed insight into the structure and interactions of porous materials, affording further opportunities to optimise catalysts for the BR.[14]

5.1.1 Probing hierarchical porosity of zeotype materials: positron annihilation lifetime spectroscopy

Since heterogeneous catalysis is confined to the interface between fluid-phase reagents and solid-phase catalyst, the accessibility of the active sites is crucial. Accordingly, the porosity of zeotype materials has been widely exploited in heterogeneous catalysis. The relatively large internal surface area of a porous framework can enhance catalytic turnover by exposing more active sites per gram of catalyst, whilst the confinement of the pores may induce shape-selective transformations. Nonetheless, the steric constraints of the small micropores can impose mass transport restrictions that prevent the efficient utilisation of the internal active sites. Therefore, hierarchical materials have been designed to balance the catalytic functionalities of the microporous zeotype with the improved mass transport of an auxiliary meso- and/or macro-pore network.[15]

The nature of the porosity in a hierarchical zeotype is important, as the shape, size, and connectivity of the various pore networks will influence its catalytic capabilities.[16] Since commercial manometric apparatus is quite widely available, gas adsorption is frequently used to obtain surface areas, pore volumes, and pore-size distributions.[17] However, quantitative analysis of gas-sorption data depends on the validity of a number of assumptions about the pore geometry and the nature of the surface-probe interactions (**Section 2.2.2.5**).[18] As such, the accuracy of physisorption data can be compromised by disordered porosity, surface heterogeneities, and non-specific interactions between the probe and adsorbent.[19] Furthermore, gas adsorption relies on the diffusion of molecules into the pores, making it impossible to identify closed pores by this technique.[20] In the case of complex pore architectures, it is often challenging to deconvolute the gas adsorption in different pore structures, which might otherwise be used to extract information about the nature, quantity, and interconnectivity of the different pore types.[20]

In the last few decades, positron annihilation lifetime spectroscopy (PALS) has emerged as an informative technique for the quantitative analysis of porosity in solids.[20-26] In essence, PALS is a non-destructive technique that monitors the matter-antimatter annihilation of the *ortho*-positronium (*o*-Ps, a metastable system comprising a positron and an electron) in order to extract information about the location of the annihilation event. For textural characterisation, PALS exploits the tendency of *o*-Ps to localise in electron-deficient defects (e.g. such as pores and voids) in an insulating material (**Figure 5.1.1**). Although implanted directly into the bulk of a sample, *o*-Ps will diffuse into a porous network and, where accessible, move into increasingly larger void spaces (driven by a decreasing zero-point energy) until annihilation.[22] If the *o*-Ps is not destroyed by pickoff annihilation with an electron from the surrounding matrix, it annihilates with an intrinsic vacuum lifetime of 142 ns. Therefore, any structural feature that increases the probability of pickoff annihilation (e.g. closed or narrow pores) will increase the probability of *o*-Ps annihilating with a lifetime < 142 ns. By applying suitable models (usually the Tao-Eldrup model[27, 28] and its extensions[29, 30]), it is possible to relate the *o*-Ps lifetime to the size of the void in which it was annihilated. Significantly, the number of *o*-Ps annihilating at a particular lifetime is directly related to the contribution of each annihilation site; hence, the PALS intensity reflects the relative quantity and accessibility of the pores in a sample.

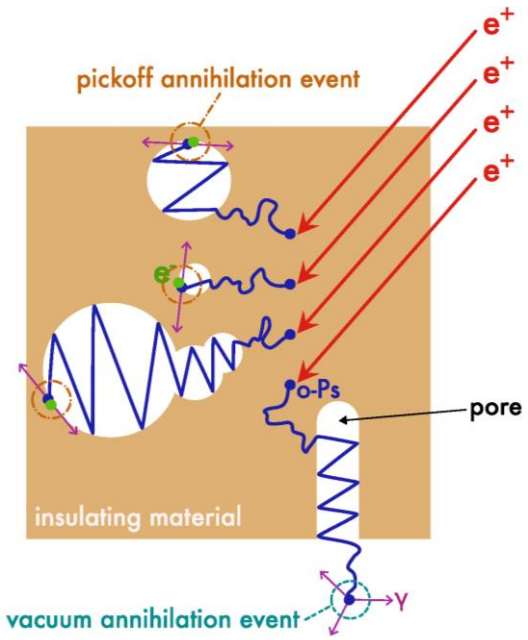

Figure 5.1.1: A depiction of positron (e^+) formation and annihilation in porous materials.[25] Positrons implanted into an insulating material may capture an electron to form the *o*-Ps species. *o*-Ps will tend to localise in the pores, travelling into increasingly larger voids (where accessible). The *o*-Ps may undergo pickoff annihilation with an electron (e^-) from the surrounding matrix, or otherwise escape to the surroundings and annihilate in vacuum. In either case, annihilation occurs with the production of gamma photons (γ).

The *o*-Ps is sufficiently long-lived to quantify pore dimensions in the range 0.3 - 30 nm, and thus PALS can probe both the micro-(< 2 nm) and meso-pore (2 - 50 nm) range.[25] Moreover, the resolution of PALS is sufficient to be able to discriminate different pore architectures that fall within same pore-size regime. For instance, Dutta *et al.* undertook to compare the N_2 gas adsorption and PALS techniques by assessing the porosity of faujasitic zeolites.[31] Whilst the calculated pore dimensions were largely in agreement in the mesopore range, PALS was able to measure the microporosity of the samples with greater accuracy, and could distinguish the microporous void spaces of the α- and β-cages within the FAU framework.

A particular advantage of the PALS technique over gas adsorption is that the nanosized positronium probe (Bohr radius = 0.53 Å)[21] can occupy micropores that are inaccessible to a conventional probe gas (N_2 at 77 K = 0.162 nm^2, Ar at 87 K = 0.142 nm^2).[32] Furthermore, PALS does not rely on the diffusion of the probe in order to access the porosity. Since the positron is directly implanted into a sample, PALS can be used to characterise closed porosity. As a result, PALS analyses have revealed significant porosity in materials that were apparently non-porous by N_2 adsorption measurements.[21, 33] **Table 5.1.1** presents a comparison of N_2 adsorption-desorption and PALS for the characterisation of porous materials.

Table 5.1.1: A comparison of N_2 gas adsorption and positron annihilation lifetime spectroscopy as techniques to assess porosity.[22, 25, 34-36] Table continued overleaf.

Feature	Gas adsorption	Positron Annihilation Lifetime Spectroscopy
Micropore analysis	BJH pore-size analysis is only valid for pore diameters > 2 nm.	Only limited by the Bohr radius of the positron (0.53 Å).
Mesopore analysis	Good, but pore-size estimates may be inferior at the lower limit of the mesopore regime (< 5 nm) due to capillary condensation.	Limited (< 30 nm) by the vacuum lifetime of *o*-Ps (142 ns.)
Information obtained	Pore-size distribution, quantitative surface area estimates, pore volumes, pore morphologies, surface adsorption-desorption processes.	Pore size distribution, pore connectivity, pore interconnection lengths, details of the micro-electronic environment at the annihilation site.
Dependence of the commonly adopted model for pore-size distribution on pore geometry	The BJH model, which uses the Kelvin equation, assumes a cylindrical pore.	The Tao-Eldrup model assumes a spherical pore.

Table 5.1.1 continued: A comparison of N_2 gas adsorption and positron annihilation lifetime spectroscopy as techniques to assess porosity.[22, 25, 34-36]

Feature	Gas adsorption	Positron Annihilation Lifetime Spectroscopy
Non-destructive?	Yes	Yes
Materials scope	Used to study a wide range of solid, porous materials.	The sample material must form the metastable positronium (Ps) species. Most insulating materials readily form Ps, but positrons tend to annihilate rapidly in materials containing free electrons (e.g. metals, semiconductors).
Sample environment	Low temperature (77 K), and ambient-to-low pressure of gas.	Wide temperature range, but the sample must be under vacuum.
Experimental setup	Often bulky and requires a gas supply.	Compact, bench-top device.
Accessibility of technique	Widely accessible.	Currently of relatively limited accessibility.
Notable advantages	Molecular probe provides a more realistic impression of pore accessibility and substrate-induced changes in pore structure.	Capable of depth profiling. Implantation of positrons within the sample allows study of closed pores. The positron can enter narrow windows and occupy very small micropores.
Notable disadvantages	Interactions of N_2 are sensitive to the surface chemistry, which can lead to unreliable data. Irreversible gas adsorption within mesopores can create discrepancies in pore size calculated from gas adsorption and desorption processes.	Interpretation of the trends in PALS data is not often straightforward. Data analysis and deconvolution of PALS spectra need further development.

In one investigation, PALS was used to study the porosity of molecular sieve silica membranes, whose apparent non-porosity (by N_2 adsorption) belied their gas-sieving capabilities.[21] Analysis of the PALS data yielded three lifetime components, identifying a trimodal pore system in the silica membranes. The shortest *o*-Ps lifetime component characterised ~ 3 Å micropores, which proved consistent with the observed size-discrimination for gases permeating across the membranes. The remaining two lifetime components characterised larger micropores of ~ 8 and 12 Å, but since the silica membranes exhibited a high selectivity for the size of the permeating gas, it was concluded that these larger pores must be isolated from each other, and the external surface (**Figure 5.1.2**).

Nonetheless, the presence of the larger, internal micropores could be correlated with increased permeation of gas across the silica membrane.

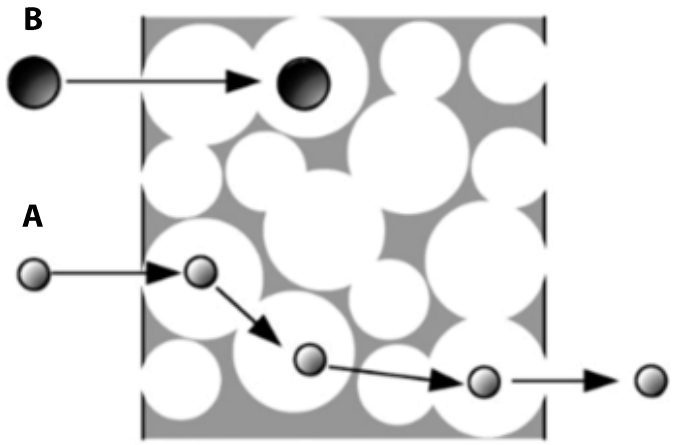

Figure 5.1.2: A schematic showing the multimodal pore architecture of a silica membrane used to sieve gas molecule **A** from a mixture with gas molecule **B**.[21] Figured adapted with permission from John Wiley and Sons.

Where PALS is able to separate and quantify porosity over multiple length scales, it has proven well suited to the study of hierarchical porosity.[20-25, 33, 37] In particular, recent studies have sought to exploit the unique capabilities of the PALS technique in order to quantify the interconnectivity of micro- and meso-pores in hierarchical zeolites.[20-25]

In a PALS experiment, the longest lifetime component is the vacuum annihilation of the *o*-Ps (142 ns).[25] Whilst the *o*-Ps lifetime is likely to be reduced by confinement within a pore, it will tend towards the self-annihilation lifetime if the *o*-Ps can move into increasingly larger void spaces. Ultimately, if the *o*-Ps can escape from the external surface of the sample ('out-diffusion'),[20] then it will self-annihilate at the vacuum lifetime. In a hierarchical system, the proportion of *o*-Ps annihilating in the micro- and meso-pores will depend on their relative pore volume and interconnectivity.[23] Thus, it follows that the contribution of vacuum annihilation will reflect the ease with which *o*-Ps can access the external surface by migrating through the intracrystalline pore system. It was on this basis that Milina *et al.* proposed that the fraction of *o*-Ps vacuum annihilation provided a metric to assess the impact of secondary mesoporosity on the mass transport properties of a zeolite.[23]

It was in seeking a descriptor for the efficacy of hierarchical zeolite syntheses, that Milina *et al.* used PALS to investigate the connectivity of the micro- and meso-pores in demetallated ZSM-5 zeolite.[23] When the hierarchical zeolites were tested in the methanol-to-hydrocarbon (MTH) reaction, the frameworks with open and interconnected mesoporosity were found to have greater resistance to coking. The authors also identified a close correlation between the

fraction of *o*-Ps annihilated in vacuum and catalyst lifetime in the MTH reaction, which vindicated *o*-Ps out-diffusion as a measure of pore connectivity. Later, the same authors defined a 'global pore connectivity' to quantify the pore-connectivity in hierarchical zeotypes.[24] The global pore connectivity was calculated as the number of *o*-Ps annihilated in vacuum as a fraction of the total number *o*-Ps annihilated.

PALS has since been used to examine the impact of post-synthetic (acid, base, and steam) treatments on the mass transport properties of hierarchically-porous (HP) faujasitic zeolites.[20] Initially, Ar adsorption (87 K) was used to classify the mesoporous architectures in the hierarchical faujasites by the relative diameter of pore body (d_{meso}) to pore window (d_{win}), yielding pyramidal (d_{meso} > 2 nm, d_{win} > d_{meso}), constricted (d_{win} > 2 nm, d_{win} < d_{mes}), and occluded (d_{win} < 1 nm, d_{win} << d_{meso}) mesopores (**Figure 5.1.3**). PALS analysis revealed that the microporous lifetime component in FAU zeolite was severely diminished (or otherwise absent) after post-synthetic modification, consistent with an increased diffusion of *o*-Ps out of the micropores. Furthermore, the larger proportion of *o*-Ps vacuum annihilation in pyramidal and constricted mesopores identified their positive influence on diffusion within the FAU zeolite, whereas the narrow, occluded mesopores were found to hinder the out-diffusion of *o*-Ps. As such, PALS provided a means to quantify the mass transport properties of hierarchical zeolites with respect to the geometry of their mesoporous voids.

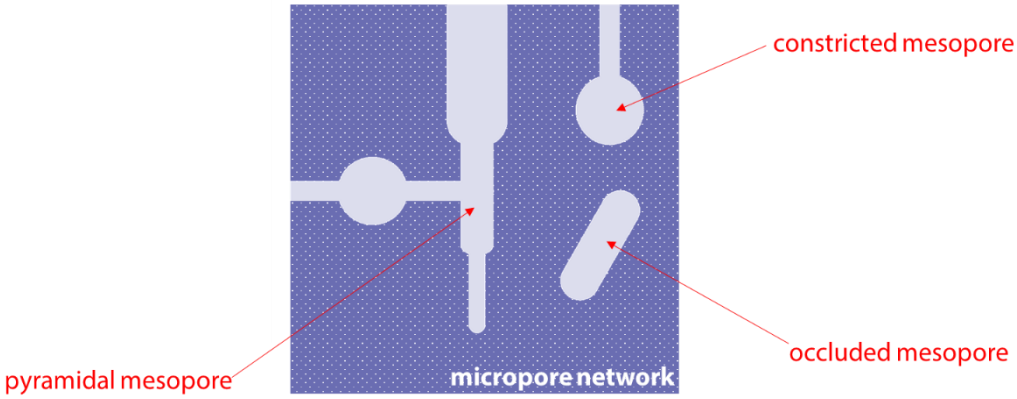

Figure 5.1.3: A schematic of pyramidal (d_{meso} > 2 nm, d_{win} > d_{meso}), constricted (d_{win} > 2 nm, d_{win} < d_{mes}), and occluded (d_{win} < 1 nm, d_{win} << d_{meso}) mesopores.

Overall, PALS is providing unique insights into the structure of nanoporous materials,[25] offering a level of detail beyond the remit of conventional gas adsorption techniques.[21, 31] For the study of complex pore architectures, PALS has demonstrated a capability to differentiate the size, quantity, and accessibility of distinct void structures that coexist within the same material.[25, 33, 37] Significantly, the use of PALS to quantify the efficacy of hierarchical syntheses (based on the connectivity and accessibility of the pore network) might be exploited in the design of hierarchical catalysts.[20, 22-24]

5.1.2 Probe-based techniques to study the acidity of zeotype materials

The intrinsic acidity of zeotype materials has been widely utilised in heterogeneous catalysis, with structural and compositional diversity providing immense scope to tune catalyst properties to a target reaction.[38] Accordingly, there has been considerable effort to develop reliable characterisation tools that can measure zeotype acidity, and monitor its evolution on exposure to physical or chemical alterants.[39] However, the acidity of a zeotype is not the product of a single type of acid site; rather, it is an aggregate of many different acidic sites in, and upon, a continuous, porous framework.[38] Therefore, a comprehensive assessment of zeotype acidity must consider a number of factors, including the nature (Brønsted or Lewis), quantity, strength, and accessibility of the acid sites. Often, a variety of characterisation tools are used to study zeolitic acid sites. Whilst some techniques may be used to characterise the acid sites directly (e.g. MAS NMR,[40, 41] FTIR[42, 43]), many indirect, probe-based methods have been developed to obtain a more meaningful measure of framework acidity.[38, 39, 44]

Probe-based techniques exploit the acid-base interaction between a zeotype and a basic molecule, where the latter can be chosen to evaluate specific aspects of framework acidity (i.e. the amount, type, strength, and distribution of acid sites).[45] Broadly, techniques used to characterise framework-probe interactions are divided into spectroscopic (e.g. FTIR, MAS NMR) and adsorption-desorption (e.g. TPD, catalysis) methods.[39] Spectroscopically, framework acidity is evaluated through the perturbation, loss, or development of characteristic bands associated with adsorbed species and/or framework acid sites.[45] In sorption methods, the energy change associated with the adsorption or desorption of a probe molecule is related to the strength of its interaction with the acidic surface.

A number of criteria have been specified to assess the suitability of a probe molecule for characterisation solid-acids:[39, 45-47]

- The interactions of the probe molecule should be predominantly basic;
- Interactions with different types of acid site should be reliably differentiated;
- The probe should be sensitive to the strength of the acid site (and for quantitative analysis, create a measurable perturbation);
- For quantitative analysis, the concentration of each type acid site should be determinable;
- The dimensions of probe should be similar to those of the substrate in order to simulate acid-site accessibility. (Although probes of varying kinetic diameter may be used to ascertain the location of acid sites);[48, 49]
- The stoichiometry of the acid-base complex should be known;

- The probes should be chemically unreactive under the conditions of the characterisation experiment.

Numerous probe molecules have been identified to (largely) satisfy these requirements,[47] including (alkyl)amine,[50] (alkyl-substituted)pyridine,[48] (alkyl-substituted)benzene, nitriles,[51, 52] and carbon monoxide.[53] The diversity in size and basicity of acceptable probe molecules offers considerable scope to target acid-site studies to identify the location and/or strength-distribution of acid sites in a sample.

Amongst the aforementioned probes, the pyridine molecule has been widely used for the study of surface acidity using both sorption[54-56] and spectroscopic[54, 57-60] techniques. In particular, by labelling pyridine with the spin-½, ^{15}N nucleus it is possible to study its acid-base interactions *via* NMR spectroscopy.[61-64] ^{15}N MAS NMR is very sensitive to interactions involving the pyridine lone pair, as this has a direct influence on the chemical shift of the ^{15}N resonance (**Figure 5.1.4**).[61, 63] Moreover, the large chemical shift range for interactions at ^{15}N (from 317 ppm for liquid pyridine, to ~200 ppm for the pyridinium ion) allows for different strength surface-probe interactions (and hence acid sites) to be distinguished.[62, 64]

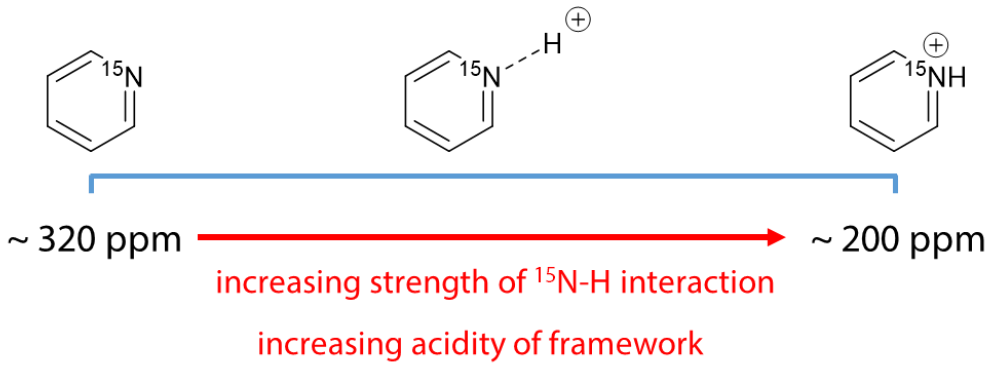

Figure 5.1.4: The ^{15}N MAS NMR chemical shift of the ^{15}N-pyridine resonance provides a measure of strength of the acid-base interaction at basic nitrogen.

Illustratively, Maciel *et al.* used ^{15}N MAS NMR to differentiate a variety of acid sites in a silica-alumina by the adsorption of ^{15}N-pyridine.[63] At low coverage, a ^{15}N resonance at ~280 ppm identified the formation of a Lewis acid-base complex of ^{15}N-pyridine, but as the pyridine loading was increased, the resonance was shifted to ~ 293 ppm due to an increase in surface-probe, hydrogen-bonding interactions. When the silica-alumina was then subject to pre-treatment with HCl, two forms of protonated pyridine were identified *via* ^{15}N resonances at 265 ppm (the average of neat and protonated pyridine) and 198 ppm.

Adsorbed pyridine is more often studied by FTIR spectroscopy;[54, 57-60] usually *via* perturbations to characteristic ring modes (**Figure 5.1.5**)[65] in the 1400 -1700 cm^{-1} range - these being particularly sensitive to intermolecular interactions at nitrogen.[66]

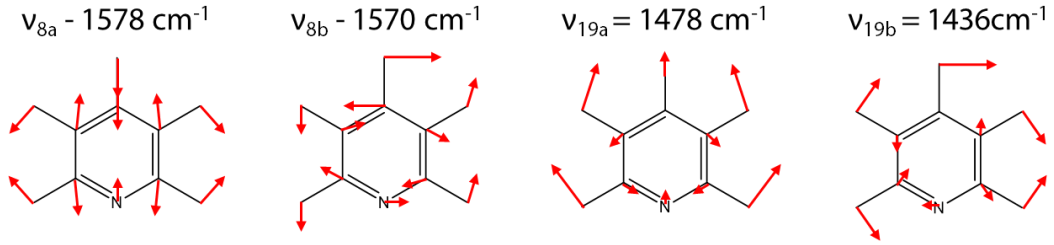

Figure 5.1.5: A representation of the calculated vibrations of the in-plane, normal modes of free pyridine[67] that are typically used for probe-based FTIR studies, and the wavenumber of these modes as observed in the liquid phase.[68]

A particular advantage of studying the pyridine ring-modes is that their high extinction coefficients are suitable for quantitative analysis using the Beer-Lambert law (i.e. the amount of adsorbed probe is related to the intensity of a characteristic FTIR band, **Section 2.2.6.3**).[69] Barzetti *et al.* determined the concentration of Brønsted and Lewis sites in a variety of aluminosilicate materials, using the characteristic ring-modes of protonated (1545 cm^{-1}) and Lewis-complexed (1455 cm^{-1}) pyridine, respectively.[60] The authors identified a positive correlation between the amount of protonated pyridine adsorbed on the aluminosilicate and its activity in the dehydration of 2-(2-hydroxyethyl)pyridine to 2-vinylpyridine (**Figure 5.1.6**). Since no relationship was identified between the Lewis acidity of the catalysts and their dehydration activity, the Brønsted acid sites were identified as the catalytically-active sites.

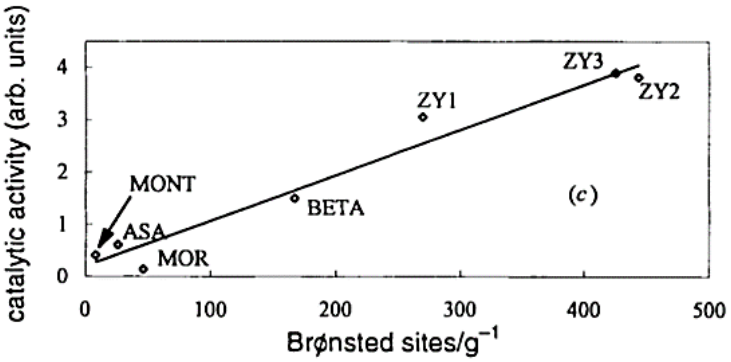

Figure 5.1.6: The correlation between the concentration of Brønsted sites in aluminosilicate materials (by FTIR study of pyridine adsorption) and their catalytic activity in the dehydration of 2-(2-hydroxyethyl)pyridine to 2-vinylpyridine.[60] Key: MONT = montmorillonite, ZY = zeolite-Y, BETA = beta-zeolite, MOR = mordenite, ASA = amorphous silica-alumina. Figure reproduced with the permission from the Royal Society of Chemistry.

However, the use of pyridine for quantitative, acid-site analysis of microporous samples is treated with caution,[44, 69] since the steric constraints of small-pore networks can restrict surface-probe interactions. For this reason, the total acidity of a porous framework may be quantified using a small, strong base (e.g. ammonia)[3, 60, 69-71] that is largely indiscriminate of the strength and location of the acid sites.[44] Nevertheless, larger probe molecules can provide a useful insight into the relative accessibility of acid sites in porous materials.

The size-exclusion of bulky probe molecules has been widely exploited to characterise the acidity of hierarchical zeotypes.[3, 48, 49, 70, 72, 73] Using probe-based FTIR, Thibault-Starzyk *et al.* defined an accessibility index (ACI) to quantify the accessibility of Brønsted acid sites in HP zeolites, and hence evaluate the efficacy of their synthesis.[48] As reported, the ACI is defined as the number of acid sites detected by the adsorption of a (bulky) probe molecule, as a fraction of the total quantity of Brønsted acid sites in the sample. In their derivation of the ACI, Thibault-Starzyk *et al.* investigated the adsorption of pyridine and alkyl-substituted derivatives, on hierarchical ZSM-5 zeolites prepared by alkaline desilication. It was reasoned that pyridine (kinetic diameter = 5.7 Å) would interact with most of the acid sites in ZSM-5 (pore diameter = 5.1 - 5.6 Å)[74] and thus the amount of probe adsorbed was correlated with the total acidity (i.e. the ACI of pyridine ≈ 1). In contrast, bulkier 2,6-lutidine and 2,4,6-collidine probes (kinetic diameter = 6.7 Å and 7.4 Å, respectively) could only interact with a fraction of the Brønsted sites that were accessible to pyridine. It was observed that as the mesopore surface area was increased from 58 to 277 m^2 g^{-1} by desilication, the ACI of pyridine increased only slightly.[48] However, the ACI of the alkyl-substituted probes was increased substantially on introducing mesoporosity: from 0.47 to 1 for lutidine, and 0.06 to 0.38 for collidine (**Figure 5.1.7**).

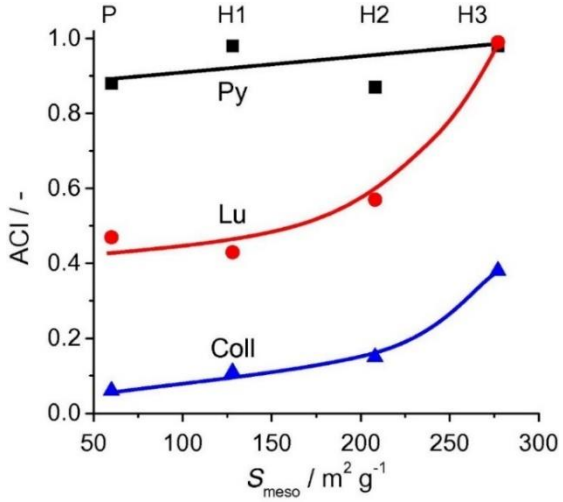

Figure 5.1.7: The relationship between the accessibility index (ACI) of pyridine, 2,6-lutidine, and 2,4,6-collidine and the mesopore surface area of microporous (P) and hierarchical (H1, H2, H3) ZSM-5 zeolites.[48] Figure reproduced with permission from Elsevier.

Later, Xue *et al.* evaluated the ACI of a series of organosilane-templated, hierarchical ZSM-5 samples by quantifying the adsorption of pyridine and 2,6-lutidine using FTIR spectroscopy.[73] A positive relationship was identified between the ACI of lutidine and the external surface area of the zeolite (by N_2 adsorption) and this, in turn, correlated with improved catalytic activity and longevity in the benzylation of benzene using benzyl alcohol.

For better discrimination of acid sites located within large pores or on external surfaces, the adsorption of 2,6-di-*tert*-butyl-pyridine (2,6-dTBP, kinetic diameter = 10.5 Å)[3] may be quantified by FTIR.[75] The 2,6-dTBP molecule is reported to interact selectivity with Brønsted sites, but the steric hindrance at nitrogen is so substantial that protonation only occurs at very strong acid sites, *via* a long-distance proton jump.[76] Recently, Góra-Marek *et al*. used 2,6-dTBP to probe the accessibility of the Brønsted sites in a variety of HP zeolites.[49] By determining the extinction coefficient of the characteristic band of protonated 2,6-dTPB (i.e. 2,6-dTBPH$^+$) at 1615 cm^{-1}, its adsorption was quantified. The authors identified a strong correlation between the ACI of 2,6-dTBP and the mesopore surface area of the zeolite (**Figure 5.1.8**).

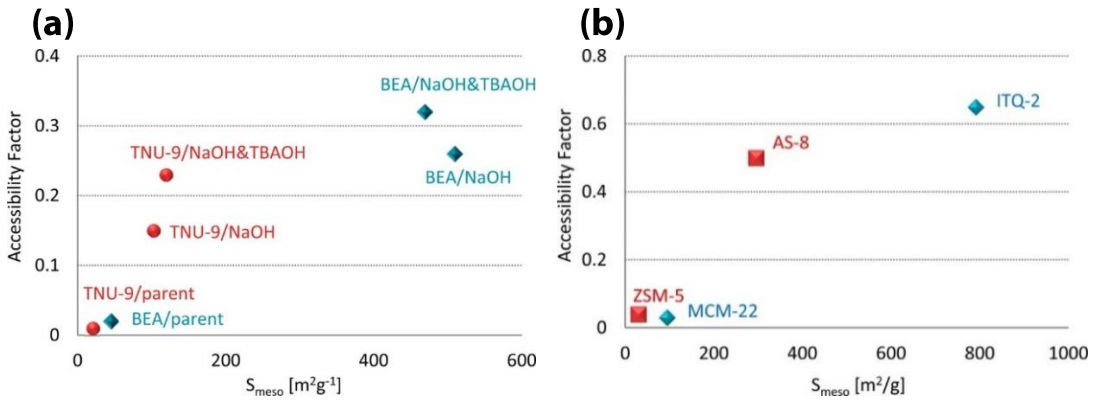

Figure 5.1.8: The relationship between the accessibility factor (ACI) for 2,6-dTBP and the mesopore surface area of monoporous zeolites (BEA, TNU-9, ZSM-5, MCM-22) and their hierarchical analogues.[49] Key: **(a)** TNU-9 and BEA zeolites desilicated with NaOH, or NaOH and TBAOH; **(b)** AS-8 = delaminated ZSM-5, ITQ-2 = delaminated MCM-22. Figures reproduced with the permission from the American Chemical Society.

2,6-dTBP has also been used as a probe of acid-site accessibility in hierarchically-porous silicoaluminophosphate (HP SAPO). Miletto *et al*. reported a synthetic methodology to produce HP SAPO-34 using cetyltrimethylammonium bromide (CTAB) surfactant, encapsulated within MCM-41 as the mesoporogen.[3] To assess both the porosity and acidity of the HP SAPO-34 material, the authors used FTIR to study the adsorption of pyridine, 2,4,6-collidine, and 2,6-di-*tert*-butyl-pyridine. Due to the small pore apertures of the SAPO-34 framework (pore diameter = 3.8 Å), the pyridine probes were not anticipated to interact with

acid sites inside the micropores. As such, the adsorption of pyridine and alkylpyridines could be attributed to interaction with acid sites located on the surface, or within the mesopores (of diameter 33 and 51 Å) in HP SAPO-34. Using NH_3 to quantify the total acidity of the HP SAPO-34, an accessibility factor was determined for each pyridine probe molecule. Although the trend in ACI was correlated with the kinetic diameter of the probe, the ACI of 2,4,6-collidine and 2,6-di-*tert*-butyl-pyridine was essentially the same, which suggested these were only adsorbed on the external surfaces (**Table 5.1.2**). When the HP SAPO-34 was subsequently tested in the vapour-phase Beckmann rearrangement of cyclohexanone oxime, its acid characteristics and hierarchical structure conferred high activity and a resistance to coking.[3]

Table 5.1.2: The accessibility factor of basic probes of varying kinetic diameter, when adsorbed in HP SAPO-34. The accessibility factor has been calculated as the amount of adsorbed probe, given as fraction of the total acidity quantified by ammonia adsorption.[3]

Probe molecule	Kinetic diameter / nm	Accessibility Factor
ammonia	0.33	1
pyridine	0.54	0.107
2,4,6-collidine	0.74	0.038
2,6 di-*tert*-butyl-pyridine	1.05	0.037

5.1.3 SAPO-37

With a void volume of 51 %, faujasite (FAU) possesses the most open structure of the naturally-occurring zeolites.[77] In FAU, the [AlO_4] and [SiO_4] primary building units are assembled as sodalite (β-)cages, connected *via* double 6-rings to define a larger super- (α-)cage. The supercage encloses a void-space of ~ 13 Å, which is accessible in three dimensions *via* four, 7.4 Å aperture, twelve-ring windows (**Figure 5.1.9**).[78]

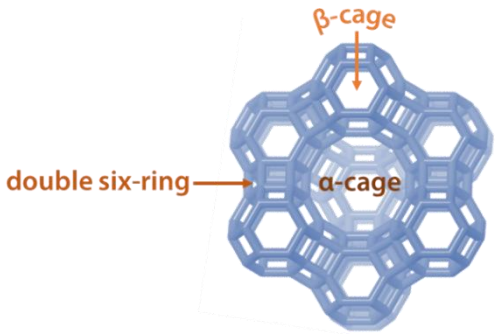

Figure 5.1.9: A section of a faujasitic framework, highlighting the smaller sodalite (β-)cage, which connect *via* double six-rings to form a larger super-(α-)cage.

SAPO-37 is a microporous silicoaluminophosphate with a faujasitic structure.[79] In general, Si can be incorporated into a SAPO framework by either the Type II or Type III isomorphous substitution mechanisms, leading to the formation of isolated Brønsted sites or silicon islands, respectively.[80] In the case that a SAPO undergoes purely Type II substitution of P, the framework composition is $(Si_xAl_{0.5}P_{(0.5-x)})O_2$. However, if any Type III substitution occurs, then Si-O-Si bonding reduces the proportion of Al in the framework and the composition is $(Si_xAl_{(0.5-(x/2))}P_{(0.5-(x/2))})O_2$.[81] The tendency of an AlPO to undergo Type II or III substitution with Si is a characteristic of the framework type. For example, even at relatively low dopant levels, frameworks such as SAPO-5 (AFI) and SAPO-11 (AEL) incorporate a substantial proportion of their silicon through Type III substitution.[82, 83] In contrast, SAPO-37 materials can be prepared with an Al fraction close to 0.5, due to a preference for incorporating Si *via* the Type II mechanism (**Figure 5.1.10**).[84-86] Therefore, at low Si loading ($x \leqslant 0.2$),[87] SAPO-37 contains a relatively homogeneous distribution of isolated Brønsted acid sites, and these are less acidic than the aluminosilicate regions that may otherwise be developed by Type III substitution .[88]

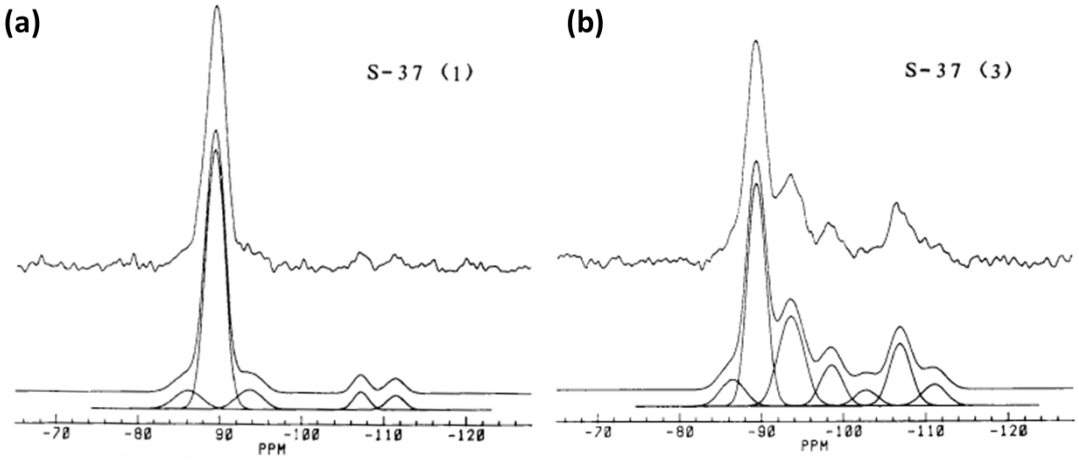

(c)

SAPO-37	Experimental Composition			Contribution of Domains	
	% Si	% Al	% P	SAPO	Aluminosilicate
(a) S-37(1)	15	50	35	95	5
(b) S-37(2)	23	47	30	79	21

Figure 5.1.10: The deconvoluted ^{29}Si MAS NMR spectra of SAPO-37 samples.[81] **(a)** At lower Si loading, the dominant signal at ~ 90 ppm is attributed to Si(4Al) sites from Type II substitution of Si (i.e. SAPO domains). **(b)** At higher loading of Si, increased signal intensity at -94 ppm [Si(1Si,3Al)], -98 ppm [Si(2Si,2Al)], -102 ppm [Si(3Si,1Al)] and -106 ppm [Si(4Si)] reveals a significant concentration of aluminosilicate domains from Type III substitution of Si. **(c)** A summary of the composition and acidic domains in of the SAPO-37 materials reported in **(a)** and **(b)**. Figure adapted with permission from Elsevier.

For certain applications, the moderate acidity of SAPO-37 has proven advantageous. Recently, Potter *et al.*, reported a SAPO-37 catalyst that achieved near-quantitative yield of ε-caprolactam within 6 hours in the liquid-phase Beckmann rearrangement (BR) of cyclohexanone oxime.[89] Using a range of characterisation tools (including NH_3-TPD, MAS NMR, and FTIR), the authors studied the effect of Si-loading on the acid characteristics SAPO-37. Significantly, selectivity towards caprolactam was found to correlate with lower Si loadings (i.e. fewer silicon islands) and weaker framework acidity. The same authors later investigated the activity of SAPO-37 by studying the mobility of cyclohexanone oxime in FAU frameworks using quasi-elastic neutron spectroscopy (QENS).[90] At 373 K, it was found that, the oxime travelled within SAPO-37 by jump diffusion, with a jump distance of 4.5 Å (the separation between the faujasitic supercages). This diffusion behaviour contrasted with the smooth, Fickian diffusion of cyclohexanone oxime sorbed inside the Zeolite-Y (FAU) framework (**Figure 5.1.11**). The jump diffusion behaviour was attributed to interaction between the oxime and the internal acid sites of SAPO-37, which were identified by inelastic neutron scattering experiments. The authors concluded that favourable interactions between cyclohexanone oxime and the Brønsted sites in SAPO-37 (identified by neutron spectroscopies) were responsible for the high yield of caprolactam in the liquid-phase BR.[90]

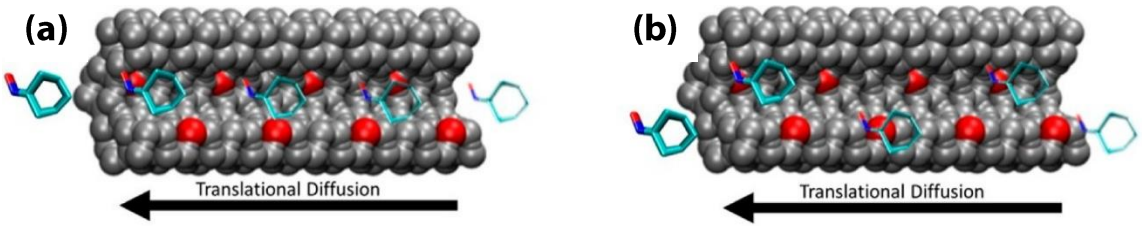

Figure 5.1.11: A depiction of **(a)** the Fickian diffusion of cyclohexanone oxime in Zeolite-Y, and **(b)** the jump diffusion of cyclohexanone oxime in SAPO-37.

5.1.3.1 Hierarchically-porous SAPO-37

Conceivably, the acid characteristics of SAPO-37[89-91] might be supplemented by an auxiliary mesopore network, since dual-porosity in SAPOs has been demonstrated to retain physicochemical attributes of the crystalline microporous phase, whilst improving both activity and lifetime in the liquid and vapour-phase BR.[3, 4, 70] For the liquid-phase BR in particular, improved diffusion to the internal active sites of SAPO-37 could increase catalyst turnover and hence reduce the overall reaction time.

Hierarchical, faujasitic zeolites are widely reported in the literature, having been synthesised by post-synthetic treatment (using steam, or acid/base-leaching) and by a bottom-up, dual-templating approach (using surfactant soft-template).[92] Yet, only one research group has reported the synthesis of a hierarchical SAPO-37 material.[93-97] In the preparation of MESO-SAPO-37, Yadav *et al.* prepared a SAPO-37 precursor gel that was crystallised for 6 hours at 200 °C, before it was added to a solution of the CTAB mesoporogen. Although the authors identified mesoporosity by N_2 gas adsorption and low-angle XRD, the high-angle XRD pattern of the MESO-SAPO-37 was markedly different from that of microporous SAPO-37 (**Figure 5.1.12**),[78] which suggests that the microporous framework was not crystallised.

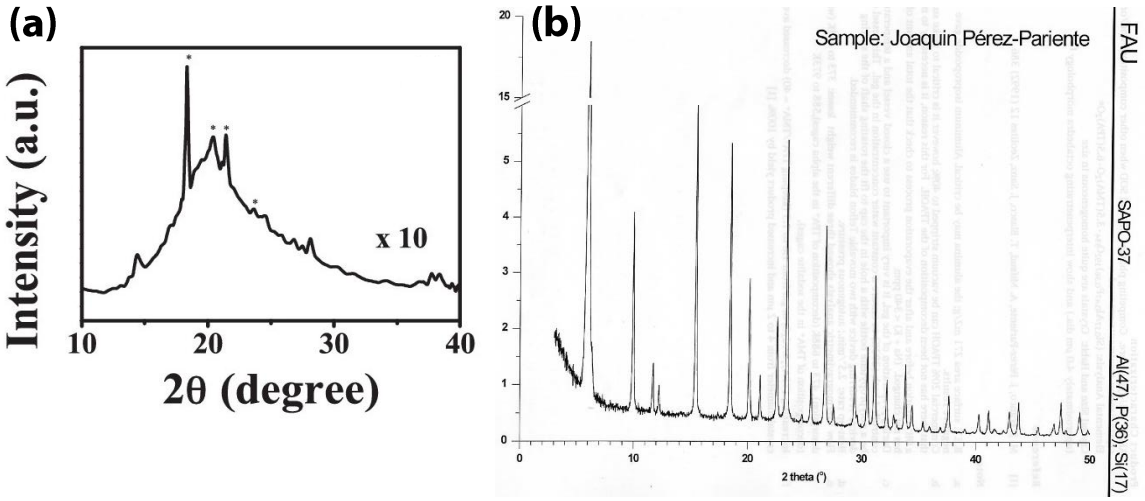

Figure 5.1.12: (a) The powder XRD pattern of the MESO-SAPO-37 catalyst reported by Yadav *et al.*.[95] Figure modified with permission of Elsevier. **(b)** The powder XRD pattern of microporous SAPO-37[98] extracted from the IZA Database of Zeolite Structures.[78]

5.2 Aims

Recently, Potter *et al.* demonstrated the high performance of MP SAPO-37 in the acid-catalysed Beckmann rearrangement (BR) of cyclohexanone oxime.[89-91] Despite achieving near-quantitative yield of ε-caprolactam under liquid-phase conditions, the MP SAPO-37 catalyst did not achieve maximum conversion until ~ 6 hours.[89] If slow, internal mass transport played a limiting role in catalyst turnover, an auxiliary mesoporous network may improve the activity of SAPO-37 in the BR, by enhancing diffusion to/from the internal active sites.[15, 70, 99, 100] Whilst a CTAB-templated, mesoporous SAPO-37 has been reported in the literature,[93-97] inspection of the XRD data raises doubts as to its purity and crystallinity.[95] In this case, the aim was to introduce mesoporosity into SAPO-37, whilst maintaining the catalytic properties that favour high caprolactam yield in the BR. For this undertaking, a well-established,[4, 101, 102] soft-templating route was applied to the synthesis of HP SAPO-37 for the first time. The chosen organosilane mesoporogen has previously been used in the synthesis of HP SAPOs, with excellent retention of the crystalline structure of the parent framework.[4, 103]

To assess the efficacy of the soft-templating strategy, the physicochemical characteristics of the HP SAPO-37 were contrasted with the MP analogue. The long-range structure of the catalyst was assessed by XRD, whilst the atomic-level structure of the framework was probed by (^{1}H, ^{27}Al, ^{31}P, ^{29}Si) MAS NMR. The porosity of HP SAPO-37 was of particular importance, since micro- and meso-pores should be interconnected and open to the external surface in order to benefit from the HP structure. As well as identifying the mesoporosity by low-angle XRD and TEM, N_2 adsorption was used to obtain a quantitative estimate of surface area, pore volume, and mesopore size. In addition, the unique capabilities of PALS were used to assess the size, quantity, and connectivity of the pores in HP and MP SAPO-37. In the BR, framework acidity is also crucial to catalytic performance; hence, the acid sites of HP SAPO-37 were characterised in detail. In particular, acid-site characterisation aimed to assess whether the acidity of SAPO-37 was modified by the use of organosilane mesoporogen, as this template has previously been found to generate weakly acidic silanol sites within the mesopores.[4, 102] In this undertaking, a variety of probe-based techniques were used to evaluate the strength, quantity, and accessibility of the acid sites. The interactions of pyridine were contrasted between HP and MP SAPO-37 using MAS NMR and FTIR spectroscopies. Furthermore, the adsorption of 2-6-di-*tert*-butylpyridine was quantified by FTIR in order to determine an accessibility factor for the Brønsted sites in HP SAPO-37.

Finally, HP SAPO-37 was investigated as a catalyst for the BR of cyclohexanone oxime. It was anticipated that the structural and chemical characterisation of MP and HP SAPO-37 would

provide a means to identify structure-activity relationships to vindicate the soft-templating strategy, or provide further insight into the catalytic performance of SAPO-37 in the BR.

5.3 Experimental

5.3.1 HP SAPO-37 synthesis

The synthesis of HP SAPO-37 and MP SAPO-37 followed the same procedure, except that the latter did not include the addition of dimethyloctadecyl[(3-(trimethoxysilyl)propyl] ammonium chloride.

Solution A: Phosphoric acid (9.25 g, 85 wt. % in water, Sigma Aldrich) and deionised water (20 mL) were stirred together in a Teflon beaker, to which *pseudo*-boehmite (5.58 g, Condea Vista) was added over the course of 1 hour. Solution A was stirred for 7 hours.

Solution B: Tetra-*n*-propylammonium hydroxide (TPAOH, 38.69 g, 40 wt. % in water, Alfa Aesar), tetramethylammonium hydroxide pentahydrate (TMAOH, 0.37 g, Sigma Aldrich) and fumed silica (1.00 g, Sigma Aldrich) were stirred for 2 hours in a glass beaker.

Solution B was added dropwise to Solution A and stirred for 68 hours. Dimethyloctadecyl[3-(trimethoxysilyl)propyl]ammonium chloride solution (DMOD, 3.43 mL, 42 wt. % in methanol) was added dropwise to the gel, which was stirred for 2 hours.

The gel was transferred to a Teflon-lined, stainless steel reactor and crystallised at 200 °C for 24 hours. The reactor was allowed to cool to ambient temperature before its contents were removed and distributed between 4 x 100 mL centrifuge tubes. The solid in each tube was washed 3 times with deionized water at 10,000 rpm, and then dried overnight in an oven at 80 °C. The solid (~ 32 g) was calcined in batches (~ 2 g) by heating to 550 °C (ramp rate of 2 °C min^{-1}) for 16 hours.

Table 5.3.1: The synthesis gel ratio and empirical elemental composition of the calcined MP SAPO-37 and HP SAPO-37 catalysts.

Catalyst	Gel Composition	ICP-OES elemental analysis
MP SAPO-37	1 Al: 1.36 P: 0.21 Si : 0.95 TPAOH: 0.03 TMAOH : 30 H_2O	16.5 wt. % Al; 13.8 wt. % P; 4.0 wt. % Si
HP SAPO-37	1 Al: 1.36 P: 0.21 Si : 0.95 TPAOH: 0.03 TMAOH : 0.03 DMOD : 30 H_2O	21.5 wt. % Al; 10.7 wt. % P; 5.1 wt. % Si

5.3.2 Characterisation

Powder X-ray diffraction patterns were acquired using a Bruker D2 diffractometer with Cu $K_{\alpha 1}$ radiation. Unit cell refinements were performed using the CelRef software.[104] Low-angle X-ray diffraction patterns were obtained using a Rigaku SmartLab diffractometer with Cu rotating anode source.

Nitrogen adsorption measurements were performed at 77K using the Micromeritics Gemini 2375 Surface Area Analyser. Samples were degassed, under vacuum, at 120 °C for 12 hours prior to measurement.

For ICP-OES elemental analysis, samples were subject to HNO_3/H_2O_2 digestion before analysis in the Varian Vista MPX CCD Simultaneous Axial ICP-OES.

NH_3-TPD measurements were performed using the Quantachrome Autosorb iQ-Chemi apparatus. Catalysts were pre-treated at 150 °C under a flow of helium gas for 2 hours. The samples were then dosed with ammonia gas for three hours at 100 °C, before desorption under a flow of helium gas, with a temperature ramp of 10 °C min^{-1} up to 600 °C.

Carbon, hydrogen, and nitrogen (CHN) elemental analysis was performed using the Thermo Carlo Erba Flash 2000 Elemental Analyser.

Thermogravimetric analysis was performed on the Netzsch TG 209 F1 Libra by heating under air from 30 - 900 °C at a ramp rate of 10 °C min^{-1}.

TEM images were acquired using the Hitachi HT7700 Transmission Electron Microscope with Morada G3 camera.

5.3.2.1 Positron annihilation lifetime spectroscopy (PALS)

The catalyst powders were packed to 2 mm either side of a Mylar sealed $^{22}NaCl$ positron source. The samples were measured at room temperature, under high vacuum (5×10^{-6} Torr) and placed between two EG&G Ortec spectrometers for a minimum of 4.5×10^6 integrated counts. The final spectra were analysed using LT (Version 9.0) software[105] using a source correction (1.486 ns and 3.593 %). The spectra were best fitted to 5 components; the first component being fixed to 125 ps due to *para*-positronium decay, and the second at ~400 ps due to free annihilation within the sample. The remaining three lifetimes were attributed to *ortho*-positronium decay, and associated with a tri-modal pore structure within the materials.

The zeolites featured intrinsic micro-porosity (τ_3) due to the porous zeolite cages and channels, the inter-particle micropores (τ_4) and larger mesopores (τ_5).[106] The lifetimes were converted to average pore diameters using the Tao-Eldrup equation for τ_3 and the Rectangular Tao-Eldrup equation for τ_4 and τ_5.[27-29] The pore-size distribution was calculated using PAScual (Version 1.4) software.[107]

5.3.2.2 MAS NMR characterisation of the framework

The calcined catalyst was packed in a 4 mm rotor before drying overnight in a fan-assisted oven at 100 °C. Whilst still hot, the rotors were sealed by capping with a turbine. All NMR experiments were performed at a sample rotation frequency of 11 kHz, on a 9.4 WB Ascend Bruker magnet with a Neo console, using a triple resonance 4 mm RevolutionNMR probe. The ^{1}H NMR spectra were referenced to adamantane at 1.8 ppm.[108] The ^{29}Si NMR spectra were referenced to tetrakis(thrimethylsiloxy)silane at -9.8 and -135.4 ppm.[108] The ^{31}P spectra were referenced to phosphoric acid (85 % in H_2O) at 0 ppm. The ^{27}Al spectra were referenced to $AlCl_3$ (1 M in H_2O) at 0 ppm. The ^{29}Si cross-polarisation experiments were obtained with ramped cross polarisation[109] are the result of 24576 scans, with a contact time of 3 ms and spinal decoupling at 80 kHz during acquisition. The ^{31}P NMR experiments were recorded with direct excitation using 2 scans and 180 seconds between scans. Proton decoupling using SPINAL64 was applied during acquisition. The ^{27}Al experiments were recorded with one pulse excitation and no decoupling with 64 scans.

5.3.2.3 Probe-based MAS NMR with ^{15}N-pyridine

Calcined catalyst was transferred to a ceramic boat and sealed inside a Schlenk tube. The Schlenk tube was transferred to a furnace to dry under vacuum at 120 °C for 12 hours. After isolation from the vacuum, the Schlenk tube was cooled to room temperature and transferred to a glove back under N_2 atmosphere. 7 µL of ^{15}N-labelled pyridine (Sigma Aldrich) was added to the catalyst (0.07 g) with mechanical mixing. The catalyst-pyridine sample was packed into a 3.2 mm thin wall pencil rotor and closed with a turbine. The experiments were performed on a narrow bore 14.1 T Agilent DDR2 spectrometer equipped with a 3.2mm triple resonance Agilent probe, at a spinning speed of 13 kHz. ^{1}H NMR spectra were referenced to adamantane at 1.8 ppm.[108] ^{15}N spectra were referenced to NH_4Cl at 39.3 ppm. The direct excitation was recorded with 300 scans, and a pulse delay of 300 s between scans.

5.3.2.4 Probe-based FTIR studies

FTIR spectra of self-supporting pellets were collected under vacuum conditions (residual pressure $<10^{-5}$ mbar) using a Bruker Equinox 55 spectrometer equipped with a pyroelectric detector (DTGS type) with a resolution of 4 cm^{-1}. NH_3, pyridine, and 2,6-di-*tert*-butylpyridine were each adsorbed at room temperature using specially designed cells, permanently connected to a vacuum line for *in situ* adsorption–desorption measurements. FTIR spectra were normalized with respect the pellet weight and, whenever specified, are reported in difference-mode by subtracting the spectrum of the sample in vacuum, from the spectrum with adsorbed molecules. The total number of accessible Brønsted acid sites (N) was estimated using the Lambert–Beer law in the form $A = \varepsilon N \rho$, where A is the integrated area of the bands of the protonated species, ε is the molar extinction coefficient ($cm^2\ mmol^{-1}$), N is the concentration of the vibrating species (mmol g^{-1}), and ρ is the density of the disk (mass/area ratio of the pellet, mg cm^{-2}). The accessibility factor (AF) is defined as the number of Brønsted sites detected by, 2,6-di-*tert*-butylpyridine adsorption, divided by the total number of Brønsted acid sites detected by ammonia adsorption.

5.3.3 Catalysis

5.3.3.1 The liquid-phase Beckmann rearrangement

A portion of calcined catalyst was degassed by heating overnight at 120 °C, under vacuum. A 3-neck round bottom flask was charged with a stirrer bar, cyclohexanone oxime (0.1 g, Sigma Aldrich), anhydrous chlorobenzene (internal standard, 0.1 g, Sigma Aldrich), dried catalyst (0.1 g), and anhydrous benzonitrile (20 mL, Sigma Aldrich). The reaction vessel was sealed with a rubber septum, glass stopper, and reflux condenser. The reaction was transferred to a pre-heated oil bath at 130 °C and stirred under a constant nitrogen atmosphere. Aliquots of the reaction mixture were extracted hourly over a 6 hour reaction period, and analysed by gas chromatography using the Clarus 480 apparatus with flame ionisation detector and an Elite 5 column. Products were identified using authenticated standards, and quantified against the internal standard, chlorobenzene.

5.3.3.2 The vapour-phase Beckmann rearrangement

Pelletised catalyst (0.2 g) was sandwiched between glass beads (1 mm diameter) within a cylindrical, quartz, fixed-bed reactor tube (4 mm diameter). The tube was transferred to within the heater unit of a flow-reactor setup, and the catalyst pre-treated by heating at 400 °C for 1 hour under a flow of He gas (50 mL min^{-1}). For catalysis, the temperature and He flow were reduced to 300 °C and 33.3 mL min^{-1}, respectively. A liquid-feed of 100 g L^{-1} of cyclohexanone oxime in ethanol was supplied to the reactor *via* electronic syringe pump, to maintain a weight hourly space velocity (WHSV) of 0.79 hr^{-1}. Simultaneously, an external standard feed of 100 g L^{-1} of mesitylene in ethanol was introduced into the exit feed at a WHSV of 0.79 h^{-1}. Once steady-state was established, samples were collected on an hourly basis, and analysed using the Clarus 480 gas chromatograph with FID detector and Elite-5 column.

5.4 Results and discussion

5.4.1 Characterisation of the SAPO-37 catalysts

Hierarchically-porous (HP) SAPO-37 was prepared by soft-templating, using organosilane as the mesoporogen.[101, 102] In an aqueous synthesis gel, the amphiphilic organosilane molecules (dimethyloctadecyl[(3-(trimethoxysilyl)propyl]ammonium chloride, 'DMOD') spontaneously coalesce to form supramolecular micelles (**Figure 5.4.1**). The trimethoxysilyl components form covalent bonds between each other and the framework precursors, preventing expulsion of the micelles from the crystallising microporous phase. On calcination, the organic component of the surfactant is eliminated and a HP structure is formed, with siliceous species incorporated into the walls of the mesopores.[4] As a result, the organosilane templating strategy has implications for both the pore architecture and acid characteristics of a HP framework.

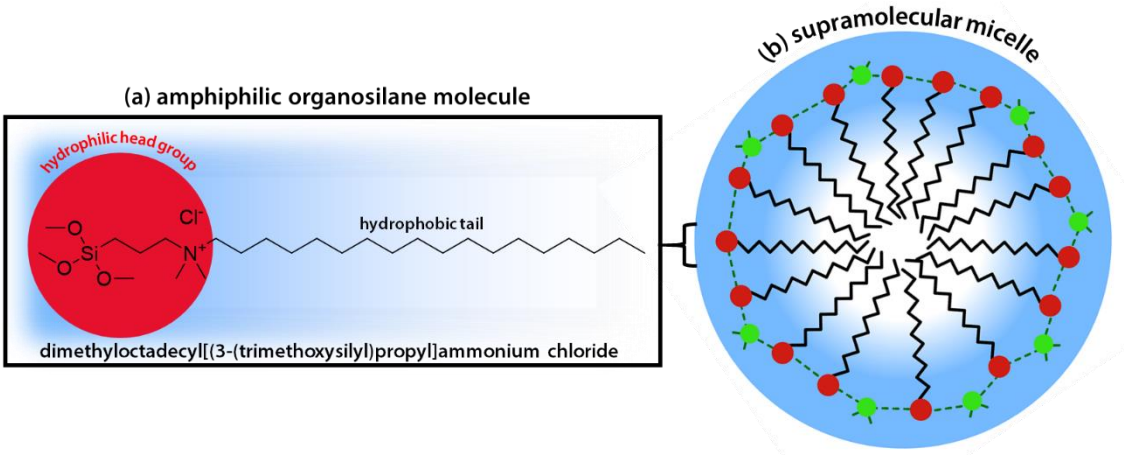

Figure 5.4.1: (a) The structure of the amphiphilic organosilane molecule 'DMOD'. **(b)** In aqueous solution (blue), the organosilane surfactant molecules spontaneously assemble into a supramolecular micelle, with the hydrophilic head groups (red spheres) in contact with the aqueous environment, and the hydrophobic tails forming the core of the micelle. The surfactant molecules can form bonds (dashed line) to each other and the framework precursors (green spheres) *via* the trimethoxysilyl component of the surfactant head group.

Conventionally, the organosilane is added to the SAPO precursor gel mid-synthesis, with the micropore structure-directing agent (SDA).[4, 102] However, the typical methodology was found to interfere with the crystallisation of the microporous (MP) SAPO-37 framework, so the DMOD mesoporogen was added to the SAPO-37 synthesis gel in the final step, prior to crystallisation. To establish whether the surfactant had been incorporated during crystallisation of the HP framework, the as-synthesised MP and HP SAPO-37 catalysts were subject to elemental analysis (for carbon, hydrogen, nitrogen: CHN) and thermogravimetric

analysis (TGA). For comparison, CHN and TGA data was also acquired after the SAPO-37 catalysts had been calcined in air at 550 °C. The CHN analysis (**Table 5.4.1**) indicated that a similar quantity of organic template was incorporated into HP and MP SAPO-37 prior to calcination. However, the slightly lower nitrogen content of HP SAPO-37 may be consistent with the loss of SDA molecules from within the volume occupied by the organosilane micelle (i.e. the number of displaced SDA molecules > the number of organosilane molecules in the micelle).

Table 5.4.1: Carbon, hydrogen and nitrogen elemental analysis of HP and MP SAPO-37 catalysts as-synthesised, and after calcination in air at 550 °C.

Catalyst		Elemental analysis		
		% C	% H	% N
HP SAPO-37	as-synthesised	20.08	3.95	1.86
	calcined	0.17	2.29	0.00
MP SAPO-37	as-synthesised	20.45	4.49	1.98
	calcined	0.08	2.75	0.00

TGA provided better insight into the origin of the organic material within the as-synthesised catalysts (**Figure 5.4.2**), since the three-step weight loss observed for the MP catalyst is characteristic of SAPO-37.[84]

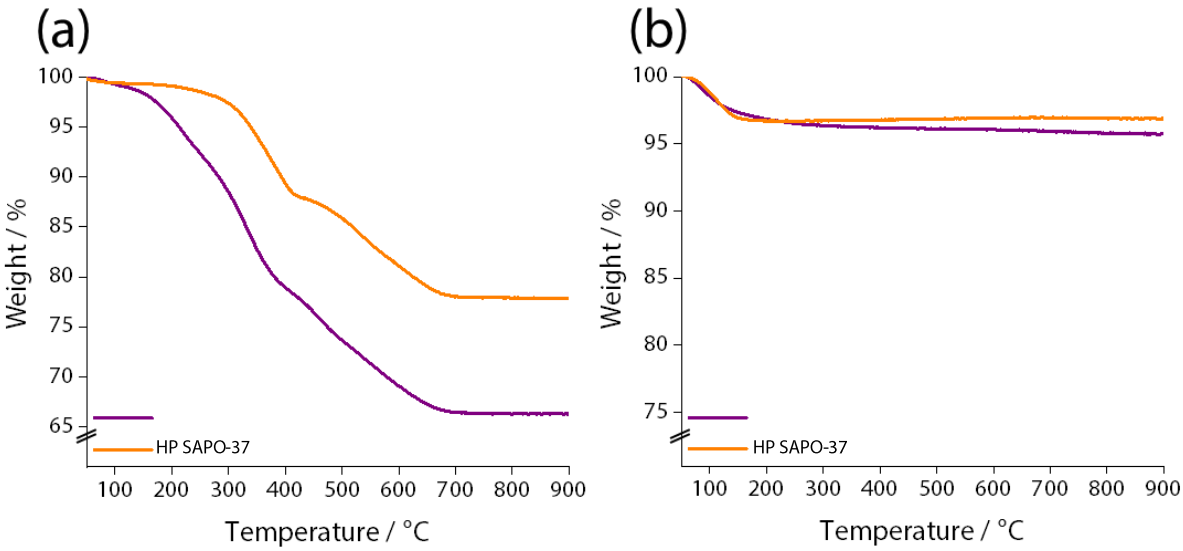

Figure 5.4.2: Thermogravimetric analysis of **(a)** as-synthesised and **(b)** calcined HP SAPO-37 and MP SAPO-37, acquired by heating in air from 30 - 900 °C at a ramp rate of 10 °C min^{-1}. Weight losses at > 200 °C were attributed to the removal of organic templates.

Small initial weight losses due to the desorption of water were followed by the decomposition of the tetrapropylammonium SDA from within the supercage (200 - 400 °C), and finally the removal of tetramethylammonium SDA from within the β-cages (400 - 700 °C).[84] In the as-synthesised HP SAPO-37, considerably more water was desorbed < 200 °C than from MP SAPO-37, which suggested that there were more defect sites (e.g. P-OH, Si-OH, Al-OH) in the HP catalyst.[110-112] Although the loss of SDA was also identified for HP SAPO-37, these occurred at lower temperature than for MP SAPO-37. Significantly, the weight loss at ~ 350 °C identified the elimination of the DMOD surfactant,[4] which confirmed its incorporation into the crystallised HP SAPO-37 material. Thus, the lower temperature at which the SDA was lost from HP SAPO-37 may be due to easier escape of the decomposition products *via* the mesopores. After aerobic calcination, MP and HP SAPO-37 exhibited only a small net weight loss (3.1 % and 4.2 %, respectively) due to the removal of water during TGA. However, the adsorbed water was removed more gradually from HP SAPO-37 than MP SAPO-37, which indicated that some water was more strongly bound to the HP framework.

The efficacy of the dual-templating procedure was assessed by powder X-ray diffraction (XRD) analysis of the calcined product. Importantly, the powder pattern of the soft-templated SAPO correlated with both the conventional MP SAPO-37 material, and also the faujasite structure reported in the literature[78] (**Figure 5.4.3**). Thus, phase-pure HP SAPO-37 was templated successfully, notwithstanding the organosilane surfactant.

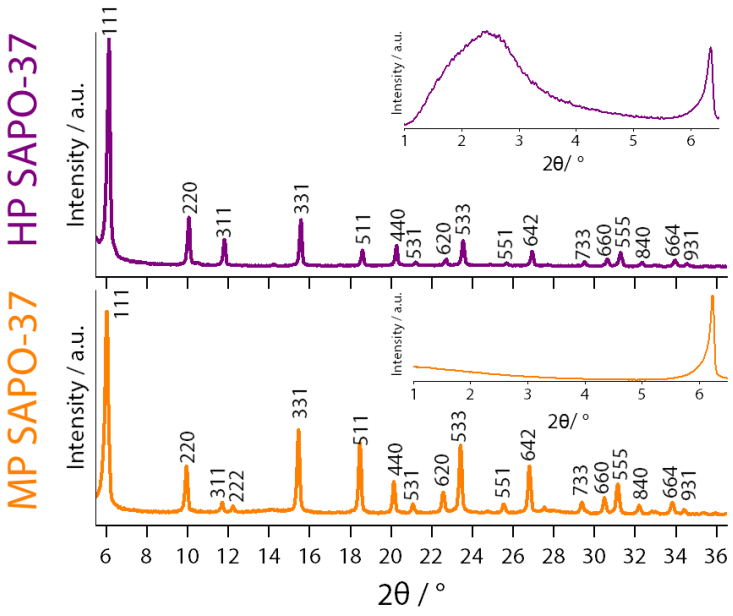

Figure 5.4.3: The indexed powder XRD patterns of HP SAPO-37 and MP SAPO-37 confirmed that the catalysts were phase pure. The slight variation in peak intensities between the two samples, and the loss of the 222 peak in the spectrum of HP SAPO-37 are attributed to a preferred orientation of the HP SAPO-37 crystallites. The low-angle XRD spectra (inset) revealed a peak in HP SAPO-37 that was indicative of mesopores.

Significantly, refinement of the cubic unit cell parameters (**Table 5.4.2** and **Table 5.4.3**) revealed that the lattice dimensions of the soft-templated SAPO-37 exceeded those of the microporous analogue (**Table 5.4.4**), which was indicative of a mesopore-related unit cell expansion. Mesoporosity was also evidenced by a broad peak at $2\theta \sim 2.5$ ° in the low-angle XRD spectrum of HP SAPO-37 (**Figure 5.4.3**, inset); [4, 101, 113] a similar feature was not observed for the MP catalyst.

Table 5.4.2: Unit cell refinements for MP SAPO-37.

λ /Å	*a* / Å	*b* / Å	*c* / Å	α / °	β / °	γ / °	Volume / Å³
1.5406	24.4233	24.4233	24.4233	90	90	90	14568.4
0	0.031	0	0	0	0	0	
h	***k***	***l***	**2θ(Obs) / °**	**2θ-Zero / °**	**2θ(Cal) / °**	**Dif. / °**	
1	1	1	6.217	6.217	6.263	-0.046	
0	2	2	10.188	10.188	10.236	-0.048	
1	1	3	11.97	11.97	12.0088	-0.0388	
3	1	3	15.779	15.779	15.8039	-0.0249	
3	3	3	18.817	18.817	18.8649	-0.0479	
0	4	4	20.56	20.56	20.5549	0.0051	
3	1	5	21.512	21.512	21.5078	0.0042	
6	0	2	23.051	23.051	23.0124	0.0386	
5	3	3	23.821	23.821	23.872	-0.051	
4	4	4	25.158	25.158	25.2434	-0.0854	

Table 5.4.3: Unit cell refinements for HP SAPO-37.

λ /Å	*a* / Å	*b* / Å	*c* / Å	α / °	β / °	γ / °	Volume / Å³
1.5406	24.761	24.761	24.761	90	90	90	15181.2
0	0.0178	0	0	0	0	0	
h	***k***	***l***	**2θ(Obs) / °**	**2θ-Zero / °**	**2θ(Cal) / °**	**Dif. / °**	
1	1	1	6.136	6.136	6.1775	-0.0415	
0	2	2	10.066	10.066	10.096	-0.03	
1	1	3	11.809	11.809	11.8444	-0.0354	
3	1	3	15.556	15.556	15.5869	-0.0309	
3	3	3	18.595	18.595	18.6053	-0.0103	
0	4	4	20.276	20.276	20.2715	0.0045	
5	1	3	21.208	21.208	21.211	-0.003	
2	0	6	22.707	22.707	22.6943	0.0127	
5	3	3	23.537	23.537	23.5417	-0.0047	
4	4	4	24.874	24.874	24.8935	-0.0195	

Table 5.4.4: The optimised unit cell parameters for MP SAPO-37 and HP SAPO-37 catalysts.

Catalyst	Lattice Parameters		Space Group	Unit Cell Volume / Å^3
	$a = b = c$ / Å	α = β = γ / °		
MP SAPO-37	24.46	90	Fd-3m	14628
HP SAPO-37	24.76	90	Fd-3m	15180

To examine the pore structure of the SAPO catalysts in more detail, N_2 gas adsorption-desorption measurements were undertaken (**Figure 5.4.4**). Whilst the Type I isotherm of MP SAPO-37 characterised a microporous framework, the Type IV isotherm of HP SAPO-37 was indicative of significant mesoporosity.[32] In particular, the Type H4 hysteresis produced by the HP SAPO-37 identified narrow mesopores.

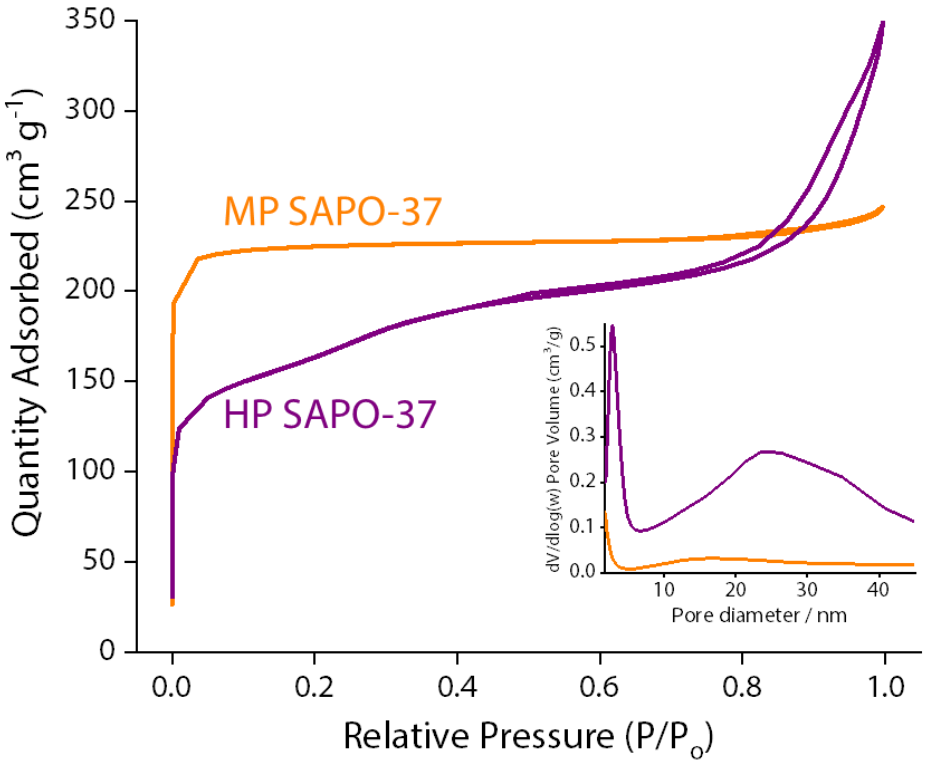

Figure 5.4.4: The N_2 gas adsorption-desorption isotherms of MP SAPO-37 (Type I = micropores) and HP SAPO-37 (Type IV = mesopores), with their respective BJH adsorption pore-size distributions, inset.

BJH analysis of the N_2 gas-adsorption data was used to obtain a pore-size distribution (PSD) for the two catalysts. The PSD of HP SAPO-37 comprised a sharp peak at 2.7 nm, and a broad feature between 10 – 40 nm (**Figure 5.4.4**, inset). The latter of these features was attributed to intercrystalline porosity, caused by the adsorption of probe gas between aggregates of catalyst particles.[99] However, the peak at 2.7 nm (notably absent in the MP SAPO-37) was

consistent with the presence of micelle-templated mesopores in HP SAPO-37, since both the pore dimension (~ 3 nm) and narrow size-distribution are characteristic of the mesopores generated by the DMOD template.[101] Interestingly, the calculated BET surface area of HP SAPO-37 was lower than that of MP SAPO-37 (**Table 5.4.5**), contrary to the trend in the literature.[4, 102] The reduced surface area of HP SAPO-37 was thus attributed to the open, FAU topology,[77] wherein the replacement of micropore surface by mesoporous void space might significantly reduce the total surface area available to adsorb a N_2 monolayer.

Table 5.4.5: The textural properties of MP SAPO-37 and HP SAPO-34 determined by N_2 adsorption-desorption studies.

Catalyst	BET surface area / $m^2\ g^{-1}$	Micropore volume / $cm^3\ g^{-1}$	Mesopore volume / $cm^3\ g^{-1}$	External surface area / $m^2\ g^{-1}$	BJH mesopore diameter / Å
MP SAPO-37	693	0.31	-	76	-
HP SAPO-37	551	0.12	0.29	230	26

In complement to the gas adsorption studies, the porosity of the SAPO-37 catalysts was quantified by positron annihilation lifetime spectroscopy (PALS). The PALS spectra were acquired by measuring the lifetime of *ortho*-positronium (*o*-Ps) species that were annihilated within the powder sample. The *o*-Ps lifetimes were then used to determine the size of the void at the site of annihilation (since *o*-Ps lifetime is reduced if a pickoff electron is nearby), whilst the number of annihilations at each site was related to the relative quantity of that void-type.[21, 27]

o-Ps lifetimes were extracted from the PALS spectra by best fit to 5 components. The first component was fixed at 125 ps due to *para*-positronium decay, and the second at ~ 400 ps due to free annihilation within the sample. The remaining three lifetimes (τ_3, τ_4, τ_5) were attributed to *ortho*-positronium (*o*-Ps) decay, and thus identified a tri-modal structure within the SAPOs. The results of the PALS data analysis is reported in **Table 5.4.6**, and the pore-size distribution (PSD) is presented in **Figure 5.4.5**.

Table 5.4.6: The processed PALS data for MP SAPO-37 and HP SAPO-37. The three lifetime components (τ) associated with *o*-Ps annihilation in the catalyst pores are reported with their corresponding intensities (I). An average pore diameter (d) has been calculated from each lifetime component.

Sample	Lifetime / ns			Intensity / %			Average Pore Diameter / nm		
	τ_3	τ_4	τ_5	I_3	I_4	I_5	d_3 [a]	d_4 [b]	d_5 [b]
MP SAPO-37	0.965 ±0.085	8.468 ±0.405	33.067 ±4.885	18.0 ±4.2	10.7 ±0.5	3.5 ±0.5	0.32 ±0.03	1.34 ±0.03	2.75 ±0.30
HP SAPO-37	0.848 ±0.024	5.891 ±0.232	61.168 ±3.012	18.7 ±1.9	3.1 ±0.1	6.7 ±0.2	0.28 ±0.01	1.13 ±0.02	5.08 ±0.34

[a] Lifetime converted to average pore diameter using the Tao-Eldrup equation.[27, 28]

[b] Lifetime converted to average pore diameter using the rectangular Tao-Eldrup equation.[29]

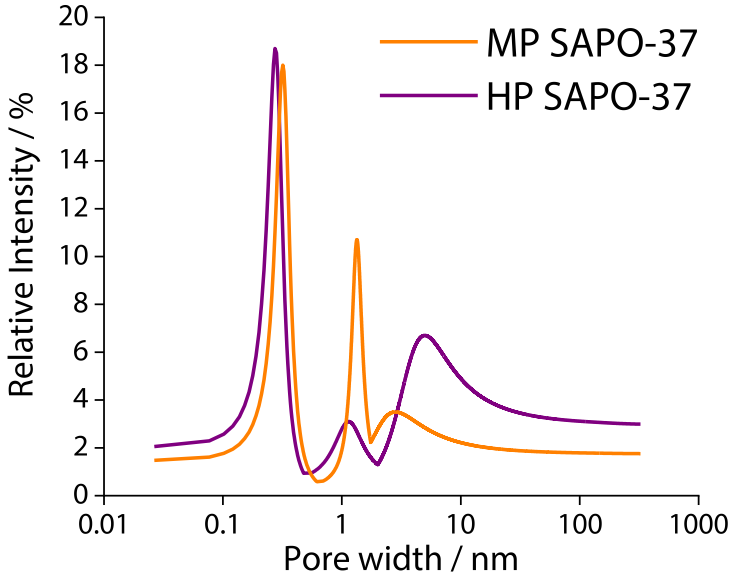

Figure 5.4.5: The pore-size distribution of MP and HP SAPO-37 obtained by PALS.

Unlike gas adsorption, positrons are implanted directly into the sample and do not rely on diffusion to gain entry to pores and cavities. Furthermore, the small dimensions of positronium (Bohr radius = 0.53 Å)[21] allow *o*-Ps to occupy void spaces that are inaccessible to a larger, molecular probe.[21] Consequently, a rationalisation of the PALS data requires a consideration of the smallest pores and cavities in the sample. SAPO-37 is a faujasitic framework, and thus comprises sodalite cages (or β-cages) connected by double-6-rings to form a larger α-cage (**Figure 5.4.6**). Some key dimensions associated with the α- and β-cages are reported in **Table 5.4.7**.

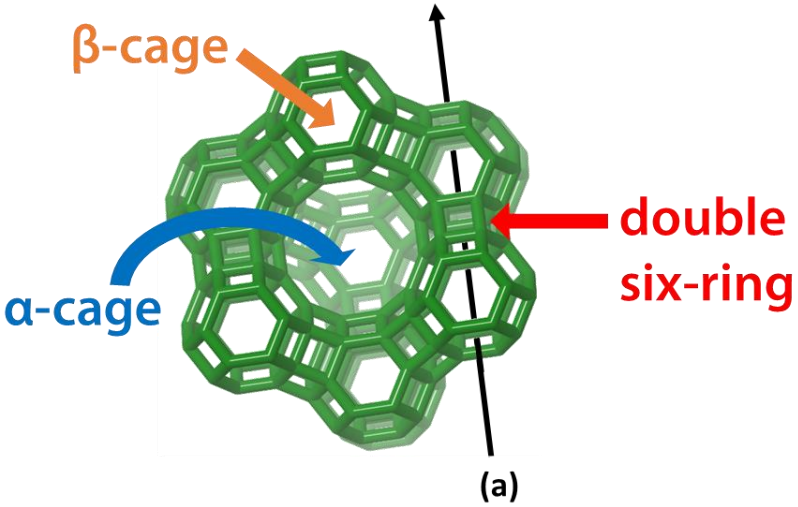

Figure 5.4.6: A section of the faujasite structure, indicating the sodalite (β-)cages that connect *via* double six-ring units to define a super-(α-)cage. The arrow marked **(a)** indicates the path of a diameter of a sphere < 2.53 Å within a channel formed by the double six-rings and the interior of the sodalite cages.

Table 5.4.7: The computed[114] diameter of the largest free-sphere that can diffuse through, and be included within the α- and β-cages of the faujasite framework.[78]

	Structural component of the FAU framework	
	β-cage (sodalite)	**α-cage**
Maximum diameter of a sphere that can be included / Å	6.23	11.24
Maximum diameter of a sphere that can diffuse along/ Å	2.53	7.35

The shortest *o*-Ps lifetime component (τ_3), yielded a void dimension (d_3) of 0.28 nm for HP SAPO-37, and 0.32 nm for MP SAPO-37. Therefore, the τ_3 component is associated with the intrinsic, zeolitic porosity (i.e. the structural microporosity) of the SAPO-37 samples.[106] Specifically, d_3 is attributed to *o*-Ps annihilating within the smaller β-cages and double six-rings (**Figure 5.4.6 a**). Since the average diameter (d) and contribution (% I) of the τ_3 component are comparable for HP SAPO-37 (0.28 nm, 18.7 %) and MP SAPO-37 (0.32 nm, 18.0 %), it is concluded that there is no significant difference in the intrinsic microporosity of the two samples. The relatively large fraction of *o*-Ps annihilating with the τ_3 lifetime reflects the longer diffusion path inside the SAPO-37 micropores.[23]

The τ_4 and τ_5 components were found to differ quite significantly between the HP and MP catalysts. Average pore diameters (d_4) of 1.34 and 1.13 nm were calculated from the τ_4 components of microporous and hierarchical SAPO-37, respectively, and these are in accord

with *o*-Ps annihilating within the FAU supercage. However, the τ_4 component made a significantly larger contribution to the PSD of MP SAPO-37(I_4 = 10.7%) than HP SAPO-37 (I_4 = 3.1 %). The smaller I_4 intensity in HP SAPO-37 was consistent the increased diffusion of *o*-Ps out of the FAU micropores. In PALS, there is an energetic driving force for the movement of *o*-Ps into increasingly larger void spaces, ultimately leading to escape from the surface of the crystallite (out-diffusion), if the is *o*-Ps not first annihilated.[22] Therefore, the relative fraction of *o*-Ps annihilating in the micro- and meso-pores reflects both their pore volume and interconnectivity. The PALS data suggested that the transit of *o*-Ps out of the FAU pores was easier in HP SAPO-37 than MP SAPO-37, and this was consistent with the presence of mesopores in the hierarchical framework.

An *o*-Ps lifetime of $\tau > 30$ ns (as was observed for the τ_5 component) is usually attributed to *o*-Ps annihilating within a mesopore or in vacuum (i.e. outside the framework).[20] For MP SAPO-37, the d_5 pore diameter (2.75 nm, due to *o*-Ps annihilating within intercrystalline pores, in vacuum, or at defect sites)[20] made relatively small contribution (I_5 = 3.5 %) to the PSD of the MP SAPO. However, for HP SAPO-37, the d_5 pore diameter was considerably larger, and more intense (d_5 = 5.1 nm, I_5 = 6.7 %), indicating significantly more mesoporosity than MP SAPO-37. As the d_5 diameter of HP SAPO-37 (5.1 nm) was significantly larger than that determined by N_2 gas adsorption studies (2.7 nm), it is likely that vacuum annihilation contributed to the τ_5 component. Therefore, the PALS analysis revealed that HP SAPO-37 is more mesoporous than MP SAPO-37, and that the additional mesoporosity facilitates the diffusion of *o*-Ps from the micropores to the mesopores, and thence to the external surface. Since most of the *o*-Ps were annihilated within the micropores of MP SAPO-37, the improved mass transport characteristics of HP SAPO-37 can be inferred.

Transmission electron microscopy (TEM) provided visual evidence of the mesoporosity in HP SAPO-37 (**Figure 5.4.7 a & b**) as striations in the HP SAPO-37 crystallites.[4, 115-117] Moreover, the TEM images identify a significant change in crystallite morphology, from the 2-3 µm octahedral particles of MP SAPO-37[87, 118] (**Figure 5.4.7 c & d**), to the aggregated, rod-like structures of HP SAPO-37. The elongated particles of HP SAPO-37 may explain the preferred orientation that was evidenced in the powder XRD pattern of HP SAPO-37 (**Figure 5.4.3**).

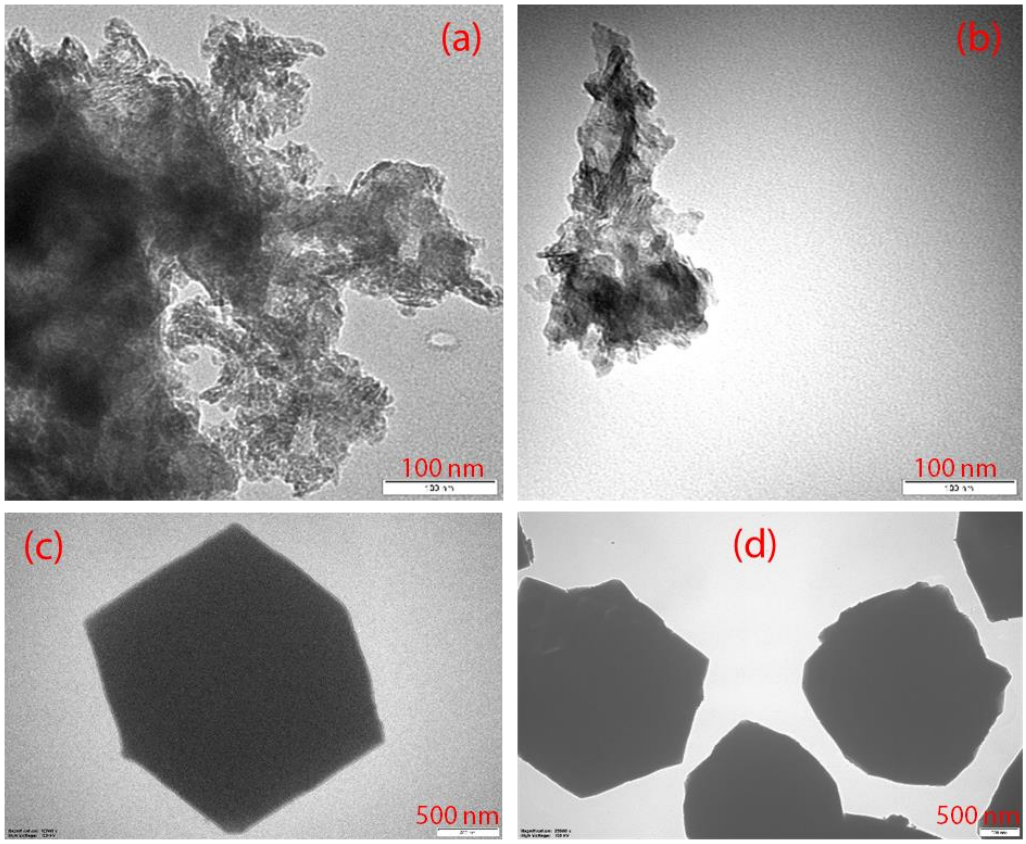

Figure 5.4.7: (a & b) TEM images of HP SAPO-37 showing aggregated, rod-like crystallites that contain striations attributed to mesoporosity.[4, 115-117] Accelerating voltage 100 kV, magnification 200,000x. **(c & d)** The cubic crystallites of MP SAPO-37 (2.5 – 3.0 µm). Accelerating voltage 100 kV, magnification 40,000x.

Magic-angle spinning (MAS) NMR measurements were undertaken in order to probe the local coordination environment of the framework atoms in HP and MP SAPO-37 (**Figure 5.4.8**). Typical resonances of ^{27}Al, ^{29}Si, ^{1}H, and ^{29}Si nuclei in SAPOs are reported in **Table 5.4.8**.

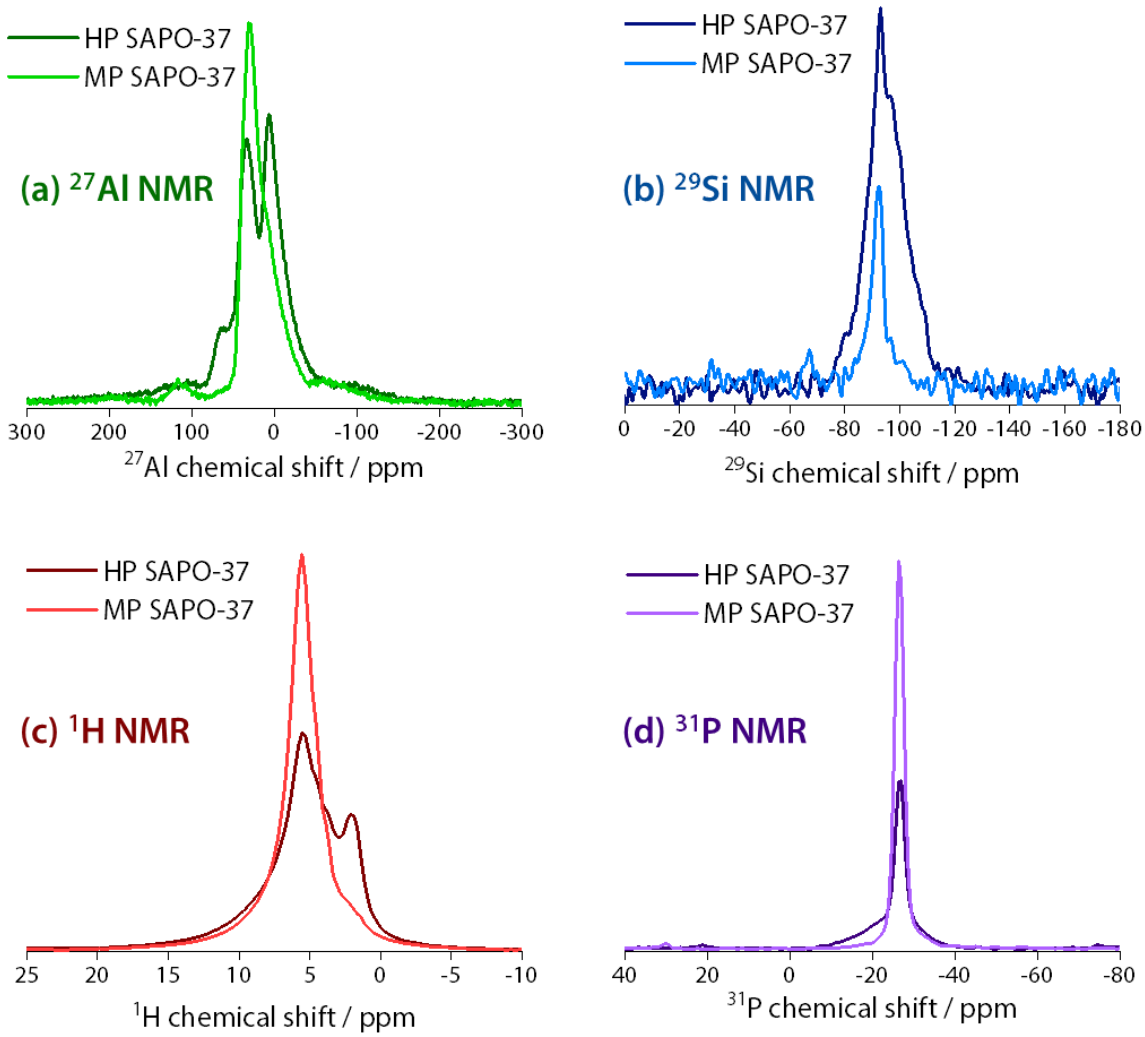

Figure 5.4.8: The **(a)** ^{27}Al, **(b)** ^{29}Si, **(c)** ^{31}P, and **(d)** ^{1}H MAS NMR spectra of HP SAPO-37 and MP SAPO-37 catalysts acquired at 400 MHz and 10 kHz spinning speed. Y axes show signal intensity in arbitrary units.

Table 5.4.8: The typical resonances of SAPO framework atoms in MAS NMR spectroscopy.

Nucleus	δ / ppm	Assignment	Reference
^{27}Al	-10	Six-coordinate Al	80, 81, 83, 119, 120
	6 to 13	Five-coordinate Al	
	31 to 44	Tetrahedral Al(4P), AlPO	
	60	Tetrahedral Al(4Si), zeolitic	
^{29}Si	-85 to - 88	Si(4Al), aluminosilicate region	80-82, 87, 119-121
	-89 to -92	Si(4Al9P), SAPO-type	
	-92 to -94	Si(3AlSi), aluminosilicate region	
	-98	Si(2Al2Si), aluminosilicate region	
	-101 to -106	Si(1Al3Si), aluminosilicate region	
	-106 to -112	Si(4Si), siliceous region	
^{31}P	-26 to -28	P(4Al)	80, 81, 83, 119, 120
	-16 to-14	P-OH defect sites	
^{1}H	3.6 to 4.8	Si-O(H)-Al, Brønsted sites	120, 122, 123
	1.6 to 2.2	Si-OH, silanol sites	

The ^{27}Al NMR spectrum of MP SAPO-37 contained a single peak at 29.5 ppm, corresponding to Al in tetrahedral coordination [Al(4P)] within the framework.[83, 119] However, the slight asymmetry of the ^{27}Al resonance was indicative of a small number of 5- or 6-coordinated aluminium defect sites in the MP SAPO.[124] In HP SAPO-37, two tetrahedral ^{27}Al sites were identified: whilst the peak at 33.5 ppm was consistent with Al(4P) sites, the shoulder at 62.9 ppm evidenced zeolitic Al(4Si),[125] originating from Al located within the siliceous mesopores. Noticeably, HP SAPO-37 also contained a significant quantity of 5-coordinate Al (6.3 ppm).[120, 125, 126] The more highly-coordinated Al is a known artefact of the organosilane templating procedure[103, 126-128] and may be due to of extra-framework Al species,[103] an amorphous Al coordination environment,[125] or hydrated tetrahedral Al sites.[102] The presence of Al defect sites was also consistent with the hydrophilicity of the HP SAPO-37 framework identified by TGA (**Figure 5.4.2**),

The ^{29}Si MAS NMR of MP SAPO-37 revealed a single Si environment at -92.1 ppm, corresponding to isolated Si(4Al9P) species in tetrahedral coordination within the framework.[120] Implicitly, the Si(4Al9P) resonance also characterised bridging Brønsted acid sites in SAPO-37, which accompany the (preferred)[84, 121] Type II substitution of Si(IV) for P(V). The isolated, SAPO-type Si sites were also prominent in the ^{29}Si NMR of HP SAPO-37, however significant intensity in the region up to -120 ppm identified the Si-O-Si bonding within the siliceous mesopores (derived from the organosilane template).

In accord with the ^{29}Si NMR data, MP SAPO-37 exhibited a relatively well-defined ^{1}H proton resonance at 5.5 ppm, which was assigned to the bridging Si-O(H)-Al sites.[120] Likewise, Brønsted protons were also present in HP SAPO-37 (5.4 ppm), as well as silanol sites (1.9 ppm) from the organosilane-templated mesopores.[129, 130] Intensity in the region between the peaks of the Brønsted and silanol sites identified the protons that are associated with defects (P-OH , Al-OH), or aluminosilicate regions in the mesopores.[39, 131]

Finally, both HP and MP SAPO-37 exhibited a sharp ^{31}P resonance at -26.3 ppm, which was consistent with the tetrahedral P(4Al) sites of the silicoaluminophosphate backbone.[80] The downfield 'tail' of the ^{31}P resonance in HP SAPO-37 may, however, reveal the presence of P-OH defect sites.[83]

5.4.2 Characterisation of the acidity of SAPO-37 catalysts

The activity of a catalyst for the Beckmann rearrangement is intrinsically linked to its acidity.[6, 8, 132] As such, an assessment of the nature, strength, and quantity of acid sites in the SAPO-37 catalysts is fundamental for a rationalisation of their catalytic performance in the BR. For this undertaking, the catalysts were analysed in a series of probe-based experiments, exploiting the interactions of basic molecules with the acid sites in the SAPO frameworks in order to study their acid characteristics.

The results of temperature-programmed desorption (NH_3-TPD) from MP and HP SAPO-37 are reported in **Figure 5.4.9** and **Figure 5.4.10**.

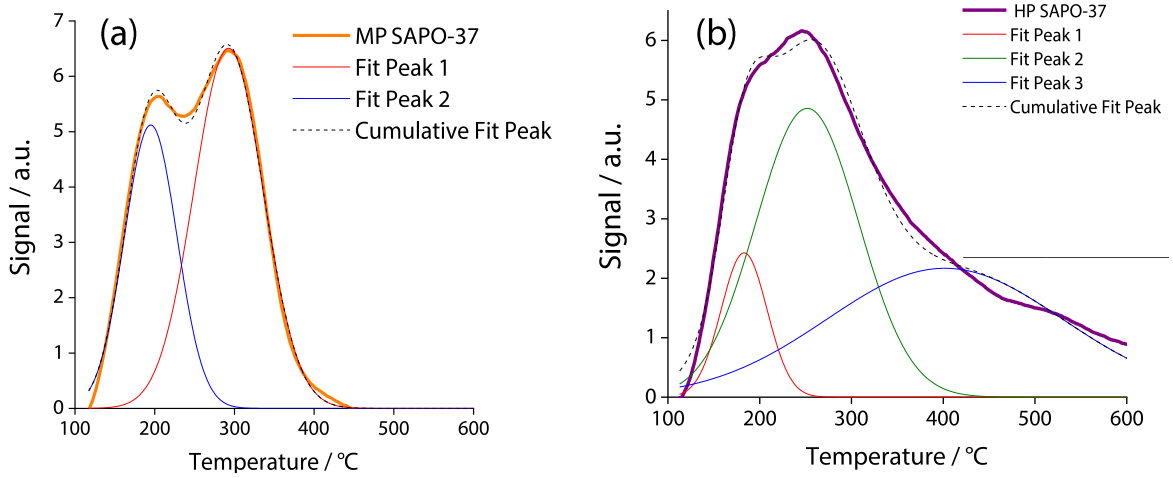

Figure 5.4.9: The fitted NH_3-TPD profiles of **(a)** MP SAPO-37 and **(b)** HP SAPO-37, acquired at a ramp rate of 10 °C min^{-1}, after dosing with NH_3 gas at 100 °C for 3 hours.

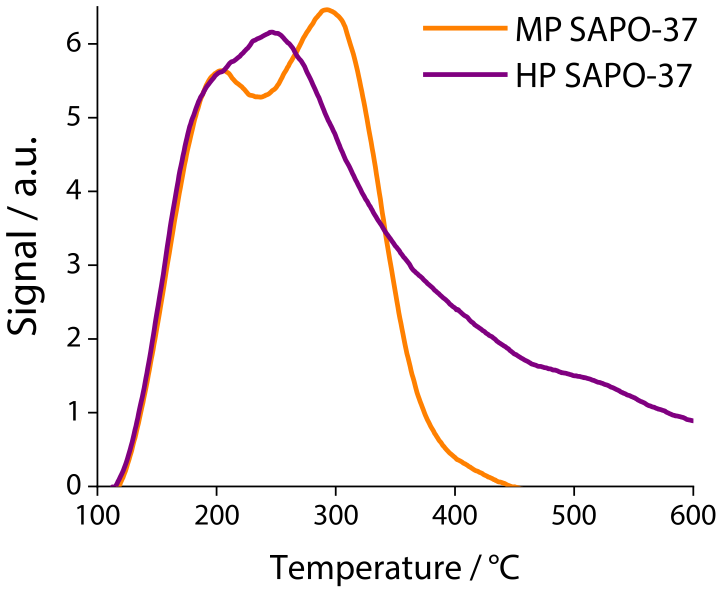

Figure 5.4.10: The NH_3-TPD profiles of MP SAPO-37 and HP SAPO-37, acquired at a ramp rate of 10 °C min^{-1}, after dosing with NH_3 gas at 100 °C for 3 hours. Spectra not mass normalised.

Table 5.4.9: Quantitative analysis of NH_3-TPD data for MP and HP SAPO-37, including temperatures for the onset of NH_3 desorption and the loss of weakly and more strongly bound NH_3, and the total quantity of ammonia desorbed between 100 – 600 °C.

Catalyst	Onset of ammonia desorption / °C	Peak maximum for loss of weakly-bound NH_3 / °C	Peak maximum for loss of more strongly-bound NH_3 / °C	Completion of NH_3 desorption / °C	Total quantity of NH_3 desorbed < 600 °C / (mmol NH_3) (g^{-1} catalyst)
MP SAPO-37	115	200	295	450	1.77
HP SAPO-37	115	200	250	> 600	1.39

The NH_3-TPD trace of MP SAPO-37 exhibited two desorption peaks (**Figure 5.4.9 a**). The first peak, observed at 200 °C, was attributed to the loss of ammonia that was physisorbed within the SAPO pores, or weakly bound to defect sites (e.g. P-OH, Al-OH).[133, 134] Based on the ^1H MAS NMR data, the second desorption peak of MP SAPO-37 was assigned to the loss of ammonia from the more acidic, bridging Brønsted sites (from Type II substitution of Si(IV) for P(V)).[89-91, 135]

Although the thermodesorption of ammonia from HP SAPO-37 occurred as a single peak, this was a convolution of multiple desorption processes (**Figure 5.4.9 b**). As in MP SAPO-37, the loss of weakly bound ammonia occurred at 200 °C for HP SAPO-37. However, the lower

temperature desorption was a shoulder on a more intense desorption centred at 250 °C. Therefore, the desorption of ammonia from the bridging Brønsted sites occurred 45 °C lower in HP SAPO-37 than MP SAPO-37. The moderation of framework acidity by the siliceous mesopore network has been reported previously,[136-138] and has been observed for other MP and HP SAPO catalysts templated by organosilane (**Chapter 3** and **4**). Nevertheless, HP SAPO-37 also contained sites that were considerably more acidic than those found in SAPO-37. The stronger acid sites may have arisen due structural distortions in the proximity of a Brønsted site, or due to aluminosilicate regions in the mesopores.[90, 102] Whilst more ammonia was desorbed from MP SAPO-37 than HP SAPO-37 at < 600 °C, desorption was incomplete by 600 °C in HP SAPO-37.

When ^{15}N-pyridine was adsorbed in HP and MP SAPO-37, the ^{15}N MAS NMR spectra both exhibited a single resonance (**Figure 5.4.11**), although the ^{15}N chemical shift differed quite significantly between the two frameworks.

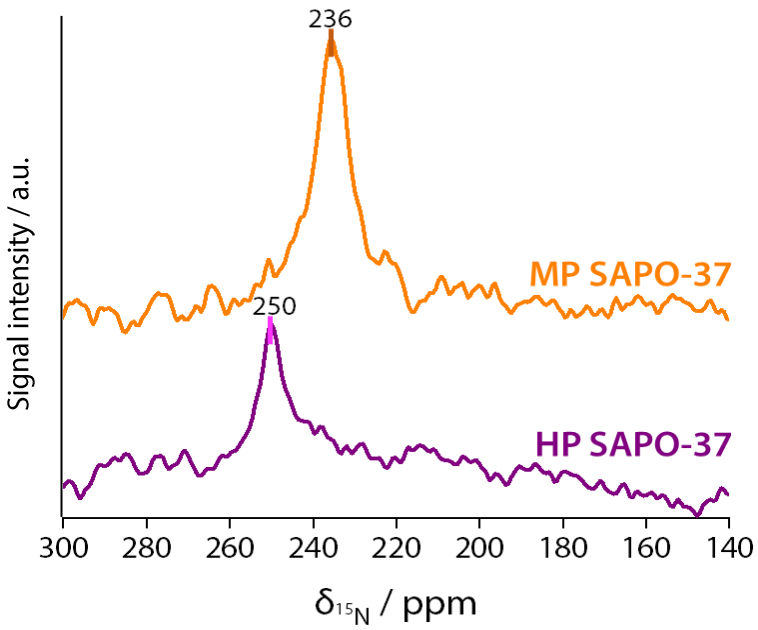

Figure 5.4.11: The ^{15}N MAS NMR spectrum of ^{15}N-pyridine adsorbed in MP SAPO-37 and HP SAPO-37 revealed that hydrogen-bonding interactions between the framework and probe were stronger in the MP catalyst. Data acquired at 600 MHz and 22kHz spinning speed.

In HP SAPO-37, the ^{15}N peak at 250 ppm was consistent with pyridine hydrogen bonded to the weakly acidic silanols in the mesopores.[139] Based on the relationship between ^{15}N-pyridine chemical shift and the strength of the ^{15}N-H interaction (**Figure 5.1.4**),[130] the more upfield resonance observed with MP SAPO-37 (236 ppm) was indicative of a stronger hydrogen bonding interaction with pyridine than that in HP SAPO-37. Thus, the ^{15}N NMR data was aligned with the NH_3-TPD analysis, as both characterised the predominance of stronger acidity in MP SAPO-37 *versus* HP SAPO-37.

The corresponding ^{1}H MAS NMR spectra of the SAPO/^{15}N-pyridine samples are shown in **Figure 5.4.12**. In the 5 - 8 ppm region, peak intensity was attributed to a convolution of the pyridine ring-protons (reported at 7.4 - 8.6 ppm)[140] and framework Brønsted sites that are hydrogen-bonded to pyridine (reported at ~ 6 ppm),[141] in accord with the ^{15}N MAS NMR spectrum. Significantly, a peak at 14.2 -14.4 ppm identified pyridinium species (typically 12-16 ppm)[141-143] in both HP and MP SAPO-37. Only in the spectrum of MP SAPO-37, was a small high-field peak at 3.0 ppm resolved due to pyridine hydrogen-bonded with Si-OH or Al-OH defect sites.[144] The broad, high-field peak at -1 ppm in the HP SAPO-37 sample has not been reported in the literature. However, the negative ^{1}H chemical shift indicated that a number of protons were very strongly shielded; this may be consistent with Si-OH···π interactions, if the pyridine molecules were oriented parallel to the surface of the mesopores.

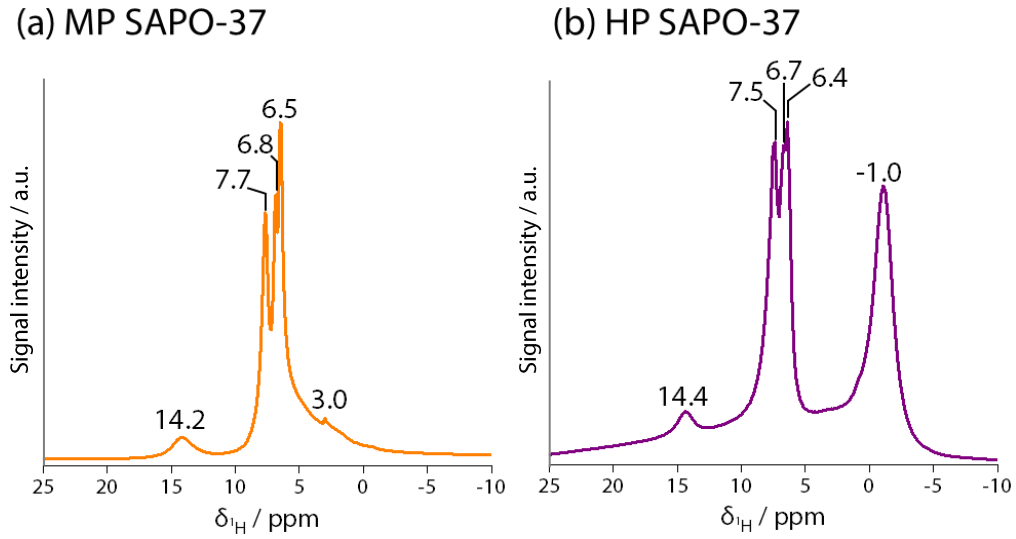

Figure 5.4.12: The ^{1}H MAS NMR spectrum of ^{15}N-pyridine adsorbed in MP SAPO-37 and HP SAPO-37. Data acquired at 600 MHz and 22kHz spinning speed.

The adsorption of pyridine was also studied by FTIR spectroscopy. The FTIR spectra and peak assignments for pyridine adsorbed on MP and HP SAPO-37 are reported in **Figure 5.4.13** and **Table 5.4.10**, respectively.

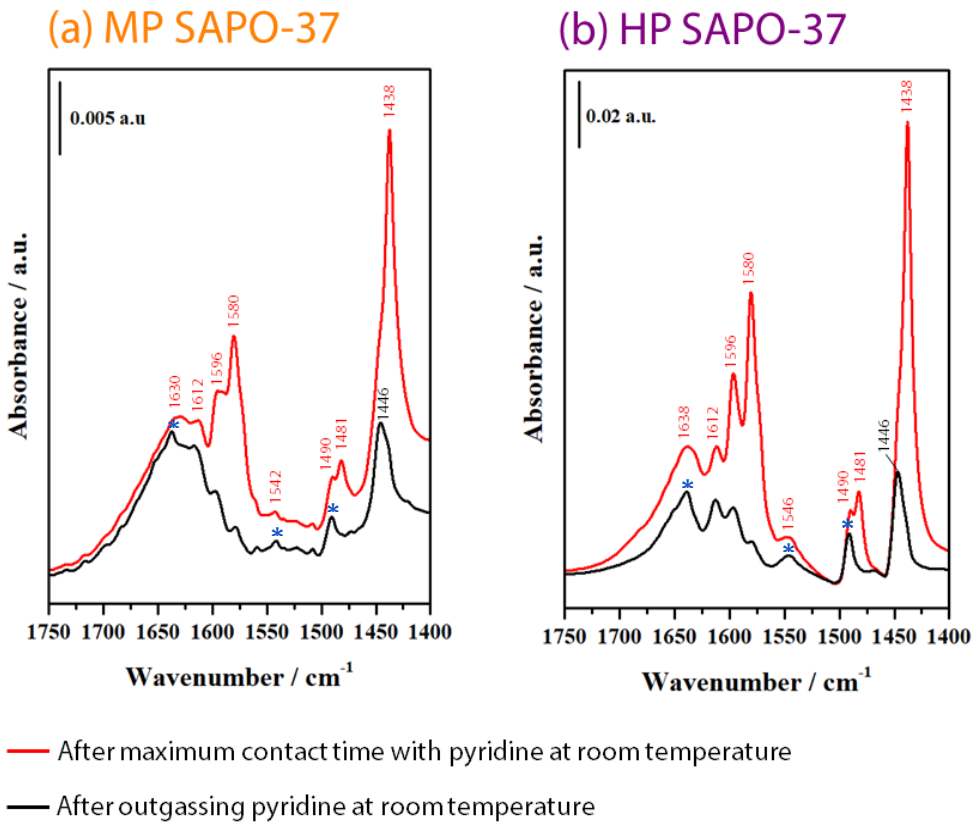

Figure 5.4.13: The FTIR spectra of **(a)** MP SAPO-37 and **(b)** HP SAPO-37 on exposure to pyridine vapour at room temperature (red line) and after outgassing at room temperature (black line). * identifies the peaks that are associated with the protonation of pyridine.

Table 5.4.10: Assignment of the aromatic ring vibrations between 1400 – 1700 cm^{-1} in the FTIR spectra (**Figure 5.4.13**) of pyridine adsorbed on MP and HP SAPO-37.

Wavenumber / cm^{-1}	Sample		Assignment	Ref.
	MP SAPO-37	HP SAPO-37		
1638	×	✓	ν_{8a} - protonated pyridine	58, 145
1630	✓	×	ν_{8a} - protonated pyridine	66, 145
1612	✓	✓	ν_{8a} – hydrogen-bonded pyridine	145
1596	✓	✓	ν_{8b} - hydrogen-bonded pyridine	3, 58
1580	✓	✓	ν_{8b} - physisorbed pyridine	3, 58
1546	×	✓	ν_{19b} - protonated pyridine	58, 145
1542	✓	×	ν_{19b} - protonated pyridine	145
1490	✓	✓	ν_{19a} - protonated pyridine	3, 58, 145
1481	✓	✓	ν_{19a} - physisorbed pyridine	3
1446	✓	✓	ν_{19b} - hydrogen-bonded pyridine	3, 58
1438	✓	✓	ν_{19b} - physisorbed pyridine	3, 58, 145

From initial inspection of the peak intensities, it was apparent that HP SAPO-37 adsorbed significantly more pyridine than MP SAPO-37. Since the measured surface area of HP SAPO-37 was smaller than MP SAPO-37 (**Table 5.4.5**), the increased adsorption of pyridine was attributed to the greater (meso)pore volume and number of acidic adsorption sites (i.e. silanols and Brønsted sites) in the HP catalyst. On removing the physisorbed pyridine, vibrations due to hydrogen bonded and protonated pyridine were identified in both catalysts, consistent with the NMR data. In general, the FTIR spectra were largely comparable between the two catalysts, which confirmed that the micropores of SAPO-37 (7.4 Å) were accessible to pyridine (kinetic diameter = 5.4 Å).[3] However, the slightly higher energy of the ν_{8a} and ν_{19b} modes of protonated pyridine in HP SAPO-37 (incidentally the most sensitive modes to interaction at nitrogen)[66] may have alluded to the presence of the strongest acid sites identified by NH_3-TPD (**Figure 5.4.10**).

The probe-based FTIR technique was also used to contrast the accessibility of the Brønsted acid sites in HP and MP SAPO-37. First, ammonia was adsorbed in both catalysts to quantify the total amount of (weak and strong) acid sites in the micropores and mesopores (**Figure 5.4.14**).

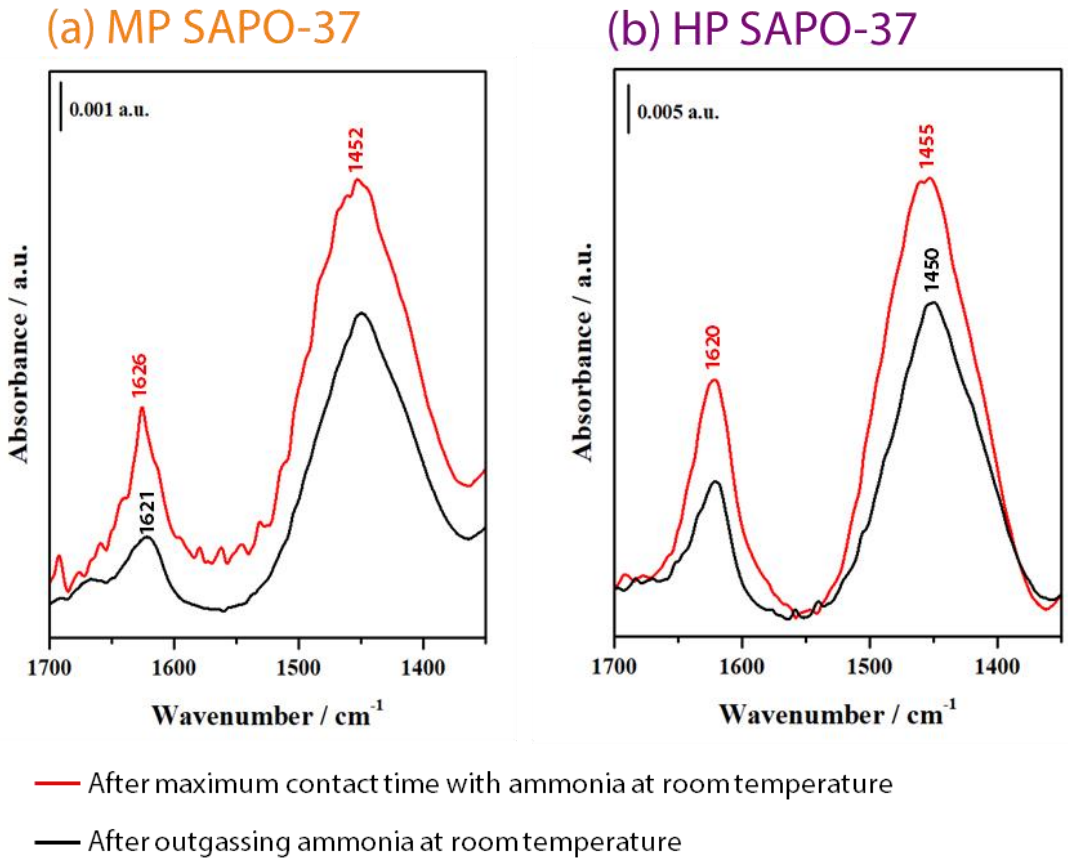

Figure 5.4.14: The FTIR spectra of **(a)** MP SAPO-37 and **(b)** HP SAPO-37 on exposure to 30 mbar ammonia at room temperature (red line) and after outgassing at room temperature (black line).

In the 1700 - 1300 cm^{-1} range, the FTIR spectra of NH_3 adsorbed on MP and HP SAPO-37 exhibited two peaks. The peak centred at ~ 1620 cm^{-1} was attributed to ammonia that was hydrogen bonded to the SAPO framework, whilst the band centred at ~ 1450 cm^{-1} identified the asymmetric bending mode (δ_{asym}) of NH_4^+ species arising from the protonation of ammonia at the stronger, Brønsted acid sites.[3]

In the subsequent experiment, the bulkier 2,6-di-*tert*-butylpyridine probe (2,6-dTBP) was adsorbed on the SAPO catalysts (**Figure 5.4.15**). Due to steric hindrance, 2,6-dTBP can only interact with the most accessible acid sites, for example those located on the catalyst surface, or within the mesopores.[3, 49, 70, 75] From the relative intensities of the characteristic modes, the FTIR spectra showed that considerably more 2,6-dTBP was adsorbed in HP SAPO-37 than MP SAPO-37, demonstrating the improved accessibility of the HP framework *via* the mesopores.

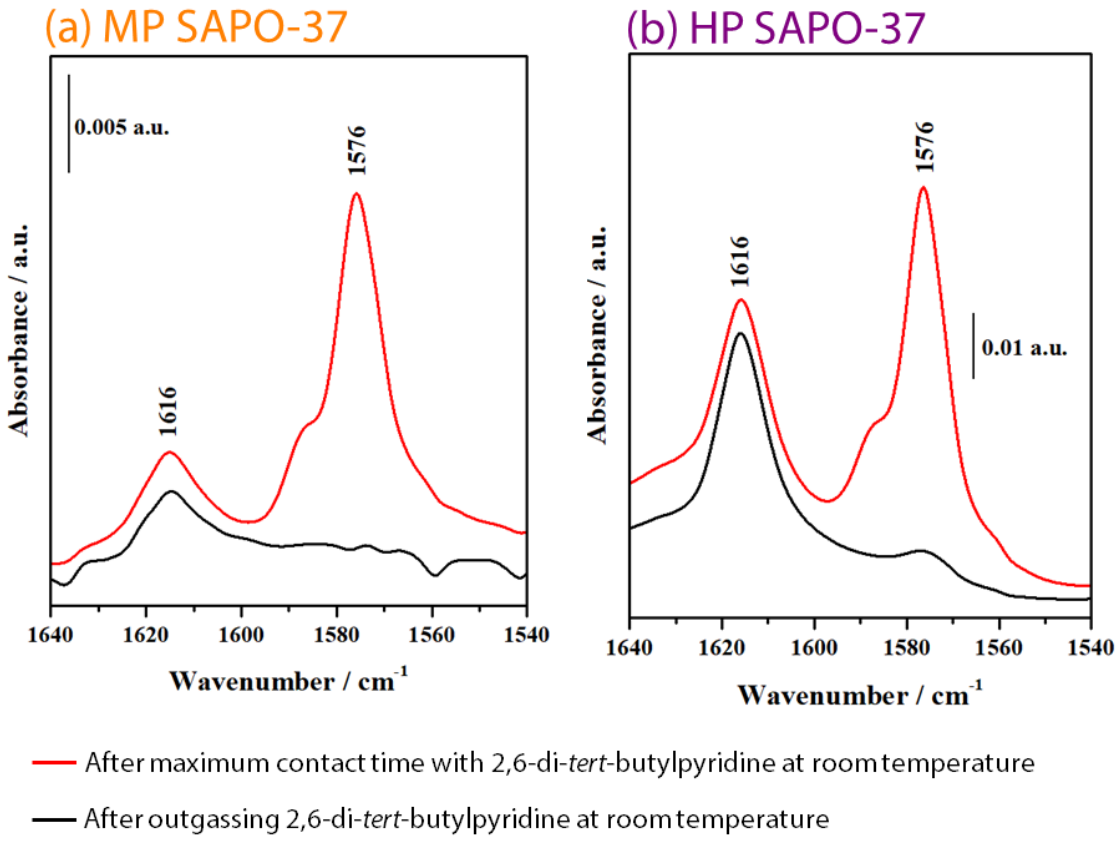

Figure 5.4.15: The FTIR spectra of **(a)** MP SAPO-37 and **(b)** HP SAPO-37 on exposure to 2,6-di-*tert*-butylpyridine at room temperature (red line) and after outgassing at room temperature (black line).

In the FTIR region associated with 2,6-dTBP aromatic ring-modes (1700 – 1540 cm^{-1}) two peaks were observed.[3, 49, 70] The higher energy band, centred at 1616 cm^{-1}, characterised the protonated 2,6-dTBPH$^+$ species, and hence the Brønsted acid sites in HP and MP SAPO-37.

The ν_{8a} mode at 1576 cm^{-1} was attributed to weaker, hydrogen-bonding interactions between 2,6-dTBP and the SAPO-37 catalysts, which could be removed by outgassing at 298 K.

An accessibility factor[48] was calculated for the adsorption of 2,6-dTBP in HP SAPO-37 (**Table 5.4.11**). The amount of 2,6-dTBPH$^+$ adsorbed on HP SAPO-37 was quantified using the characteristic ν_{8a} mode, and then reported as a fraction of the total number of Brønsted sites (quantified by the adsorption of ammonia).[49] Due to the significant steric bulk of the 2,6-dTBP, the accessibility factor reports the fraction of Brønsted sites located on the external surface of the catalyst or within the mesopores.[49, 75]

Table 5.4.11: The concentration of accessible Brønsted acid sites and the accessibility factor calculated from the ratio of the amount of 2,6-dTBP and ammonia adsorbed to Brønsted acid sites in HP SAPO-37.

Protonated probe species	Characteristic IR mode	Position of characteristic IR mode / cm^{-1}	Concentration of accessible active sites / mmol g^{-1}	Accessibility Factor
NH_4^+	δ_{asym}	1450 [a]	19.0	1
2,6-dTBPH$^+$	ν_{8a}	1618 [b]	1.3	0.068
[a] ε = 0.147 cm^2 μmol^{-1} [71] [b] ε = 0.5 cm^2 μmol^{-1} [49]				

Overall, probe-based techniques have revealed some significant differences in the acid character of MP and HP SAPO-37 catalysts. By NH_3-TPD, MP SAPO-37 was found to contain a larger proportion of moderate-to-strong Brønsted acid sites than HP SAPO-37, the acidity of the latter being moderated by the presence of weakly acidic silanols in the mesopores. Nevertheless, NH_3-TPD identified a number of very strong acid sites in HP SAPO-37, which may have arisen due to structural distortions at the Brønsted sites, caused by the mesopore network. The net stronger acidity of MP SAPO-37 was evidenced by a larger upfield shift of the ^{15}N MAS NMR resonance of adsorbed ^{15}N-pyridine, although both samples appeared only to engage in hydrogen-bonding interactions with the probe. However, on inspecting the corresponding ^1H MAS NMR, it was revealed that pyridine was not only hydrogen bonded to the framework, but also protonated at the Brønsted acid sites. The FTIR of adsorbed ammonia, pyridine, and 2,6-dTBP identified both weak (Si-OH, Al-OH, P-OH) and strong (Brønsted) acid sites in MP and HP SAPO-37, but a larger amount of probe was adsorbed to HP SAPO-37, which was consistent with the larger number of acid sites (i.e. silanols and Brønsted sites).

5.4.3 Catalysis: the Beckmann rearrangement of cyclohexanone oxime

Initially, MP and HP SAPO-37 were investigated as catalysts for the liquid-phase BR of cyclohexanone oxime (**Figure 3.4.5**).

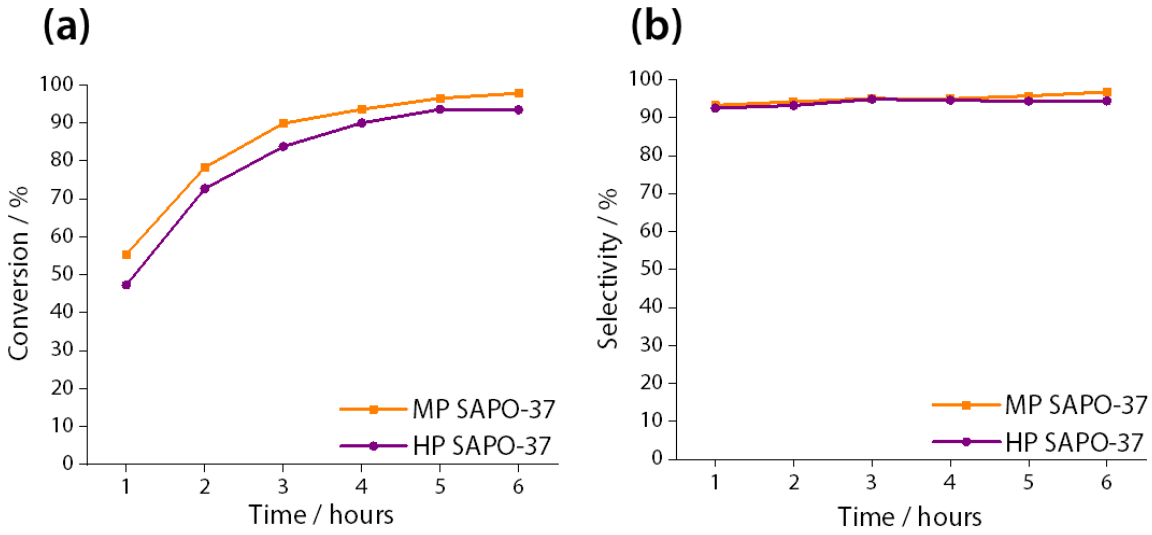

Figure 5.4.16: The **(a)** conversion of cyclohexanone oxime and **(b)** selectivity towards ε-caprolactam in the liquid-phase Beckmann rearrangement (130 °C, benzonitrile solvent) catalysed by MP SAPO-37 and HP SAPO-37. Cyclohexanone was the only by-product.

The catalytic data revealed that, under liquid-phase conditions, the mesopore network of HP SAPO-37 offered no mass transport advantage *versus* the three-dimensional FAU micropore network (pore diameter 7.4 Å)[78] in the conversion of cyclohexanone oxime (~ 6 Å).[126] Rather, the activity of the organosilane-templated HP SAPO-37 was slightly inferior to MP SAPO-37 in the BR. It has been reported[100, 146, 147] that under the relatively low-temperature conditions of the liquid-phase BR, stronger acid sites are required in order to overcome the activation barrier to the BR, and produce caprolactam in good yield. Since, the previous acid-site characterisation of HP SAPO-37 had revealed the acidity of the SAPO-37 framework to be moderated by the presence of the weakly acidic silanols in the mesopores,[4] it was likely that the reduced activity of HP SAPO-37 *versus* MP SAPO-37 was due to the net weaker acidity of the soft-templated framework.

Nevertheless, weak acid sites have been demonstrated to enhance the yield of caprolactam in the vapour-phase BR.[89-91] On this basis, the HP and MP SAPO-37 catalysts were subsequently tested in the vapour-phase BR of cyclohexanone oxime at 325 °C (**Figure 5.4.17**).

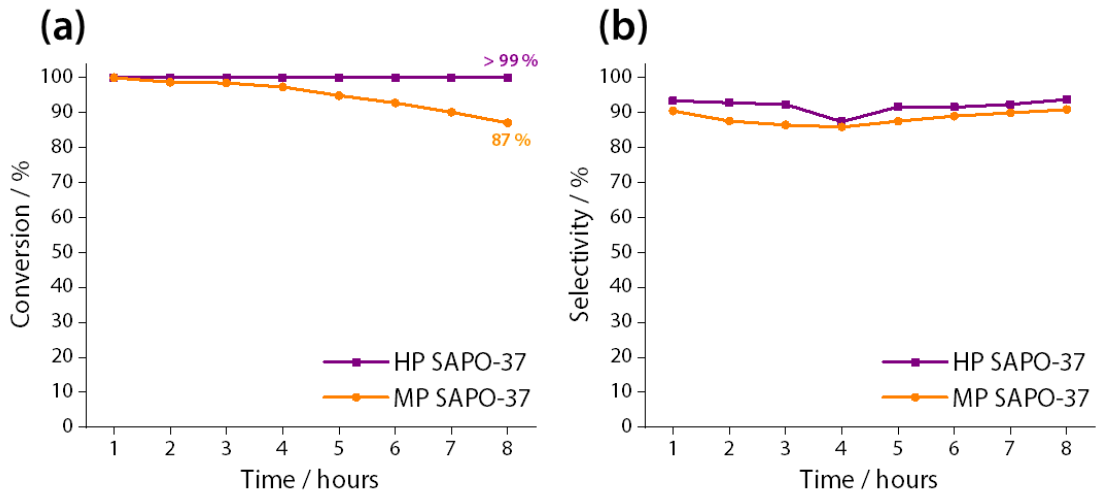

Figure 5.4.17: The **(a)** conversion of cyclohexanone oxime and **(b)** selectivity towards ε-caprolactam in the vapour-phase Beckmann rearrangement (325 °C, 0.79 hr^{-1}, oxime 10 g L^{-1} in ethanol) catalysed by MP SAPO-37 and HP SAPO-37.

Over the 8 hour reaction, HP SAPO-37 was found to sustain > 99 % conversion of cyclohexanone oxime, whilst the conversion of oxime over MP SAPO-37 declined to 87 % over the same period. The loss of activity in MP SAPO-37 was consistent with gradual blockage of the micropores due to accumulation of coke and nitrogenous residues,[148] as this would increasingly hinder access to the internal active sites. The observation that HP SAPO-37 was resistant to deactivation, implied that the active sites (whether in the micropores or mesopores) remained accessible with time-on-stream. HP SAPO-37 also showed a slightly higher selectivity towards caprolactam than MP SAPO-37, which was consistent with their relative acidities, and the tendency for stronger acid catalysts (i.e. MP SAPO-37) to retain and re-adsorb the lactam product. In fact, the stronger acidity of MP SAPO-37 may have contributed to its deactivation by promoting the accumulation of by-product at Brønsted sites inside the micropores.

The enhanced activity of HP SAPO-37 in the vapour-phase BR 325 °C provided vindication of the improved mass transport properties of the mesopores and the acidity-moderating effect of its silanols. Thus, it was proposed that the beneficial influence of the mesopores in HP SAPO-37 might be accentuated by reducing the reaction temperature, as a slowed diffusion and desorption of reactive species were expected to affect the MP catalyst more acutely. Therefore, MP and HP SAPO-37 catalysts were tested in the vapour-phase BR at 300 °C (**Figure 5.4.18**).

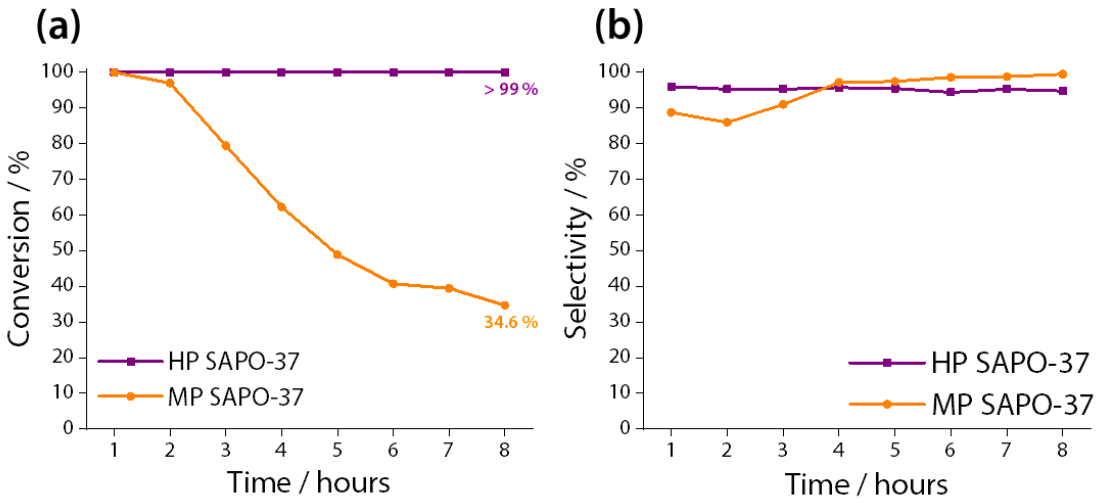

Figure 5.4.18: The **(a)** conversion of cyclohexanone oxime and **(b)** selectivity towards ε-caprolactam in the vapour-phase Beckmann rearrangement (300 °C, 0.79 hr^{-1}, oxime 10 g L^{-1} in ethanol) catalysed by MP SAPO-37 and HP SAPO-37.

Indeed, the difference in the activity of HP SAPO-37 and MP SAPO-37 was marked at 300 °C. Whilst HP SAPO-37 sustained > 99 % conversion of cyclohexanone oxime for 8 hours on-stream, conversion over MP SAPO-37 declined to just 34.6 % in the same period. Interestingly, the selectivity of MP SAPO-37 was found to increase with time-on-stream, which suggested that some of the strongest and most unselective Brønsted acid sites were deactivated by coke deposition.[132]

To confirm that pore blockage was responsible for the deactivation of MP SAPO-37 in the vapour-phase BR, both catalysts were characterised post-catalysis. Powder XRD confirmed that the FAU structure was retained in both HP and MP SAPO-37 after catalysis, and thus framework collapse was excluded as the cause of MP SAPO-37 deactivation (**Figure 5.4.19 a**).

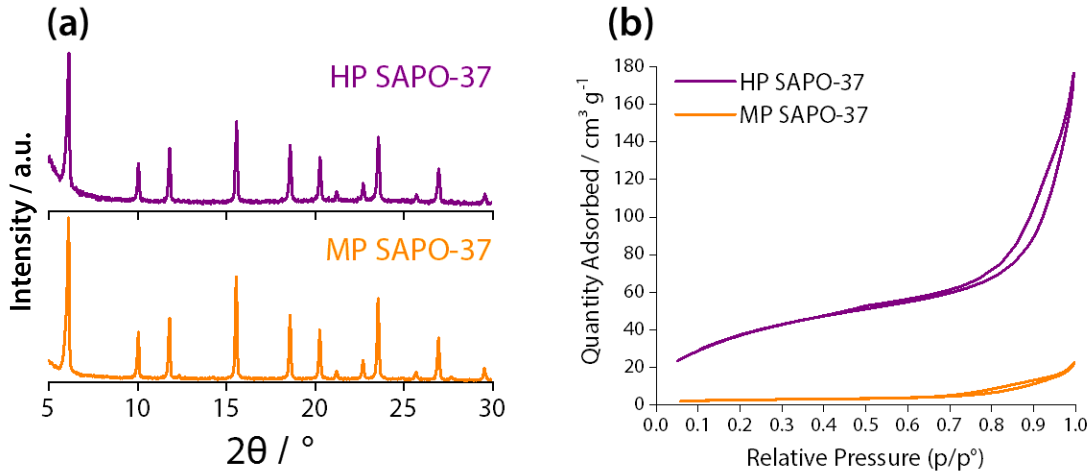

Figure 5.4.19: (a) The powder XRD pattern and **(b)** N_2 gas adsorption-desorption isotherm of HP SAPO-37 and MP SAPO-37 after 8 hours on-stream in the vapour-phase Beckmann rearrangement at 300 °C.

N_2 adsorption experiments revealed that the surface area of HP SAPO-37 was severely diminished post-catalysis (from 551 to 141 $m^2 g^{-1}$), yet the mesopore volume (0.28 $cm^3 g^{-1}$) was essentially unchanged. However, at the end of the same 8 hour BR reaction, MP SAPO-37 was essentially non-porous (BET surface area < 10 $m^2 g^{-1}$). A micropore volume could not be calculated for either catalyst, which suggested that the micropores were inaccessible in both MP and HP SAPO-37. Nevertheless, the inaccessibility of the internal Brønsted sites of HP SAPO-37 appeared to have no effect on its catalytic activity. Therefore, the BR in HP SAPO-37 may have occurred predominantly at the less acidic (and therefore more selective)[8] silanol sites in the mesopores.

The post-catalysis SAPOs were also subject to CHN (**Table 5.4.12**) and thermogravimetric analyses (**Figure 5.4.20**) in order to characterise the source of the micropore blockage.

Table 5.4.12: Carbon, hydrogen and nitrogen elemental analysis of HP and MP SAPO-37 after 8 hours on-stream in the vapour-phase Beckmann rearrangement at 300 °C.

Catalyst	Elemental analysis		
	% C	% H	% N
HP SAPO-37	11.73	1.05	1.75
MP SAPO-37	17.89	3.19	1.66

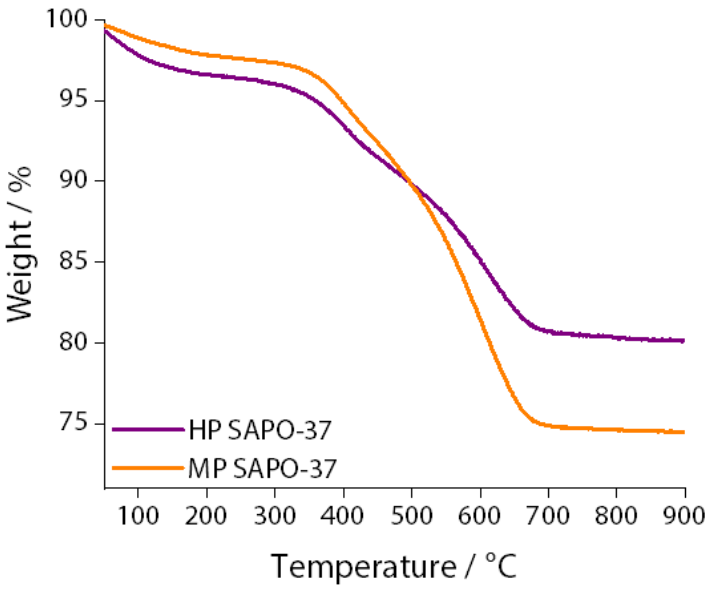

Figure 5.4.20: Thermogravimetric analysis of the HP SAPO-37 and MP SAPO-37 catalysts after 8 hours on-stream in the vapour-phase Beckmann rearrangement at a reaction temperature of 300 °C. TGA profile acquired by heating in air from 30 - 900 °C at a ramp rate of 10 °C min^{-1}.

CHN analysis of the post-reaction catalysts revealed a larger deposit of carbonaceous and nitrogenous material in MP SAPO-37 *versus* HP SAPO-37, which correlated with the net stronger acidity of the MP framework.[6] This observation was also supported by TGA, as a larger % weight loss occurred from MP SAPO-37 than HP SAPO-37. In the TGA trace, weight loss that occurred at temperatures < 200 °C was attributed to the desorption of water, whilst those at > 200 °C were assigned to the decomposition of nitrogenous and carbonaceous deposits from the vapour-phase reaction. A '% weight loss due to coke' ($wt.\ \%_{coke}$) was calculated for each catalyst using **Equation 5.4.1**, where $wt.\ \%_{200°C}$ and $wt.\ \%_{900°C}$ are the % weight of the sample after heating to 200 °C (i.e. after water loss) and 900 °C, respectively.

Equation 5.4.1: $$wt.\%_{coke} = wt.\%_{200\,°C} - wt.\%_{900\,°C}$$

HP SAPO-37: $wt.\ \%_{coke}$ = 96.6 % - 80.1 % = 16.5 %

MP SAPO-37: $wt.\ \%_{coke}$ = 97.8 % - 74.5 % = 23.3 %

The TGA and CHN data indicated that the deactivation of MP SAPO-37 was exacerbated by its tendency to accumulate coke deposits (likely due to its stronger acidity).[6] Nonetheless, the fact that MP SAPO-37 retained some activity, irrespective of the pore blockage, suggested that there was catalytic turnover at active sites on the surface of the SAPO-37 crystallites.[149] For HP SAPO-37, the acidity-moderating effect of the silanols in the mesopores was found to reduce the amount of coke that was accumulated within the framework, relative to MP SAPO-37. Whilst TGA and CHN evidenced a significant accumulation of coke and nitrogenous residues in HP SAPO-37, the presence of the mesopores conferred greater resistance to pore-blockage, hence its sustained, high activity with time-on-stream.[132]

Subsequently, the HP SAPO-37 catalyst was regenerated by calcination in air (16 hours, 550 °C). Encouragingly, when the recycled catalyst was tested in the vapour-phase BR at 300 °C, it was found to retain the performance of the fresh catalyst (**Figure 5.4.21**).

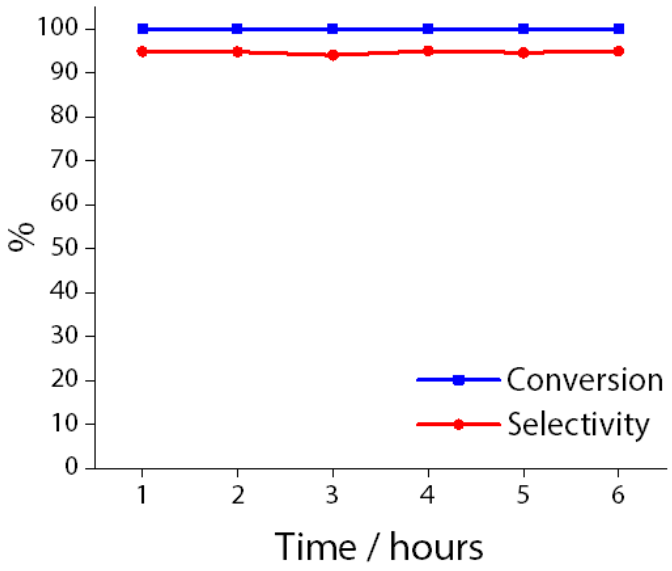

Figure 5.4.21: The conversion of cyclohexanone oxime (blue line), and selectivity towards ε-caprolactam (red line) in the vapour-phase Beckmann rearrangement (300 °C, 0.79 hr^{-1}, oxime 10 g L^{-1} in ethanol) catalysed by HP SAPO-37 after recycle (air, 550 °C, 16 hours).

5.5 Conclusions and future work

In previous reports, MP SAPO-37 has facilitated the liquid-phase Beckmann rearrangement of cyclohexanone oxime with near-quantitative yield of ε-caprolactam by 6 hours.[89-91] However, it was proposed that the activity of SAPO-37 might be enhanced by the introduction of an auxiliary mesopore network, which has been demonstrated to improve the performance of SAPO catalysts in both the liquid and vapour-phase BR.[3, 4, 70] Whilst a preparation for HP SAPO-37 has been reported in the literature,[93-97] the purity and crystallinity of the CTAB-templated material was questionable. Given the excellent selectivity of MP SAPO-37 in the BR, it was desirable to preserve the physicochemical characteristics of the framework in a hierarchical analogue. As such, HP SAPO-37 was targeted with an established, soft-template synthesis, previously shown to produce phase-pure and crystalline HP (Si)AlPOs.[4, 102]

HP SAPO-37 was prepared *via* a 'one-pot' synthesis with an amphiphilic organosilane as the mesoporogen.[101] Elemental (CHN) and thermogravimetric analyses indicated that the surfactant was successfully incorporated in the as-synthesised product. Subsequent XRD analysis of the calcined HP SAPO-37 revealed excellent retention of the crystalline FAU-type structure, notwithstanding the presence of the mesoporous architectures (evidenced by low-angle XRD, gas adsorption studies, and TEM imaging). Positron annihilation lifetime

spectroscopy revealed an enhanced diffusion within HP SAPO-37 and, more specifically, an interconnectivity of the micropore and mesopore networks, with improved access to the external surface. These observations vindicated the organosilane-template synthesis as an effective route to prepare HP SAPO-37 with improved mass transport characteristics. To the best of our knowledge, these studies represent the only example of organosilane-templated SAPO-37, and perhaps the only example of hierarchically-porous SAPO-37 with a phase-pure and crystalline FAU network in the bulk.

^{29}Si MAS NMR revealed siliceous zones in HP SAPO-37 that were consistent with the incorporation of the organosilane head-group within the walls of the mesopores.[4] Concurrently, the ^{1}H MAS NMR spectrum of HP SAPO-37 identified a significant concentration of silanols groups that, by their absence from the microporous SAPO, were located within the mesopores. These observations were significant, since the siliceous mesopores of organosilane-templated HP (Si)AlPOs have previously been linked to the development of weak acidity in these materials.[4, 102]

NH_3-TPD analysis identified that the most abundant acid sites in HP SAPO-37 were less acidic than those in MP SAPO-37, and thus the silanols in the mesopores were identified to moderate the acidity of the bulk acid sites HP SAPO-37. Nevertheless, HP SAPO-37 also contained a number of acid sites that were considerably stronger than any acid sites characterised in MP SAPO-37, and these were attributed to structural distortions near the Brønsted acid sites (caused by the mesopore network).

Following adsorption of ^{15}N-pyridine in HP SAPO-37, the single ^{15}N MAS NMR resonance was shifted $\Delta\delta$ = -70 ppm relative to the free probe, which indicated significant hydrogen bonding between the basic probe and the acid sites of the catalyst. However, the upfield shift of the ^{15}N-pyridine resonance was larger in the presence of MP SAPO-37 ($\Delta\delta$ = -84 ppm), which was consistent with stronger acidity. Interestingly, the ^{1}H MAS NMR spectra of the ^{15}N-pyridine/SAPO samples not only detected hydrogen bonding interactions, but also the formation of a small quantity of pyridinium ions at the stronger acid sites in both MP and HP SAPO-37. These observations were corroborated by FTIR analysis of adsorbed pyridine, whereby the assignment of the aromatic ring vibrations identified both hydrogen-bonded, and protonated pyridine in MP and HP SAPO-37.

The probe-based FTIR technique was also used to assess the accessibility of the Brønsted acid sites in HP and MP SAPO-37. In particular, it was found that significantly more of the bulky 2,6-di-*tert*-butylpyridine base was adsorbed in HP SAPO-37 *versus* MP SAPO-37, which indicated that acid sites were more accessible in the former. Even so, in the liquid-phase

Beckmann rearrangement of cyclohexanone oxime, the mesoporosity in HP SAPO-37 yielded no improvement in catalytic activity relative to MP SAPO-37. In fact, the conversion of cyclohexanone oxime was slightly less with HP SAPO-37 catalyst, this being attributed to the relative inactivity of its weaker acid sites under the moderate reaction conditions. However, it was hypothesised that the weaker acidity and mesoporosity of HP SAPO-37 might offer an advantage for catalyst activity and lifetime against MP SAPO-37 in the vapour-phase BR.[4, 8] Indeed, the effect of the siliceous mesopore network was noticeable in the BR at 300 °C, with HP SAPO-37 sustaining > 99 % conversion (at > 94 % selectivity for ε-caprolactam) over 8 hours on-stream, whilst conversion declined to < 35 % using MP SAPO-37.

To rationalise the improved performance of the HP SAPO-37, the post-catalysis samples were subject to characterisation. TGA and elemental analyses identified a significantly larger carbonaceous/nitrogenous deposit in the MP SAPO-37 than HP SAPO-37, which was attributed to the increased formation of by-products on the strong acid sites of MP SAPO-37.[8] Whilst coke deposition was observed on the HP SAPO-37 catalyst, N_2 adsorption studies indicated that some porosity (predominantly mesoporosity) was retained. Therefore, the role of the mesopores in the sustained performance of HP SAPO-37 was two-fold, since the weakly acidic silanol sites retarded coke deposition, and the larger pore volume of the mesopores were slower to become blocked by coke. Encouragingly, the HP SAPO-37 catalyst could be reactivated by calcination, with complete retention of catalytic performance in the vapour-phase BR at 300 °C.

Future characterisation of HP SAPO-37 might seek to probe the structure and distribution of the mesopores in more detail. For example, high-resolution TEM[150, 151] and electron tomography[152, 153] can offer superior visualisation of mesoporous constructs in hierarchically-porous zeolites,[154] and might be coupled with the selective growth of platinum nanowires in the mesopores to enhance contrast against the zeotype framework.[155, 156] In addition, the reduced BET surface area of HP SAPO-37 *versus* MP SAPO-37, and the decreased micropore surface of the hierarchical material (also identified in the organosilane-templated HP SAPOs reported in **Chapter 3** and **Chapter 4**) could be probed further.

Another aspect of the HP SAPO-37 structure that might be probed in more detail is the incorporation of Si into the framework, this being linked to the intrinsic acidity of the framework. Whilst the isomorphous substitution of Si in SAPO-37 has been characterised extensively,[81-83, 87] the local environment of Si in the organosilane-templated mesopores has been studied in less detail. Unfortunately, the low receptivity of the ^{29}Si nucleus at natural abundance, combined with the low intrinsic sensitivity of the NMR technique, predisposes conventional techniques to low resolution and long acquisition times. For this reason, the

enhanced sensitivity of dynamic nuclear polarisation (DNP) MAS NMR might be explored as means to acquire ^{29}Si MAS NMR for ^{29}Si-^{29}Si correlation in HP SAPO-37.

The underlying principle of the DNP technique[157] is that sensitivity towards a nucleus of low gyromagnetic ratio (γ, e.g. ^{29}Si) can be enhanced by transferring polarisation from a spin with a larger γ. However, unlike conventional nuclear cross-polarization techniques, DNP MAS NMR exploits the large γ of the unpaired electron to achieve a significant improvement in signal : noise ratio. Practically, the unpaired electrons are introduced as a biradical polarising agent (e.g. AMUPol, **Figure 5.5.1 a**), which can be irradiated with high-power microwaves to saturate electron paramagnetic resonance transitions.

The direct ^{29}Si MAS NMR spectrum for HP SAPO-37 is shown in **Figure 5.5.1**, with and without the DNP effect. Due to technical issues with the spectrometer and the pulse sequence, it was not possible to complete the 2D ^{29}Si DNP MAS NMR experiment. Nonetheless, the signal enhancement in the ^{29}Si DNP MAS NMR spectrum reveals the capabilities of the technique. It is anticipated that the increased signal associated with DNP might facilitate a 2D ^{29}Si MAS NMR study of HP SAPO-37, where the low natural abundance and relatively large spatial separation of ^{29}Si would require a prohibitively long acquisition times by conventional MAS NMR. These investigations could also be extended to probe-based studies (akin to the ^{15}N-pyridine experiment), in order to improve the signal : noise ratio of the ^{15}N MAS NMR spectrum, and to characterise the adsorption sites of the probe *via* ^{15}N-^{29}Si correlations.

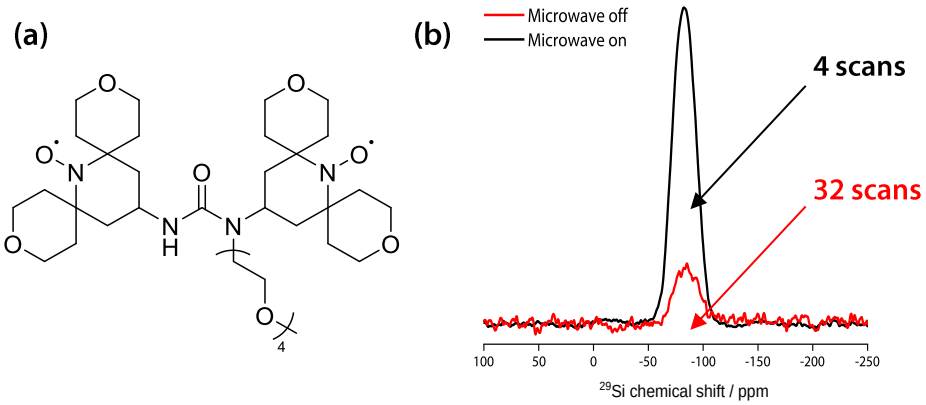

Figure 5.5.1: (a) The structure of AMUPol. **(b)** The ^{29}Si MAS NMR spectrum of HP SAPO-37 dosed with AMUPol, with (microwave on) and without (microwave off) the DNP effect. Experiments were performed on a 14.09 T AVANCE III HD spectrometer with a 3.2 mm triple resonance, wide-bore probe and a 395 GHz gyrotron microwave source. Spectrum acquired at < 100 K and 8 kHz spinning speed. The spectrum is not referenced against a ^{29}Si standard.

5.6 References

1. H. Kath, R. Gläser and J. Weitkamp, *Chem. Eng. Technol.*, 2001, **24**, 150-153.
2. H. Ichihashi, M. Ishida, A. Shiga, M. Kitamura, T. Suzuki, K. Suenobu and K. Sugita, *Catal. Surv. Asia*, 2003, **7**, 261-270.
3. I. Miletto, G. Paul, S. Chapman, G. Gatti, L. Marchese, R. Raja and E. Gianotti, *Chem. – A Eur. J.*, 2017, **23**, 9952-9961.
4. S. H. Newland, W. Sinkler, T. Mezza, S. R. Bare, M. Carravetta, I. M. Haies, A. Levy, S. Keenan and R. Raja, *ACS Catal.*, 2015, **5**, 6587-6593.
5. H. Sato, K. Hirose, M. Kitamura and Y. Nakamura, *Stud. Surf. Sci. Catal.*, 1989, **49**, 1213-1222.
6. T. Takahashi, M. N. A. Nasution and T. Kai, *Appl. Catal. A: Gen.*, 2001, **210**, 339-344.
7. G. Dahlhoff, J. P. M. Niederer and W. F. Hoelderich, *Catal. Rev.*, 2001, **43**, 381-441.
8. Y. Izumi, H. Ichihashi, Y. Shimazu, M. Kitamura and H. Sato, *Bull. Chem. Soc. Jpn.*, 2007, **80**, 1280-1287.
9. H. Sato, *Catal. Rev.*, 1997, **39**, 395-424.
10. H. Ichihashi and M. Kitamura, *Catal.Today*, 2002, **73**, 23-28.
11. S. Hiroshi and H. Ken-ichi, *Chem. Lett.*, 1993, **22**, 1765-1766.
12. J. Sirijaraensre and J. Limtrakul, *Phys. Chem. Chem. Phys.*, 2009, **11**, 578-585.
13. G. P. Heitmann, G. Dahlhoff and W. F. Hölderich, *J. Catal.*, 1999, **186**, 12-19.
14. S. Chapman, M. Potter and R. Raja, *Molecules*, 2017, **22**, 2127.
15. M. Hartmann, *Angew. Chem. Int. Ed.*, 2004, **43**, 5880-5882.
16. M. Thommes and K. A. Cychosz, *Adsorption*, 2014, **20**, 233-250.
17. *Characterization of Solid Materials and Heterogeneous Catalysts: From Structure to Surface Reactivity*, eds. M. Che and J. C. Vedrine, Wiley-VCH, Weinheim, 2012.
18. J. Rouquerol, P. Llewellyn and F. Rouquerol, in *Characterization of Porous Solids VII*, eds. P. Llewellyn, F. Rodriguez-Reinoso, J. Rouquerol and N. Seaton, Elsevier, Amsterdam, 2007, vol. 160, pp. 49-56.
19. K. Sing, *Colloids Surf., A*, 2001, **187-188**, 3-9.
20. J. Kenvin, S. Mitchell, M. Sterling, R. Warringham, T. C. Keller, P. Crivelli, J. Jagiello and J. Pérez-Ramírez, *Adv. Funct. Mater.*, 2016, **26**, 5621-5630.
21. M. C. Duke, S. J. Pas, A. J. Hill, Y. S. Lin and J. C. D. d. Costa, *Adv. Funct. Mater.*, 2008, **18**, 3818-3826.
22. A. Zubiaga, R. Warringham, M. Boltz, D. Cooke, P. Crivelli, D. Gidley, J. Pérez-Ramírez and S. Mitchell, *Phys. Chem. Chem. Phys.*, 2016, **18**, 9211-9219.

23. M. Milina, S. Mitchell, P. Crivelli, D. Cooke and J. Pérez-Ramírez, *Nature Commun.*, 2014, **5**, 3922.

24. M. Milina, S. Mitchell, D. Cooke, P. Crivelli and J. Pérez-Ramírez, *Angew. Chem.*, 2015, **127**, 1611-1614.

25. D. W. Gidley, H.-G. Peng and R. S. Vallery, *Annu. Rev. Mater. Res.*, 2006, **36**, 49-79.

26. H. Nakanishi and Y. Ujihira, *J. Phys. Chem.*, 1982, **86**, 4446-4450.

27. S. J. Tao, *J. Chem. Phys.*, 1972, **56**, 5499-5510.

28. M. Eldrup, D. Lightbody and J. N. Sherwood, *Chem. Phys.*, 1981, **63**, 51-58.

29. T. L. Dull, W. E. Frieze, D. W. Gidley, J. N. Sun and A. F. Yee, *J. Phys. Chem. B*, 2001, **105**, 4657-4662.

30. K. Ito, H. Nakanishi and Y. Ujihira, *J. Phys. Chem. B*, 1999, **103**, 4555-4558.

31. D. Dutta, S. Chatterjee, B. N. Ganguly and K. T. Pillai, *J. Appl. Phys.*, 2005, **98**, 033509.

32. M. Thommes, K. Kaneko, V. Neimark Alexander, P. Olivier James, F. Rodriguez-Reinoso, J. Rouquerol and S. W. Sing Kenneth, *Pure Appl. Chem.*, 2015, **87**, 1051-1069.

33. J. Jagiello, M. Sterling, P. Eliášová, M. Opanasenko, A. Zukal, R. E. Morris, M. Navaro, A. Mayoral, P. Crivelli, R. Warringham, S. Mitchell, J. Pérez-Ramírez and J. Čejka, *Phys. Chem. Chem. Phys.*, 2016, **18**, 15269-15277.

34. Y. C. Jean, J. D. Van Horn, W.-S. Hung and K.-R. Lee, *Macromolecules*, 2013, **46**, 7133-7145.

35. D. Dutta, S. Chatterjee, K. T. Pillai, P. K. Pujari and B. N. Ganguly, *Chem. Phys.*, 2005, **312**, 319-324.

36. R. Zaleski, A. Kierys, M. Dziadosz, J. Goworek and I. Halasz, *RSC Adv.*, 2012, **2**, 3729-3734.

37. B. Zhu, C. M. Doherty, X. Hu, A. J. Hill, L. Zou, Y. S. Lin and M. Duke, *Micropor. Mesopor. Mater.*, 2013, **173**, 78-85.

38. W. E. Farneth and R. J. Gorte, *Chem. Rev.*, 1995, **95**, 615-635.

39. L.-E. Sandoval-Díaz, J.-A. González-Amaya and C.-A. Trujillo, *Micropor. Mesopor. Mater.*, 2015, **215**, 229-243.

40. M. Hunger, *Catal. Rev.*, 1997, **39**, 345-393.

41. R. R. Pinto, P. Borges, M. A. N. D. A. Lemos, F. Lemos, J. C. Védrine, E. G. Derouane and F. R. Ribeiro, *Appli. Catal. A: Gen.*, 2005, **284**, 39-46.

42. L. M. Kustov, V. Y. Borovkov and V. B. Kazansky, *J. Catal.*, 1981, **72**, 149-159.

43. J. A. Lercher and A. Jentys, in *Introduction to Zeolite Science and Practice*, eds. J. Čejka, H. van Bekkum, A. Corma and F. Schüth, Elsevier, Amsterdam, 3 edn., 2007, vol. 168, ch. 13, pp. 435-476.

44. E. G. Derouane, J. C. Védrine, R. R. Pinto, P. M. Borges, L. Costa, M. A. N. D. A. Lemos, F. Lemos and F. R. Ribeiro, *Catal. Rev.*, 2013, **55**, 454-515.

45. E. A. Paukshtis and E. N. Yurchenko, *Russ. Chem. Rev.*, 1983, **52**, 242-258.

46. H. Knözinger, in *Elementary Reaction Steps in Heterogeneous Catalysis*, eds. R. W. Joyner and R. A. van Santen, Springer, Dordrecht, 1993, pp. 267-285.

47. J. A. Lercher, C. Gründling and G. Eder-Mirth, *Catal. Today*, 1996, **27**, 353-376.

48. F. Thibault-Starzyk, I. Stan, S. Abelló, A. Bonilla, K. Thomas, C. Fernandez, J.-P. Gilson and J. Pérez-Ramírez, *J. Catal.*, 2009, **264**, 11-14.

49. K. Góra-Marek, K. Tarach and M. Choi, *J. Phys. Chem. C*, 2014, **118**, 12266-12274.

50. D. J. Parrillo, A. T. Adamo, G. T. Kokotailo and R. J. Gorte, *Appl. Catal.*, 1990, **67**, 107-118.

51. K. Sadowska, K. Góra-Marek and J. Datka, *J. Phys. Chem. C*, 2013, **117**, 9237-9244.

52. A. G. Pelmenschikov, R. A. van Santen, J. Janchen and E. Meijer, *J. Phys. Chem.*, 1993, **97**, 11071-11074.

53. L. Kubelková, S. Beran and J. A. Lercher, *Zeolites*, 1989, **9**, 539-543.

54. F. Jin and Y. Li, *Catal. Today*, 2009, **145**, 101-107.

55. X. S. Zhao, G. Q. Lu, A. K. Whittaker, G. J. Millar and H. Y. Zhu, *J. Phys. Chem. B*, 1997, **101**, 6525-6531.

56. H. G. Karge, V. Dondur and J. Weitkamp, *J. Phys. Chem.*, 1991, **95**, 283-288.

57. B. Chakraborty and B. Viswanathan, *Catal. Today*, 1999, **49**, 253-260.

58. R. Buzzoni, S. Bordiga, G. Ricchiardi, C. Lamberti, A. Zecchina and G. Bellussi, *Langmuir*, 1996, **12**, 930-940.

59. C. A. Emeis, *J. Catal.*, 1993, **141**, 347-354.

60. T. Barzetti, E. Selli, D. Moscotti and L. Forni, *J. Chem. Soc., Faraday Trans.*, 1996, **92**, 1401-1407.

61. J. F. Haw, I. S. Chuang, B. L. Hawkins and G. E. Maciel, *J. Am. Chem. Soc.*, 1983, **105**, 7206-7207.

62. W. R. Gunther, V. K. Michaelis, R. G. Griffin and Y. Román-Leshkov, *J. Phys. Chem. C*, 2016, **120**, 28533-28544.

63. G. E. Maciel, J. F. Haw, I. S. Chuang, B. L. Hawkins, T. A. Early, D. R. McKay and L. Petrakis, *J. Am. Chem. Soc.*, 1983, **105**, 5529-5535.

64. M. S. Solum, K. L. Altmann, M. Strohmeier, D. A. Berges, Y. Zhang, J. C. Facelli, R. J. Pugmire and D. M. Grant, *J. Am. Chem. Soc.*, 1997, **119**, 9804-9809.

65. C. H. Kline Jr. and J. Turkevich, *J. Chem. Phys.*, 1944, **12**, 300-309.

66. M. Akçay, *Appl. Catal. A: Gen.*, 2005, **294**, 156-160.

67. M. Castellà-Ventura, Y. Akacem and E. Kassab, *J. Phys. Chem. C*, 2008, **112**, 19045-19054.

68. N. S. Gill, R. H. Nuttall, D. E. Scaife and D. W. A. Sharp, *J. Inorg. Nucl. Chem.*, 1961, **18**, 79-87.

69. G. V. A. Martins, G. Berlier, C. Bisio, S. Coluccia, H. O. Pastore and L. Marchese, *J. Phys. Chem. C*, 2008, **112**, 7193-7200.

70. I. Miletto, C. Ivaldi, G. Paul, S. Chapman, L. Marchese, R. Raja and E. Gianotti, *ChemistryOpen*, 2018, **7**, 297-301.

71. J. Datka, B. Gil and A. Kubacka, *Zeolites*, 1995, **15**, 501-506.

72. A. Erigoni, S. H. Newland, G. Paul, L. Marchese, R. Raja and E. Gianotti, *ChemCatChem*, 2016, **8**, 3161-3169.

73. Z. Xue, T. Zhang, J. Ma, H. Miao, W. Fan, Y. Zhang and R. Li, *Micropor. Mesopor. Mater.*, 2012, **151**, 271-276.

74. C. Baerlocher, L. B. McCusker, W. M. Meier and D. H. Olson, *Atlas of Zeolite Framework Types*, Elsevier, Amsterdam, 6 edn., 2007.

75. A. Corma, V. Fornés, L. Forni, F. Márquez, J. Martínez-Triguero and D. Moscotti, *J. Catal.*, 1998, **179**, 451-458.

76. D. Fărcaşiu, R. Leu and A. Corma, *J. Phys. Chem. B*, 2002, **106**, 928-932.

77. S. Bhatia, *Zeolite Catalysts: Principles and Applications*, CRC Press, Florida, 1989.

78. Database of Zeolite Structures, http://www.iza-structure.org/databases, (accessed January 2019).

79. B. M. Lok, C. A. Messina, R. L. Patton, R. T. Gajek, T. R. Cannan and E. M. Flanigen, *J. Am. Chem. Soc.*, 1984, **106**, 6092-6093.

80. C. S. Blackwell and R. L. Patton, *J. Phys. Chem.*, 1988, **92**, 3965-3970.

81. J. A. Martens, C. Janssens, P. J. Grobet, H. K. Beyer and P. A. Jacobs, *Stud. Surf. Sci. Catal.*, 1989, **49**, 215-225.

82. J. A. Martens, P. J. Grobet and P. A. Jacobs, *J. Catal.*, 1990, **126**, 299-305.

83. R. B. Borade and A. Clearfield, *J. Mol. Catal.*, 1994, **88**, 249-265.

84. L. Sierra de Saldarriaga, C. Saldarriaga and M. E. Davis, *J. Am. Chem. Soc.*, 1987, **109**, 2686-2691.

85. D. Barthomeuf, *J. Phys. Chem.*, 1993, **97**, 10092-10096.

86. M. Briend, M. J. Peltre, A. Lamy, P. P. Man and D. Barthomeuf, *J. Catal.*, 1992, **138**, 90-100.

87. P. P. Man, M. Briend, M. J. Peltre, A. Lamy, P. Beaunier and D. Barthomeuf, *Zeolites*, 1991, **11**, 563-572.

88. D. Barthomeuf, *Zeolites*, 1994, **14**, 394-401.

89. M. E. Potter, S. Chapman, A. J. O'Malley, A. Levy, M. Carravetta, T. M. Mezza, S. F. Parker and R. Raja, *ChemCatChem*, 2017, **9**, 1897-1900.

90. M. E. Potter, A. J. O'Malley, S. Chapman, J. Kezina, S. H. Newland, I. P. Silverwood, S. Mukhopadhyay, M. Carravetta, T. M. Mezza, S. F. Parker, C. R. A. Catlow and R. Raja, *ACS Catal.*, 2017, **7**, 2926-2934.

91. M. E. Potter, J. Kezina, R. Bounds, M. Carravetta, T. M. Mezza and R. Raja, *Catal. Sci. Technol.*, 2018, **8**, 5155-5164.

92. D. Verboekend, N. Nuttens, R. Locus, J. Van Aelst, P. Verolme, J. C. Groen, J. Pérez-Ramírez and B. F. Sels, *Chem. Soc. Rev.*, 2016, **45**, 3331-3352.

93. R. Yadav and A. Sakthivel, *Appl. Catal. A: Gen.*, 2014, **481**, 143-160.

94. R. Yadav, A. K. Singh and A. Sakthivel, *Chem. Lett.*, 2013, **42**, 1160-1162.

95. R. Yadav, A. K. Singh and A. Sakthivel, *Catal. Today*, 2015, **245**, 155-162.

96. R. Yadav, A. K. Singh and A. Sakthivel, *Catal. Lett.*, 2016, **146**, 800-810.

97. R. Yadav, A. K. Singh and A. Sakthivel, *Emerging Mater. Res.*, 2016, **5**, 232-239.

98. M. J. Franco, J. Pérez-Pariente, A. Misud, T. Blasco and J. Sanz, *Zeolites*, 1992, **12**, 386-394.

99. J. Pérez-Ramírez, C. H. Christensen, K. Egeblad, C. H. Christensen and J. C. Groen, *Chem. Soc. Rev.*, 2008, **37**, 2530-2542.

100. P. Botella, A. Corma, S. Iborra, R. Montón, I. Rodríguez and V. Costa, *J. Catal.*, 2007, **250**, 161-170.

101. M. Choi, H. S. Cho, R. Srivastava, C. Venkatesan, D.-H. Choi and R. Ryoo, *Nature Mater.*, 2006, **5**, 718.

102. M. Choi, R. Srivastava and R. Ryoo, *Chem. Commun.*, 2006, DOI: 10.1039/B612265E, 4380-4382.

103. Q. Sun, N. Wang, D. Xi, M. Yang and J. Yu, *Chem. Commun.*, 2014, **50**, 6502-6505.

104. CelRef Version 3, http://www.ccp14.ac.uk/tutorial/lmgp/celref.htm (accessed August 2018).

105. J. Kansy, *Nucl. Instrum. Methods Phys. Res. A*, 1996, **374**, 235-244.

106. B. Zhu, L. Zou, C. M. Doherty, A. J. Hill, Y. S. Lin, X. Hu, H. Wang and M. Duke, *J. Mater. Chem.*, 2010, **20**, 4675-4683.

107. C. Pascual-Izarra, A. W. Dong, S. J. Pas, A. J. Hill, B. J. Boyd and C. J. Drummond, *Nucl. Instrum. Methods Phys. Res. A*, 2009, **603**, 456-466.

108. H. Shigenobu and H. Kikuko, *Bull. Chem. Soc. Jpn.*, 1991, **64**, 685-687.

109. G. Metz, X. L. Wu and S. O. Smith, *J. Magn. Reson., Ser. A*, 1994, **110**, 219-227.

110. K. Zhang, R. P. Lively, J. D. Noel, M. E. Dose, B. A. McCool, R. R. Chance and W. J. Koros, *Langmuir*, 2012, **28**, 8664-8673.

111. K. Tsutsumi, K. Mizoe and K. Chubachi, *Colloid Polym. Sci.*, 1999, **277**, 83-88.

112. A. Endoh, K. Mizoe, K. Tsutsumi and T. Takaishi, *J. Chem. Soc., Faraday Trans. 1*, 1989, **85**, 1327-1335.

113. K. Na, C. Jo, J. Kim, K. Cho, J. Jung, Y. Seo, R. J. Messinger, B. F. Chmelka and R. Ryoo, *Science*, 2011, **333**, 328.

114. M. D. Foster, I. Rivin, M. M. J. Treacy and O. Delgado Friedrichs, *Micropor. Mesopor. Mater.*, 2006, **90**, 32-38.

115. B. P. S. Santos, N. C. Almeida, I. S. Santos, M. d. F. V. Marques and L. D. Fernandes, *Catal. Lett.*, 2018, **148**, 1870-1878.

116. R. H. P. R. Poladi and C. C. Landry, *J. Solid State Chem.*, 2002, **167**, 363-369.

117. Y.-P. Guo, H.-J. Wang, Y.-J. Guo, L.-H. Guo, L.-F. Chu and C.-X. Guo, *Chem. Eng. J.*, 2011, **166**, 391-400.

118. E. V. Spinacé, D. Cardoso and U. Schuchardt, *Zeolites*, 1997, **19**, 6-12.

119. A. F. Ojo, J. Dwyer, J. Dewing and K. Karim, *J. Chem. Soc., Faraday Trans.*, 1991, **87**, 2679-2684.

120. A. Buchholz, W. Wang, A. Arnold, M. Xu and M. Hunger, *Micropor. Mesopor. Mater.*, 2003, **57**, 157-168.

121. M. J. Peltre, P. P. Man, M. Briend, M. Derewinski and D. Barthomeuf, *Catal. Lett.*, 1992, **16**, 123-128.

122. B. Zibrowius, E. Löffler and M. Hunger, *Zeolites*, 1992, **12**, 167-174.

123. M. Hunger, M. W. Anderson, A. Ojo and H. Pfeifer, *Micropor. Mater.*, 1993, **1**, 17-32.

124. C. A. Fyfe, K. C. Wong-Moon, Y. Huang and H. Grondey, *Micropor. Mater.*, 1995, **5**, 29-37.

125. J. A. Martens, C. Janssens, P. J. Grobet, H. K. Beyer and P. A. Jacobs, *Stud. Surf. Sci. Catal.*, 1989, **49**, 215-225.

126. M. Linares, C. Vargas, A. García, C. Ochoa-Hernández, J. Čejka, R. A. García-Muñoz and D. P. Serrano, *Catal. Sci. Technol.*, 2017, **7**, 181-190.

127. C. H. L. Tempelman, X. Zhu, K. Gudun, B. Mezari, B. Shen and E. J. M. Hensen, *Fuel Process. Technol.*, 2015, **139**, 248-258.

128. K. Qiao, F. Zhou, Z. Han, J. Fu, H. Ma and G. Wu, *Micropor. Mesopor. Mater.*, 2019, **274**, 190-197.

129. M. Hunger, J. Kärger, H. Pfeifer, J. Caro, B. Zibrowius, M. Bülow and R. Mostowicz, *J. Chem. Soc., Faraday Trans. 1*, 1987, **83**, 3459-3468.

130. M. Hunger, *Solid State Nucl. Magn. Reson.*, 1996, **6**, 1-29.

131. T.-H. Chen, B. H. Wouters and P. J. Grobet, *J. Phys. Chem. B*, 1999, **103**, 6179-6184.

132. P. O'Sullivan, L. Forni and B. K. Hodnett, *Ind. Eng. Chem. Res.*, 2001, **40**, 1471-1475.

133. L. Marchese, A. Frache, G. Gatti, S. Coluccia, L. Lisi, G. Ruoppolo, G. Russo and H. O. Pastore, *J. Catal.*, 2002, **208**, 479-484.

134. M. Popova, C. Minchev and V. Kanazirev, *Appl. Catal. A: Gen.*, 1998, **169**, 227-235.

135. H. B. Mostad, M. Stöcker, A. Karlsson and T. Rørvik, *Appl. Catal. A: Gen.*, 1996, **144**, 305-317.

136. S.-T. Yang, J.-Y. Kim, H.-J. Chae, M. Kim, S.-Y. Jeong and W.-S. Ahn, *Mater. Res. Bull.*, 2012, **47**, 3888-3892.

137. S. Tao, X. Li, G. Lv, C. Wang, R. Xu, H. Ma and Z. Tian, *Catal. Sci. Technol.*, 2017, **7**, 5775-5784.

138. C. Wang, M. Yang, P. Tian, S. Xu, Y. Yang, D. Wang, Y. Yuan and Z. Liu, *J. Mater. Chem. A*, 2015, **3**, 5608-5616.

139. I. G. Shenderovich, G. Buntkowsky, A. Schreiber, E. Gedat, S. Sharif, J. Albrecht, N. S. Golubev, G. H. Findenegg and H.-H. Limbach, *J. Phys. Chem. B*, 2003, **107**, 11924-11939.

140. D. Freude, *Chem. Phys. Lett.*, 1995, **235**, 69-75.

141. A. Zheng, S.-B. Liu and F. Deng, *Solid State Nucl. Magn. Res.*, 2013, **55-56**, 12-27.

142. D. Freude, M. Hunger, H. Pfeifer and W. Schwieger, *Chem. Phys. Lett.*, 1986, **128**, 62-66.

143. J. Huang, Y. Jiang, V. R. Reddy Marthala, Y. S. Ooi, J. Weitkamp and M. Hunger, *Micropor. Mesopor. Mater.*, 2007, **104**, 129-136.

144. M. Xu, A. Arnold, A. Buchholz, W. Wang and M. Hunger, *J. Phys. Chem. B*, 2002, **106**, 12140-12143.

145. W. P. J. H. Jacobs, D. G. Demuth, S. A. Schunk and F. Schüth, *Micropor. Mater.*, 1997, **10**, 95-109.

146. M. A. Camblor, A. Corma, H. García, V. Semmer-Herlédan and S. Valencia, *J. Catal.*, 1998, **177**, 267-272.

147. C. Ngamcharussrivichai, P. Wu and T. Tatsumi, *J. Catal.*, 2004, **227**, 448-458.

148. P. Albers, K. Seibold, T. Haas, G. Prescher and W. F. Hölderich, *J. Catal.*, 1998, **176**, 561-568.

149. T. Yashima, K. Miura and T. Komatsu, *Stud. Surf. Sci. Catal.*, 1994, **84**, 1897-1904.

150. Z. Hu, H. Zhang, L. Wang, H. Zhang, Y. Zhang, H. Xu, W. Shen and Y. Tang, *Catal. Sci. Technol.*, 2014, **4**, 2891-2895.

151. J. C. Groen, L. A. A. Peffer, J. A. Moulijn and J. Pérez-Ramírez, *Chem. - A Eu. J.*, 2005, **11**, 4983-4994.

152. A. H. Janssen, A. J. Koster and K. P. d. Jong, *Angew. Chem. Int. Ed.*, 2001, **40**, 1102-1104.

153. J. Garcia-Martinez, C. Xiao, K. A. Cychosz, K. Li, W. Wan, X. Zou and M. Thommes, *ChemCatChem*, 2014, **6**, 3110-3115.

154. S. Mitchell, N.-L. Michels, K. Kunze and J. Pérez-Ramírez, *Nature Chem.*, 2012, **4**, 825.

155. K. Cho, H. S. Cho, L.-C. de Ménorval and R. Ryoo, *Chem. Mater.*, 2009, **21**, 5664-5673.

156. C. H. Ko and R. Ryoo, *Chemical Communications*, 1996, **21**, 2467-2468.

157. T. Kobayashi, F. A. Perras, I. I. Slowing, A. D. Sadow and M. Pruski, *ACS Catal.*, 2015, **5**, 7055-7062.

Chapter 6 Conclusions

Motivated by the enhanced performance of organosilane-templated, HP SAPOs (hierarchically-porous silicoaluminophosphates) in the Beckmann rearrangement (BR), a spectroscopic investigation was undertaken to determine the role of the siliceous mesopore network. In characterising the interactions of cyclohexanone oxime with HP SAPO, the frameworks SAPO-34, HP SAPO-34, and HP AlPO-5 were selected in order to deconvolute the catalytic contributions of the silanols, from the mass transport effects of the mesopores. INS, MAS NMR, and FTIR spectroscopies identified a limited interaction between cyclohexanone oxime and microporous SAPO-34 at ambient temperatures, with spectral features attributed to the framework Brønsted acid sites largely retained on exposure to the oxime. These observations reflected the inaccessibility of the internal Brønsted sites *via* the micropores, under the conditions required for these fundamental studies. In contrast, when cyclohexanone oxime was combined with a HP catalyst, significant substrate-framework interactions were observed. Where INS studies indicated that weakly acidic silanol sites within the mesopores disrupt the stable, hydrogen-bonded trimer of the solid oxime, DFT calculations found this to be an energetically favourable process. Notably, HP SAPO-34 was the only system where there was (MAS NMR and FTIR) evidence for the formation of the *N*-protonated oxime at ambient temperature. Since cyclohexanone oxime was not protonated by HP AlPO-5 under the same conditions, protonation by the weakly acidic silanols was excluded. Equally, there was no evidence of oxime protonation by the external Brønsted acid sites of SAPO-34. Therefore, in a physical mixture, neither Brønsted sites, nor silanols alone, effected protonation of cyclohexanone oxime.

Thus, it was proposed that the enhanced catalytic performance of HP SAPO-34 was due to the cooperativity of silanol and Brønsted acid sites, as well as the mass transport capabilities of the mesopores. Computational and spectroscopic analyses indicated that the uptake of the oxime occurred *via* the mesopores, where hydrogen-bonding interactions with the local silanol sites led to disintegration of the trimeric oxime structure. There was evidence that the isolated oxime molecules could then participate in activating interactions, predominantly through *N*-hydrogen bonding (and some *O*-hydrogen bonding) to the silanols. However, where a Brønsted acid site was made accessible through the interconnectivity of the micro- and mesoporous structures (as in HP SAPO-34), the theoretical studies gave indication of an energetic driving force for the oxime to bind to the stronger acid sites. It was proposed that the lower deprotonation energy of the Brønsted site (versus the silanol) facilitated the *N*-protonation observed spectroscopically, at ambient temperature.

The interactions identified by INS, FTIR, and NMR spectroscopies were also found to influence the mobility of cyclohexanone oxime in HP SAPO. In a QENS investigation, the molecular dynamics of cyclohexanone oxime was studied in MP and HP SAPO-5, since the micropore dimensions were expected to allow intracrystalline diffusion. The motion of the oxime was monitored by means of an elastic window scan from < 50 - 373 K, which delineated three temperature regimes. From < 50 - 200 K, the mobility of cyclohexanone oxime increased to a similar degree with both MP and HP SAPO-5 adsorbents. As the temperature was raised further, the increased proton dynamics in HP *versus* MP SAPO-5 was thought to reflect the greater freedom for movement available in the mesopores. Significantly, at > 320 K, the trend in mobility was reversed and the oxime was relatively more mobile in MP SAPO-5 than HP SAPO-5. Neutron diffraction data revealed that in the presence of MP SAPO-5, cyclohexanone oxime retained some long-range order up to 338 K. In contrast, diffraction analysis of the HP SAPO-5 sample showed no evidence of crystalline oxime, even at < 50 K. It was proposed that, in HP SAPO-5, the long-range structure of the solid oxime was disrupted by the same type of hydrogen bonding interactions that were evidenced in HP SAPO-34 and HP AlPO-5. Therefore, the reduced mobility of cyclohexanone oxime in HP SAPO-5 at > 320 K was attributed to the adsorption of oxime molecules at silanol sites in the mesopores. Further analysis indicted that the proton dynamics in HP and MP SAPO-5 were largely due to the localised motion of the oxime. Specifically, the motion of the oxime was best fit to isotropic rotation, which (being identical in both geometry and rate in both frameworks) was thought to occur within the micropores. The data fitting quantified a larger fraction of immobile oxime in HP SAPO-5 (0.54) than MP SAPO-5 (0.23), which was consistent with the adsorption of some oxime molecules within the mesopores.

Since the hydrogen-bonding interactions in HP SAPO-5 had consequences for the mobility of the BR substrate, it was considered that a similar interaction might also affect the mobility of BR the product (with implications for the catalyst selectivity). However, the elwins obtained in a QENS study of ε-caprolactam sorbed in HP and MP SAPO-5 were near identical between < 70 – 373 K. So although the diffraction data suggested that lactam-silanol hydrogen bonding interactions were active in HP SAPO-5, these had less impact on the mobility of caprolactam than on the mobility of cyclohexanone oxime. Analysis of the QENS spectra at 373 K suggested that isotropic rotation of the lactam occurred in both frameworks (at the same rotational rate), yet the mobile fraction of lactam was slightly larger in MP SAPO-5 (0.45) than HP SAPO-5 (0.34). Nevertheless, the QENS study indicated that lactam-silanol hydrogen bonding interactions were less detrimental to the total caprolactam mobility than the steric confinement of the micropores.

Where these (and other) studies have demonstrated the enhanced activity and lifetime of hierarchically-porous SAPOs in the BR, a new synthetic target was identified. MP SAPO-37 is high-yielding catalyst for the BR, but its performance in the liquid-phase transformation is subject to low activity, and its lifetime in the vapour-phase reaction is restricted by coking. Thus, an opportunity was identified to use hierarchical structuring to improve the mass transport properties of SAPO-37. A hierarchical (HP) SAPO-37 material was prepared with retention of the microporous, faujasitic structure by soft-templating with an organosilane mesoporogen. Low-angle XRD, N_2 gas adsorption, and TEM imaging identified the presence of mesoporous structures in HP SAPO-37. Moreover, positron annihilation lifetime spectroscopy indicated that the interconnectivity of the micro- and meso-pores improved the accessibility of the external surface. MAS NMR revealed siliceous regions in HP SAPO-37 deriving from the mesopore template agent, which were associated with the development of silanol sites in the mesopores. NH_3-TPD analyses suggested that the bulk acidity of HP SAPO-37 was moderated by the presence of the silanols, yet HP SAPO-37 also contained a smaller number of strong acid sites that were not identified in MP SAPO-37. Nonetheless, probe-based characterisation *via* NMR and FTIR spectroscopies indicated that the acid-base interactions of HP SAPO-37 were dominated by the weaker acid sites. The weaker acidity of HP SAPO-37 (*versus* MP SAPO-37) was exploited in the vapour-phase BR at 300 °C. Under these conditions, HP SAPO-37 sustained > 99 % conversion (at > 94 % selectivity for ε-caprolactam) over 8 hours on-stream, whilst conversion declined to < 35 % using MP SAPO-37. Chemical and physical analysis of the post-catalysis samples indicated that the siliceous mesopores in HP SAPO-37 had increased its resistance to deactivation by coking.

Collectively, the investigations reported in this thesis have provided an insight into the impact of organosilane soft-templating on the structure and chemistry of the HP SAPO, and go some way to evaluating the structure-activity relationships that underpin their activity in the BR. More broadly, these studies demonstrate how a multidisciplinary approach to materials characterisation can provide a mechanistic rationale for targeted catalyst design.